Adam Mickiewicz University in Poznań

Uniwersytet im. Adama Mickiewicza w Poznaniu

DOCTORAL THESIS

Teng Zheng

Lanthanide (III or II) activated SrB_4O_7 and $BaTiO_3$ materials for luminescent manometry and non-linear optical thermometry

in the form of a thematically coherent series of scientific articles published in scientific journals, prepared in the field of Science, in the discipline of Chemical Sciences

Supervisor: prof. dr hab. Stefan Lis

Acknowledgements

Upon the completion of this thesis, I am so grateful to those who provided me great encouragement and support during my PhD studies. First of all, I wish to express my deepest grateful acknowledgement to my supervisor Prof. Stefan Lis, who gave me the great opportunity to travel abroad to Poland and gave me considerable help in my studies and research work during my doctoral studies. His enthusiasm and kind help have supported me whenever I faced a problem. I do appreciate his patience, encouragement, and professional instructions while doing and writing my dissertation. Second, I would like to express my heartfelt gratitude to Dr. Marcin Runowski, whose encouragement and unwavering support has sustained me through frustration and depression by means of suggestion, comments, and criticism. He spent so much time reading and correcting each draft of our scientific papers and the thesis, and provided me with inspiring advices. Without his patient instruction, insightful criticism and expert guidance, the completion of the fruitful scientific research would not have been possible. Besides my supervisors, I benefited from many other teachers and professors, thank you for your kind help and patience.

Moreover, I sincerely acknowledge the national and international collaboration from different countries. I would like to thank Prof. Victor Lavin, Prof. Inocencio Martin, Mr. Kevin Soler-Carracedo and other members of this group from the University of La Laguna. Thank you for your hospitality in Tenerife, stimulating talks and kindly support. I also sincerely acknowledge the great help from Prof. Eugeniusz Zych and Dr. Małgorzata Sójka from University of Wroclaw. Thank you so much for the inspiring comments and the rich scientific results we have obtained from the cooperation. In addition, I also would like to express my gratefulness to Prof. Peng Du, Prof. Laihui Luo, who helped me with the publications and gave me great suggestions for my scientific career.

I have a special debt of gratitude to our excellent colleagues, especially Mrs. Małgorzata Skwierczyńska, Dr. Szymon Goderski, Dr. Przemysław Woźny, Mrs. Natalia Stopikowska, who gave me their help and time listen to me and help me solve my problems during my 4-year PhD studies. It was their kindness and care that made me study and happily live in AMU.

Finally, I would like to thank my beloved family for their unfailing love and support. For so many years, they have always been supporting me and respecting me. Their love and care are the greatest fortune of my life. I also would like to express my heart-felt thanks to my girlfriend, Ruifang. Thank you for your great patience and loving considerations, that are the source of my strength toward future challenges.

Teng Zheng

01.02.2022 Poznań

This research was financed by European Union through the European Social Fund under the Operational Program Knowledge Education Development (grant No. POWR.03.02.00–00-i020/17)

which is greatly appreciated

Table of Content

List of acronyms

Energy transfer - ET

Ground state absorption - GSA

Near infrared - NIR

High pressure - HP

Fluorescence/luminescence intensity ratio - FIR/LIR

Thermally coupled levels - TCL

Lanthanide - Ln

Rare earth - RE

Electric dipole -ED

Photoluminescence – PL

Upconversion - UC

Upconversion Luminescence - UCL

Second harmonic generation – SHG

1. The objectives of the dissertation

Temperature and pressure, as important and fundamental physical variables, influence all physicochemical processes in natural and engineered systems, ranging from macroscopic environments, micron- and nano-sized spaces, to the interactions between molecular, ions and atoms. Therefore, the precise determination of temperature and pressure is very important in not only scientific research, but also for industrial manufacturers. The main aim of the dissertation was to investigate whether the carefully designed SrB_4O_7 and $BaTiO_3$ host matrices combined with selected lanthanide ions enable the design of a luminescent manometer and a nonlinear optical thermometer with excellent sensing performances. The choice of the oxide matrix host is to ensure high chemical stability of the composition structure in a given temperature and pressure range.

The idea of using the inter-configurational 5d-4f transition for optical thermometry and manometry is related to the fact that the interaction of the crystal field with 5d-electrons is ~50 times more intense than with 4f electrons, resulting from the electrons in the 5d orbitals being exposed directly to the external environment. In order to find a suitable host, we explore the influence of the borate matrix on the PL properties, as well as the stabilization of Eu^{2+}, in order to find the best matrix host for Eu^{2+}, which are presented in article **A1**. Moreover, I investigated the energy transfer process in a Sm^{2+}-Eu^{2+} co-doped SrB_4O_7 system (host with the best stabilization of Ln^{2+}) and use the ET for enhancement of the Sm^{2+} pressure sensing signal, as shown in article **A2**. Subsequently, the HP-enhanced 4f-4f transition of Eu^{2+} for use in high pressure sensing was explored, as demonstrated in article **A3**. Finally, I successfully stabilized the Tm^{2+} ion in SrB_4O_7 and used it as a bifunctional platform for both temperature and pressure sensing, as presented in article **A4**.

Importantly, the idea of non-linear optical thermometry is inspired by the observation of the SHG signal as well as the intense UCL in the $BaTiO_3$ material doped with Er^{3+}-Yb^{3+} or Ho^{3+}-Yb^{3+}, as presented in articles **A5** and **A6**. SHG is a polarization-sensitive, instantaneous nonlinear optical process that is very sensitive to the change in symmetry of materials (between centrosymmetric and non-centrosymmetric structure). With increasing temperature, different phase transitions of $BaTiO_3$, especially cubic to tetragonal, lead to interesting spectroscopic changes in both SHG and UCL, leading to the feasibility of nonlinear optical thermometry using the band intensity ratio of SHG/UCL as a thermometric parameter.

The presented doctoral dissertation is based on the following scientific articles:

Appendix **A1**: **Teng Zheng**, Marcin Runowski, Przemysław Woźny, Stefan Lis, Influence of matrix on the luminescence properties of Eu^{2+}/Eu^{3+} doped strontium borates: SrB_4O_7, SrB_2O_4 and $Sr_3(BO_3)_2$, exhibiting multicolor tunable emission, Journal of Alloys and Compounds (IF = 5.316, MNiSW = 100), 2020, 822, 153511-153519 (9).

Appendix **A2**: **Teng Zheng**, Marcin Runowski, Przemysław Woźny, Stefan Lis, Victor Lavin, Huge enhancement of Sm^{2+} emission via Eu^{2+} energy transfer in a SrB_4O_7 pressure sensor, Journal of Materials Chemistry C (IF = 7.393, MNiSW=140), 2020, 8, 4810-4817(8).

Appendix **A3**: **Teng Zheng,** Marcin Runowski, Plácida Rodríguez-Hernández, Alfonso Muñoz, Francisco J. Manjón, Małgorzata Sójka, Markus Suta, Eugeniusz Zych, Stefan Lis and Víctor Lavín, Pressure-driven Configurational Crossover between $4f^7$ and $4f^65d^1$ States – Giant Enhancement of Narrow Eu^{2+} UV-Emission Lines in SrB_4O_7 for Luminescence Manometry, Acta Materialia (IF = 8.203, MNiSW = 200), 2022, 231, 117886**.**

Appendix **A4**: **Teng Zheng,** Małgorzata Sójka, Marcin Runowski, Przemysław Woźny, Stefan Lis, and Eugeniusz Zych, Tm^{2+} Activated SrB_4O_7 Bifunctional Sensor of Temperature and Pressure — Highly Sensitive, Multi-Parameter Luminescence Thermometry and Manometry, Advanced Optical materials (IF = 9.926, MNiSW = 140), 2021, 2101507.

Appendix **A5**: **Teng Zheng,** Marcin Runowski, Inocencio R. Martín, Stefan Lis, Mauricio Vega, and Jaime Llanos, Nonlinear Optical Thermometry — A Novel Temperature Sensing Strategy via Second Harmonic Generation (SHG) and Upconversion Luminescence in $BaTiO_3$: Ho^{3+}, Yb^{3+} Perovskite, Advanced Optical Materials (IF = 9.926, MNiSW = 140), 2021, 9, 2100386

Appendix **A6**: **Teng Zheng**, Marcin Runowski, Przemysław Woźny, Bolesław Barszcz, Stefan Lis, Mauricio Vega, Jaime Llanos, Kevin Soler-Carracedo and Inocencio R. Martín, Boltzmann vs. non-Boltzmann (non-linear) Thermometry - Yb^{3+}-Er^{3+} Activated Dual-mode Thermometer and Phase Transition Sensor via Second Harmonic Generation, Journal of Alloys and Compounds, Journal of Alloys and Compounds (IF = 5.316, MNiSW = 100), 2022, 906, 164329.

Other scientific publications (not included in the doctoral dissertation)

Teng Zheng, Laihui Luo, Peng Du, Stefan Lis, Ulises R Rodríguez-Mendoza, Víctor Lavín, Marcin Runowski, Pressure-triggered Enormous Redshift and Enhanced Emission in

$Ca_2Gd_8Si_6O_{26}:Ce^{3+}$ phosphors: Ultrasensitive, Thermally-stable and Ultrafast Response Pressure monitoring, Chemical Engineering Journal (IF=13.273, MNiSW = 200), 443 (2022) 136414**.**

Teng Zheng, Laihui Luo, Peng Du, Stefan Lis, Ulises R. Rodríguez-Mendoza, Víctor Lavín, Marcin Runowski, Highly-efficient double perovskite Mn^{4+}-activated Gd_2ZnTiO_6 phosphors: A bifunctional optical sensing platform for luminescence thermometry and manometry, Chemical Engineering Journal, (IF=13.273, MNiSW = 200), accepted**.**

Teng Zheng, Laihui Luo, Peng Du, Anmeng Deng, Weiping Li. Ferroelectric, upconversion emission and optical thermometric properties of color-controllable Er^{3+}-doped $Pb(Mg_{1/3}Nb_{2/3})O_3$-$PbTiO_3$-$Pb(Yb_{1/2}Nb_{1/2})O_3$ piezoelectric ceramics. Journal of the European Ceramic Society (IF = 5.302, MNiSW = 140), 38 (2018) 575-583.

Teng Zheng, Marcin Runowski, Natalia Stopikowska, Małgorzata Skwierczyńska, Stefan Lis, Peng Du, Laihui Luo, Dual-center thermochromic $Bi_2MoO_6:Yb^{3+}$, Er^{3+}, Tm^{3+} phosphors for ultrasensitive luminescence thermometry, Journal of Alloys and Compounds (IF = 5.316, MNiSW = 100), 2021,890,161830.

Teng Zheng, Xujun Qiu, Luhui Zhou, Marcin Runowski, Stefan Lis, Peng Du, Laihui Luo, Multiple ratiometric nanothermometry operating with Stark thermally and non-thermally-coupled levels in upconverting $Y_{2-x}MoO_6:xEr^{3+}$ nanoparticles, Journal of Alloys and Compounds (IF = 5.316, MNiSW = 100), 2021-864,158891.

Teng Zheng, Laihui Luo. Linear response fluorescent temperature sensing properties and strategy based on Stark sublevels of Er^{3+}-doped $0.86(Pb(Mg_{1/3}Nb_{2/3})O_3$-$PbTiO_3)$-$0.14Pb(Yb_{1/2}Nb_{1/2})O_3$ ceramics. Ceramics International (IF = 4.527, MNiSW = 100). 44 (2018) 12670-12675.

Teng Zheng, Luhui Zhou, Xujun Qiu, Dan Yang, Marcin Runowski, Stefan Lis, Peng Du, Laihui Luo, Er^{3+}, Yb^{3+} co-doped $Sr_3(PO_4)_2$ phosphors: A ratiometric luminescence thermometer based on Stark levels with tunable sensitivity, Journal of luminescence (IF= 3.599, MNiSW=100), 2020, 227, 117517.

Małgorzata Sójka, Marcin Runowski, **Teng Zheng,** Andrii Shyichuk, Dagmara Kulesza, Eugeniusz Zych and Stefan Lis, Eu^{2+} emission from thermally coupled levels – new frontiers for ultrasensitive luminescence thermometry, Journal of Materials Chemistry C (IF=7.393, MNiSW = 140), 2022, 10, 1220-1227.

Marcin Runowski, **Teng Zheng,** Przemysław Woźny, Peng Du. NIR Emission of Lanthanides for Ultrasensitive Luminescence Manometry - Er^{3+}-activated Optical Sensor of High Pressure, Dalton Transactions (IF = 4.39, MNiSW = 140), 2021, 1772.

2. Scientific resume

Teng Zheng

Gender: Male Date of Birth: 04/12/1992

Mobile: +48669697422 Email: zhengteng945@gmail.com

Address: ul. Piątkowska 80B, 60-649 Poznan, Poland

EDUCATIONAL BACKGROUND

Adam Mickiewicz University Poznan, Poland **10/2018- present**

Doctoral degree in Material Chemistry (in English)

Ningbo University Zhejiang, China **09/2015-06/2018**

Master's degree in Optoelectronic Physics

Hunan University of science and technology Hunan, China **09/2011-06/2015**

Bachelor's degree in Physics

RESEARCH FIELDS

- Nonlinear optical process, **optical second harmonic generation** phenomenon in inorganic crystals.
- **High-pressure photoluminescence/Structural properties** of d-block element and lanthanide doped inorganic materials.
- **Non-invasive temperature sensing** technique, optical Boltzmann thermometry, non-Boltzmann thermometry, temperature sensing based on Stark sublevels.
- **Lanthanide based Up-conversion/downshifting Nano-/microparticles.**
- **Phase transitions of inorganic materials under temperature and pressure.**

◆ Piezoelectric and **ferroelectric ceramics** and thin film and so on.

RESEARCH PAPERS

Published papers (Total 15 papers, first author of 12 SCI papers, IF total: 108.473)

Teng Zheng, Laihui Luo, Peng Du, Stefan Lis, Ulises R Rodríguez-Mendoza, Víctor Lavín, Marcin Runowski, Pressure-triggered Enormous Redshift and Enhanced Emission in $Ca_2Gd_8Si_6O_{26}:Ce^{3+}$ phosphors: Ultrasensitive, Thermally-stable and Ultrafast Response Pressure monitoring, Chemical Engineering Journal (IF=13.273), 443 (2022) 136414**.**

Teng Zheng, Laihui Luo, Peng Du, Stefan Lis, Ulises R. Rodríguez-Mendoza, Víctor Lavín, Marcin Runowski, Highly-efficient double perovskite Mn^{4+}-activated Gd_2ZnTiO_6 phosphors: A bifunctional optical sensing platform for luminescence thermometry and manometry, Chemical Engineering Journal, (IF=13.273), accepted**.**

Teng Zheng, Marcin Runowski, Inocencio R. Martín, Stefan Lis, Mauricio Vega, and Jaime Llanos, Nonlinear Optical Thermometry - A Novel Temperature Sensing Strategy via Second Harmonic Generation (SHG) and Upconversion Luminescence in $BaTiO_3$: Ho^{3+}, Yb^{3+} Perovskite, Advanced Optical materials (IF = 9.926), 2021, 9, 2100386

Teng Zheng, Małgorzata Sójka, Marcin Runowski, Przemysław Woźny, Stefan Lis, and Eugeniusz Zych, Tm^{2+} Activated SrB_4O_7 Bifunctional Sensor of Temperature and Pressure - Highly Sensitive, Multi-Parameter Luminescence Thermometry and Manometry, Advanced Optical materials (IF = 9.926), 2021, 2101507.

Teng Zheng, Marcin Runowski, Plácida Rodríguez-Hernández, Alfonso Muñoz, Francisco J. Manjón, Małgorzata Sójka, Markus Suta, Eugeniusz Zych, Stefan Lis and Víctor Lavín, Pressure-driven Configurational Crossover between $4f^7$ and $4f^65d^1$ States – Giant Enhancement of Narrow Eu^{2+} UV-Emission Lines in SrB_4O_7 for Luminescence Manometry, Acta Materialia (IF=8.203), 231(2022)117886**.**

Teng Zheng, Marcin Runowski, Przemysław Woźny, Stefan Lis, Victor Lavin, Huge enhancement of Sm^{2+} emission via Eu^{2+} energy transfer in a SrB_4O_7 pressure sensor, Journal of Materials Chemistry C (IF =7.393), 2020, 8, 4810-4817(8).

Teng Zheng, Laihui Luo, Peng Du, Anmeng Deng, Weiping Li. Ferroelectric, upconversion emission and optical thermometric properties of color-controllable Er^{3+}-doped $Pb(Mg_{1/3}Nb_{2/3})O_3$-

$PbTiO_3$-$Pb(Yb_{1/2}Nb_{1/2})O_3$ piezoelectric ceramics. Journal of the European Ceramic Society (IF = 5.302), 38 (2018) 575-583.

Teng Zheng, Marcin Runowski, Natalia Stopikowska, Małgorzata Skwierczyńska, Stefan Lis, Peng Du, Laihui Luo, Dual-center thermochromic Bi_2MoO_6:Yb^{3+}, Er^{3+}, Tm^{3+} phosphors for ultrasensitive luminescence thermometry, Journal of Alloys and Compounds (IF= 5.316), 2021,890,161830.

Teng Zheng, Xujun Qiu, Luhui Zhou, Marcin Runowski, Stefan Lis, Peng Du, Laihui Luo, Multiple ratiometric nanothermometry operating with Stark thermally and non-thermally-coupled levels in upconverting $Y_{2-x}MoO_6$:xEr^{3+} nanoparticles, Journal of Alloys and Compounds (IF = 5.316), 2021-864,158891.

Teng Zheng, Marcin Runowski, Przemysław Woźny, Stefan Lis, Influence of matrix on the luminescence properties of Eu^{2+}/Eu^{3+} doped strontium borates: SrB_4O_7, SrB_2O_4 and $Sr_3(BO_3)_2$, exhibiting multicolor tunable emission, Journal of Alloys and Compounds (IF= 5.316), 2020, 822, 153511-153519 (9).

Teng Zheng, Marcin Runowski, Przemysław Woźny, Bolesław Barszcz, Stefan Lis, Mauricio Vega, Jaime Llanos, Kevin Soler-Carracedo and Inocencio R. Martín, Boltzmann vs. non-Boltzmann (non-linear) Thermometry - Yb^{3+}-Er^{3+} Activated Dual-mode Thermometer and Phase Transition Sensor via Second Harmonic Generation, Journal of Alloys and Compounds, Journal of Alloys and Compounds (IF= 5.316), 2022, 906, 164329.

Teng Zheng, Laihui Luo. Linear response fluorescent temperature sensing properties and strategy based on Stark sublevels of Er^{3+}-doped $0.86(Pb(Mg_{1/3}Nb_{2/3})O_3$-$PbTiO_3)$-$0.14Pb(Yb_{1/2}Nb_{1/2})O_3$ ceramics .Ceramics International (IF= 4.527). 44 (2018) 12670-12675.

Teng Zheng, Luhui Zhou, Xujun Qiu, Dan Yang, Marcin Runowski, Stefan Lis, Peng Du, Laihui Luo, Er^{3+}, Yb^{3+} co-doped $Sr_3(PO_4)_2$ phosphors: A ratiometric luminescence thermometer based on Stark levels with tunable sensitivity, Journal of luminescence (IF = 3.599), 2020, 227, 117517.

Małgorzata Sójka, Marcin Runowski, **Teng Zheng,** Andrii Shyichuk, Dagmara Kulesza, Eugeniusz Zych and Stefan Lis, Eu^{2+} emission from thermally coupled levels – new frontiers for ultrasensitive luminescence thermometry, Journal of Materials Chemistry C (IF=7.393), 2021.

Marcin Runowski, **Teng Zheng,** Przemysław Woźny, Peng Du. NIR Emission of Lanthanides for Ultrasensitive Luminescence Manometry - Er^{3+}-activated Optical Sensor of High Pressure, Dalton Transactions (IF = 4.39), 2021, 1772.

AWARDS

Rector's Grant for PhD students (stypendium rektora doktorant – studia stacjonarne) - 2021 - Adam Mickiewicz University;

UAM doctoral student scholarship - Styoendium doktoranckie UAM – 2018-2022 – Adam Mickiewicz University;

Cao Guangbiao Science scholarship -2018- Ningbo University, twice;

Ningbo Univerisity Master-students reward for– 2015-2018-Ningbo University.

INTERNATIONAL CONFERENCE

- 9 - 14. June. 2019, Wrocław - **8th International Symposium on Optical Materials** - **T. Zheng**; M. Runowski; P. Woźny; S. Lis. Influence of reaction temperature and Sm^{2+} concentration on structural and Spectroscopic Properties of SrB_4O_7: Sm^{2+} and SrB_6O_{10}: Sm^{2+} nanomaterials - (poster presentation).
- 14 - 16. April. 2019, Poznań - **12th Frolic Goats Workshop on High Pressure Diffraction** - **T. Zheng**; M. Runowski; P. Woźny; S. Lis. Influence of Matrix on the Luminescence Properties of Eu^{2+}/Eu^{3+} Doped Strontium Borates: SrB_4O_7, $Sr(B_2O_4)$ and $Sr_3(BO_3)_2$, exhibiting multicolor tunable luminescence - (poster presentation).
- 13 - 15. October. 2020, online - **Symposium on Advanced Technologies and Materials (preATAM 2020 online)** - **T. Zheng**; M. Runowski; P. Woźny; S. Lis; V. Lavin. Huge Enhancement of Sm^{2+} luminescence via Eu^{2+} codoping in Strontium Tetraborates – Studies under High Pressure and Temperature conditions - (poster presentation).
- 29. March - 1. April. 2021, online - **23rd JCF-Frühjahrssymposium online conference** - **T. Zheng**; M. Runowski; P. Woźny; S. Lis; V. Lavin. Highly Enhanced Sm^{2+} Emission by Energy Transfer in SrB_4O_7: Eu^{2+}, Sm^{2+} Optical Pressure Sensor - (**oral presentation**).
- 19 - 20. April. 2021, Poznan, Poland. **14th Frolic Goat High-pressure Diffraction**

conference (online)- **T. Zheng**; M. Runowski; P. Woźny; S. Lis; V. Lavin. Giant Enhancement of Sm^{2+} Emission via Eu^{2+} Codoping in Strontium Tetraborates for Pressure Sensing - (**oral presentation**).

- 26-30. June, 2021, Changchun, China. **19th International Conference on Luminescence (ICL2020 online)** - **T. Zheng**; M. Runowski; I.R. Martín; S. Lis; M. Veg; J. Llanos. Nonlinear optical thermometry – A novel strategy to probe temperature using second harmonic generation (SHG) and upconversion luminescence - (**oral presentation**).
- 30 August to 10 September, 2021, Valencia, Spain. **High Pressure Spanish School 2021 (EEAP 2021) – T. Zheng**; M. Runowski; P. Woźny; S. Lis; V. Lavin. Huge Enhancement of Sm^{2+} Emission via Eu^{2+} Codoping in Strontium Tetraborates (SrB_4O_7) for Pressure Sensing application - **(oral presentation**).
- 06-11, September, 2020, Tenerife, Spain - **58th EHPRG International Conference on High pressure science and technology** – M. Runowski, **T. Zheng**, P. Woźny, S. Lis, I. R. Martín and V. Lavín - Development of new optical sensors of low and high pressure, based on luminescence of lanthanide ions.

RESEARCH PROJECTS

- **Doctoral Project - Department of Rare-earth, Adam Mickiewicz University, Poznan, Poland**

Surface modified multifunctional, luminescent hybrid nanomaterials and their biological importance *(Polish name: Powierzchniowo modyfikowane hybrydowe, wielofunkcyjne nanomateriały luminescencyjne i ich znaczenie biologiczne)*

Group leader: Prof. dr. hab. Stefan Lis

Grant number: 2016/21/B/ST5/00110 *Total funding: 1 246 800,00 PLN (about 277 000 euro)*

Duration: 3 years *Relationship: Employed with salary as a PhD student*

Main responsibility:

Search literature, optimize experimental methods under the guidance;

Synthesis of inorganic nanomaterials doped with lanthanides (using sol-gel method, modified Pechini method)

Physicochemical characterization of the synthesized samples, writing publications.

- **Doctoral Project - Department of Rare-earth, Adam Mickiewicz University, Poznan, Poland**

Investigation of the high-pressure influence on the spectroscopic, structural and morphological properties of the luminescent nano- and microcrystalline, lanthanide doped materials *(Polish name: Badanie wpływu wysokiego ciśnienia na właściwości spektroskopowe, strukturalne i morfologiczne luminescencyjnych materiałów nano- i mikrokrystalicznych, domieszkowanych jonami lantanowcó)*

Group leader: Dr. Marcin Runowski

Grant number: 2016/23/D/ST4/00296 *Total funding: 667 500,00 PLN (about 148 000 euro)*

Duration: 3 years *Relationship: Common papers affiliated*

Main responsibility:

Search literature, optimize experimental methods under the guidance;

Synthesis of inorganic nano/micro-materials doped with lanthanide ions

Physicochemical characterization under high-pressure condition of the synthesized samples, writing publications.

- **Doctoral Project – Faculty of Chemistry, Adam Mickiewicz University, Poznan, Poland**

High-Chem Project for Doctoral students

Grant number: grant no. POWR.03.02.00-00-I020/17 *Relationship: Employed with salary as a PhD student*

Granting agency: The European Union through the European Social Fund under the Operational Program Knowledge Education Development.

◆ **Master Project - Department of Optoelectronics, Ningbo Univeristy, China 8/2015-07/2018**

Rare earth doped PMN-PT single crystal Up-conversion luminescence and piezoelectric coupling - National Natural Science Foundation of China

Group leader: Prof. Laihui Luo *Relationship: Common papers affiliated*

Collected Literature information and customized experimental process;

Synthesizing the PMN-PT samples and performing the measurements about electronic and photoluminescence properties of the PMN-PT samples

Visualizing and analyzing the data of PMN-PT samples.

SCIENTIFIC SKILLS

➢ Proficient in applying fluorescence spectrometer for measurements in the optical second harmonic generation (SHG) and luminescence properties (up-conversion and downshifting emission);

➢ Proficient in high-pressure experiment applying diamond anvil cell (DAC) technique with luminescence spectroscopy, Raman spectroscopy, including DAC loading, high pressure photoluminescence characterization, pressure calibration, *etc*.

➢ Experienced at different chemical synthesis method to obtained nano/micro-particles and bulk materials, e.g., solid-state high-temperature method, sol-gel method, hydro-thermal method, modified Pechini method, etc.

➢ Adequate understanding of the functional ceramic synthetic process and ferroelectric properties of PMN-PT, PYN-PT ceramics;

➢ Experienced use of X-ray diffractometer to test sample phase structure, impedance analyzer to test sample dielectric temperature spectrum and dielectric constant and ferroelectric analyzer to measure the P-E curve of samples.

➢ Experienced use of laboratory ball-mill equipment for chemical synthesis and particle size minimizing via mechanochemical method.

TEACHING EXPERIENCES

- The importance of rare earth elements in the issues of forensic chemistry, Adam Mickiewicz University in Poznań. (Prof. dr. hab. Stefan Lis and Dr. Marcin Runowski), May-June. 2021.
- Nanomaterials based on inorganic matrices doped with d- and f- electron elements, Adam Mickiewicz University in Poznań. (Prof. dr. hab. Stefan Lis and Dr. Agata Szczeszak). May-June. 2021 and May-June. 2020.

RESEARCH INTERNSHIP

International Internship in Faculty of Physics, University of La Laguna, Tenerife, Spain 02/09/2021-03/12/2021

Invited by Prof. Victor Lavin, Director of Physics Department, University of La Laguna

Main research: Photoluminescence/structural properties under high pressure and temperature in C_3N_4 two-dimensional materials, Lanthanide (Eu^{2+}, Ce^{3+}) and d-block element (Mn^{4+}, Mn^{2+}) doped phosphors, KNN ceramics, BNT based ceramics.

LANGUAGE LEVEL

- College English Test-6 (CET-6): 471 points;
- College English Test-4(CET-4): 542 points;
- The courses taught during the doctoral period were all in English. During my tenure as the professor assistant, I taught in English for undergraduate and master students;
- Good English listening, speaking, reading, and writing skills;
- Polish language level A1.

3. State of the art

3.1. Basic knowledge about Ln ions

In the past, nowadays, and probably in the future, rare-earth ions had been, are and will be an important part in development of science and technology and our life, from material sciences, medical/biological applications, advances in green technology, sustainable chemistry, to quantum computing. Due to the unique features of the intra-configurational 4f-4f transitions, Ln^{3+} ions (*e.g.*, Er^{3+}, Tm^{3+}, Ho^{3+}) have been applied as effective and irreplaceable dopants, endowing the host matrices various optical, electronic, and magnetic properties.[1–6] Currently, Ln based luminescent materials are used in various fields: I) lighting industry, that is the design and engineering of phosphors, solid-state lighting, white light-emitting diode (LED), electroluminescent materials for organic-LED; II) solar cells, optoelectronic devices; III) photocatalysis, green chemistry; IV) optical fibres for telecommunications; V) plant-growth lamp for agricultural purpose; VI) biological assays and medical imaging purposes, e.g., bio-marker, photodynamic therapy; VII) optical sensing techniques of temperature and pressure, other sensing techniques, anticounterfeiting, etc (see **Figure 1a**). The assembly of the family of 17 almost-indistinguishable lustrous silvery-white soft heavy metal elements, i.e., the 15 f-electron Ln elements from the sixth period, from lanthanum to lutetium, along with transition metals scandium (Sc) and yttrium (Y), are called rare-earth elements. And the name of "rare-earth" is originated from the rareness of these minerals in nature. In particular, Y and Sc are considered to be rare-earth elements due to the presence of the same ore deposits as Ln, moreover, they also show similar chemical features (e.g., Y has the same ionic radius as Ho), but different electronic and magnetic properties.[7] In general, enabled by the intra-configurational 4f-4f and inter-configurational 4f-5d transitions within Ln ions, Ln doped materials shows different optical features depending on the emission wavelength, emission/excitation band shape, luminescence lifetime, etc.

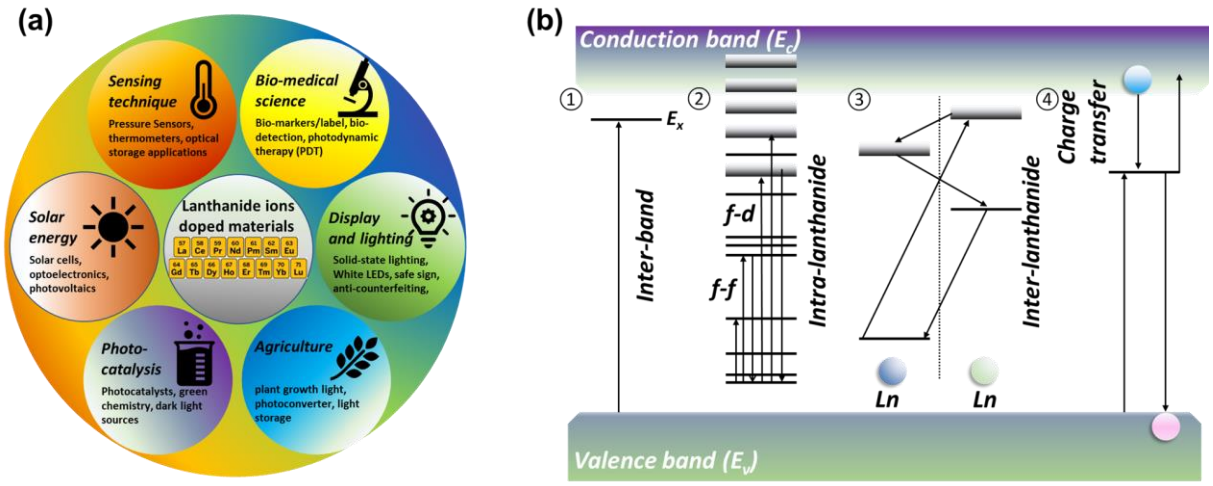

Figure 1. (a) The various application fields of Ln-doped phosphors. (b) Schematic diagram presenting four different categories of electronic transition in optically active inorganic compounds based on Ln ions, i.e., inter-lanthanide transition, intra-lanthanide transition, interband transition and charge transfer.

Luminescent materials based on Ln ions have been developed over decades and have passed many millstones.[8] The word "luminescence" is invented by Eilhardt Wiedemann, a German physicist, in order to characterize the emission of light that is not conditioned/influenced by elevated temperature.[9] After that, the Ln doped materials begin to develop. The discovery of the highly emissive Y_2O_3:Eu^{3+} material opens the gate of the Ln-based materials, which are the crucial source of phosphors for cathode-ray tubes and fluorescent lamps, still intensively exploited. Another breakthrough came with the discoveries of the neodymium YAG (Yttrium Aluminium Garnet) lasers in 1964, which later become an important source of lasers. In 1987, the Er-doped optical fibres were developed, which significantly accelerate the development of optical telecommunications. In the mid-1970s, Finnish researchers developed Eu^{3+} and Tb^{3+} (later also Sm^{3+} and Dy^{3+}) polyaminocarboxylates and β-diketonates as bio-probes in time-resolved luminescent immunoassays, which had a huge impact at that time. This new technology was further developed, largely promoting the development of the applications of Ln luminescent bio-probes in many fields of biological systems. And nowadays, Ln-doped materials have found applications in various fields, not only in many aspects of our daily life and industrial development.

In case of Ln series, the inner-shell (intra-configurational) 4f-4f transitions of the Ln^{3+} are forbidden by the Laporte selection rules, resulting in long radiative lifetimes (in the range of micro-

and milliseconds). Whereas, the sharp/narrow character of the absorption and emission lines of Ln^{3+} ions is due to the fact that the 4f electrons (orbitals) are shielded by the $5s^2$ and $5p^6$ ones, resulting in relatively low sensitivity to the crystal-field effects. Thus the emission characteristics do not vary significantly in different chemical environments, in which the Ln^{3+} ions are inserted.[10] Moreover, luminescence of Ln^{3+} ions is also characterized by the appearance of emission lines in the UV, visible and NIR ranges, excellent photo-stability of the materials containing Ln^{3+} ions, absence of background auto-fluorescence, etc.

There are four basic types of electronic transitions that occur in Ln doped inorganic materials, i.e., inter-lanthanide transition, intra-lanthanide transition, interband transition and charge transfer, as shown in **Figure 1b**. The inter-lanthanide transition is based on the electron transfer between any dual Ln ions adjacently doped in the host matrices, while the intra-lanthanide transition is a process by which an electron is excited from the Ln's occupied 4f orbitals to its unoccupied 4f or 5d orbitals. In addition, the interband transition is related to the process by which an electron is excited from the top of the valence to an exciton state, i.e., transitions to the conduction band and the photoionization effect. Charge transfer refers to transfer of electrons between the dopant and the host, usually from O^{2-} (or from S^{2-}) to Ln^{3+} (or Ln^{4+}). Not all transitions are allowed since they must obey the Laporte's selection rule and others (see **Table 1**). The so-called ''forbidden'' and ''allowed'' transitions are, as a matter of fact, not completely allowed or forbidden, namely, a forbidden transition has a low probability and an allowed transition a high probability of occurrence. This is due to that the selection rules for electron transitions are derived based on several conditions and hypotheses, in the case of Ln ion doped materials, which are not always completely fulfilled (the 4f wavefunctions are not totally pure, as there is some admixing of the 5d states, the so called "J-J mixing"). When the Ln^{3+} ions are doped into a chemical environment, due to the crystal-field (ligand-field) effect, the (2J+1)-degenerate J-level are split into Stark sub-levels. The number of the corresponding Stark sub-levels is related to the site symmetry of the transition metal ion in the inorganic matrix host. The different spectroscopic properties of the different Ln ions, the emission of which varies from the UV to NIR region, are originated from their various ladder-like energy level structure. The typical PL emission spectra of Ln complexes in liquid solution, showing the sharp emission bands based on Ln^{3+} ions are shown in **Figure 2**, obtained from the literature.[11]

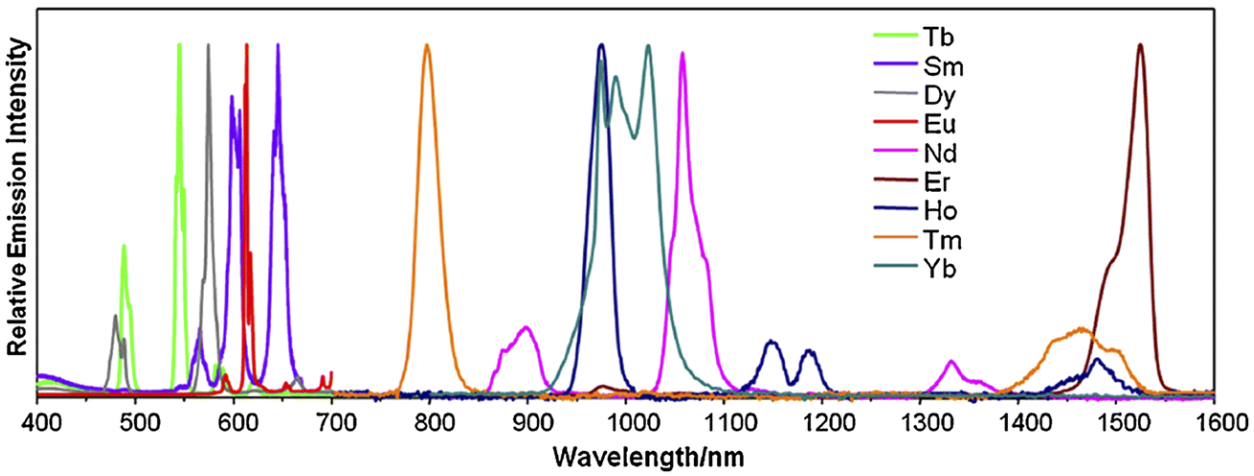

Figure 2. Normalized emission spectra of luminescent Ln complexes in liquid solution, illustrating the sharp emission bands and minimal overlap of Ln luminescence. The spectra are obtained from the reference.[11]

Table 1. Selection rules for f-f and f-d transition. S, L and J are quantum numbers for the electron transitions. Please note, a) L=0 ↔ L'=0 transitions are always forbidden; b) J=0 ↔ J'=0 transitions are always forbidden; c) Spin-allowed transitions, spin-forbidden transitions are about 100 times less intense.

Transition	ΔS	$\lvert\Delta L\rvert$	$\lvert\Delta J\rvert$	Oscillator Strength
ED (d-f)	0	≤1	≤1	~0.01 - 1
Forced ED (f-f)	0	≤6 (2, 4, 6 if L or L' =0)	≤6 (2, 4, 6 if J or J' =0)	~10^{-4} - 10^{-5}
Vibronic (ED, f-f)	0	≤6 (2, 4, 6 if L or L' =0)	≤6 (2, 4, 6 if J or J' =0)	~10^{-7}- 10^{-10}
MD (f-f)	0	0	0, ±1	~10^{-5} - 10^{-6}
EQ (f-f)	0	0, ±1, ±2	0, ±1, ±2	~10^{-10}

Table 2. The electronic structure of Ln ions.

Ln^{3+}	Atom. No.	Atom. weight	Atom. Radius	Config. of Ln^{3+}	Config. of Ln^{2+}/Ln^{4+}	Config. of Ln	Emission colour of Ln^{3+}
La	57	138.9055	1.03	[Xe]	-	[Xe]$5d^1 6s^2$	Colourless

Ce	58	140.12	1.01	$[Xe]4f^1$	Ce^{4+}: [Xe]	$[Xe]4f^15d^16s^2$	Colourless
Pr	59	140.9077	0.99	$[Xe]4f^2$	Pr^{4+}: $[Xe]4f^1$	$[Xe]4f^36s^2$	Green
Nd	60	144.24	0.98	$[Xe]4f^3$	Nd^{4+}: $[Xe]4f^2$; Nd^{2+}: $[Xe]4f^4$	$[Xe]4f^46s^2$	Violet
Pm	61	145	-	$[Xe]4f^4$	-	$[Xe]4f^56s^2$	Pink
Sm	62	150.36	0.96	$[Xe]4f^5$	Sm^{2+}: $[Xe]4f^6$	$[Xe]4f^66s^2$	Yellow
Eu	63	151.96	0.95	$[Xe]4f^6$	Eu^{2+}: $[Xe]4f^7$	$[Xe]4f^76s^2$	Pale pink
Gd	64	157.25	0.94	$[Xe]4f^7$	-	$[Xe]4f^75d^16s^2$	Colourless
Tb	65	158.9254	0.92	$[Xe]4f^8$	Tb^{4+}: $[Xe]4f^7$	$[Xe]4f^96s^2$	Pale pink
Dy	66	162.50	0.91	$[Xe]4f^9$	Dy^{4+}: $[Xe]4f^8$; Dy^{2+}: $[Xe]4f^{10}$	$[Xe]4f^{10}6s^2$	Yellow
Ho	67	164.93	0.9	$[Xe]4f^{10}$	-	$[Xe]4f^{11}6s^2$	Pale yellow
Er	68	167.26	0.89	$[Xe]4f^{11}$	-	$[Xe]4f^{12}6s^2$	Pink
Tm	69	168.93	0.88	$[Xe]4f^{12}$	Tm^{2+}: $[Xe]4f^{13}$	$[Xe]4f^{13}6s^2$	Pale green
Yb	70	173.04	0.87	$[Xe]4f^{13}$	Yb^{2+}: $[Xe]4f^{14}$	$[Xe]4f^{14}6s^2$	Colourless
Lu	71	174.967	0.86	$[Xe]4f^{14}$	-	$[Xe]4f^{14}5d^16s^2$	Colourless

In comparison to the parity-forbidden $4f^n \leftrightarrow 4f^n$ transitions within the f-manifold of the $Ln^{2+/3+}$, the $4f^n \leftrightarrow 4f^{n-1}5d^1$ transitions of the $Ln^{2+/3+}$ are allowed and show a very broad excitation/emission band, high radiative emission probability, short emission lifetime (on the nanosecond scale). In principle, the inter-configurational $4f^n \leftrightarrow 4f^{n-1}5d^1$ transitions are ED, thus their oscillator strengths are much bigger, leading to transitions with higher intensity in the spectra. Importantly, 5d orbitals are not shielded by outer filled orbitals, thus they are more prone to the effects of the local coordinating environment, unlike 4f orbitals. This is due to the fact that the crystal field interaction with 5d-electrons is ~50 times more intense than with 4f electrons, and the energies of the 5d-level strongly depend on the local crystal environment, resulting from that the 5d-orbital extends beyond the [Xe] core, contrary to the 4f ones.[12] The ED allowed for $4f^{n-1}5d \leftrightarrow 4f^n$ (n = 1–14) transitions of Ln^{3+} ions vary from the UV range to NIR range, depending on the particular ion and different host matrix. Due to the high sensitivity of the 5d orbitals to the nature of chemical bonds to the surrounding ligands in the given host compound, the wide tunability of the spectroscopic properties may realize under the contraction/expansion of the lattice volume, a

change in site symmetry caused by different dopant concentration, temperature, or pressure variation, etc.

3.2. Ln^{2+} ions and 5d-4f emission

3.2.1. General remarks

Conventional luminescence based on Ln ions is a Stokes process, which emit lower-energy photons under the higher-energy photon excitation. Thanks to their ladder-like energy level structure, the Ln ions combined with different organic/inorganic host, can exhibit various optical/spectroscopic properties. Thus, $Ln^{2+/3+}$ are widely utilized as activators in luminescent materials for various applications. The characteristic sharp-line luminescence of the Ln ions originates from the 4f−4f intra-configurational transitions. In general, the 4f−4f intra-configurational transitions are well-studied and well-understood. Under the influence of the excitation with high-energy photons, most of the Ln ions exhibit PL activity, usually from the lowest $4f^n$ excited states, but sometimes also from the higher $4f^n$ excited states,[13] which is due to relatively slow non-radiative relaxation from high to low excited states, according to the Kasha's rule.[14] The broad-band luminescence arising from the inter-configurational $4f^n \leftrightarrow 4f^{n-1}\ 5d^1$ (f-d) transitions is however not as well-understood. Importantly, there are still some mysteries regarding nonradiative decay processes related to $4f^n \leftrightarrow 4f^{n-1}\ 5d^1$ transitions. Only the emission from the lowest excited $4f^{n-1}\ 5d^1$ state is typically observed, because excitation to the higher excited states typically leads to a rapid non-radiative relaxation to the lowest excited state. To figure out the answers to the questions remain open, except for the Ln^{3+} ions, the divalent and Ln^{4+}, i.e., Eu^{2+},[15–18] Sm^{2+},[19] Yb^{2+},[20,21] Tm^{2+},[22–24] Nd^{2+},[25,26] Dy^{2+},[27,28] Ce^{4+},[29,30] Pr^{4+},[31] Nd^{4+},[32] Tb^{4+} [33] and Dy^{4+},[34] are attracting more and more attentions of the researchers.

3.2.2. Eu^{2+} ion

Divalent europium doped inorganic phosphors are particularly well known for their excellent optical properties, e.g., high brightness (large quantum efficiency), large absorption band, broad emission bands after excitation, tuneable emission wavelength, originating from the parity-allowed electron transitions of $4f^6 5d^1 \rightarrow 4f^7$. Up to now, Eu^{2+} is the most characterized ion in terms of its

5d-4f luminescence properties, which have been compiled for over 300 compounds.[15,35,36] This is related to several reasons. Eu^{2+} has a relatively low reduction potential (-0.36 V compare to NHE, normal hydrogen electrode)[37] and good stability in different inorganic matrix host. Importantly, due to its tuneable $4f^6 5d \leftrightarrow 4f^7$ transitions, the emission band can be tuned from UV-violet,[38–43] blue,[44] cyan, green,[45,46] yellow,[47] orange,[17] red,[16] to the NIR region,[48] by varying the type of host material. A detailed table showing the relationship between the emission range and the matrix host can be found in references.[15,35,36] This means that the appropriate emission band shape or emission wavelengths can be strongly affected by the host lattice in which the Ln ion inserted with regard to the length of the anionic-Eu^{2+} bond, the coordination number of the corresponding cation, the nephelauxetic effect and the local crystal field symmetry. This is related to the covalence and the bond length between cation and ligands.[36] The Eu^{2+} is particularly attractive for its important role in light-emitting diodes (LED) and optical displays, due to its largely tuneable, broad $4f^6 5d \leftrightarrow 4f^7$ emission band leading to good colour rendering properties.[49–52]

In case of Eu^{2+}, the lowest 5d configuration may have a higher position than the excited 4f configuration if the influence of the crystal field and the nephelauxetic effect is weak, thus, the $4f^7(^6P_{7/2})$- $4f^7(^8S_{7/2})$ emission is possibly detected. A simplified diagram of the Eu^{2+}energy levels for SrB_4O_7 is shown in **Figure 3a**. A few cases are also reported about the sharp band emission originated from $4f^7$-$4f^7$ transition of Eu^{2+}.[53–55] For instance, upon doping of Eu^{2+} ions into the SrB_4O_7 crystal structure, Meijerink *et al*. observed sharp lines caused by the transitions within the $4f^7$ ground configuration at low temperatures and demonstrated that the configuration crossover between the $4f^7$ and $4f^6 5d^1$ configuration of Eu^{2+} can be stimulated by temperature variation.[38] The emission of Eu^{2+} associated with the alternatively possible intra-configurational $4f^7$ $(^6P_{7/2}) \rightarrow$ $4f^7$ $(^8S_{7/2})$ transitions characterized by several sharp, narrow ($\approx$ 1-2 nm width in the wavelength domain) emission lines in the UV range at around 360 nm are only occasionally reported and typically observed in other highly ionic host compounds.[53–55] Understanding the mechanisms that control the appearance of this unusual type of luminescence of Eu^{2+} is important not only from a fundamental perspective but also important for potential industrial applications.[56–61]

3.2.3. Sm^{2+} ion

As illustrated in Table 2, the Sm^{2+} ion has a $4f^6$ ground configuration isoelectronic to the Eu^{3+} ion. The excited $4f^55d^1$ levels and the spin-orbit coupling constant with lower energies of Sm^{2+} are related to the difference in the oxidation state and atomic number of Sm^{2+}, compared to Eu^{3+}. A simplified diagram of the energy levels of Sm^{2+} (in the SrB_4O_7 host) is presented in **Figure 3b**. In particular, the influence of crystal symmetry and local field strength on the splitting pattern of the $4f^6 \leftrightarrow 4f^6$ transitions of Sm^{2+} are like Eu^{3+}. Due to the similarity between the two ions, the Sm^{2+} ion can be utilized as an experimental tool for studying the number of the site symmetry - in a similar manner to the $^5D_0 \rightarrow {}^7F_0$ transition of Eu^{3+} ion.[62,63] By analysing the asymmetric shape of the emission line (the number of lines observed) of Sm^{2+} originated from the transition of $4f^6(^5D_0) \rightarrow 4f^6(^7F_0)$ (0-0 transition), one can directly indicate the number of the occupied sites with a crystallographic-difference in the structure. In the case of a single crystallographic site substituted by the Sm^{2+} ion in the structure, the 0-0 transition should not be split (asymmetric structure of the band), due to the crystal field is $(2J+1) = 1$. The phenomenon of any splitting of the band can be identified as representative proof to verify that there are crystallographically different sites occupied by Sm^{2+} in the structure. For instance, Ellen et al. illustrated in their work that using the Sm^{2+} emission in $BaMgAl_{10}O_{17}$ host as an optical probe for the number of luminescence sites of Eu^{2+}.[64]

The $4f^6 \leftrightarrow 4f^6$ and $4f^55d^1 \leftrightarrow 4f^6$ transitions of Sm^{2+} are very sensitive to external stimuli. When the state function of pressure or temperature varies, the spectroscopic features of Sm^{2+} change significantly because the excited state of the $4f^55d$ levels and the excited $4f^6$ (^5D_J) levels are energetically close to each other. Up to date, the Sm^{2+} ion is mainly used in terms of the $4f^6 \leftrightarrow 4f^6$ and $4f^55d \leftrightarrow 4f^6$ transitions as a function of external stimuli such as temperature or pressure, which allows its application as optical sensors. Many Sm^{2+} doped materials were applied for sensing purpose of state function of temperature and pressure. In recent decades, many works have been reported on the Sm^{2+}-activated borate group materials. e.g., barium octaborate (BaB_8O_{13}),[65] barium chloroborates ($Ba_2B_5O_9Cl$),[66] $BaBPO_5$,[67,68] $Ba_3BP_3O_{12}$,[69] $LiBaB_9O_{15}$,[70] borophosphates,[71] strontium borates.[63,67,72,73] This is due to the borated groups, which present high ionicity, typically shift the excited $4f^55d$ configuration to higher energies (lower wavelengths), so that the $4f^6$-$4f^6$ transitions are more dominant. Several papers have also reported that the same

phenomenon can be observed in some materials from the fluoride group, e.g., $SrMgF_4$,[74] $BaMgF_4$,[75] $SrAlF_5$.[76] Besides the applications, Sm^{2+} doped materials are also applied in photon-gated spectral hole burning properties,[77,78] X-ray storage phosphors,[79,80] halide-based scintillators.[80,81]

3.2.4. Tm^{2+} ion.

It is known that Tm^{2+} is less stable than Eu^{2+}, Sm^{2+} and Yb^{2+}. In the case of the Tm^{2+} ion, the 4f orbital is filled with 13 electrons, i.e., has a $4f^{13}$ ground configuration, isoelectronic to Yb^{3+}. Compared to the Ln^{2+} ions mentioned above, the 5d configuration of Tm^{2+} is located at a lower energy, as shown in **Figure 3c**. Considering that the spin-orbit coupling is neglected, the lowest excited states ($4f^{12}5d^1$ configuration) of Tm^{2+} have a higher spin multiplicity, in comparison to its ground states, as predicted by Hund's rules.[82] In the case of the SrB_4O_7 matrix host, it was reported that the emission band attributed to the spin-forbidden $4f^{12}5d$ (high spin) $\rightarrow 4f^{13}$ ($^2F_{7/2}$) transition is located in the orange-red range (~600 nm, ~17210 cm^{-1}).[83] Moreover, the emission related to three $4f^{n-1}5d^1$ states is only observed in Tm^{2+}, different from the other Ln dopants. In the case of halidoperovskites ($CsCaX_3$, X=Cl, Br, I), it is reported that Tm^{2+} shows several other $4f^{12}5d \rightarrow 4f^{13}$ ($^2F_{7/2}$) transitions all over the visible range, that is, there are three emissive transitions between 10000 and 15000 cm^{-1}. The lowest energetic transition is the spin-forbidden $4f^{12}5d^1(HS) \rightarrow 4f^{13}(^2F_{7/2})$ transition, and the second lowest one is spin-enabled $4f^{12}5d^1$ (LS) $\rightarrow$ $4f^{13}(^2F_{7/2})$ transition. In emission, excitation and absorption spectra, these two transitions are not always very well resolved.

It was reported that Tm^{2+} has a characteristic narrow emission band in the NIR range (~1100 nm) attributed to the $4f^{13}$ ($^2F_{5/2}$) $\leftrightarrow$ $4f^{13}$ ($^2F_{7/2}$) transition.[84,85] Because of its $4f^{12}5d^1 \leftrightarrow 4f^{13}$ transition which is located in the visible range and has an isoelectric structure to Yb^{3+}, it can works as an up-conversion activator in inorganic compounds, showing interesting spectroscopic properties. For instance, the up-conversion process, in the case of $SrCl_2$:Tm^{2+}, is highly efficient so that it occurs even using a conventional Xe arc lamp as the excitation source.[86] This is related to the second ED-allowed $4f^{13}$ ($^2F_{5/2}$) $\rightarrow$ $4f^{12}$ ($^3H_6$)$5d^1$ based excited state absorption process and the final up-converted ED allowed nature of the emission at 13900 cm^{-1} (red region). In principle, such a process makes Tm^{2+} an excellent up-conversion activator, showing a much higher up-

conversion efficiency than the commonly used Ln^{3+} pairs (e.g., Er^{3+}-Yb^{3+}, Tm^{3+}-Yb^{3+} pairs). Moreover, Tm^{2+} doped materials are also used in excited state excitation spectroscopy.[87]

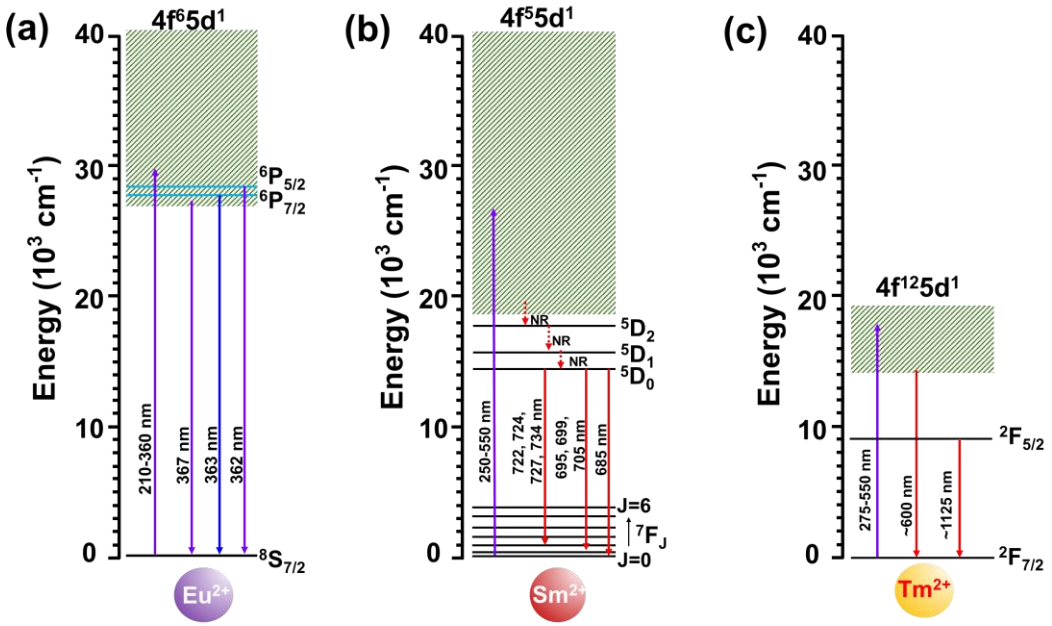

Figure 3. Energy level diagram of (a) Eu^{2+}, (b) Sm^{2+} and (c) Tm^{2+} in the case of the SrB_4O_7 host lattice.

3.3.Up-conversion luminescence of Ln^{3+} ions

3.3.1. General remarks

Up-conversion luminescence, as a distinct anti-Stokes process, is a non-linear optical process based on multiphoton absorption processes in which the emitted photons have a higher energy than the photons from the excitation light. Ln^{3+} can serve as dopant ions in certain inorganic matrix host to achieve unique up-conversion luminescent characteristics. The up-conversion luminescence is a process that, in principle, the electrons in the ground state of the emitting centre (activator ion) can be pumped into the excited state via the absorption of an excitation photon, or via a corresponding energy transfer (ET) process from the adjacent sensitizer ion (usually Yb^{3+}). Afterward, another photon from the excitation source will be absorbed by the emitter, or a corresponding ET process from sensitizer to activator will take place to pump the electrons to the excited state in the emitting centre. Emission will then be produced, attributing to the radiative

transitions from this excited state to the ground state or that excited state to another lower-energy state will take place. The metastable intermediate excited state is achieved by an up-conversion luminescence process, which shows a significant difference compared to the two-photon process. In order to keep a large population in an intermediate excited state prior the second excitation energy, such a metastable intermediate excited state should have a relatively long lifetime.[88] Noteworthy, the Yb^{3+} ion is widely used as a sensitizer ion because it has the largest absorption cross-section (~10^{-20} cm^2), among the Ln activators. Moreover, the Yb^{3+}: $^2F_{7/2} \rightarrow {}^2F_{5/2}$ transition is resonant with many 4f−4f transitions within Ln^{3+} ions, such as Er^{3+}, Ho^{3+} and Tm^{3+}, thus allowing efficient ET from Yb^{3+} to the activator ions (emitting centre).[89–96] Thus, Yb^{3+} is often co-doped with Er^{3+}, Tm^{3+} or Ho^{3+} as a sensitizer to enhance up-conversion emission. In order to match the $^2F_{7/2} \rightarrow {}^2F_{5/2}$ transition of Yb^{3+}, a continuous wave laser in the NIR range (usually ~980 nm) can applied as the excitation source. There are five basic mechanisms to achieve photon UC: I) excited state absorption; II) cooperative upconversion; III) ET up-conversion; IV) energy migration up-conversion; V) and photon avalanche.[97]

Absolute quantum yield (QY) is usually used to describe the efficiency of luminescence in Ln doped materials. QY is defined as the ratio of the number of emitted up-conversion photons to that of absorbed photons. In general, the Ln doped should exhibit high luminescence efficiency, in order to meet the requirements of practical and commercial applications. Researchers commonly use the sensitizer ions, CT/ET effects, sensitization via allowed 4f-5d transitions (e.g., Ce^{3+} and Eu^{2+}) or organic ligands for enhancing PL. Under excitation light, based on the recorded emission spectra, the internal (IQE) and external quantum efficiency (EQE) of luminescent materials can be determined using of the following expressions:[98]

$$\mathrm{IQE} = \frac{\int L_S}{\int E_R - \int E_S} \times 100\% \quad (1)$$

$$\mathrm{AE} = \frac{\int E_R - \int E_S}{\int E_R} \times 100\% \quad (2)$$

$$\mathrm{EQE} = \mathrm{AE} \times \mathrm{IQE} \quad (3)$$

where L_S represent the emission spectrum of the sample, E_S and E_R denote the excitation light with and without the sample in the integrating sphere, respectively; and AE is the absorption efficiency.

3.3.2. Er^{3+}-Yb^{3+} and up-conversion emission.

Among the Ln^{3+} series, the Er^{3+} ion has a $4f^{11}$ electronic arrangement. Er^{3+} is an effective luminescent emitting ion used to generate up-conversion luminescence from NIR to visible UCL. Importantly, the combination of a pair of dopants Er^{3+}-Yb^{3+} is often used to insert into an inorganic matrix, as mentioned above, because Yb^{3+} can act as an NIR absorber, effectively sensitizing the Er^{3+} ion as an emitter (activator) through ET in materials. In the up-conversion system of Yb^{3+}-Er^{3+} co-doped materials, under NIR excitation, the green emission at ~525 nm and ~550 nm and the red emission at ~675 nm are most commonly observed and studied (sometimes the emission at ~415 nm can also appear). Many works have shown that green and red emissions are often generated in two-photon processes. The UC mechanisms in Er^{3+}-Yb^{3+} co-doped $BaTiO_3$ system are shown in **Figure 4a**. It is obvious that between the Yb^{3+}: $^2F_{7/2}\rightarrow{}^2F_{5/2}$ transition and the Er^{3+}: $^4I_{15/2}\rightarrow{}^5I_{11/2}$ transition a superb resonance is presented, which offers highly efficient ET from Yb^{3+} to Er^{3+}. Under the influence of NIR laser irradiation, NIR photons are absorbed by Yb^{3+} via the transition of $^2F_{7/2}\rightarrow{}^2F_{5/2}$. Afterward, it transfers the energy resonantly to nearby Er^{3+}, while in the Yb^{3+} ion, the electrons populated in the $^2F_{7/2}$ ground state relax back to $^2F_{5/2}$. The energy donated by Yb^{3+} promotes the Er^{3+} ions to their excited state via $^4I_{15/2}\rightarrow{}^4I_{11/2}$. Afterward, a similar resonant ET from the Yb^{3+} sensitizer to Er^{3+} activator via $^4I_{11/2}\rightarrow{}^4F_{7/2}$ or $^4I_{13/2}\rightarrow{}^4F_{9/2}$ process take place. The electrons at $^4F_{7/2}$ level relax non-radiatively to the $^2H_{11/2}$ and $^4S_{3/2}$ states. Then, the green emission will be generated, respectively. Alternatively, after non-radiative relaxation to $^4S_{3/2}$, another non-radiative transition from $^4S_{3/2}$ to $^4F_{9/2}$ take place, and finally radiatively relax to the $^4I_{15/2}$ ground state via the $^4F_{9/2}\rightarrow{}^4I_{15/2}$ transition, resulting in emissions in red region. Therefore, the emissions in the green and red regions can be obtained simultaneously through two-photon UC processes. Thus, for the Yb^{3+}-Er^{3+} up-conversion system, the green emissions located around 525 and 550 nm are originated from the $^2H_{11/2}$ and $^4S_{3/2}$ excited states to the $^4I_{15/2}$ ground state, respectively. The emission bands centred at 675 nm in the red region can also be observed, for the transition from the $^4F_{9/2}$ excited state to the ground state. In some cases, the system also produces weak blue emissions located at ~450, ~470 and 495 nm, arising from the $^4F_{5/2}\rightarrow{}^4I_{15/2}$, $^2P_{3/2}\rightarrow{}^4I_{11/2}$, and $^4F_{7/2}\rightarrow{}^4I_{15/2}$ transitions, respectively. In addition, the emission bands at 390 and 410 nm in the blue region can be observed at a high concentration of Yb^{3+}, as a result of the four-photon process, with a high excitation power density.[99] Er^{3+} ion is widely used for the purpose of thermal sensing

thanks to the thermally coupled energy levels of $^2H_{11/2}$ and $^4S_{3/2}$, as well as the very efficient up-conversion luminescence in Er^{3+}-Yb^{3+} materials. This is due to the energy gap between the barycentre of these two energy levels of $^2H_{11/2}$ and $^4S_{3/2}$ is ~700 cm^{-1} and their comparative populations are impacted by temperature, conforming to the Boltzmann distribution, which will be discussed in the section of luminescent thermometry.

3.3.3. Ho^{3+}-Yb^{3+} and up-conversion emission.

The Ho^{3+} ion, which has the $4f^{10}$ electron arrangement, is an excellent activator for NIR to short-wavelength up-conversion emissions due to its favourable intra-atomic 4f energy level structure. Moreover, the $^5I_7$ level can act as a population reservoir for UC processes, thanks to the rich structure of energy levels from UV to NIR region. Importantly, the adjacent levels of $^5G_6$/$^5F_1$ and $^5F_{2,3}$/$^3K_8$ in Ho^{3+} are thermally coupled ($\Delta E \approx 1300$ cm^{-1}), thus many Ho^{3+} doped materials are targeted into Boltzmann thermometers. Yb^{3+} ions are commonly co-doped as a sensitizer to Ho^{3+} ions (activator) upon NIR excitation due to the large absorption cross-section in the NIR region as well as the proper energy overlap between Yb^{3+} and Ho^{3+} ions, resulting in an efficient ET from Yb^{3+} to Ho^{3+} ions and enhancing the UC emission performances of the Ho^{3+} ions. Similar function can be applied to Tm^{3+}, Er^{3+}, etc. Take as an example $BaTiO_3$:Ho^{3+}, Yb^{3+}, as shown simplified energy level diagram in **Figure 4b**, under 976 nm excitation, the $^5I_6$ state of the Ho^{3+} ion is populated via the GSA of the NIR photon and the ET process of Yb^{3+}-Ho^{3+}. Subsequently, the excited electrons in the $^5I_6$ state are again promoted to the $^5F_4$ and $^5S_2$ levels via the excited state absorption and the efficient ET process from Yb^{3+} to Ho^{3+}. The electrons populated at $^5F_4$ and $^5S_2$ level relax non-radiatively to the $^5F_5$ level via multi-phonon relaxation, and then undergo radiative relaxation to the ground state producing red emission at ~655 nm. Furthermore, the upper levels are also populated by the three photon absorption processes and give emissions around 550 nm via a series of non-radiation transitions and the $^5F_4 \rightarrow {}^5I_8$ transitions. Therefore, for Yb^{3+}/Ho^{3+}-co-doped up-conversion materials, the green emissions located at the range of 510-570 nm are attributed to the $^5F_4$, $^5S_2 \rightarrow {}^5I_8$ transitions are observed, while the red emission centred at 655 nm can be detected, which is attributed to the transition from the $^5F_5$ excited state to the ground state $^5I_8$. It is worth noting that in some matrix hosts, blue up-conversion emission centred at ~486 nm and NIR up-conversion emission at ~751 nm can be observed, which are ascribed to the $^4F_3 \rightarrow {}^5I_8$

transition and the $^5F_4$, $^5S_2 \rightarrow {}^5I_7$ transition, respectively, which did not appear in the case of $BaTiO_3$.[88]

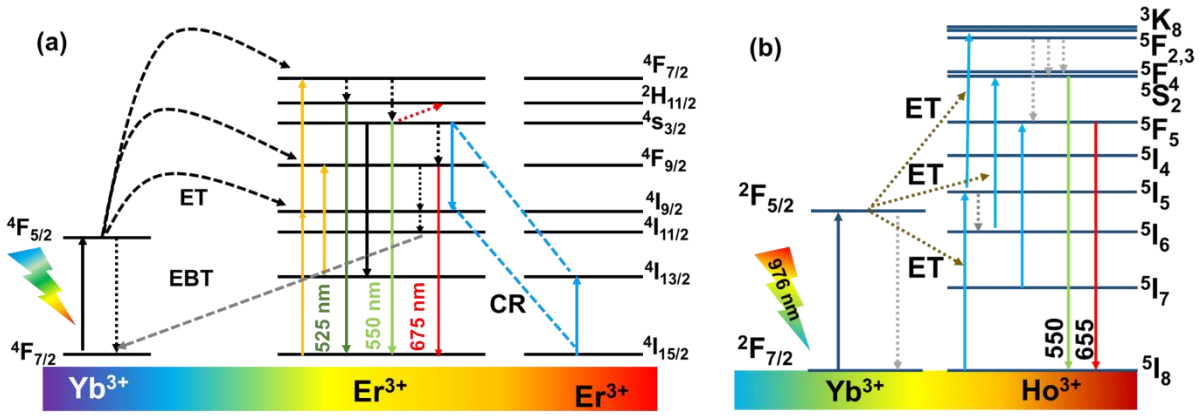

Figure 4. Energy level diagrams of (a) Er^{3+}-Yb^{3+} and (b) Ho^{3+}-Yb^{3+} in case of $BaTiO_3$ material.

3.4. Inorganic host matrices

3.4.1. Strontium tetraborate host matrix

Borates, which are naturally deposited in the sediments of ancient lakes or in hydrothermal solutions in products of the hervidero hotbed,[100] play an irreplaceable role in industrial and scientific fields. In general, Ln^{2+} can be reduced from Ln^{3+} and stabilized in the host matrix in a reducing atmosphere, such as H_2 and H_2/N_2, using the common raw materials containing Ln^{3+} ions, e.g., Eu_2O_3, Sm_2O_3, etc. Noteworthy, the reduction process from Ln^{3+} to Ln^{2+} ions can also take place in some hosts even in the air.[105,106] Strontium tetraborates (SrB_4O_7) are considered to be the most prominent Ln^{2+}stabilizing matrices. SrB_4O_7 is a special case that has a huge potential to stabilize Ln^{2+}, e.g., Eu^{2+}, Sm^{2+}, Yb^{2+}, Tm^{2+} and Nd^{2+} in reduction atmosphere or even in the air. This is due to the following reasons: I) According to the Vegard's rule,[107] the difference in ionic radii between the host ions and the dopant ion is less than 15%, e.g., $R_{eu}{}^{2+}$= 1.39 Å; $R_{Sm}{}^{2+}$=1.41 Å and $R_{Sm}{}^{2+}$=1.40 Å. In such a case, the Ln^{2+} dopant ions can isomorphically substitute the host ions in the selected crystalline structures without significant distortion of the lattice. This phenomenon are only observed in the case of strontium borate matrices.[108] II) Strontium tetraborate (SrB_4O_7)

is a well-known luminescent host material, showing main advantages like high non-linear optical coefficients, high optical damage thresholds, non-linear optical properties, high chemical and physical stability neutron sensitivity, wide optical transparency in the UV-vacuum range, with the fundamental absorption edge below 120 nm (~83333 cm^{-1}) that extends towards ~ 3250 nm (~ 3077 cm^{-1}) in the IR range.[101–104] III) As shown in **Figure 5a**, due to the rigid three-dimensional lattice of the corner-linked tetrahedral $(BO_4)^{5-}$ anion structure groups of the boron-oxygen framework, SrB_4O_7 shows excellent stabilization of the Ln^{2+} ions even in air.[56]

Huppertz *et al*. described the HP *β*-CaB_4O_7 phase, which crystallizes isotypically to SrB_4O_7 in the space group $Pnm2_1$ (no. 31).[109] Upon doping of Eu^{2+} ions into the SrB_4O_7 crystal structure, Machida *et al*. observed a very efficient broad luminescence band at about 367 nm at room temperature, which is assigned to the $4f^65d \rightarrow 4f^7(^8S_{7/2})$ transition of Eu^{2+}.[110] On the other hand, Meijerink *et al*. observed sharp lines caused by the transitions within the $4f^7$ ground configuration at low temperatures [38] and showed that the configuration crossover between the $4f^7$ and $4f^65d^1$ configuration of Eu^{2+} can be stimulated by temperature variation, as recently confirmed our group. We also reported that the difference in the strontium borate structure (see **Figure 5a-c**) leads to a difference in the reduction process of Ln^{3+} to Ln^{2+}, i.e., the host matrix of $Sr_3(BO_3)_2$ (R3c space group), SrB_2O_4 (Pbcn space group) and SrB_4O_7($Pmn2_1$ space group), have a great influence on the reduction process of Ln^{2+} ($SrB_4O_7 > SrB_2O_4 > Sr_3(BO_3)_2$).[56]

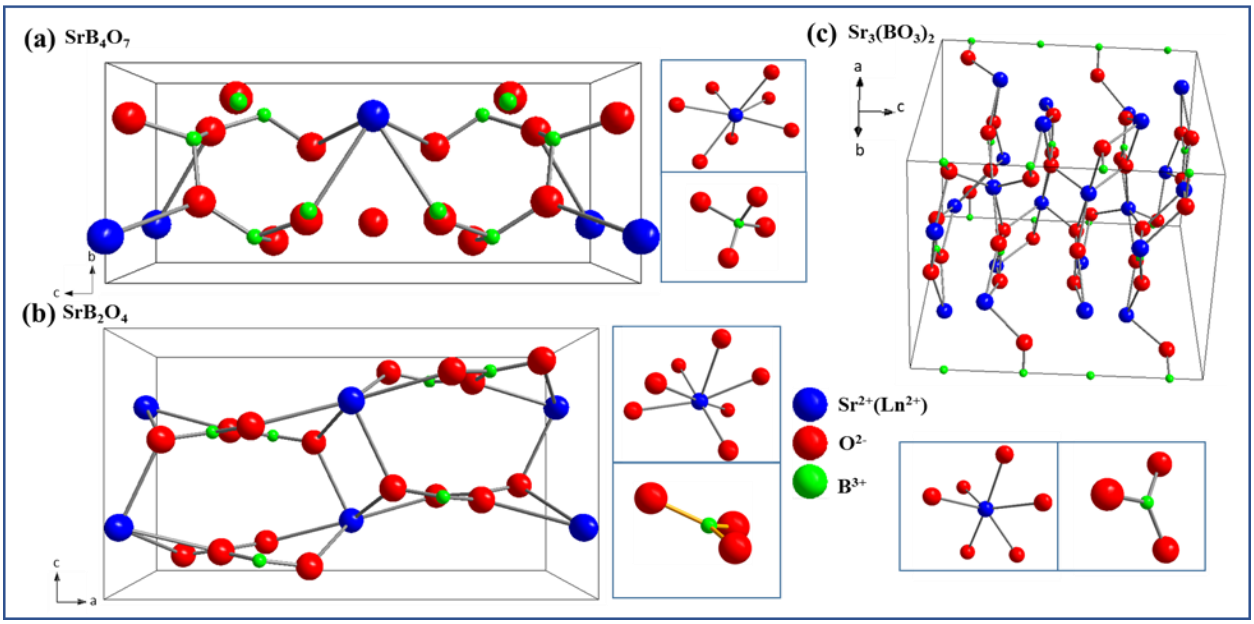

Figure 5. The crystal structure presentation of orthorhombic (a) SrB_4O_7, (b) SrB_2O_4 and (c) $Sr_3(BO_3)_2$ matrices. The cationic (Sr^{2+} or B^{3+}) coordination environment are also presented.

Combining with the thermal and chemical stability of SrB_4O_7, the spectroscopic properties based on the narrow emission line (located at ~14599 cm^{-1}, ~685 nm) of the $^5D_0$-$^7F_0$ transition of Sm^{2+} can be applied as an optical probe of temperature and pressure. In the case of pressure sensing, the spectroscopic features of the isolated, narrow (FWHM~0.13 nm) and intense 0-0 line, as well as negligible temperature dependence and high-pressure shift, make it an excellent candidate for pressure sensing application.[43,63,73,111] However, with increasing pressure, the optical determination of the pressure values based on Sm^{2+} in SrB_4O_7 materials is influenced by the signal quenching effect under pressure, due to the solidification of the pressure transmitting medium in diamond anvil cell, which will be discussed in the following paragraphs. On the other hand, the SrB_4O_7 materials can also be applied in various fields. Zhongming Cao et al. reported multimode temperature sensing based on SrB_4O_7:Sm^{2+}, using the band intensity ratio of 585/685 nm and lifetime as thermal sensing parameters. C.B. Palan et al. reported that SrB_4O_7 doped with Eu^{2+} can be used in radiation dosimetry applications, showing optically stimulated luminescence sensitivity of 33%.[103] Sun Jiayue et al. reported that SrB_4O_7:Sm^{2+} can be used as a light conversion agent.[102]

3.4.2. Barium titanium matrix

Perovskite materials are initially a calcium titanium oxide mineral composed of calcium titanate ($CaTiO_3$). There are also several compounds showing the type of crystal structure as $CaTiO_3$ (ABX_3). In the ABX_3 perovskite, the A-site ion located in the centre of the lattice, which is usually an alkaline earth or rare-earth element, while the B-site ions are positioned on the corners of the lattice, which are 3d, 4d, and 5d transition metal elements, and the X-site ions are ions (frequently oxide) that bind to both ions (usually O^{2-}). Perovskite materials show unique features that make them promising candidates in various fields, such as solar cells, ferroelectric materials, solid-state lasers, etc.[112–118] Titanate perovskites have received extensive attention, especially thanks to their excellent piezoelectric and emissive properties.[119,120] Among them, barium titanate ($BaTiO_3$) has been extensively studied in recent decades.[116–118,121–127] In addition to the ferroelectric and dielectric properties, the introduction of appropriate Ln^{3+} dopant ions into the host matrix can give

$BaTiO_3$ the PL properties. To obtain an efficient up-conversion luminescence, the low phonon energy of the host matrix is very important. For instance, in an Er^{3+}-Yb^{3+} up-conversion system, low phonon energies can inhibit multi-phonon relaxation of the $^4S_{3/2}$ level to the $^4F_{9/2}$ red-emitting level located at lower energy, leading to more efficient green emission. $BaTiO_3$ has a relatively low phonon energy (~700 cm^{-1}), which favours superior up-conversion luminescence efficiency and satisfactory optical temperature sensing performance.[128] Noteworthy, $BaTiO_3$ adopts different phases over a wide temperature range, from rhombohedral, orthorhombic, tetragonal to cubic structure.[129,130] The change in structure from rhombohedral to cubic with increasing temperature can be seen in **Figure 6**. In the case of cubic $BaTiO_3$ ($Pm\bar{3}m$, No.221), the Ti^{4+} ions are positioned in the centre of the 6-neighboring-oxygen-formed octahedron with O_h symmetry, while for the tetragonal phase, the Ti^{4+} ions have the symmetry of C_{4v}, where the O^{2-} anion is supposed to be slightly shifted towards the *c* axis. When the temperature is cooled down to room temperature, a non-centrosymmetric structure (tetragonal phase) is obtained, due to the fact that the centre ion Ti^{4+} ion and the oxygen octahedron (O_3 local symmetry) displace non-uniformly with respect to the corner ion Ba^{2+}.[130,131] When the temperature decreases below ~278 K, $BaTiO_3$ shows an orthorhombic structure (Amm2). With further decreasing the temperature below ~183 K, a rhombohedral structure (space group R3c) can be obtained. As the temperature changes, different regions of the material change their crystallographic orientations, altering the crystal structure symmetry, and a phase transition (tetragonal to cubic) occurs, leading to huge variation in the electric and spectroscopic features of the material.[129,132] Importantly, tetragonal crystals transform into a cubic phase above the Curie temperature (T_C, ~393 K) in $BaTiO_3$, as shown in previous literature data, leading to a sharp and significant change in their dielectric and ferroelectric properties, induced by an intrinsic change in crystal structure. [129,130,133]

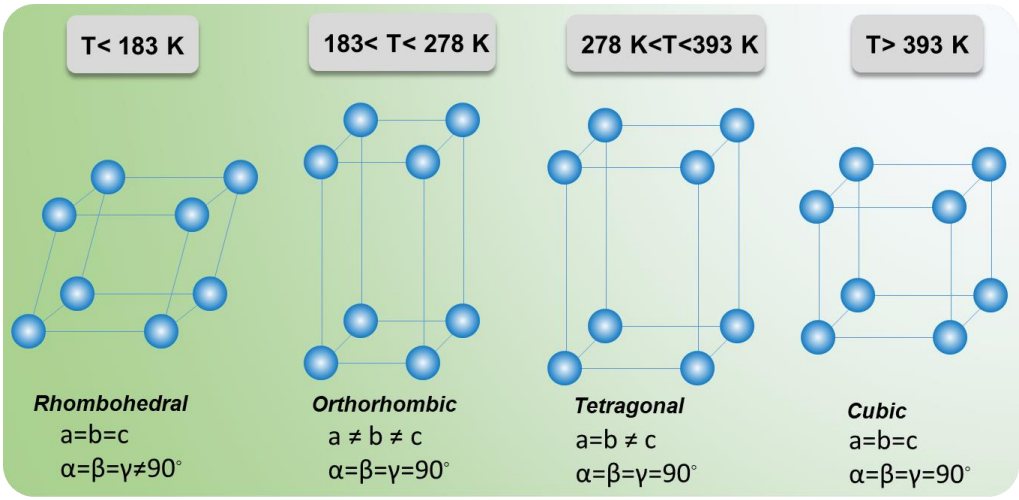

Figure 6. Phase transformations in barium titanate from the rhombohedral, orthorhombic, tetragonal systems to the cubic crystal system with increasing temperature.

3.5. Luminescence sensing techniques

3.5.1. HP experiments and optical manometry

The interest in the participation of variable volume in the study of materials by exerting pressure arises from the fact that a large proportion of the matter known in the universe was formed under extreme conditions of pressure, often accompanied by temperature changes. Pressure shapes galaxies, stars and planets, crosses islands, continents, and oceans, and affects our lives. A clear example is the earth, which can be considered a laboratory with all kinds of extreme conditions due to the combination of high pressures and high temperatures with other processes such as strong variations in pH, catalytic reactions, microbial activity, etc.[134] The pressure also has a significant influence on the physicochemical features of materials. The implementation of HP in scientific research based on the compression of materials has found wide application in the study of pressure-triggered variations in the structural, magnetic and spectroscopic properties of substances, phase transformations and the formation of new materials under extreme conditions, as well as an in-depth insight into the intriguing and conclusive mechanisms that have made great progress in solid-state physics/chemistry, material science, and geophysics, spectroscopic and structural change of the chemical compounds, etc.[135–143] In response to external mechanical stimuli such as pressure, significant changes in the material occur through changes in interatomic distances,[144] alteration

in electronic orbitals,[145] *etc*.[146,147] These changes are usually accompanied by alterations in the nature of the chemical bonds and coordination numbers, leading to other types of structures with different electronic properties in HP.[148–152] Therefore, it is extremely important to determine the local occurring pressure in a quick, non-contact and precise manner.

For a static HP experiment under a hydrostatic pressure condition, a typical assemble of optical pressure sensor, hydrostatic pressure transmitting medium (PTM) as well as a small amount of targeted sample (~100-500 μm) are loaded into the diamond anvil cell (DAC) for further characterization. The HP DAC is a typical setup to mimic HP conditions to perform spectroscopic measurements under hydrostatic or quasi-hydrostatic conditions (a detailed scheme is shown in Fig. 8, Chapter 4.2.5). Such a DAC chamber, consisting of a metal cover, closed with screws, a metal gasket, two parallel diamonds and a pressure sensor, as well as a hydrostatic PTM, is used to squeeze and compress the investigated materials on a laboratory scale. Due to the transparency in the visible range and the ultrahigh hardness of diamonds (usually IIac or IIas diamonds), it is possible to monitor the physicochemical alterations (mainly spectroscopic and structural) of the compressed materials, depending on the applied pressure.[153] In order to imitate and simulate high-pressure conditions up to tens or even hundreds of GPa, a very high force acting per small area is required, i.e., a small diamond culet size <500 μm. It is worth noting that due to pressure-induced solidification of the PTMs and subsequent loss of hydrostaticity in the sample´s chamber,[73,154–156] the selection of PTM is also very crucial for obtaining HP values. PTM of methanol/ethanol/water (16/3/1) are commonly used for achieve hydrostatic or quasihydrostatic conditions that are hydrostatic up to ~ 10.5 GPa. However, silicon oil has hydrostaticity limits to a few GPa, and in the category of liquid gas as PTM, the highest hydrostaticity limit of ~30 GPa can be achieved using liquid helium. As a matter of fact, under nonhydrostatic conditions, the HP measurements performed may sometimes not be perfectly repeatable and reproducible, e.g., the pressure values of the phase transitions may slightly differ because different and nonhomogeneous forces applied in different directions to the crystals in the DAC.

Optical pressure calibrators (noncontact pressure sensor) are based on spectroscopic variations as a function of pressure in optically active materials doped with Ln ions or d-block ions. As shown in **Figure 7**, the interesting spectroscopic effects of $Ln^{2+/3+}$, *i.e.*, spectral shift, bandwidth variation, intensity ratiometric change, shortening of PL lifetimes, as a function of pressure and temperature

conditions, can be utilized for pressure and temperature determination in a non-invasive approach.[2,3,157–161] The pressure sensing materials should have the following ideal properties, as reported by Barnett et al. and Tröster:[162,163] I) the emission spectrum measured of an optical pressure sensor should consist of a single emission band. With increasing the pressure, the emission band with no significant broadening or weakening is preferred; II) large spectral shift of the emission line with pressure (dλ/dP); III) the line shift should be as temperature-independent as possible (dλ/dT); IV) the material of the pressure sensor should be structurally stabile under high temperature and pressure conditions; V) the optically active ions (usually Ln or transition metal ions) in the pressure sensor can be easily excited by low cost commercial lasers; VI) a smaller linewidth Γ (FHWM) of the emission band is preferred.

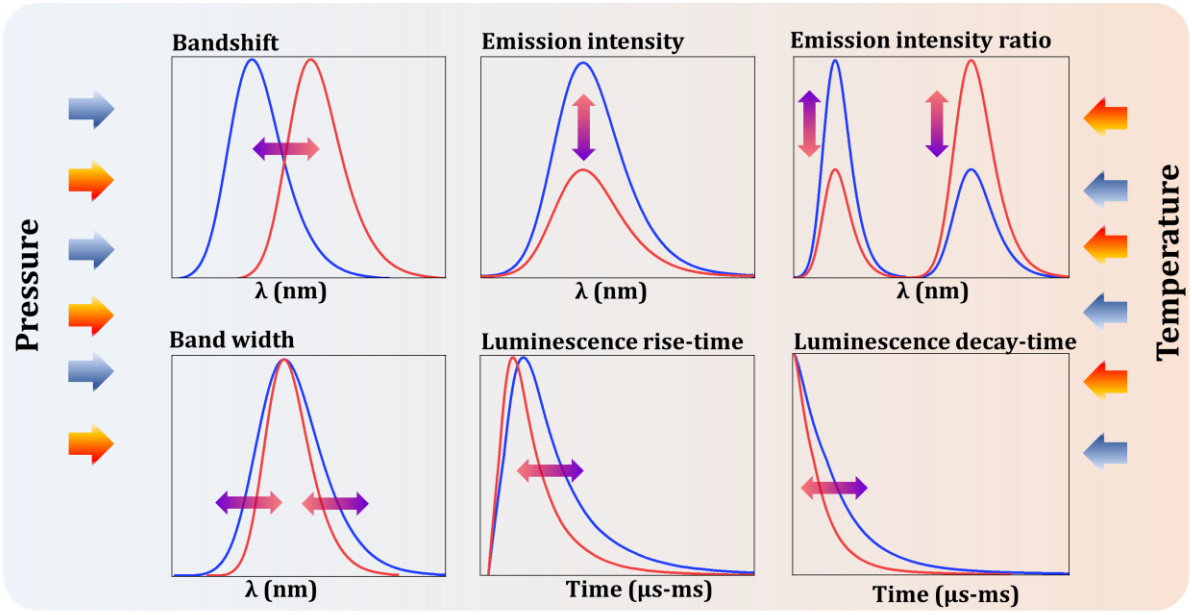

Figure 7. Presentation of the concept of the luminescent manometry and thermometry, i.e., the pressure- and temperature-induced luminescence properties of $Ln^{2+/3+}$-doped materials.

Currently, a common approach for optical pressure sensing is to use the calibration of the line shift (usually red shift) of the emission band in the sensor material. The dependence of the line shift as a function of pressure can be fitted to a linear function [43,63,164,165] or to a polynomial function.[1,22] The main effects responsible for the commonly observed pressure-triggered red-shift in luminescent materials are the most plausibly: I) an amplified nephelauxetic effect induced by a decrease of free-ion parameters with compression, leading to an increase in the covalent character

of bonding (shorter bonds), and narrowing energy separation/gap between the ground and excited states;[1,22,43] and II) improved splitting of the ground and excited configurations, which is triggered by the enhanced crystal-field strength at HP, due to shorter interionic distances leading to stronger interactions between ions. Overall, the observed shift towards lower energies (longer wavelengths) is related to the overall contraction of the $4f^N$ ground configuration, resulting in a reduction of the energy difference between the ground state and the excited state of the $^{2S+1}L_J$ multiplet. This effect originates from the reduction of the Coulomb and spin-orbit interactions under extreme condition of pressure, leading to a spectral red-shift of the 5d multiplets or 4f levels.

A commonly used method for the pressure determination is based on the emission line of Cr^{3+} ion located at 694 nm in ruby ($Al_2O_3:Cr^{3+}$), showing the pressure-induced spectral shift of $d\lambda/dp \approx 0.35$ nm/GPa.[156,166–168] However, due to the relatively broad (≈0.8 nm at ambient condition) emission bands of ruby and the strong overlapping of the ruby peaks (R_1 and R_2) under non-hydrostatic, high-pressure conditions, there is usually a large error in the ruby spectral data for pressure-determination analysis, thanks to whereby the precision of the determination of pressure is significantly reduced when very HP conditions (above ~10 GPa) are required. This is usually due to the solidification of the commonly used PTMs (methanol/ethanol/water) triggered by pressure as well as the resulting loss of hydrostaticity in the DAC chamber.[73,154–156] It is worth noting that the ruby line depends on temperature and the shift is $d\lambda/dT \approx 0.007$ nm/K, which largely limits the ability to measure pressure to a narrow temperature range..

Many works have suggested that the use of $SrB_4O_7:Sm^{2+}$, i.e., the pressure-induced spectral shift of the Sm^{2+}: $^5D_0 \rightarrow {}^7F_0$ emission band (0–0) at ~685 nm, may be as an excellent alternative to ruby as a pressure sensor. This is due to several benefits: 1) HP -induced shift of $d\lambda/dP = 0.255$ nm/GPa; 2) the emission band is isolated and narrow; 3) the temperature-dependence of the pressure sensing parameter is relatively low. As with other pressure sensors based on Ln ions or transition metal ions, the ubiquitous and progressive compression-induced quenching of emission of the Sm^{2+} luminescence under pressure, which is a notoriously observed effect,[127,144,169] greatly limits pressure sensing accuracy and range detected. It is still a bottleneck in experimental pressure-sensing techniques based on PL to significantly improve the accuracy of pressure measurements and broaden the pressure sensing range covered by these techniques. Moreover, with the development of science and technique, the pursuit of better pressure sensing properties,

including higher pressure sensitivity, lower temperature-dependence, faster response, etc., and the discovery of novel pressure sensing materials are the trends in the field of pressure sensing.

3.5.2. Luminescence thermometry

Temperature is a central concept and variables in not only scientific research, especially thermodynamics and statistical mechanics, but also industrial manufacturing and our daily life. Temperature, as one of the most crucial physical parameters, from the atomic scale up to macroscopic levels, influences the molecular dynamics, thermodynamics and the practical viability of all natural and engineering systems.[5,6,170–176] To date, common traditional thermometers, such as thermoelectric couples, liquid-filled thermometers, and pyrometers are based on the principle of liquid and metal expansion. However, they usually require physical contact (invasive), thus in general, need conductive heat transfer and require to reach heat equilibrium between the targeted object and the thermal sensor. Conventional thermometers are no longer able to fulfil the increasing requirement for temperature determination, due to their low-resolution, long-time response, relatively large dimensions, invasive character, *etc*. Moreover, they are generally not suitable for some special environments such as submicron-sized objects, power stations, living biological cells, *etc*.[177–180] Thus, it is necessary to develop novel thermometric techniques.

System temperature determination can be effectively realized with an optical, noncontact approach using organic fluorophores, metal complexes, gold nanorods, quantum and carbon dots, materials based on Ln ions, etc., which can optically examine the temperature distribution in submicron-sized objects/scale with outstanding benefits, including high sensitivity, high spatial resolution, fast response, contactless approach, and so on.[169,181–186] More and more attention is paid to Ln-doped materials due to their characteristic spectroscopic properties.[187–189] As mentioned above (see **Figure 7**), the temperature determination of the system based on spectroscopic properties of the materials as a function of temperature, i.e., the shape of the emission band, emission intensity changes, bandwidth (full width half maximum, FWHM), spectral line shift, variation in luminescence rise or decay times, which can act as luminescence thermometric parameters.

In order to implement noncontact thermometry, the most common approach is to use the FIR/LIR of dual energy levels, i.e., FIR/LIR technique, which applying various temperature responses of FIR/LIR values of the emission bands originating from the TCLs of Ln ions. Importantly, the FIR/LIR technique allows to avoid technical errors in spectroscopic measurements arising from the difference in the dopant content in the luminescent material, inhomogeneous distribution of the dopant in the synthesized particle, and fluctuations in the power of the excitation sources, etc. By using the FIR/LIR technique, external disruptions may be mitigated or removed to some degree, such as the effect of variation of the irradiation force, variance in loss of communication in the optical pass and the photo-bleaching influence of organic dyes, which is beneficial for the steadiness, precision, and dependability of thermal sensors. The FIR/LIR technique based on the TCLs of Ln^{3+} ions has become a hot topic in recent decades. TCLs have an appropriate energy separation between the thermalized states, usually meeting the requirement of $200 \leq \Delta E \leq 2000$ cm^{-1} to avoid intensive overlapping between the two emission bands and to allow the upper level a minimum population of optically active Ln ions in the measured temperature range. Such TCLs are fulfilled in the structures of the energy levels of many Ln ions, such as Er^{3+}, Tm^{3+}, Nd^{3+},[187–189] *etc*. Due to the thermalization processes between the two TCLs, with elevation of temperature, the relative population of the upper energy level (I_2) and the lower energy level (I_1) are consistent with the Boltzmann distribution,[171,190] which can be described using the following equation:

$$FIR = \frac{I_2}{I_1} = A \times \exp\left(\frac{-\Delta E}{k_B T}\right) \quad (4)$$

where A is a coefficient, which depends on the branching ratio of the transitions, related to the rates of total spontaneous emission, degeneration of states and transitions angular frequencies, etc.[2,6,191] Whereas k, ΔE and T refer to the Boltzmann constant, the energy gap between the two TCLs, and the absolute temperature, respectively. The ΔE values can be obtained based on the PL emission spectra or the alignment offset during the fitting process of the related FIR/LIR as a function of temperature. In the case of experimental overlapping of the emission bands corresponding to the different components of the crystal field, an additional coefficient B is sometimes included in the formula, that is, using the following fitting equation:[192]

$$FIR = \frac{I_2}{I_1} = A \times \exp\left(\frac{-\Delta E}{k_B T}\right) + B \quad (5)$$

It is worth noting that the above Equation 4 can also be tuned into a linear formula, *i.e.*,

$$\ln(FIR) = A - \frac{\Delta E}{k_B T} \quad (6)$$

As mentioned above, the population of two TCLs are sensitive to the temperature change, due to the thermal population – thermalization effects. The most commonly used Ln^{3+} for a luminescent thermometer is Er^{3+} with the TCLs $^2H_{11/2}$ and $^4S_{3/2}$, between which the energy gap is ~750-850 cm^{-1}.[193–195] As predicted by the Boltzmann distribution, the greater the energy separation of TCLs leads to a higher sensitivity of the thermal sensor. Thus, the challenge towards higher sensitivity is limited due to the restriction of the energy separation between TCLs (200 cm^{-1}<ΔE< 2000 cm^{-1}). As a result, more and more researchers are starting to design a new strategy to improve detection sensitivity for temperature sensing. Recently, some researchers have been focusing on the use of non-thermally coupled levels (non-TCLs), which may achieve an even higher relative sensitivity theoretically unlimited, which, in fact does not depend on the energy difference between the corresponding levels in this case, but related to thermal quenching rates and the temperature-governed ET, etc. [173,189,191,196] Since no suitable physical model has been reported to describe the temperature-dependences of LIR values for non-TCLs of Ln^{3+}, the means of empirical functions, usually exponential or polynomial, are commonly applied. [3,173]

The Population redistribution ability (PRA) as a function of temperature is often applied for examining the rate of the population change between the TCLs:

$$PRA = \frac{I_2}{I_2 + I_1} = \frac{A}{A + \exp(\Delta E / k_B T)} \quad (7)$$

Importantly, the most important and basic parameter describing the temperature detection ability of the developed sensor are the absolute thermal sensitivity (S_a) and relative thermal sensitivity (S_r), which can be calculated via the following equation:

$$S_a = 100\% \times \frac{\partial(FIR)}{\partial T} \quad (8)$$

$$S_r = 100\% \times \frac{1}{FIR} \times \frac{\partial(FIR)}{\partial T} \quad (9)$$

In some cases, the FIR/LIR may not be well fitted using the functions. To remain an independent form of the fitting constant and to avoid the strong dependence on the calibration model and the adopted fitting parameters, the S_r value can be estimated by a more general method:

$$S_r\ (T_0) = \frac{1}{FIR(T_0)} \times \frac{FIR(T_1) - FIR(T_0)}{T_1 - T_0} \quad (10)$$

Where T_0 and T_1 are the first and second measured temperature values, $T_1 > T_0$, $FIR(T_1)$ is the FIR value at T_1 temperature, $FIR(T_0)$ is the FIR value at T_0 temperature. Additionally, more generally,

for different measured parameters (MP) at elevated temperature,[197] the S_a and S_r values can also be estimated by using the following functions:

$$S_r = 100\% \times \frac{1}{MP} \times \left|\frac{\partial MP}{\partial T}\right| \quad (11)$$

$$S_a = 100\% \times \left|\frac{\partial MP}{\partial T}\right| \quad (12)$$

The unit of S_r is expressed as the change (percentage) in temperature per Kelvin (% K^{-1}) or per Celsius (% $^{\circ}C^{-1}$).[192] Noteworthy, for quantitatively comparison of the thermometric performance of different temperature sensors, a more reasonable way is to compare the S_r value, rather than S_a. This is due to the independence of S_r on the nature of the samples and the experimental setup applied during the thermal measurement.

Importantly, it is also worth mentioning the temperature resolution or temperature uncertainty (δT or ΔT). δT is the smallest detectable change of temperature in a given measurement and can be generally defined as[197]:

$$\delta T = \frac{1}{S_r} \times \frac{\partial MP}{MP} \quad (13)$$

when the FIR is used, it can also be expressed as:

$$\delta T = \frac{1}{S_r} \times \frac{\partial FIR}{FIR} \quad (14)$$

where δFIR is the uncertainty of the determined LIR, which can be further estimated using the following expression:

$$\delta LIR = LIR \times \sqrt{\left(\frac{\delta I_1}{I_1}\right)^2 + \left(\frac{\delta I_2}{I_2}\right)^2} \quad (15)$$

here, δI_1 and δI_2 refer to the determination the uncertainty of the corresponding emission intensities i.e., the noise-to-signal ratio, which can be estimated from the integrated intensity of the spectral background noise divided by the integrated emission intensity of the emission band.

Importantly, the **r**epeatability (R) of the measured parameter (MP) in an optical thermometer is also a vital parameter for further test the validity of the developed optical thermometers. R can be estimated using the following equation:

$$R\ (T) = 100\% \times \left[1 - \frac{\left|MP^i(T) - \langle MP(T)\rangle\right|_{max}}{\langle MP(T)\rangle}\right] \quad (16)$$

where MP^i is the measured parameter in the *i*th cycle, while ⟨MP(T)⟩ is the mean value of MP over several heating and cooling cycles (5-10 cycles are usually required). Good repeatability in the developed thermometer should not show signs of thermal hysteresis in cyclic plots.

3.6.Literature

[1] M. Runowski, P. Woźny, N. Stopikowska, Q. Guo, S. Lis, *ACS Appl. Mater. Interfaces* **2019**, *11*, 4131.

[2] M. Runowski, A. Shyichuk, A. Tymiński, T. Grzyb, V. Lavín, S. Lis, *ACS Appl. Mater. Interfaces* **2018**, *10*, 17269.

[3] M. Runowski, N. Stopikowska, D. Szeremeta, S. Goderski, M. Skwierczyńska, S. Lis, *ACS Appl. Mater. Interfaces* **2019**, *11*, 13389.

[4] A. Kovalenko, P. O. Rublev, L. O. Tcelykh, A. S. Goloveshkin, L. S. Lepnev, A. S. Burlov, A. A. Vashchenko, L. Marciniak, A. M. Magerramov, N. G. Shikhaliyev, S. Z. Vatsadze, V. V. Utochnikova, *Chem. Mater.* **2019**, *31*, 759.

[5] K. Maciejewska, L. Marciniak, *Chem. Eng. J.* **2020**, *402*, 126197.

[6] C. D. S. Brites, A. Millán, L. D. Carlos, In *Handbook on the Physics and Chemistry of Rare Earths*, Elsevier B.V., **2016**, pp. 339–427.

[7] N. G. Connelly, T. Damhus, *Nomenclature of Inorganic Chemistry: IUPAC Recommendations 2005*, Cambridge: RSC Publishing, **2005**.

[8] S. V. Eliseeva, J. C. G. Bünzli, *Lanthanide luminescence for functional materials and bio-sciences*, Vol. 39, **2010**, pp. 189–227.

[9] E. N. Harvey, *A history of luminescence from the earliest times until 1900.*, American Philosophical Society, Philadelphia, **2011**.

[10] G. Blasse, B. C. Grabmaier, *Lumin. Mater.* **1994**, 1.

[11] R. Wang, F. Zhang, In *RSC Nanoscience and Nanotechnology*, Royal Society of Chemistry, **2016**, pp. 1–39.

[12] P. Dorenbos, *ECS J. Solid State Sci. Technol.* **2013**, *2*, R3001.

[13] G. H. Dieke, *Spectra and Energy Levels of Rare Earth Ions in Crystals*, Interscience, **1968**.

[14] K. Michael, *Discuss. Faraday Soc.* **1950**, *9*, 14.

[15] H. Terraschke, C. Wickleder, *Chem. Rev.* **2015**, *115*, 11352.

[16] K. Horky, W. Schnick, *Chem. Mater.* **2017**, *29*, 4590.

[17] W. Sun, Y. Jia, R. Pang, H. Li, T. Ma, D. Li, J. Fu, S. Zhang, L. Jiang, C. Li, *ACS Appl. Mater. Interfaces* **2015**, *7*, 25219.

[18] M. Suta, F. Lavoie-Cardinal, C. Wickleder, *Angew. Chemie - Int. Ed.* **2020**, *59*, 10949.

[19] M. Runowski, P. Woźny, V. Lavín, S. Lis, *Sensors Actuators, B Chem.* **2018**, *273*, 585.

[20] B. Moine, B. Courtois, C. Pedrini, *J. Phys. Fr.* **1989**, *50*, 2105.

[21] Z. Dai, J. Chen, B. Yang, *J. Phys. Chem. Lett.* **2021**, *12*, 10093.

[22] T. Zheng, M. Sójka, M. Runowski, P. Woźny, S. Lis, E. Zych, *Adv. Opt. Mater.* **2021**, *2101507*, 1.

[23] O. M. Ten Kate, K. W. Krämer, E. Van Der Kolk, *Sol. Energy Mater. Sol. Cells* **2015**, *140*, 115.

[24] P. Solarz, J. Komar, M. Głowacki, M. Berkowski, W. Ryba-Romanowski, *RSC Adv.* **2017**, *7*, 21085.

[25] M. E. Fieser, M. R. Macdonald, B. T. Krull, J. E. Bates, J. W. Ziller, F. Furche, W. J. Evans, *J. Am. Chem. Soc.* **2015**, *137*, 369.

[26] M. Karbowiak, C. Rudowicz, *Eur. J. Inorg. Chem.* **2018**, *2018*, 1660.

[27] M. Karbowiak, C. Rudowicz, J. Cichos, *J. Phys. Chem. A* **2018**, *122*, 923.

[28] J. J. Schuyt, G. V. M. Williams, *Radiat. Meas.* **2020**, *134*, 106326.

[29] M. Shang, S. Liang, H. Lian, J. Lin, *Inorg. Chem.* **2017**, *56*, 6131.

[30] C. T. Zeyrek, H. Ünver, Ö. T. Arpaci, K. Polat, N. O. Iskeleli, M. Yildiz, *J. Mol. Struct.* **2015**, *1081*, 22.

[31] D. Pawlak, Z. Frukacz, Z. Mierczyk, A. Suchocki, J. Zachara, *J. Alloys Compd.* **1998**, *275–277*, 361.

[32] H. Li, X. Y. Kuang, Y. Y. Yeung, *J. Phys. B At. Mol. Opt. Phys.* **2014**, *47*.

[33] R. K. Verma, K. Kumar, S. B. Rai, *Solid State Sci.* **2010**, *12*, 1146.

[34] T. P. Gompa, A. Ramanathan, N. T. Rice, H. S. La Pierre, *Dalt. Trans.* **2020**, *49*, 15945.

[35] P. Dorenbos, *J. Alloys Compd.* **2002**, *341*, 156.

[36] P. Dorenbos, *J. Lumin.* **2003**, *104*, 239.

[37] W. J. Evans, *Perspectives in reductive lanthanide chemistry*, Vol. 206–207, Elsevier, **2000**, pp. 263–283.

[38] A. Meijerink, J. Nuyten, G. Blasse, *J. Lumin.* **1989**, *44*, 19.

[39] L. Yang, Y. Wan, Y. Huang, X. Wang, H. Cheng, H. J. Seo, *Mater. Lett.* **2016**, *172*, 23.

[40] A. Meijerink, G. Blasse, *J. Lumin.* **1989**, *43*, 283.

[41] S. G. Jantz, F. Pielnhofer, L. van Wüllen, R. Weihrich, M. J. Schäfer, H. A. Höppe, *Chem. - A Eur. J.* **2018**, *24*, 443.

[42] M. Sójka, M. Runowski, T. Zheng, A. Shyichuk, D. Kulesza, E. Zych, S. Lis, *J. Mater. Chem. C* **2022**.

[43] T. Zheng, M. Runowski, P. Woźny, S. Lis, V. Lavín, *J. Mater. Chem. C* **2020**, *8*, 4810.

[44] K. Song, H. Yu, Q. Nie, Y. Bai, Y. Guan, J. Yu, L. Guo, *J. Lumin.* **2020**, *224*, 117317.

[45] M. Suta, P. Larsen, F. Lavoie-Cardinal, C. Wickleder, *J. Lumin.* **2014**, *149*, 35.

[46] A. M. Srivastava, H. A. Comanzo, S. Camardello, S. B. Chaney, M. Aycibin, U. Happek, *J. Lumin.* **2009**, *129*, 919.

[47] M. Suta, C. Wickleder, *J. Mater. Chem. C* **2015**, *3*, 5233.

[48] Z. Tang, Q. Zhang, Y. Cao, Y. Li, Y. Wang, *Chem. Eng. J.* **2020**, *388*, 124231.

[49] M. Suta, C. Wickleder, *J. Lumin.* **2019**, *210*, 210.

[50] M. Runowski, A. Bartkowiak, M. Majewska, I. R. Martín, S. Lis, *J. Lumin.* **2018**, *201*, 104.

[51] J. C. G. Bünzli, C. Piguet, *Taking advantage of luminescent lanthanide ions*, Vol. 34,

2005, pp. 1048–1077.

[52] X. Qin, X. Liu, W. Huang, M. Bettinelli, X. Liu, *Chem. Rev.* **2017**, *117*, 4488.

[53] A. Baran, S. Mahlik, M. Grinberg, E. Zych, *J. Phys. Condens. Matter* **2013**, *25*.

[54] K. Winskiewski, S. Mahlik, M. Grinberg, H. J. Seo, *J. Lumin.* **2011**, *131*, 306.

[55] R. A. Hewes, M. V Hoffman, G. E. Company, *J. Lumin.* **2000**, *3*, 261.

[56] T. Zheng, M. Runowski, P. Woźny, S. Lis, *J. Alloys Compd.* **2020**, *822*, 1.

[57] J. Zhang, R. Li, Q. Chen, G. Zhao, J. Jia, *Mater. Lett.* **2018**, *233*, 302.

[58] J. Qiao, G. Zhou, Y. Zhou, Q. Zhang, Z. Xia, *Nat. Commun.* **2019**, *10*, 1.

[59] M. Zhao, Q. Zhang, Z. Xia, *Accounts Mater. Res.* **2020**, *1*, 137.

[60] G. J. Hoerder, M. Seibald, D. Baumann, T. Schröder, S. Peschke, P. C. Schmid, T. Tyborski, P. Pust, I. Stoll, M. Bergler, C. Patzig, S. Reißaus, M. Krause, L. Berthold, T. Höche, D. Johrendt, H. Huppertz, *Nat. Commun.* **2019**, *10*, 1.

[61] P. Pust, V. Weiler, C. Hecht, A. Tücks, A. S. Wochnik, A. K. Henß, D. Wiechert, C. Scheu, P. J. Schmidt, W. Schnick, *Nat. Mater.* **2014**, *13*, 891.

[62] K. Binnemans, *Coord. Chem. Rev.* **2015**, *295*, 1.

[63] Q. Jing, Q. Wu, L. Liu, J. A. Xu, Y. Bi, Y. Liu, H. Chen, S. Liu, Y. Zhang, L. Xiong, Y. Li, J. Liu, *J. Appl. Phys.* **2013**, *113*, 023507.

[64] A. Ellens, F. Zwaschka, F. Kummer, A. Meijerink, M. Raukas, K. Mishra, *J. Lumin.* **2001**, *93*, 147.

[65] Q. Zeng, Z. Pei, Q. Su, S. Lu, *J. Lumin.* **1999**, *82*, 241.

[66] Q. Zeng, N. Kilah, M. Riley, H. Riesen, *J. Lumin.* **2003**, *104*, 65.

[67] K. Jang, I. Kim, S. Park, Y. Huang, H. J. Seo, C. Kim, *J. Phys. Chem. Solids* **2006**, *67*, 2316.

[68] Y. Huang, W. Zhao, L. Shi, H. J. Seo, *J. Alloys Compd.* **2009**, *477*, 936.

[69] J. Wang, Y. Huang, Y. Li, H. J. Seo, *J. Am. Ceram. Soc.* **2011**, *94*, 1454.

[70] J. Wang, Y. Li, Y. Huang, L. Shi, H. J. Seo, *Mater. Chem. Phys.* **2010**, *120*, 598.

[71] Q. Zeng, N. Kilah, M. Riley, *J. Lumin.* **2003**, *101*, 167.

[72] Z. Cao, X. Wei, L. Zhao, Y. Chen, M. Yin, *ACS Appl. Mater. Interfaces* **2016**, *8*, 34546.

[73] F. Datchi, R. LeToullec, P. Loubeyre, *J. Appl. Phys.* **1997**, *81*, 3333.

[74] H. Hagemann, F. Kubel, H. Bill, F. Gingl, *J. Alloys Compd.* **2004**, *374*, 194.

[75] F. Kubel, H. . Hagemann, H. . Bill, *Mater. Res. Bull.* **1997**, *32*, 263.

[76] Frank Kubel, *Zeitschrift für Anorg. und Allg. Chemie* **1998**, *624*, 1105.

[77] A. Winnacker, R. M. Shelby, R. M. Macfarlane, *Opt. Lett.* **1985**, *10*, 350.

[78] K. Holliday, C. Wei, M. Croci, U. P. Wild, *J. Lumin.* **1992**, *53*, 227.

[79] H. Riesen, K. Badek, T. M. Monro, N. Riesen, *Opt. Mater. Express* **2016**, *6*, 3097.

[80] X. L. Wang, Z. Q. Liu, M. A. Stevens-Kalceff, H. Riesen, *Inorg. Chem.* **2014**, *53*, 8839.

[81] L. C. Dixie, A. Edgar, M. C. Bartle, *J. Lumin.* **2014**, *149*, 91.

[82] H. Lueken, *Magnetochemie: Eine Einführung in Theorie und Anwendung*.

[83] W. J. Schipper, A. Meijerink, G. Blasse, *J. Lumin.* **1994**, *62*, 55.

[84] E. S. Sabisky, C. H. Anderson, *Phys. Rev.* **1967**, *159*, 234.

[85] Z. J. Kiss, *Phys. Rev.* **1962**, *127*, 718.

[86] O. S. Wenger, C. Wickleder, K. W. Krämer, H. U. Güdel, *J. Lumin.* **2001**, *94–95*, 101.

[87] M. De Jong, A. Meijerink, L. Seijo, Z. Barandiarán, *J. Phys. Chem. C* **2017**, *121*, 10095.

[88] J. Zhou, Q. Liu, W. Feng, Y. Sun, F. Li, *Chem. Rev.* **2015**, *115*, 395.

[89] D. Chen, Z. Wan, Y. Zhou, X. Zhou, Y. Yu, J. Zhong, M. Ding, Z. Ji, *ACS Appl. Mater. Interfaces* **2015**, *7*, 19484.

[90] F. Vetrone, R. Naccache, A. Zamarrón, A. J. De La Fuente, F. Sanz-Rodríguez, L. M.

Maestro, E. M. Rodriguez, D. Jaque, J. G. Sole, J. A. Capobianco, *ACS Nano* **2010**, *4*, 3254.

[91] A. Siaï, P. Haro-González, K. Horchani-Naifer, M. Férid, *Sensors Actuators, B Chem.* **2016**, *234*, 541.

[92] M. K. Mahata, T. Koppe, K. Kumar, H. Hofsäss, U. Vetter, *Sci. Rep.* **2016**, *6*, 1.

[93] S. Zhou, S. Jiang, X. Wei, Y. Chen, C. Duan, M. Yin, *J. Alloys Compd.* **2014**, *588*, 654.

[94] R. Marin, D. Jaque, A. Benayas, *Nanoscale Horizons* **2021**, *6*, 209.

[95] C. S. Lim, A. Aleksandrovsky, V. Atuchin, M. Molokeev, A. Oreshonkov, *Crystals* **2020**, *10*, 1.

[96] C. S. Lim, A. S. Aleksandrovsky, M. S. Molokeev, A. S. Oreshonkov, D. A. Ikonnikov, V. V. Atuchin, *Dalt. Trans.* **2016**, *45*, 15541.

[97] M. V. DaCosta, S. Doughan, Y. Han, U. J. Krull, *Anal. Chim. Acta* **2014**, *832*, 1.

[98] X. Huang, J. Liang, S. Rtimi, B. Devakumar, Z. Zhang, *Chem. Eng. J.* **2021**, *405*, 126950.

[99] G. Y. Chen, Y. Liu, Z. G. Zhang, B. Aghahadi, G. Somesfalean, Q. Sun, F. P. Wang, *Chem. Phys. Lett.* **2007**, *448*, 127.

[100] C. Helvacı, *Miner. Depos.* **1984**, *19*, 217.

[101] M. Mohapatra, B. Rajeswari, R. M. Kadam, M. Kumar, T. K. Seshagiri, N. K. Porwal, S. V. Godbole, V. Natarajan, *J. Alloys Compd.* **2014**, *611*, 74.

[102] J. Sun, J. Zhu, X. Liu, H. Du, *J. Rare Earths* **2012**, *30*, 1084.

[103] C. B. Palan, N. S. Bajaj, S. K. Omanwar, *Mater. Res. Bull.* **2016**, *76*, 216.

[104] V. V. Atuchin, V. G. Kesler, A. I. Zaitsev, M. S. Molokeev, A. S. Aleksandrovsky, A. A. Kuzubov, N. Y. Ignatova, *J. Phys. Condens. Matter* **2013**, *25*.

[105] Z. Pei, Q. Su, J. Zhang, *J. Alloys Compd.* **1993**, *198*, 51.

[106] M. Peng, N. Da, S. Krolikowski, A. Stiegelschmitt, L. Wondraczek, *Opt. Express* **2009**, *17*, 21169.

[107] V. Darakchieva, M. Y. Xie, F. Tasnádi, I. A. Abrikosov, L. Hultman, B. Monemar, J. Kamimura, K. Kishino, *Appl. Phys. Lett.* **2008**, *93*, 261908.

[108] P. Mikhail, J. Hulliger, *Comments Inorg. Chem.* **1999**, *21*, 263.

[109] H. Huppertz, *Zeitschrift fur Naturforsch. - Sect. B J. Chem. Sci.* **2003**, *58*, 278.

[110] K. Machida, G. Adachi, J. Shiokawa, *J. Lumin.* **1979**, *21*, 101.

[111] C. Zhao, H. Li, Y. Wang, J. Jiang, Y. He, *High Press. Res.* **2017**, *37*, 18.

[112] L. Gil-Escrig, M. Roß, J. Sutter, A. Al-Ashouri, C. Becker, S. Albrecht, *Sol. RRL* **2021**, *5*.

[113] P. S. C. Schulze, A. J. Bett, M. Bivour, P. Caprioglio, F. M. Gerspacher, Ö. Kabaklı, A. Richter, M. Stolterfoht, Q. Zhang, D. Neher, M. Hermle, H. Hillebrecht, S. W. Glunz, J. C. Goldschmidt, *Sol. RRL* **2020**, *4*, 1.

[114] F. Di Mei, L. Falsi, M. Flammini, D. Pierangeli, P. Di Porto, A. J. Agranat, E. DelRe, *Nat. Photonics* **2018**, *12*, 734.

[115] M. Li, Y. Xu, S. Han, J. Xu, Z. Xie, Y. Liu, Z. Xu, M. Hong, J. Luo, Z. Sun, *Adv. Mater.* **2020**, *32*, 1.

[116] G. Pacchioni, *Nat. Rev. Mater.* **2021**, *6*, 108.

[117] C. Martin, *Nat. Mater.* **2012**, *11*, 1002.

[118] T. H. Han, S. Tan, J. Xue, L. Meng, J. W. Lee, Y. Yang, *Adv. Mater.* **2019**, *31*, 1.

[119] D. Liu, C. Jin, F. Shan, J. He, F. Wang, *ACS Appl. Mater. Interfaces* **2020**, *12*, 17443.

[120] D. Maurya, A. Pramanick, K. An, S. Priya, *Appl. Phys. Lett.* **2012**, *100*, 0.

[121] Y. Rong, Y. Hu, A. Mei, H. Tan, M. I. Saidaminov, S. Il Seok, M. D. McGehee, E. H. Sargent, H. Han, *Science (80-.).* **2018**, *361*.

[122] Y. M. You, W. Q. Liao, D. Zhao, H. Y. Ye, Y. Zhang, Q. Zhou, X. Niu, J. Wang, P. F. Li, D. W. Fu, Z. Wang, S. Gao, K. Yang, J. M. Liu, J. Li, Y. Yan, R. G. Xiong, *Science (80-.).* **2017**, *357*, 306.

[123] N. Nuraje, K. Su, *Nanoscale* **2013**, *5*, 8752.

[124] B. Zhuang, Y. Liu, S. Yuan, H. Huang, J. Chen, D. Chen, *Nanoscale* **2019**, *11*, 15010.

[125] D. Kumar Singh, K. Mondal, J. Manam, *Ceram. Int.* **2017**, *43*, 13602.

[126] G. Jyothi, L. S. Kumari, K. G. Gopchandran, *Ceram. Int.* **2017**, *43*, 12044.

[127] Z. Dai, J. Xie, W. Liu, X. Wang, L. Zhang, Z. Zhou, J. Li, X. Ren, *ACS Appl. Mater. Interfaces* **2020**, *12*, 30289.

[128] A. Patra, C. S. Friend, R. Kapoor, P. N. Prasad, *Chem. Mater.* **2003**, *15*, 3650.

[129] E. Aksel, J. L. Jones, *Sensors* **2010**, *10*, 1935.

[130] M. Acosta, N. Novak, V. Rojas, S. Patel, R. Vaish, J. Koruza, G. A. Rossetti, J. Rödel, *Appl. Phys. Rev.* **2017**, *4*.

[131] Q. Zhang, T. Cagin, W. A. Goddard, *Proc. Natl. Acad. Sci. U. S. A.* **2006**, *103*, 14695.

[132] H. Bae, K. T. Lee, *RSC Adv.* **2019**, *9*, 2451.

[133] P. R. Potnis, N. T. Tsou, J. E. Huber, *Materials (Basel).* **2010**, *4*, 417.

[134] An introduction to science and technology studies, Vol. 41, **2004**, pp. 41-3396-41–3396.

[135] M. Runowski, S. Sobczak, J. Marciniak, I. Bukalska, S. Lis, A. Katrusiak, *Nanoscale* **2019**, *11*, 8718.

[136] F. Bai, K. Bian, X. Huang, Z. Wang, H. Fan, *Chem. Rev.* **2019**, *119*, 7673.

[137] M. Somayazulu, P. Dera, A. F. Goncharov, S. A. Gramsch, P. Liermann, W. Yang, Z. Liu, H. K. Mao, R. J. Hemley, *Nat. Chem.* **2010**, *2*, 50.

[138] A. Cantaluppi, M. Buzzi, G. Jotzu, D. Nicoletti, M. Mitrano, D. Pontiroli, M. Riccò, A. Perucchi, P. Di Pietro, A. Cavalleri, *Nat. Phys.* **2018**, *14*, 837.

[139] Z. Ma, Z. Liu, S. Lu, L. Wang, X. Feng, D. Yang, K. Wang, G. Xiao, L. Zhang, S. A. T. Redfern, B. Zou, *Nat. Commun.* **2018**, *9*, 4.

[140] W. W. Kim, M. S. Jung, S. Lee, Y. J. Choi, J. K. Kim, S. U. Chai, W. W. Kim, D. D. G. Choi, H. Ahn, J. H. Cho, D. D. G. Choi, H. Shin, D. Kim, J. H. Park, *Adv. Energy Mater.* **2018**, *8*, 1702369.

[141] J. Song, G. Fabbris, W. Bi, D. Haskel, J. S. Schilling, *Phys. Rev. Lett.* **2018**, *121*.

[142] L. Zhang, C. C. Liu, L. Wang, C. C. Liu, K. Wang, B. Zou, *Angew. Chemie - Int. Ed.* **2018**, *57*, 11213.

[143] T. Yin, Y. Fang, W. K. Chong, K. T. Ming, S. Jiang, X. Li, J. L. Kuo, J. Fang, T. C. Sum, T. J. White, J. Yan, Z. X. Shen, *Adv. Mater.* **2018**, *30*, 1705017.

[144] M. Runowski, P. Woźny, S. Lis, V. Lavín, I. R. Martín, *Adv. Mater. Technol.* **2020**, *5*, 1901091.

[145] X. Liu, W. Xie, Y. Lü, J. Feng, X. Tang, J. Lin, Y. Dai, Y. Xie, L. Yan, *Inorg. Chem.* **2017**, *56*, 13829.

[146] J. A. Sans, V. Monteseguro, G. Garbarino, M. Gich, V. Cerantola, V. Cuartero, M. Monte, T. Irifune, A. Muñoz, C. Popescu, *Nat. Commun.* **2018**, *9*, 4554.

[147] D. Santamaria-Perez, C. McGuire, A. Makhluf, A. Kavner, R. Chuliá-Jordan, J. L. Jorda, F. Rey, J. Pellicer-Porres, D. Martinez-García, P. Rodriguez-Hernández, A. Muñoz, *Nat. Commun.* **2016**, *7*, 4.

[148] D. A. Davis, A. Hamilton, J. Yang, L. D. Cremar, D. Van Gough, S. L. Potisek, M. T. Ong, P. V. Braun, T. J. Martínez, S. R. White, J. S. Moore, N. R. Sottos, *Nature* **2009**, *459*, 68.

[149] Y. Wang, X. Tan, Y. M. Zhang, S. Zhu, I. Zhang, B. Yu, K. Wang, B. Yang, M. Li, B. Zou, S. X. A. Zhang, *J. Am. Chem. Soc.* **2015**, *137*, 931.

[150] X. Jiang, Y. Yang, M. S. Molokeev, P. Gong, F. Liang, S. Wang, L. Liu, X. Wu, X. Li, Y. Li, S. Wu, W. Li, Y. Wu, Z. Lin, *Adv. Mater.* **2018**, *30*, 1.

[151] X. Jiang, M. S. Molokeev, L. Dong, Z. Dong, N. Wang, L. Kang, X. Li, Y. Li, C. Tian, S. Peng, W. Li, Z. Lin, *Nat. Commun.* **2020**, *11*, 1.

[152] Y. N. Zhuravlev, V. V. Atuchin, *Sensors* **2021**, *21*.

[153] T. Tröster, *Handb. Phys. Chem. Rare Earths* **2003**, *33*, 515.

[154] R. J. Angel, M. Bujak, J. Zhao, G. D. Gatta, S. D. Jacobsen, *J. Appl. Crystallogr.* **2007**,

40, 26.

[155] R. J. Angel, In *Transformation Processes in Minerals*, De Gruyter Mouton, **2019**, pp. 85–104.

[156] G. J. Piermarini, S. Block, J. D. Barnett, R. A. Forman, *J. Appl. Phys.* **1975**, *46*, 2774.

[157] R. Dey, V. K. Rai, *Dalt. Trans.* **2014**, *43*, 111.

[158] X. Bai, H. Song, G. Pan, Y. Lei, T. Wang, X. Ren, S. Lu, B. Dong, Q. Dai, L. Fan, *J. Phys. Chem. C* **2007**, *111*, 13611.

[159] L. Zhou, P. Du, *Appl. Phys. A Mater. Sci. Process.* **2019**, *125*, 1.

[160] T. Grzyb, R. J. Wiglusz, A. Gruszeczka, S. Lis, *Dalt. Trans.* **2014**, *43*, 17255.

[161] T. Grzyb, K. Kubasiewicz, A. Szczeszak, S. Lis, *Dalt. Trans.* **2015**, *44*, 4063.

[162] T. Tröster, *Optical Studies of Non-Metallic Compounds under Pressure*, Vol. 33, **2003**, pp. 515–589.

[163] J. D. Barnett, S. Block, G. J. Piermarini, *Rev. Sci. Instrum.* **1973**, *44*, 1.

[164] P. Wang, D. He, C. Xu, X. Ren, L. Lei, S. Wang, F. Peng, X. Yan, D. Liu, Q. Wang, L. Xiong, J. Liu, *J. Appl. Phys.* **2014**, *115*.

[165] M. Runowski, T. Zheng, P. Woźny, P. Du, *Dalt. Trans.* **2021**, *50*, 14864.

[166] P. M. Bell, H. K. Mao, K. Goettel, *Science (80-.).* **1984**, *226*, 542.

[167] J. A. Xu, H. K. Mao, P. M. Bell, *Science (80-.).* **1986**, *232*, 1404.

[168] K. Syassen, *High Press. Res.* **2008**, *28*, 75.

[169] S. Goderski, M. Runowski, P. Woźny, V. Lavín, S. Lis, *ACS Appl. Mater. Interfaces* **2020**, *12*, 40475.

[170] C. D. S. Brites, P. P. Lima, N. J. O. Silva, A. Millán, V. S. Amaral, F. Palacio, L. D. Carlos, *Adv. Mater.* **2010**, *22*, 4499.

[171] C. D. S. Brites, P. P. Lima, N. J. O. Silva, A. Millán, V. S. Amaral, F. Palacio, L. D. Carlos, *Nanoscale* **2012**, *4*, 4799.

[172] H. Peng, M. I. J. Stich, J. Yu, L. N. Sun, L. H. Fischer, O. S. Wolfbeis, *Adv. Mater.* **2010**, *22*, 716.

[173] M. Runowski, P. Wozny, N. Stopikowska, I. R. Martín, V. Lavín, S. Lis, *ACS Appl. Mater. Interfaces* **2020**, *12*, 43933.

[174] V. V. Atuchin, E. N. Galashov, O. Y. Khyzhun, V. L. Bekenev, L. D. Pokrovsky, Y. A. Borovlev, V. N. Zhdankov, *J. Solid State Chem.* **2016**, *236*, 24.

[175] K. A. Kokh, V. V. Atuchin, T. A. Gavrilova, N. V. Kuratieva, N. V. Pervukhina, N. V. Surovtsev, *Solid State Commun.* **2014**, *177*, 16.

[176] V. V Atuchin, V. A. Golyashov, K. A. Kokh, I. V Korolkov, A. S. Kozhukhov, V. N. Kruchinin, S. V Makarenko, L. D. Pokrovsky, I. P. Prosvirin, O. K. N. Romanyuk, O. E. Tereshchenko, *Cryst. Growth Des.* **2011**, *3*, 5507.

[177] P. Löw, B. Kim, N. Takama, C. Bergaud, *Small* **2008**, *4*, 908.

[178] Y. Gao, Y. Bando, *Nature* **2002**, *415*, 599.

[179] J. Lee, A. O. Govorov, N. A. Kotov, *Angew. Chemie - Int. Ed.* **2005**, *44*, 7439.

[180] M. D. Dramićanin, *J. Appl. Phys.* **2020**, *128*.

[181] P. Du, Y. Hua, J. S. Yu, *Chem. Eng. J.* **2018**, *352*, 352.

[182] P. Du, J. S. Yu, *Chem. Eng. J.* **2017**, *327*, 109.

[183] T. Zheng, X. Qiu, L. Zhou, M. Runowski, S. Lis, P. Du, L. Luo, *J. Alloys Compd.* **2021**, *864*, 158891.

[184] W. Piotrowski, K. Trejgis, K. Maciejewska, K. Ledwa, B. Fond, L. Marciniak, *ACS Appl. Mater. Interfaces* **2020**, *12*, 44039.

[185] M. Sójka, J. F. C. B. Ramalho, C. D. S. Brites, K. Fiaczyk, L. D. Carlos, E. Zych, *Adv. Opt. Mater.* **2019**, *7*, 1.

[186] M. Sójka, C. D. S. Brites, L. D. Carlos, E. Zych, *J. Mater. Chem. C* **2020**, *8*, 10086.

[187] O. A. Savchuk, J. J. Carvajal, C. Cascales, M. Aguiló, F. Díaz, *ACS Appl. Mater.*

Interfaces **2016**, *8*, 7266.

[188] C. Pérez-Rodríguez, L. L. Martín, S. F. León-Luis, I. R. Martín, K. K. Kumar, C. K. Jayasankar, *Sensors Actuators, B Chem.* **2014**, *195*, 324.

[189] E. C. Ximendes, A. F. Pereira, U. Rocha, W. F. Silva, D. Jaque, C. Jacinto, *Nanoscale* **2019**, *11*, 8864.

[190] D. Jaque, F. Vetrone, *Nanoscale* **2012**, *4*, 4301.

[191] M. Runowski, S. Goderski, D. Przybylska, T. Grzyb, S. Lis, I. R. Martín, *ACS Appl. Nano Mater.* **2020**, *3*, 6406.

[192] S. A. Wade, S. F. Collins, G. W. Baxter, *J. Appl. Phys.* **2003**, *94*, 4743.

[193] A. Maurya, A. Bahadur, A. Dwivedi, A. K. Choudhary, T. P. Yadav, P. K. Vishwakarma, S. B. Rai, *J. Phys. Chem. Solids* **2018**, *119*, 228.

[194] S. Sinha, M. K. Mahata, K. Kumar, *New J. Chem.* **2019**, *43*, 5960.

[195] S. Zhou, K. Deng, X. Wei, G. Jiang, C. Duan, Y. Chen, M. Yin, *Opt. Commun.* **2013**, *291*, 138.

[196] E. C. Ximendes, U. Rocha, T. O. Sales, N. Fernández, F. Sanz-Rodríguez, I. R. Martín, C. Jacinto, D. Jaque, *Adv. Funct. Mater.* **2017**, *27*.

[197] A. Baker, *Water Res.* **2005**, *39*, 4405.

4. Experimental

4.1. Synthesis

A list of developed luminescent materials is as follows:

$Sr_{2.97}Eu_{0.03}(BO_3)_2$, $Sr_{0.99}Eu_{0.01}B_2O_4$ and $Sr_{0.99}Eu_{0.01}B_4O_7$;

SrB_4O_7:0.01 Sm^{2+}, *x* Eu^{2+} (where *x*=0, 0.005, 0.01, 0.03, 0.05, 0.07 and 0.09);

SrB_4O_7: 0.05 Eu^{2+}, y Sm^{2+} (where y=0.005, 0.01, 0.02, 0.03 and 0.05);

$Sr_{1-x}B_4O_7$: *x*Tm^{2+} (where x=0.001, 0.002, 0.005 and 0.01);

$BaTi_{0.95-x}O_3$: *x* Er^{3+}, 0.05 Yb^{3+} (where *x* is the molar concentration of Er^{3+}, *i.e.*, 0.01, 0.05 and 0.09);

$BaTi_{0.95-x}O_3$: 0.01 Ho^{3+}, x Yb^{3+} (where *x* is the molar concentration of Yb^{3+}, *i.e.*, 0.01, 0.05 and 0.10).

4.1.1. $Sr_{2.97}Eu_{0.03}(BO_3)_2$,$Sr_{0.99}Eu_{0.01}B_2O_4$ and $Sr_{0.99}Eu_{0.01}B_4O_7$ micro-particles

Strontium borates doped with Eu ions, i.e., $Sr_{2.97}Eu_{0.03}(BO_3)_2$, $Sr_{0.99}Eu_{0.01}B_2O_4$ and $Sr_{0.99}Eu_{0.01}B_4O_7$ were synthesized via a well-known solid-state method at high temperature. High purity H_3BO_3 (Chempur, pure p.a.), $SrCO_3$ (Sigma-Aldrich, 99.9%) and Eu_2O_3 (Alfa Aesar, 99.99%) were used as starting materials. According to the chemical formula, the stoichiometric amounts of Eu_2O_3, H_3BO_3 and $SrCO_3$ were weighted, well mixed and ground together in an agate mortar for each component, respectively. Please note, that a 50 mol% excess of H_3BO_3 was used to synthesize the pure phase structure of $Sr_{0.99}Eu_{0.01}B_4O_7$ compound, based on the experience of previous experiments. The mixtures of the grounded power were then transferred into porcelain crucibles covered with a porcelain lid, placed in an oven, and heat-treated at 700 °C for 5 h, followed by sintering at 850 °C for 5 h. Subsequently, the sintered product was transferred to an agate mortar and ground again for around 15 min, followed by a further heat-treatment at 850 °C for another 5 h. It is worth noting that all grinding must take more than 15 minutes for the powder to be evenly mixed. And covering the crucibles with a lid is very crucial to limit the amount of oxygen from the air in the system and obtain a pure Eu^{2+} phase structure.

4.1.2. SrB_4O_7: Sm^{2+}, Eu^{2+} micro-particles

The SrB_4O_7:0.01 Sm^{2+}, *x* Eu^{2+} (*x*=0, 0.005, 0.01, 0.03, 0.05, 0.07 and 0.09) and SrB_4O_7: 0.05 Eu^{2+}, y Sm^{2+} (y=0.005, 0.01, 0.02, 0.03 and 0.05) micro-particles were synthesized by means of a facile, reproducible, and cheap method, i.e., the solid-state method in the air. The stoichiometric amounts of Eu_2O_3, Sm_2O_3, H_3BO_3 and $SrCO_3$ were weighted out and ground together in an agate mortar. Please note, that for SrB_4O_7: Sm^{2+}, Eu^{2+} micro-particles, the excess amount of H_3BO_3 is only 3 mol%, which leads to smaller crystallines. Then the subsequent sintering process in the oven is the same as for $Sr_{0.99}Eu_{0.01}B_4O_7$.

4.1.3. SrB_4O_7: Tm^{2+} micro-particles

$SrCO_3$ (99.9%, Sigma-Aldrich), H_3BO_3 (pure p.a., Chempur Poland), and Tm_2O_3 (99.99%, Stanford Materials) were used as the starting materials. A high-temperature solid-state method in the air was exploited to synthesize the $Sr_{1-x}B_4O_7$: xTm^{2+} (x=0.001, 0.002, 0.005 and 0.01) materials. The stoichiometric amounts of $SrCO_3$, H_3BO_3, and Tm_2O_3 were ground for 20 min in an agate mortar. The mixture then undergoes the same sintering process mentioned above. Such materials were ground before measurements were executed.

4.1.4. $BaTiO_3$: Ho^{3+}, Yb^{3+} and $BaTiO_3$: Er^{3+}, Yb^{3+} perovskite phosphors

Stoichiometric amounts of $CH_3COO)_2Ba$ (>99.9%), $Er(NO_3)_3$ (99.9%), $Ho(NO_3)_3$ (99.9%), $Yb(NO_3)_3$ (99.9%), and $Ti(OC_4H_9)_4$ (97%), were selected and used as starting materials for both the synthesis of $BaTi_{0.95-x}O_3$: *x* Er^{3+}, 0.05 Yb^{3+} (*x* is the molar concentration of Er^{3+}, *i.e.*, 1%, 5% and 9%), and $BaTi_{0.95-x}O_3$: 1% Ho^{3+}, x Yb^{3+} (*x* is the molar concentration of Yb^{3+}, *i.e.*, 1%, 5% and 10%). The appropriate amount of $Ba(CH_3COO)_2$ was dissolved in 20 mL acetic acid (denoted as solution A). Subsequently, 2 mL of $Ti(OC_4H_9)_4$ was diluted with 8 mL of acetylacetone (denoted as solution B). Solution A was then added dropwise to solution B. This mixture was heated to 23 K on a hot plate for 2 h with continuous magnetic stirring, to form a solution containing titanium and barium cations (denoted as solution C). Afterwards, 5 mL of an aqueous solution of $Er(NO_3)_3$ and $Yb(NO_3)_3$ were added to solution C and heated to 373 K on a hot plate for 24 h, to evaporate water and obtain a powder. Finally, the product obtained was ground in an agate mortar, placed in an alumina crucible and annealed for 2 h at 1273 K in a muffle furnace, in air atmosphere, to obtain the final product.

4.2. Physicochemical characterization of the investigated microparticles

4.2.1. X-ray powder diffraction

The powder X-ray diffraction (XRD) patterns were recorded to identify the phase structure and phase purity of the materials obtained, using a Bruker D8 Advance diffractometer, which is equipped with a graphite monochromator operated at 40 kV and 30 mA, using CuKα radiation (λ = 1.54057 Å), in the 2θ range of 10 - 60°.

4.2.2. Scanning electron microscopy (SEM) and energy-dispersive X-ray (EDX)

SEM and EDX spectra and mapping were recorded with the use of a FEI Quanta 250 FEG scanning electron microscope with an EDAX detector.

4.2.3. Raman spectroscopy

To record the Raman spectra at room temperature, we applied a Renishaw research Ramanscope 1000 spectrometer equipped with a Peltier-cooled CCD detector and with Leica microscopes (λ_{ex}=785 nm). Raman spectra at various temperature were recorded using a Horiba Jobin Yvon LabRam HR800 spectrometer with a liquid nitrogen cooled CCD detector (He-Ne 632.82 nm laser, power of 1.77 mW). The signal was recorded in the backscattering geometry and the laser beam was focused using a x20 long working distance objective. The Si line at 520.7 cm^{-1} was used to calibrate the Raman Shift. A Linkam THMS 600 temperature-controlled system was applied to modulate and monitor temperature for Raman spectra measurements.

4.2.4. Luminescence spectroscopy

A typical Hitachi F7000 spectrofluorometer was applied for the room-temperature luminescence characterization (excitation and emission spectra, luminescence lifetime in microsecond scale) of the materials synthesized. All spectra in the measurements were corrected for the response of the instrument. A Photon Technology Int. Quanta Master TM 40 spectrophotometer equipped with an Opotek Inc. Opolette 355LD UVDM tuneable laser with a repetition rate of 20 Hz as the excitation source and a Hamamatsu R928 photomultiplier as a detector were used for the measurement of luminescence decay curves of the targeted sample.

4.2.5. High pressure experiment

DAC loading procedure. For high-pressure measurements, we applied a typical Merrill-Bassett diamond anvil cell (DAC), equipped with high-purity IIas diamond anvils (for Raman and

fluorescence spectroscopy), purchased from Almax easyLab. The pressure values inside the DAC chamber are regulated by three metal screws on the outside of the DAC. Stainless-steel sheets (thickness: 250 μm) with an aperture of ~150 μm (hole size) were applied as gaskets, used for high-pressure experiments in the DAC. Before loading the sample, the gaskets were pre-indented down to ~80 μm (sample thickness). Using a stereo microscope, a ruby ball (< 10 μm diameter, usually single), a very small amount of sample powder was loaded into the DAC chamber, after which the PTM (usually a solvent system of methanol/ethanol/water with a volume ratio 16:3:1 was preferred) was fulfilled in the DAC chamber for maintaining hydrostatic and quasi-hydrostatic conditions in the HP experiment (compression and decompression process).

HP Raman scattering characterization. Using a grating with 1800 grooves/mm and a power-controlled 785 nm laser diode, Raman spectra were recorded in backscattering geometry with a Renishaw InVia confocal micro-Raman system. The laser beam was well focused using an Olympus x20 SLMPlan N long working distance objective.

HP PL characterization. The scheme of the experimental setup of high-pressure spectroscopy is shown in **Figure 8a**.The PL characterization under high pressure conditions was performed by measuring the emission spectra (with a resolution of ≈0.1 nm) of the samples placed in the DAC chamber, using I) an Andor Shamrock 500i spectrometer, equipped with a detector of iDus 420 CCD camera; II) a Hitachi F7000 spectrofluorometer assembled with DAC holder and other HP setup; III) QuantaMasterTM 40 spectrophotometer (Photon Technology International) with R928 (200 - 900 nm), R5108 (400 - 1200 nm) and H10330C-75 (950 - 1700 nm) photomultipliers as detectors (from Hamamatsu) and PIXIS:256E Digital CCD Camera equipped with SP-2156 Imaging Spectrograph (Princeton Instruments). These devices were used to measure the excitation and emission spectra, as well as luminescence rise and decay curves in order to determine the corresponding emission lifetimes, band intensity ratio, energy alterations of the radiative transitions and luminescence intensity as variations in a function of increasing pressure. The UV, Vis, NIR continuous wavelength and tuneable pulsed lasers and diodes at different visible wavelength were applied, which was focused on the sample in the gasket hole of the DAC. The PL signal was collected in an optimized configuration with 180° detection geometry (back illuminated configuration). Pressure calibration of the system in the DAC chamber was based on a monitored shift of the ruby R_1 fluorescence line, using the standard ruby calibration curve from

http://kantor.50webs.com/ruby.htm. Steady state and time-resolved luminescence spectroscopy with high spectral resolution was used to analyse the spectroscopic properties of the synthesized materials under high-pressure conditions (up to ~30 GPa).

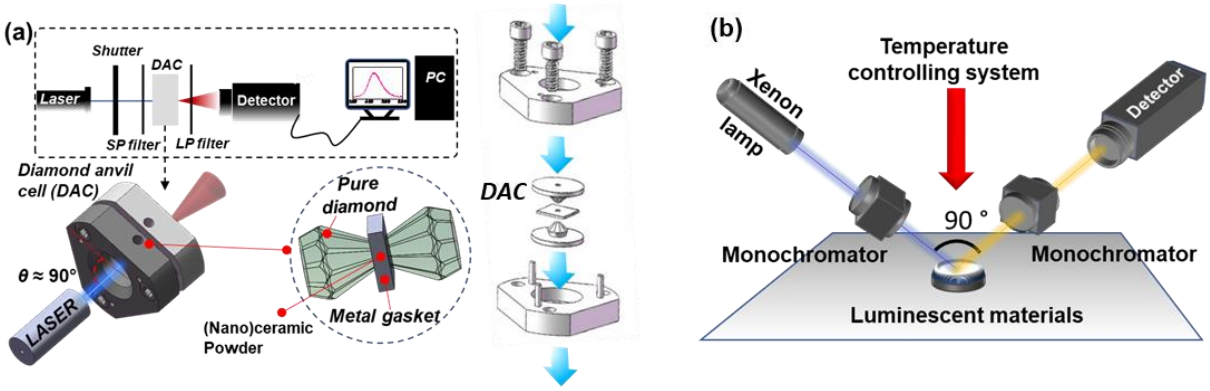

Figure 8. The scheme of experimental setup for (a) the HP PL measurements with a DAC presentation (Merrill-Bassett type) and (b) high temperature PL measurements for luminescent materials.

4.2.6. Thermal-dependent PL spectroscopy

High-temperature PL characterization. The scheme of the experimental setup of high-temperature spectroscopy is shown in **Figure 8b**. An Andor Shamrock 500i spectrometer with an iDus CCD camera as a detector was used to record UC emission spectra. The excitation source applied was a continuous wave 975 nm, fiber-coupled, solid-state diode pumped (SSDP) laser FC-975-2W (CNI), with an estimated spot size of $\approx$ 0.5 mm. For the spectroscopic measurements under changing temperature, a tube furnace with an integrated thermocouple was used, with an additional K-type thermocouple placed in the centre of the working tube, close to the sample (temperature accuracy $\pm$ 0.1 K). Recorded emission/excitation spectra were corrected for the apparatus response. Using high-spectral resolution, steady-state and time-resolved luminescence spectroscopy, the excitation/emission spectra and luminescence decay profiles were measured, to establish correlation of the measured spectroscopic parameters with temperature. The luminescence thermal quenching effect and the complex relationship between thermal-sensitive radiative or non-radiative transitions attributed to TCLs (according to Boltzmann distribution) and

non-TCLs (non-Boltzmann type) in $Ln^{2+/3+}$ ions in the obtained materials were analysed, in order to understand the effects/mechanisms responsible for the observed spectroscopic effects.

Low-temperature PL characterization. Characterization of the low-temperature PL was performed using an FLS1000 Fluorescence spectrometer (Edinburgh Instruments Ltd) with a 450-W xenon arc lamp (excitation light source) and a Hamamatsu R928P high-gain photomultiplier (cooled -20 °C). Emission spectra were collected in the temperature range 11 – 300 K, with a 10 K step. The decay curves were recorded using an EPLED285 (285 nm) picosecond pulsed light-emitting diode and the same FLS1000 spectrometer. Using Silver Adhesive 503 (Electron Microscopy Sciences), a sample for low-temperature spectroscopic measurements was mounted on the Cu-holder of a closed-cycle helium cryostat (Lake Shore Cryotronics, Inc.).

5. Physicochemical characterization of Ln^{2+} doped SrB_4O_7 materials

5.1. Influence of matrix on the luminescence properties of Eu^{2+}/Eu^{3+} doped strontium borates: SrB_4O_7, SrB_2O_4 and $Sr_3(BO_3)_2$, exhibiting multicolor tunable emission

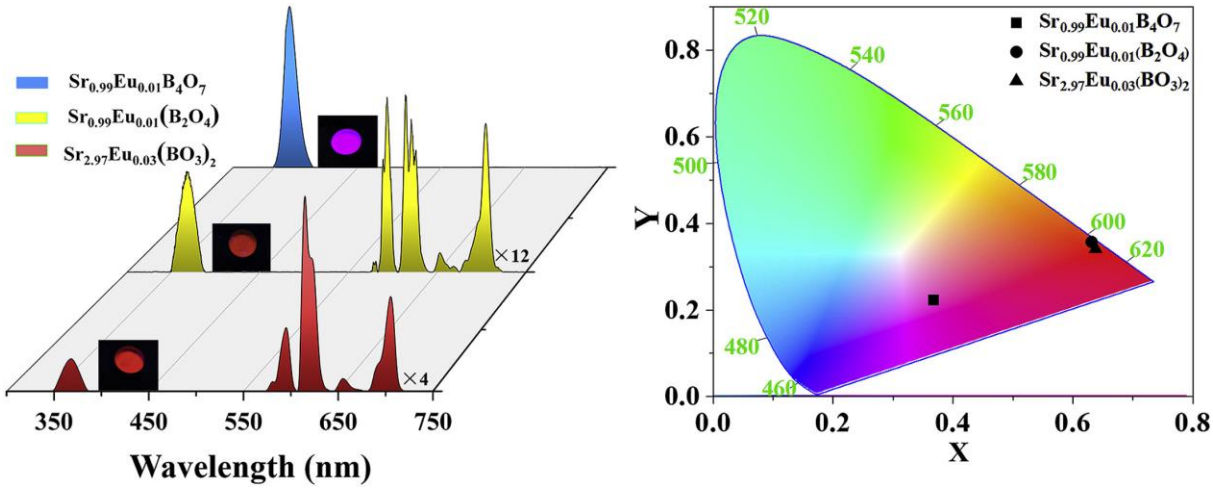

The result in this section were published in: Teng Zheng, Marcin Runowski, Przemysław Woźny, Stefan Lis, Influence of matrix on the luminescence properties of Eu^{2+}/Eu^{3+} doped strontium borates: SrB_4O_7, SrB_2O_4 and $Sr_3(BO_3)_2$, exhibiting multicolor tunable emission, Journal of Alloys and Compounds, 2020, 822, 153511-153519 (9).

Abstract of the section: At the very beginning of his doctoral thesis, the Ph. D. candidate synthesized three complex strontium borate matrices, i.e., $Sr_3(BO_3)_2$, SrB_2O_4 and SrB_4O_7 doped with $Eu^{2+/3+}$ ions, via the high-temperature solid state reaction method in the air. The morphology was characterized by X-ray and SEM analyses, confirming that all these samples are pure phase micro-sized materials. The excitation and emission spectra, including the PL decay curves and the determined lifetimes of the synthesized compounds were systematically investigated. Furthermore, the impact of strontium borate matrices on the PL properties of the $Eu^{2+/3+}$ ions was analysed. The intensity ratio of $Eu^{2+/3+}$ emission varies significantly for different matrices.

Contribution of Ph.D. student in this work: Conceptualization, material synthesis, structural and morphological characterization, conduction of the spectroscopic measurements, visualization, data analysis and curation, formal analysis, writing original draft and writing review & editing.

Journal of Alloys and Compounds 822 (2020) 153511

Contents lists available at ScienceDirect

Journal of Alloys and Compounds

journal homepage: http://www.elsevier.com/locate/jalcom

Influence of matrix on the luminescence properties of Eu^{2+}/Eu^{3+} doped strontium borates: SrB_4O_7, SrB_2O_4 and $Sr_3(BO_3)_2$, exhibiting multicolor tunable emission

Teng Zheng, Marcin Runowski, Przemysław Woźny, Stefan Lis*

Adam Mickiewicz University, Faculty of Chemistry, Uniwersytetu Poznańskiego 8, 61-614, Poznań, Poland

ARTICLE INFO

Article history:
Received 21 July 2019
Received in revised form
12 November 2019
Accepted 22 December 2019
Available online 28 December 2019

Keywords:
Luminescence color tuning
Complex borate host matrices
Eu^{2+} & Eu^{3+} emission
0-0 transition
Energy transfer & charge transfer

ABSTRACT

Three complex strontium borate matrices, i.e. $Sr_3(BO_3)_2$, SrB_2O_4 and SrB_4O_7 doped with Eu^{2+}/Eu^{3+} ions, were prepared by the solid state reaction method in the air. X-ray and SEM analyses confirmed that all these samples are pure phase micro-sized materials. The luminescence properties of the Eu^{2+} and Eu^{3+} doped compounds were investigated in detail, i.e. excitation and emission spectra, including luminescence decay curves and determined lifetimes. Furthermore, the effects of the strontium borate matrices on the luminescence properties of the Eu^{2+}/Eu^{3+} ions were discussed. The intensity ratio of Eu^{2+}/Eu^{3+} emission varies significantly in different matrices. The products obtained exhibited tunable multicolor luminescence from violet-blue to orange-red, depending on the excitation wavelength applied and the host matrix used.

1. Introduction

In recent years, the versatility of materials doped with trivalent (e.g. Eu^{3+}, Tb^{3+}, Sm^{3+}, Er^{3+}, Tm^{3+}) and some divalent (e.g. Eu^{2+}, Sm^{2+}) rare-earth (RE) ions have attracted the attention of researchers due to their efficient, tunable multicolor luminescence in the UV–vis–NIR range, large emission shift in relation to absorption, absence of auto-fluorescence, long luminescence lifetimes and sharp emission bands [1–4]. Such excellent luminescence properties are due to the forbidden *4f-4f* transitions in trivalent and some divalent RE ions, and the shielding of 4f electrons by 5s and 5p ones [5–7]. Materials doped with $RE^{2+/3+}$ ions can be successfully used as phosphors, optical storage devices, solid state lasers, light-emitting diodes, optical sensors [3,8–14].

In order to stabilize the RE^{2+} ($RE^{2+} = Eu^{2+}$, Sm^{2+}, Tm^{2+}, Yb^{2+}), many inorganic matrices, e.g. fluorides, borates, silicates, vanadates, sulphides, phosphates and so on, were extensively studied [15–23]. In particular, interest in inorganic borates compounds, e.g. CaB_4O_7, BaB_4O_7, CdB_4O_7, PbB_4O_7, and other more complexes ones, is increasing due to their strong covalent bonds and large band gaps [24–26]]. However, among all these borates, the strontium borate matrices are considered as the most promising candidates for stabilization of the RE^{2+} [27–30]. According to the Vegards rule [31], the difference in ionic radii between the dopant ($R^{2+}_{Eu} = 1.39$ Å, $R^{2+}_{Sm} = 1.41$ Å) and the host ions ($R^{2+}_{Sr} = 1.40$ Å) is significantly lower than 15%, and thus Sr^{2+} ions can be successfully substituted by the Eu^{2+} and Sm^{2+} ions in these crystalline structures. Namely, the RE^{3+} ions can be reduced to RE^{2+} by electrons from vacancies created by substitution of three Sr^{2+} ions with two RE^{3+} ions. This phenomenon occurred only in the case of strontium borate matrices [32]. Furthermore, strontium borates are very commonly used luminescent host materials due to their non-linear optical properties, transparency in the UV region, and because their high chemical and physical stability, extending their potential applications [33,34].

On the other hand, among these RE ions, the $Eu^{2+/3+}$ ions are one of the most important activators because of their special electronic shell configuration, i.e.[Xe] $4f^7$ for Eu^{2+} and [Xe] $4f^6$ for Eu^{3+} [35,36]. Eu^{3+} ions have a relatively lower reduction potential, i.e. −0.36 V vs. NHE (normal hydrogen electrode) [37], than those of other RE^{3+} ions that adopt a stable trivalent state, and exhibit two redox active states with characteristic emissions: divalent (Eu^{2+}) and trivalent (Eu^{3+}) [38]. Eu^{2+} ions in solid state compounds can generate green, blue or red emission ascribed to the transition of $4f^65d^1 \rightarrow 4f^7$, while the Eu^{3+} ions show a series of narrow red

* Corresponding author.
E-mail address: blis@amu.edu.pl (S. Lis).

https://doi.org/10.1016/j.jallcom.2019.153511
0925-8388/

emission bands corresponding to $^5D_0 \rightarrow {}^7F_J$ (J = 0–4) transitions [39,40]. In addition, the allowed processes like charge transfer (CT: $O^{2-} \rightarrow Eu^{3+}$) observed in the oxygen-based host materials can increase absorption of the excitation light and therefore enhance luminescence intensity of the system [41].

In this article, we present the synthesis protocols of three pure strontium borates, i.e. SrB_4O_7, SrB_2O_4 and $Sr_3(BO_3)_2$ doped with Eu^{2+}/Eu^{3+} ions, prepared by the solid-state method. Our aim was to explore and study the photophysical properties of phosphors exhibiting color-tunable luminescence depending on the excitation wavelength and the host matrix used. Such materials exhibit a bright, multicolor luminescence from violet-blue to orange-red as a consequence of a different Eu^{2+}/Eu^{3+} emission intensity ratio. The materials synthesized can be applied as advanced phosphors, luminescence tracers, biomarkers, optical sensors, etc.

2. Methods

2.1. Materials synthesis

$Sr_{2.97}Eu_{0.03}(BO_3)_2$, $Sr_{0.99}Eu_{0.01}B_2O_4$ and $Sr_{0.99}Eu_{0.01}B_4O_7$ were synthesized by solid-state reactions. Compounds of high purity $SrCO_3$ (Sigma-Aldrich, 99.9%), H_3BO_3 (Chempur, pure p.a.) and Eu_2O_3 (Alfa Aesar, 99.99%) were used as starting materials. On the basis of the chemical formula, the stoichiometric amounts of Eu_2O_3, H_3BO_3 and $SrCO_3$ were weighted and ground together in an agate mortar, respectively. However, in the case of $Sr_{0.99}Eu_{0.01}B_4O_7$ compound, we had to use 50 mol% excess of H_3BO_3 to get the pure phase structure. Afterwards, the mixtures were transferred to porcelain crucibles covered with a lid, placed in an oven and precalcined at 700 °C for 5 h and subsequently further heat-treated at 850 °C for 5 h. Then they were ground again in a mortar for 15 min, and then heat-treated at 850 °C for another 5 h. Covering the crucibles with a lid is crucial to limit the amount of oxygen from the air in the system.

2.2. Characterization

X-ray diffraction patterns (XRD) were recorded using a Bruker AXS D8 Advance diffractometer in Bragg-Brentano geometry, with Cu Kα1 radiation (λ = 1.5406 Å) in the 2θ range from 6° to 60°, with 0.05° step scan mode. The reference data were taken from ICDD (International Centre for Diffraction Data). Scanning electron microscopy (SEM) and energy-dispersive X-ray analysis (EDX) were obtained with a scanning electron microscope FEI Quanta 250 FEG, using an EDAX detector. The luminescence characteristics (excitation and emission spectra) of the prepared materials was investigated using a Hitachi F7000 spectrofluorometer. All the measurements were performed at room temperature and corrected for the apparatus response. The luminescence decay curves of the synthesized samples were measured on a Photon Technology Int. Quanta Master TM 40 spectrophotometer equipped with an Opotek Inc. Opolette 355LD UVDM tunable laser with a repetition rate of 20 Hz as an excitation source and a Hamamatsu R928 photomultiplier as a detector.

3. Results and discussion

3.1. Structure and morphology

The XRD patterns of the prepared samples were recorded and compared to the ICDD standards database. It is well seen in Fig. 1, the XRD pattern of $Sr_{2.97}Eu_{0.03}(BO_3)_2$ sample fits well with the reference pattern (089–1606) of rhombohedral $Eu_3(BO_3)_2$. The use of $Eu_3(BO_3)_2$ as reference is due to the absence of the XRD

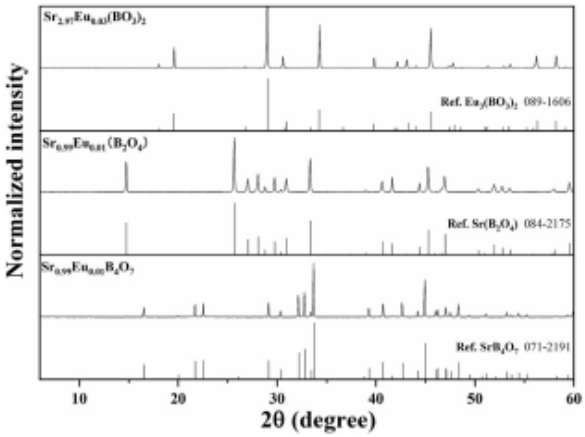

Fig. 1. XRD characterization of the $Sr_{2.97}Eu_{0.03}(BO_3)_2$, $Sr_{0.99}Eu_{0.01}B_2O_4$ and $Sr_{0.99}Eu_{0.01}B_4O_7$ phosphors. The line patterns correspond to the references from the ICDD standards database.

pattern of $Sr_3(BO_3)_2$ in the database and similar ionic radii of $Eu^{2+/3+}$ and Sr^{2+} ions. The experimental XRD pattern of the $Sr_{0.99}Eu_{0.01}B_2O_4$ can be well indexed to the orthorhombic SrB_2O_4 structure (084–2175). Meanwhile, the XRD pattern of $Sr_{0.99}Eu_{0.01}B_4O_7$ sample can be well fitted with the orthorhombic SrB_4O_7 phase (071–2191). The detail of lattice information of the prepared samples are listed in Table 1. Clearly, due to the similar ionic radii, $Eu^{2+/3+}$ dopant ions have no obvious influence on the structure of these three strontium borate hosts. Since there are no additional reflexes observed in all XRD patterns, indicating the high phase purity of all phosphors synthesized. The morphology and structure of the synthesized products were checked by SEM at various scales, as shown in Fig. 2. As disclosed, the materials obtained are composed of irregular micro-particles with the particle sizes ranging from approximately ~20–60 μm ($Sr_{0.99}Eu_{0.01}B_4O_7$), ~1–3 μm ($Sr_{2.97}Eu_{0.03}(BO_3)_2$) and ~0.5–1 μm ($Sr_{0.99}Eu_{0.01}B_2O_4$). Grains of the compounds are aggregated, nearly-spherical and inhomogeneous particles. For comparison, a much larger particle size in $Sr_{0.99}Eu_{0.01}B_4O_7$ may be attributed to the excess of H_3BO_3 that was added during the synthesis of the $Sr_{0.99}Eu_{0.01}B_4O_7$ phosphor to obtain a pure phase structure. In addition, as shown in Fig. S1, S2 and S3 of supporting information (SI), EDX spectra show peaks corresponding to Sr, B, O and Eu in each sample, further proving the formation of $Sr_{0.99}Eu_{0.01}B_4O_7$, $Sr_{0.99}Eu_{0.01}B_2O_4$ and $Sr_{2.97}Eu_{0.03}(BO_3)_2$ compounds. Moreover, elemental mapping of Sr, B, O and Eu illustrates that the chemical elements presented were equally distributed in all microparticles (Fig. S1, S2 and S3). Inductively coupled plasma mass spectrometry (ICP-MS) is performed and the result shows the atomic ratio of Eu/Sr in three samples is 1.4 mol%, 1.0 mol% and 0.8 mol%, respectively. These are close to theoretical value of 1 mol%, which further specifies that the doping concentrations in three samples are as expected.

The crystal structures of SrB_4O_7, SrB_2O_4 and $Sr_3(BO_3)_2$ are presented in Fig. 3. The insets in Fig. 3 show the corresponding cationic coordination environment. It can be seen that the coordination numbers of Sr^{2+} ion in SrB_4O_7, SrB_2O_4 and $Sr_3(BO_3)_2$ matrices are 7, 7 and 6, respectively. Such a difference in crystal structures leads to diverse stability of Eu^{2+} in the SrB_4O_7, SrB_2O_4 and $Sr_3(BO_3)_2$ structures [42,43].

Table 1
Structural information for $Sr_{2.97}Eu_{0.03}(BO_3)_2$, $Sr_{0.99}Eu_{0.01}B_2O_4$ and $Sr_{0.99}Eu_{0.01}B_4O_7$ phosphors.

Sample composition	Crystal system	Space group	Local point symmetry	Lattice parameters	Sr^{2+} site number
$Sr_{2.97}Eu_{0.03}(BO_3)_2$	rhombohedral	R3c	D_{3d}	a = 9.069 Å, c = 12.542 Å, V = 893.340 Å^3.	1
$Sr_{0.99}Eu_{0.01}B_2O_4$	orthorhombic	Pbcn	D_{2h}	a = 12.014 Å, b = 4.339 Å, c = 6.586 Å, V = 343.330 Å^3	1
$Sr_{0.99}Eu_{0.01}B_4O_7$	orthorhombic	$Pmn2_1$	C_{2v}	a = 4.426 Å, b = 10.707 Å, c = 4.234 Å, V = 200.810 Å^3	1

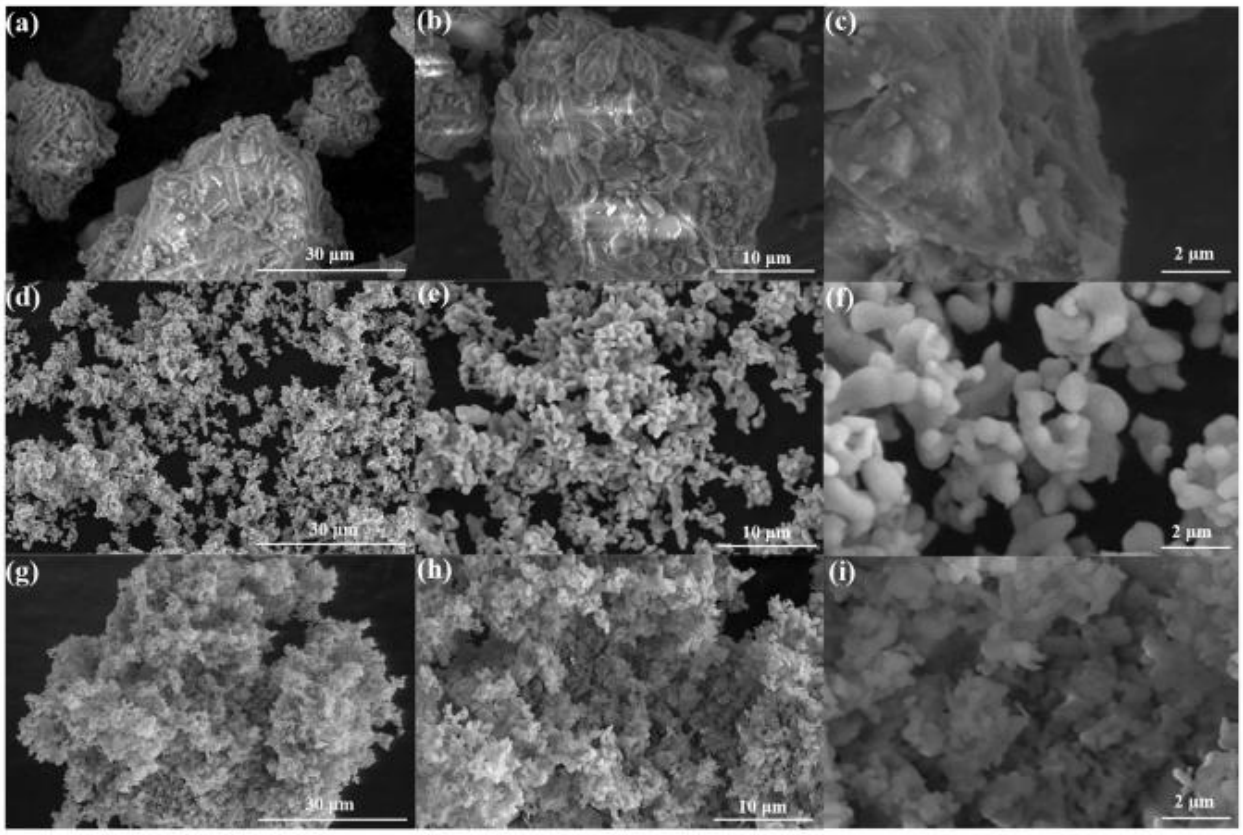

Fig. 2. SEM images of (a, b, c) $Sr_{0.99}Eu_{0.01}B_4O_7$, (d, e, f) $Sr_{2.97}Eu_{0.03}(BO_3)_2$ and (g, h, i) $Sr_{0.99}Eu_{0.01}B_2O_4$ phosphors.

3.2. Luminescence properties

In order to study the $Eu^{2+/3+}$ emission behavior in the synthesized phosphors, excitation spectra were recorded, and the corresponding results are demonstrated in Fig. 4. Excitation spectra of the synthesized phosphors at λ_{em} = 367 nm (position corresponding to the Eu^{2+}: $4f^65d^1 \rightarrow 4f^7$ transition in the emission spectra) are shown in Fig. 4(a). In the case of $Sr_{0.99}Eu_{0.01}B_4O_7$, two overlapped broad peaks with maxima around 251 nm 298 nm are observed, which correspond to splitting of 5d orbital in t_{2g} and e_g components, respectively [28,44]. This effect is the most pronounced in the $Sr_{0.99}Eu_{0.01}B_4O_7$ material because of the highest content of Eu^{2+}.

Fig. 4 (b) shows excitation spectra at λ_{em} = 615 nm (the position of the most intense Eu^{3+}: $^5D_0 \rightarrow {}^7F_2$ transition in the emission spectrum) in the range of 200–450 nm. It is indicated that the dopant emission can be efficiently excited in the $O^{2-} \rightarrow Eu^{3+}$ charge transfer (CT) band, with maxima at 220, 237 and 260 nm for the $Sr_{0.99}Eu_{0.01}B_4O_7$, $Sr_{0.99}Eu_{0.01}B_2O_4$ and $Sr_{2.97}Eu_{0.03}(BO_3)_2$ luminophores, respectively. The energy of the CT: $O^{2-} \rightarrow Eu^{3+}$ transition can be estimated using the following equation given by Jørgensen [45]:

$$E_{CT} = [\chi(l) - \chi(m)](3 \times 10^4) \quad (1)$$

where E_{CT} denotes the position of the CT band (in cm^{-1}), $\chi(l)$ and $\chi(m)$ are the optical electronegativities of the anion and the central metal cation, respectively. However, for $\chi(O) = 3.2$ and $\chi(Eu) = 1.75$ [46], the calculated CT position should be around 43 500 cm^{-1} ($\approx$230 nm), which is close to the measured positions of the CT bands in the excitation spectra of $Sr_{0.99}Eu_{0.01}B_4O_7$ and $Sr_{0.99}Eu_{0.01}B_2O_4$ compounds. The difference between the theoretical and experimental values results from the fact that the CT energy position depends on several factors, i.e. the crystal field symmetry, the strength of ions surrounding (O^{2-}), the strength of anion bonding, the size of the cation site, and the coordination number [47]. Therefore, in this case the shift in the CT band might be attributed to different effects of the crystal field and differences in the symmetry of the local environment around Eu^{3+} embedded in various borate structures. Transition bands in the spectral range of 280–300 nm are connected with energy transfer (ET) between

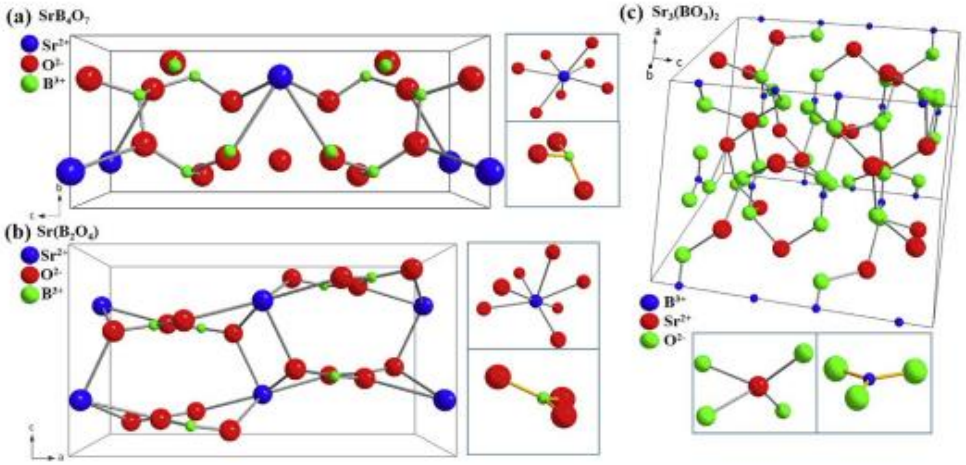

Fig. 3. Graphical representation of the crystal structure of orthorhombic (a) SrB_4O_7 ($Pmn2_1$ space group), (b) SrB_2O_4 (Pbcn space group) and (c) $Sr_3(BO_3)_2$ (R3c space group) matrices. The insets show the corresponding schematic diagram of the cationic (Sr^{2+} or B^{3+}) coordination environment.

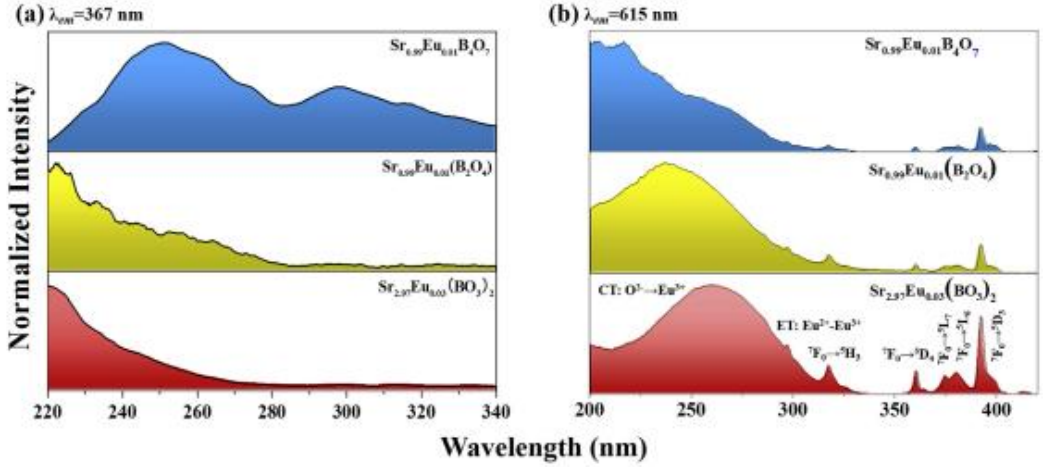

Fig. 4. (a) Excitation spectra of the synthesized phosphors at (a) λ_{em} = 367 nm and (b) λ_{em} = 615 nm.

Eu^{2+}-Eu^{3+}. In the range of 300–450 nm, the sharp excitation peaks are assigned to the $^7F_0 \rightarrow {}^5H_3$, $^7F_0 \rightarrow {}^5D_4$, $^7F_0 \rightarrow {}^5L_7$, $^7F_0 \rightarrow {}^5L_6$ and $^7F_0 \rightarrow {}^5D_3$ intra-configurational *4f-4f* transitions of Eu^{3+}, respectively. These sharp excitation bands are the consequence of the shielding properties of the 4f electrons by the 5s and 5p ones present in Eu^{3+} ions. Because of these effects, the *4f-4f* transitions are relatively insensitive to the changes of host matrices [48].

For the purpose of investigating the photoluminescence properties of the synthesized samples, the emission spectra of $Sr_{0.99}Eu_{0.01}B_4O_7$, $Sr_{0.99}Eu_{0.01}B_2O_4$ and $Sr_{2.97}Eu_{0.03}(BO_3)_2$ phosphors depending on the excitation wavelength are shown in Fig. 5(a–c). In Fig. 5(a), it is indicated that the violet/blue emission (Eu^{2+}: $4f^65d \rightarrow 4f^7$ transition) centered at 367 nm dominates in the emission spectrum of $Sr_{0.99}Eu_{0.01}B_4O_7$. . From the inset in Fig. 5(a), it can be noticed that the emission intensity of Eu^{2+} enhances as the excitation wavelength increases from 240 to 300 nm. Meanwhile, compared to Eu^{2+}, the Eu^{3+} emission intensity is extremely low, close to the level of noise (see the inset of Fig. 5(a)). This result is a good proof of the efficient reduction process of Eu^{3+} to Eu^{2+} in this material. As presented in Fig. 5(b), the $Sr_{0.99}Eu_{0.01}B_2O_4$ phosphor shows not only the characteristic *4f-4f* transitions of Eu^{3+} ions, but also the 5d-4f emission of Eu^{2+} ions of comparable intensity. The violet emission centered at 367 nm is associated with the $4f^65d \rightarrow 4f^7$ transitions of Eu^{2+} ion, and the red emission bands centered at 578, 593, 615, 654 and 705 nm are attributed to the $^5D_0 \rightarrow {}^7F_J$ (J = 0,1,2,3,4) transitions of Eu^{3+} ions, respectively. From the inset in Fig. 5(b), it can be seen that the integrated intensity of Eu^{3+} red emission increases with increasing excitation wavelength, and achieves its optimal value at λ_{ex} = 280 nm. Then it shows a decline tendency with further increase of the excitation wavelength, while the intensity of the violet/blue emission of Eu^{2+} is constantly increasing.

As shown in Fig. 5(c), the red emission predominates in the emission spectrum of $Sr_{2.97}Eu_{0.03}(BO_3)_2$, and the $Eu^{2+/3+}$ emission intensities change in a similar way. In this compound, the emission intensity of Eu^{2+} is several times smaller compared to the $Sr_{0.99}Eu_{0.01}B_2O_4$ luminophore. In addition, the Eu^{2+}/Eu^{3+} integrated intensity ratio at λ_{ex} = 300 nm is 22777, 0.307 and 0.033 for $Sr_{0.99}Eu_{0.01}B_4O_7$, $Sr_{0.99}Eu_{0.01}B_2O_4$ and $Sr_{2.97}Eu_{0.03}(BO_3)_2$ phosphors, respectively, which further confirms they have decreasing

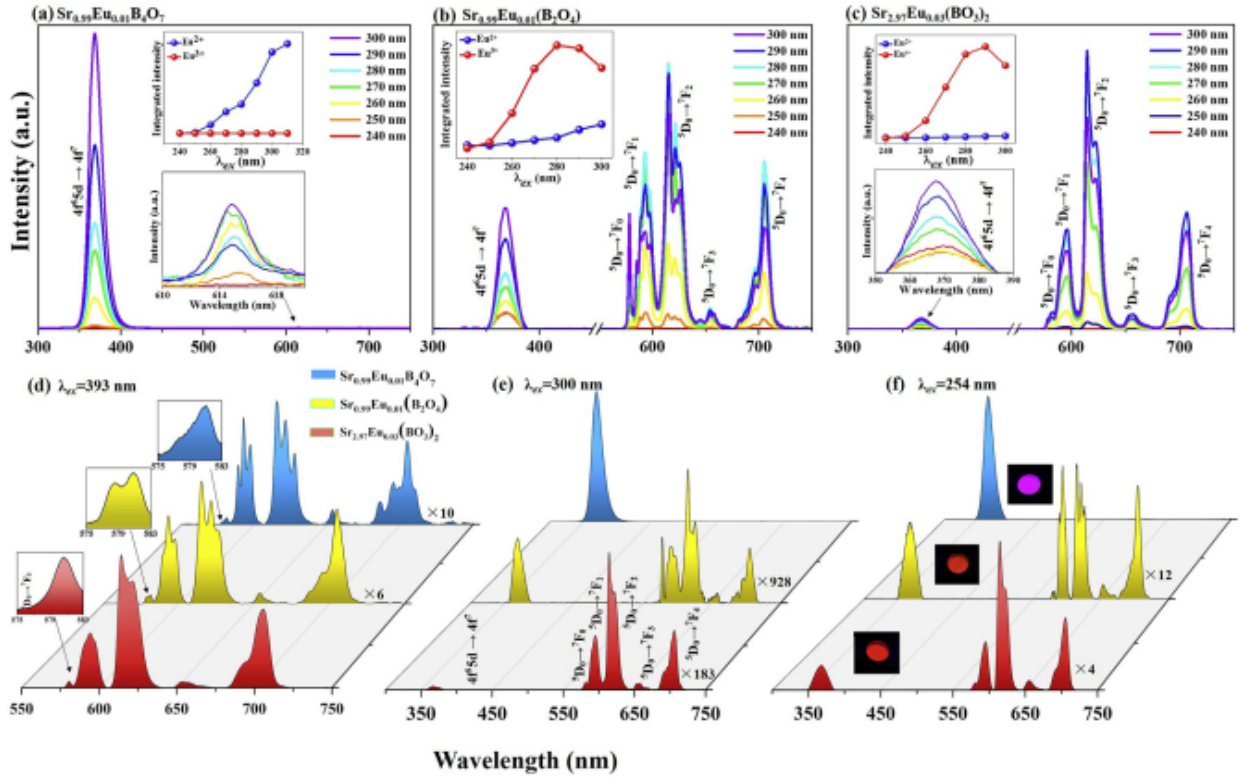

Fig. 5. Emission spectra of the (a) $Sr_{0.99}Eu_{0.01}B_4O_7$, (b) $Sr_{0.99}Eu_{0.01}(B_2O_4)$, (c) $Sr_{2.97}Eu_{0.03}(BO_3)_2$ phosphors at different excitation wavelengths. The insets illustrate the corresponding integrated emission intensity of Eu^{2+} and Eu^{3+} as a function of excitation wavelength and magnified emission spectra in certain range. The emission spectra of the obtained samples at (d) λ_{ex} = 393 nm, (e) 300 nm and (f) 254 nm are illustrated in Fig. 5(d–f). The insets in Fig. 5 (d) show magnified $^5D_0$-$^7F_0$ peaks, while the insets in Fig. 5 (f) show the corresponding photographs of luminescence colors under UV light irradiation (λ_{ex} = 254 nm). (For interpretation of the references to color in this figure legend, the reader is referred to the Web version of this article.)

effectiveness of reduction of Eu^{3+} to Eu^{2+}. All calculated values of Eu^{2+}/Eu^{3+} integrated intensity ratio for different excitation wavelength are presented in Table S1 of SI. Please note that due to the low energy of the excitation light source (xenon lamp) below ≈260 nm, the wavelength dependent emission spectra of $Sr_{0.99}Eu_{0.01}B_2O_4$ and $Sr_{2.97}Eu_{0.03}(BO_3)_2$ recorded at longer wavelengths (≈270–300 nm) are more intense, despite the fact of excitation at the edge of the CT band (see Fig. 4(b)). Apparently, at certain excitation wavelengths, the presented phosphors can generate in a controllable way the simultaneous luminescence of both Eu^{3+} and Eu^{2+} ions or exclusively the emission of the Eu^{3+} or Eu^{2+} ions, which can lead to color-tunable luminescence [49–51]. On the other hand, the emission intensities of different matrices change under different excitation wavelengths, which will be discussed in detail in the next paragraph.

For the sake of getting a detailed insight into the influence of matrix on emission behaviors of the synthesized samples, the emission spectra at different excitation wavelengths, i.e. 393 nm (Eu^{3+}), 300 nm (Eu^{2+}) and 254 nm (CT band) are illustrated in Fig. 5(d–f). When the phosphors are excited with UV light at 393 nm, the emission intensity of $Sr_{2.97}Eu_{0.03}(BO_3)_2$ is ≈ 10-times stronger than that of $Sr_{0.99}Eu_{0.01}B_4O_7$ and ≈6-times stronger than $Sr_{0.99}Eu_{0.01}B_2O_4$. On the contrary, under 300 nm UV light excitation, the emission intensity of $Sr_{0.99}Eu_{0.01}B_4O_7$ is about two orders of magnitude higher than the others. This is due to the highest content of Eu^{2+} in the SrB_4O_7 matrix, whose emission originates from the allowed $4f^65d$-$4f^7$ transition [19]. Furthermore, when the phosphors are excited with UV light at 254 nm, the emission intensity of $Sr_{0.99}Eu_{0.01}B_4O_7$ is ≈ 4-times stronger than that of $Sr_{2.97}Eu_{0.03}(BO_3)_2$ and ≈12-times stronger than $Sr_{0.99}Eu_{0.01}B_2O_4$ sample (see the multiplication factors in Fig. 5(d–f)). The emission spectra of all samples at λ_{ex} = 393 nm (see Fig. 5(d)) consist of five narrow, split bands corresponding to the $^5D_0 \rightarrow ^7F_J$ (J = 0–4) transitions, which belong to the intra-configurational *4f-4f* transitions of Eu^{3+} ion. The most pronounced splitting of the Eu^{3+} bands observed in the $Sr_{0.99}Eu_{0.01}B_4O_7$ sample is probably related to the highest crystallinity of that sample (the largest particles). Whereas, the spectra of other matrices are broadened because their particles are more irregular and smaller [52].

It is well-known that the hypersensitive electric dipole $^5D_0 \rightarrow ^7F_2$ transition is very sensitive to the site symmetry alterations around Eu^{3+} ions, and becomes partially allowed when Eu^{3+} ions occupy sites of low symmetry (without an inversion center) [53]. On the contrary, the $^5D_0 \rightarrow ^7F_1$ band corresponds to the magnetic dipole transition, insensitive to the symmetry alterations. Therefore, the intensity (I) ratio between the integrated areas of the $^5D_0 \rightarrow ^7F_2$ and $^5D_0 \rightarrow ^7F_1$ bands is informative about the structural changes in the Eu^{3+}-doped host and symmetry of the surrounding local coordination environment. The intensity ratio R is defined by the following equation:

$$R = \frac{I_{(^5D_0 \rightarrow ^7F_2)}}{I_{(^5D_0 \rightarrow ^7F_1)}} \quad (2)$$

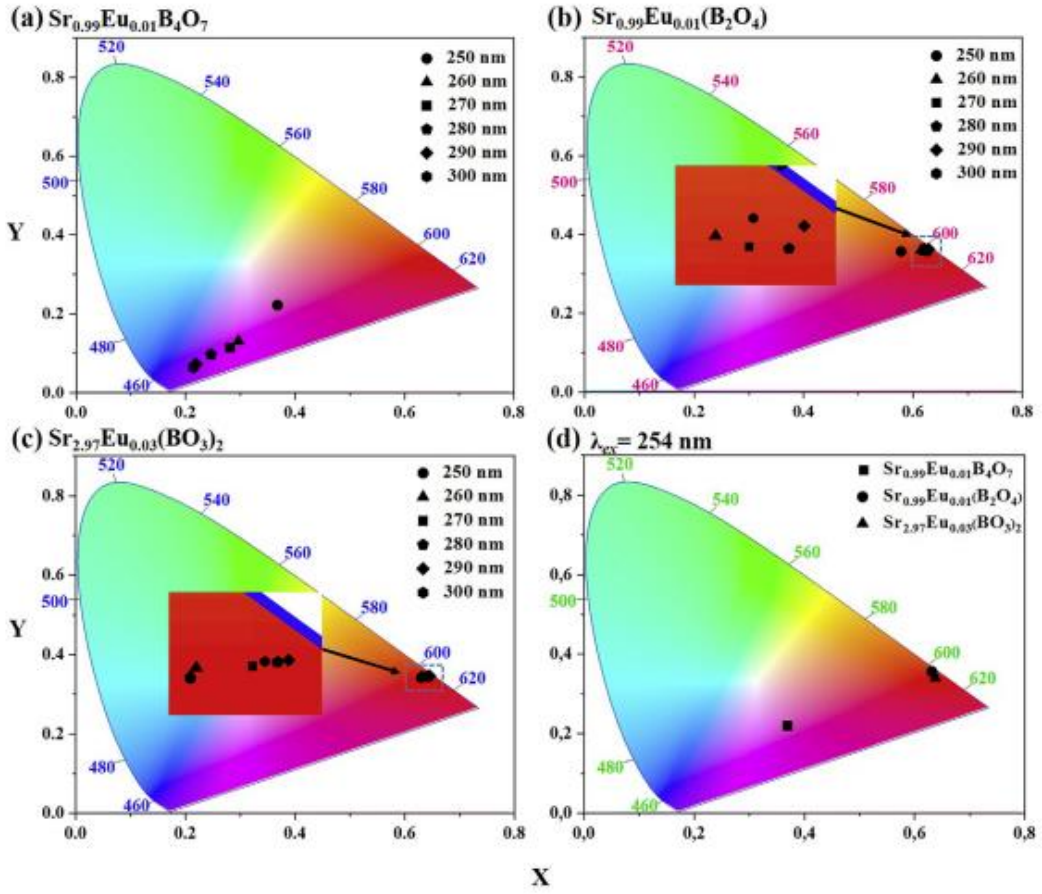

Fig. 6. Chromaticity diagrams of (a)$Sr_{0.99}Eu_{0.01}B_4O_7$, (b)$Sr_{0.99}Eu_{0.01}B_2O_4$, (c)$Sr_{2.97}Eu_{0.03}(BO_3)_2$ phosphors at various excitation wavelengths. (d) Chromaticity diagram for the synthesized phosphors at λ_{ex} = 254 nm.

The *R* values calculated for the $Sr_{0.99}Eu_{0.01}B_4O_7$, $Sr_{0.99}Eu_{0.01}B_2O_4$ and $Sr_{2.97}Eu_{0.03}(BO_3)_2$ are 1.797, 1.897 and 2.670, respectively. All the ratios are higher than 1, indicating that in all samples the Eu^{3+} ions are situated at sites without inversion symmetry. Furthermore, the increasing *R* value indicates the covalence of the Eu^{3+}-O^{2-} bond in the $Sr_{2.97}Eu_{0.03}(BO_3)_2$ compound is the strongest [54,55]. However, according to XRD analysis, the Eu^{3+} ions in the synthesized $Sr_{0.99}Eu_{0.01}B_4O_7$, $Sr_{0.99}Eu_{0.01}B_2O_4$ and $Sr_{2.97}Eu_{0.03}(BO_3)_2$ samples

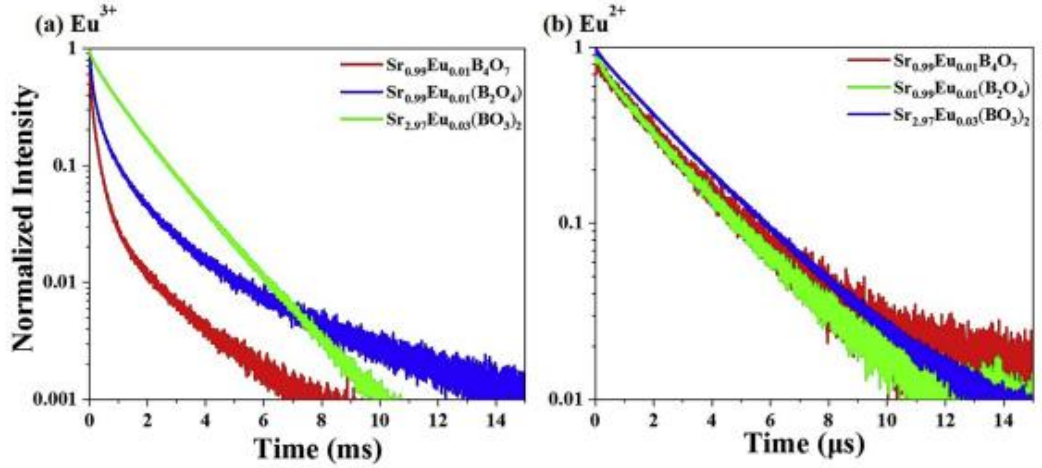

Fig. 7. Luminescence decay curves recorded for (a) the Eu^{3+} ($^5D_0 \rightarrow {}^7F_2$ transition) and (b) the Eu^{2+} ($4f^65d \rightarrow 4f^7$ transition) of the obtained samples doped with $Eu^{2+/3+}$ ions.

Table 2
Determined luminescence lifetimes for the Eu^{3+} ($^5D_0 \rightarrow {}^7F_2$) and Eu^{2+} ($4f^65d \rightarrow 4f^7$) transitions in synthesized strontium borates.

Compounds	Eu^{3+} ($^5D_0 \rightarrow {}^7F_2$)				τ (ms)	Eu^{2+} ($4f^65d \rightarrow 4f^7$)
	τ_1 (ms)	%	τ_2 (ms)	%		τ (μs)
$Sr_{0.99}Eu_{0.01}B_4O_7$	0.148 ± 0.001	81	0.677 ± 0.001	19	0.421 ± 0.001	2.430 ± 0.005
$Sr_{0.99}Eu_{0.01}B_2O_4$	0.140 ± 0.001	66	0.861 ± 0.001	34	0.688 ± 0.001	2.230 ± 0.001
$Sr_{2.97}Eu_{0.03}(BO_3)_2$	1.094 ± 0.001	100	-	-	1.094 ± 0.001	1.945 ± 0.002

occupy the sites with increasing symmetry, i.e. C_{2v}, D_{2h} and D_{3d}, respectively. The inset in Fig. 5(f) shows the photographs of the corresponding samples luminescence under UV lamp irradiation ($\lambda_{ex} = 254$ nm). Furthermore, comparing Fig. 4(b) with Fig. 5(f), it is also easily seen that there are overlaps between the excitation spectra of Eu^{3+} ion (*4f-4f* transitions of Eu^{3+} ion, from 340 to 420 nm, i.e. peaks at 375, 380 and 393 nm) and the emission spectra of Eu^{2+} ion (*5d-4f* transition, from 350 to 380 nm, i.e. peak centered at 367 nm), which provide a channel for energy transfer from Eu^{2+} to Eu^{3+} ions in the obtained phosphors [56]. It is worth noting that in the case of the $Sr_{0.99}Eu_{0.01}B_4O_7$ and $Sr_{0.99}Eu_{0.01}B_2O_4$ samples, the band around 580 nm corresponding to the forbidden $^5D_0$-$^7F_0$ transition can be deconvoluted into two separate peaks (see the insets in Fig. 5(d)). As the total angular quantum momentum (*J* number) for this transition is equal to zero, this band does not split into Stark sublevels. That is why, the number of $^5D_0$-$^7F_0$ peaks corresponds to the type of the Eu^{3+} symmetry sites present in the matrix. According to structural analysis, there is only one site for $Eu^{2+/3+}$ ions in all matrices. Hence, the presence two different site symmetries of Eu^{3+} (two peaks around 580 nm) is plausibly related to the energy transfer between Eu^{2+}-Eu^{3+} ions and the altered symmetry of the local coordination environment in those systems. In other words, part of the Eu^{3+} ions is surrounded mostly by other Eu^{3+} ions, whereas another part is surrounded by Eu^{2+} ones. This reasoning is supported by the fact that the presence of two $^5D_0$-$^7F_0$ peaks is clearly observed in the matrices with the highest content of Eu^{2+}, i.e. $Sr_{0.99}Eu_{0.01}B_4O_7$ and $Sr_{0.99}Eu_{0.01}B_2O_4$ compounds [57,58].

For a visual understanding of the color-tunable emission of the synthesized $Sr_{0.99}Eu_{0.01}B_4O_7$, $Sr_{0.99}Eu_{0.01}B_2O_4$ and $Sr_{2.97}Eu_{0.03}(BO_3)_2$ phosphors at different excitation wavelengths, one can refer to the included chromaticity diagrams (CIE 1964 10 deg observer), presented in Fig. 6(a–c), respectively. Fig. 6(d) illustrates the CIE diagram of the synthesized phosphors at $\lambda_{ex} = 254$ nm, i.e. comparison of the emission color between different matrices. The presented colors in this CIE diagram agree with the luminescence photographs in Fig. 5(f). Accordingly, the corresponding emission color can change from orange-red to violet-blue depending on different matrices used or applying different excitation wavelength.

Photoluminescence decay curves of the as-prepared $Sr_{0.99}Eu_{0.01}B_4O_7$, $Sr_{0.99}Eu_{0.01}B_2O_4$ and $Sr_{2.97}Eu_{0.03}(BO_3)_2$ phosphors are depicted in Fig. 7(a, b). The luminescence decay curves of these phosphor were obtained at $\lambda_{em} = 615$ nm for the Eu^{3+} ion ($^5D_0 \rightarrow {}^7F_2$ transition; Fig. 7(a)) after excitation at 393 nm, and at $\lambda_{em} = 367$ nm for the Eu^{2+} ions ($4f^65d \rightarrow 4f^7$ transition; Fig. 7(b)) after excitation at 300 nm. The decay curves of the Eu^{3+} emission in the $Sr_{0.99}Eu_{0.01}B_4O_7$ and $Sr_{0.99}Eu_{0.01}B_2O_4$ phosphors can be well fitted to the bi-exponential function:

$$I = A_1 \exp(-x/\tau_1) + A_2 \exp(-x/\tau_2) \quad (3)$$

where *I* is luminescence intensity at time *x*, *A* is the amplitude, τ is the emission lifetime, and the correlation coefficients (R^2) for $Sr_{0.99}Eu_{0.01}B_4O_7$ and $Sr_{0.99}Eu_{0.01}B_2O_4$ are both higher than 0.999. It is indicated that there are at least two components (τ_1 and τ_2) in the recorded decay profiles, which is related to the presence of two Eu^{3+} symmetry sites in these two crystal structure. On the other hand, the decay curve of $Sr_{2.97}Eu_{0.03}(BO_3)_2$ can be well fitted ($R^2 = 0.999$) to a single-exponential function as:

$$I = A \exp(-x/\tau) \quad (4)$$

It is indicated that in $Sr_{2.97}Eu_{0.03}(BO_3)_2$ there is only one symmetry site of Eu^{3+}. Such a result coincides well with the results from the spectra of 0-0 transition of Eu^{3+} in Fig. 5 (d). The determined emission lifetime values of Eu^{2+} and Eu^{3+} are presented in Table 2. The determined luminescence lifetimes of Eu^{3+} are about ≈0.4 and ≈ 0.7 ms in the $Sr_{0.99}Eu_{0.01}B_4O_7$ and $Sr_{0.99}Eu_{0.01}B_2O_4$ luminophores, respectively, and about 1.1 ms in the $Sr_{2.97}Eu_{0.03}(BO_3)_2$ one. In contrast, the emission lifetimes of Eu^{2+} are very similar in all samples, ranging from ≈2 to 2.4 μs The shorter lifetime of Eu^{3+} in the $Sr_{0.99}Eu_{0.01}B_4O_7$ and $Sr_{0.99}Eu_{0.01}B_2O_4$ luminophores can be attributed to the efficient non-radiative ET pathway between Eu^{2+}-Eu^{3+} ions in the systems, including inter- and intra-configurational transitions, resulting from higher content of Eu^{2+} in these two compounds. However, in order to fully confirm the reason for the short, bi-exponential decay of Eu^{3+} in the $Sr_{0.99}Eu_{0.01}B_4O_7$ and $Sr_{0.99}Eu_{0.01}B_2O_4$ structures, further studies are needed, which will be the subject of our future research.

4. Conclusions

In summary, three different complex matrices of strontium borates $Sr_3(BO_3)_2$, SrB_2O_4 and SrB_4O_7 doped with Eu^{2+}/Eu^{3+} ions were successfully prepared by the solid state reaction method in the air. According to the XRD and SEM analysis, each obtained sample has a pure crystal structure, and the $Sr_{0.99}Eu_{0.01}B_4O_7$ sample consists of irregular particles (≈10–60 μm), much larger in size than the other phosphors (≈0.5–3 μm). The phosphors exhibit a color-tunable luminescence from violet-blue to orange-red depending on the excitation wavelength and host matrix used. It results from the different content, ratio of the Eu^{2+} (violet-blue) and Eu^{3+} (red) emissions in the compounds studied. Under 300 nm UV light excitation, emission intensity of the $Sr_{0.99}Eu_{0.01}B_4O_7$ sample is two to three orders of magnitude higher than for others, which is due to the most efficient reduction process of Eu^{3+} to Eu^{2+} in this material. Due to the abundant and excellent luminescence properties, the as-prepared phosphors have potential applications in the areas of pressure/temperature sensors, new light sources, barcoding in forensics, labeling techniques, etc.

Authors contribution section

Teng Zheng: Conceptualization, Methodology, Investigation, Formal analysis, Data Curation, Writing - Original Draft, Writing - Review & Editing, Visualization. Marcin Runowski: Conceptualization, Resources, Writing - Review & Editing, Funding acquisition. Przemysław Woźny: Formal analysis, Visualization. Stefan Lis: Conceptualization, Resources, Writing - Review & Editing, Supervision, Project administration, Funding acquisition.

Declaration of competing interest

The authors declare that they have no known competing financial interests or personal relationships that could have appeared to influence the work reported in this paper.

Acknowledgements

This work was supported by the Polish National Science Centre (grant No. UMO-2016/21/B/ST5/00110) and co-financed by the European Union through the European Social Fund under the Operational Program Knowledge Education Development (grant No. POWR.03.02.00−00-i020/17 and POWR.03.02.00-00-I023/17).

Appendix A. Supplementary data

Supplementary data to this article can be found online at https://doi.org/10.1016/j.jallcom.2019.153511.

References

[1] F. Auzel, Upconversion and anti-Stokes processes with f and d ions in solids, Chem. Rev. 104 (2004) 139−174, https://doi.org/10.1021/cr020357g.
[2] H. Dong, S.R. Du, X.Y. Zheng, G.M. Lyu, L.D. Sun, L.D. Li, P.Z. Zhang, C. Zhang, C.H. Yan, Lanthanide nanoparticles: from design toward bioimaging and therapy, Chem. Rev. (2015), https://doi.org/10.1021/acs.chemrev.5b00091.
[3] J. Rocha, L.D. Carlos, F.A.A. Paz, D. Ananias, Luminescent multifunctional lanthanides-based metal-organic frameworks, Chem. Soc. Rev. (2011), https://doi.org/10.1039/c0cs00130a.
[4] H. Ye, M. He, T. Zhou, Q. Guo, J. Zhang, L. Liao, L. Mei, H. Liu, M. Runowski, A novel reddish-orange fluorapatite phosphor, $La_{6-x}Ba_4(SiO_4)_6F_2$: xSm^{3+} - structure, luminescence and energy transfer properties, J. Alloy. Comp. 757 (2018) 79−86, https://doi.org/10.1016/J.JALLCOM.2018.05.060.
[5] S. Gai, C. Li, P. Yang, J. Lin, Recent progress in rare earth micro/nanocrystals: soft chemical synthesis, luminescent properties, and biomedical applications, Chem. Rev. (2014), https://doi.org/10.1021/cr4001594.
[6] P. Dorenbos, Modeling the chemical shift of lanthanide 4f electron binding energies, Phys. Rev. B Condens. Matter Mater. Phys. (2012), https://doi.org/10.1103/PhysRevB.85.165107.
[7] X. Qin, X. Liu, W. Huang, M. Bettinelli, X. Liu, Lanthanide-Activated phosphors based on 4f-5d optical transitions: theoretical and experimental aspects, Chem. Rev. (2017), https://doi.org/10.1021/acs.chemrev.6b00691.
[8] M. Runowski, A. Shyichuk, A. Tymiński, T. Grzyb, V. Lavín, S. Lis, Multifunctional optical sensors for nanomanometry and nanothermometry: high-pressure and high-temperature upconversion luminescence of lanthanide-doped phosphates - $LaPO_4$/YPO_4:Yb^{3+}-Tm^{3+}, ACS Appl. Mater. Interfaces 10 (2018) 17269−17279, https://doi.org/10.1021/acsami.8b02853.
[9] T. Zheng, L. Luo, P. Du, A. Deng, W. Li, Ferroelectric, upconversion emission and optical thermometric properties of color-controllable Er^{3+}-doped $Pb(Mg_{1/3}Nb_{2/3})O_3$-$PbTiO_3$-$Pb(Yb_{1/2}Nb_{1/2})O_3$ ferroelectrics, J. Eur. Ceram. Soc. 38 (2018) 575−583, https://doi.org/10.1016/j.jeurceramsoc.2017.09.035.
[10] P. Du, L. Zhou, L. Luo, J.S. Yu, Facile preparation of Eu^{3+}-activated $Ca_7(VO_4)_4O$ nanoparticles: a blue light-triggered red-emitting platform for indoor solid-state lighting, New J. Chem. 43 (2019) 6688−6695, https://doi.org/10.1039/C9NJ00999J.
[11] M.D. Dramićanin, Sensing temperature via downshifting emissions of lanthanide-doped metal oxides and salts, Rev. Methods Appl. Fluoresc. 4 (2016), https://doi.org/10.1088/2050-6120/4/4/042001.
[12] J. Zhou, Q. Liu, W. Feng, Y. Sun, F. Li, Upconversion luminescent materials: advances and applications, Chem. Rev. 115 (2015) 395−465, https://doi.org/10.1021/cr400478f.
[13] T. Zheng, L. Luo, Linear response fluorescent temperature-sensing properties based on Stark sublevels of Er^{3+}-doped $Pb(Mg_{1/3}Nb_{2/3})O_3$-$PbTiO_3$-$Pb(Yb_{1/2}Nb_{1/2})O_3$ ceramics, Ceram. Int. 44 (2018) 12670−12675, https://doi.org/10.1016/j.ceramint.2018.04.067.
[14] A. Bartkowiak, M. Runowski, A. Shyichuk, M. Majewska, T. Grzyb, Tunable yellow-green up-conversion emission and luminescence lifetimes in Yb^{3+}-Er^{3+}-Ho^{3+} multi-doped β-$NaLuF_4$ crystals, J. Alloy. Comp. 793 (2019) 96−106, https://doi.org/10.1016/J.JALLCOM.2019.04.084.
[15] Q. Guo, C. Zhao, L. Liao, S. Lis, H. Liu, L. Mei, Novel apatite $KLaSr_3(PO_4)_3F$:Eu^{2+} phosphors: synthesis, structure, and luminescence properties, J. Mater. Res. 31 (2016) 3489−3497, https://doi.org/10.1557/jmr.2016.370.
[16] M. Karbowiak, P. Solarz, R. Lisiecki, W. Ryba-Romanowski, Optical spectra and excited state relaxation dynamics of Sm^{2+} ions in $SrCl_2$, $SrBr_2$ and SrI_2 crystals, J. Lumin. 195 (2018) 159−165, https://doi.org/10.1016/j.jlumin.2017.11.012.
[17] L. Wang, H. Zhou, J. Hu, B. Huang, M. Sun, B. Dong, G. Zheng, Y. Huang, Y. Chen, L. Li, Z. Xu, N. Li, Z. Liu, Q. Chen, L.D. Sun, C.H. Yan, A Eu^{3+}-Eu^{2+} ion redox shuttle imparts operational durability to Pb-I perovskite solar cells, Science 363 (2019) 265−270, https://doi.org/10.1126/science.aau5701, 80.
[18] S. Unithrattil, W. Bin Im, Blue and orange emission from Ce^{3+} and Yb^{2+} doped $KNa_3Al_4Si_4O_{16}$ phosphor: a detailed study of the luminescence mechanism, J. Alloy. Comp. (2015), https://doi.org/10.1016/j.jallcom.2014.09.001.
[19] M. Runowski, P. Woźny, N. Stopikowska, Q. Guo, S. Lis, Optical pressure sensor based on the emission and excitation band width (fwhm) and luminescence shift of Ce^{3+}-doped fluorapatite - high-pressure sensing, ACS Appl. Mater. Interfaces 11 (2019) 4131−4138, https://doi.org/10.1021/acsami.8b19500.
[20] J. Fan, J. Gou, Y. Chen, B. Yu, S.F. Liu, Enhanced luminescence and tunable color of $Sr_8CaSc(PO_4)_7$:Eu^{2+}, Ce^{3+}, Mn^{2+} phosphor by energy transfer between Ce^{3+}-Eu^{2+}-Mn^{2+}, J. Alloy. Comp. 731 (2018) 796−804, https://doi.org/10.1016/J.JALLCOM.2017.10.099.
[21] F. Ruan, D. Deng, M. Wu, B. Chen, L. Lei, R. Lei, S. Xu, Multichannel luminescence properties and ultrahigh-sensitive optical temperature sensing of mixed-valent Eu^{2+}/Eu^{3+} co-activated $Ca_8ZrMg(PO_4)_6(SiO_4)$ phosphors, J. Alloy. Comp. 784 (2019) 1153−1161, https://doi.org/10.1016/J.JALLCOM.2019.01.092.
[22] A. Dobrowolska, B. Dierre, C.M. Fang, H.T. Hintzen, P. Dorenbos, Thermal quenching of Eu^{2+} emission in Ca- and Sr-Ga_2S_4 in relation with VRBE schemes, J. Lumin. 184 (2017) 256−261, https://doi.org/10.1016/j.jlumin.2016.12.022.
[23] A. Dobrowolska, E. Zych, Spectroscopic characterization of $Ca_3Y_2Si_3O_{12}$: Eu^{2+},Eu^{3+} powders in VUV-UV-vis region, J. Phys. Chem. C 116 (2012) 25493−25503, https://doi.org/10.1021/jp306764f.
[24] I.I. Kindrat, B.V. Padlyak, Luminescence properties and quantum efficiency of the Eu-doped borate glasses, Opt. Mater. (2018), https://doi.org/10.1016/j.optmat.2018.01.019.
[25] Y. Dwivedi, S.B. Rai, Multicolour emission from surface crystallized Sm:Yb codoped spherulites rooted in borate matrix, J. Lumin. (2018), https://doi.org/10.1016/j.jlumin.2017.10.042.
[26] L. Dong, Y. Wang, B. Zhang, Z. Yang, X. Ge, K. Liu, S. Shen, $Pb_4B_6O_{13}$: a polar lead oxyborate with uncommon ∞ $(B_6O_{12})^{6-}$ layers exhibiting a large second harmonic generation response, Inorg. Chem. 58 (2019) 1750−1754, https://doi.org/10.1021/acs.inorgchem.8b03356.
[27] M. Runowski, P. Woźny, V. Lavín, S. Lis, Optical pressure nano-sensor based on lanthanide doped SrB_2O_4:Sm^{2+} luminescence - novel high-pressure nanomanometer, Sens. Actuators B Chem. 273 (2018) 585−591, https://doi.org/10.1016/j.snb.2018.06.089.
[28] R. Stefani, A.D. Maia, E.E.S. Teotonio, M.A.F. Monteiro, M.C.F.C. Felinto, H.F. Brito, Photoluminescent behavior of SrB_4O_7:RE^{2+} (RE=Sm and Eu) prepared by Pechini, combustion and ceramic methods, J. Solid State Chem. 179 (2006) 1086−1092, https://doi.org/10.1016/j.jssc.2006.01.006.
[29] P. Woźny, M. Runowski, S. Lis, Influence of boric acid/Sr^{2+} ratio on the structure and luminescence properties (colour tuning) of nano-sized, complex strontium borates doped with Sm^{2+} and Sm^{3+} ions, Opt. Mater. 83 (2018) 245−251, https://doi.org/10.1016/j.optmat.2018.06.027.
[30] Q. Zeng, Z. Pei, S. Wang, Q. Su, The reduction of Eu^{3+} in SrB_6O_{10} prepared in air and the luminescence of SrB_6O_{10}:Eu, J. Alloy. Comp. 275−277 (1998) 238−241, https://doi.org/10.1016/S0925-8388(98)00311-9.
[31] V. Darakchieva, M.-Y. Xie, F. Tasnádi, I.A. Abrikosov, L. Hultman, B. Monemar, J. Kamimura, K. Kishino, Lattice parameters, deviations from Vegard's rule, and E2 phonons in InAlN, Appl. Phys. Lett. 93 (2008) 261908, https://doi.org/10.1063/1.3056656.
[32] P. Mikhail, J. Hulliger, Sm^{2+} in oxide lattices: an unexplored chapter of crystal chemistry, Comments Inorg. Chem. (1999), https://doi.org/10.1080/02603599908012009.
[33] Q. Jing, Q. Wu, L. Liu, J.A. Xu, Y. Bi, Y. Liu, H. Chen, S. Liu, Y. Zhang, L. Xiong, Y. Li, J. Liu, An experimental study on SrB_4O_7:Sm^{2+} as a pressure sensor, J. Appl. Phys. 113 (2013), https://doi.org/10.1063/1.4774113.
[34] Z. Cao, X. Wei, L. Zhao, Y. Chen, M. Yin, Investigation of SrB_4O_7:Sm^{2+} as a multimode temperature sensor with high sensitivity, ACS Appl. Mater. Interfaces 8 (2016) 34546−34551, https://doi.org/10.1021/acsami.6b10917.
[35] J.K. Kim, E.F. Schubert, Transcending the replacement paradigm of solid-state lighting, Opt. Express 16 (2008), 21835, https://doi.org/10.1364/oe.16.021835.
[36] H. Fang, G. Qiu, J. Li, X. Wang, Sr^{2+} substitution for Ca^{2+} and Eu^{2+},Dy^{3+} co-doping enhance mechanoluminescence of $CaAl_2Si_2O_8$ phosphors, J. Alloy. Comp. 763 (2018) 267−272, https://doi.org/10.1016/J.JALLCOM.2018.05.294.
[37] W.J. Evans, Perspectives in reductive lanthanide chemistry, Coord. Chem. Rev. 206−207 (2000) 263−283, https://doi.org/10.1016/S0010-8545(00)00267-8.
[38] Q. Zeng, Z. Pei, S. Wang, Q. Su, S. Lu, ChemInform abstract: luminescent properties of divalent samarium-doped strontium hexaborate, ChemInform 30 (2010), https://doi.org/10.1002/chin.199920004 no-no.
[39] J. Heikenfeld, M. Garter, D.S. Lee, R. Birkhahn, A.J. Steckl, Red light emission by photoluminescence and electroluminescence from Eu-doped GaN, Appl. Phys. Lett. 75 (1999) 1189−1191, https://doi.org/10.1063/1.124686.
[40] T. Grzyb, A. Szczeszak, Z. Śniadecki, B. Idzikowski, S. Lis, White and red emitting LaF_3 nanocrystals doped with Eu^{2+} and Eu^{3+} ions: spectroscopic and magnetic studies, J. Alloy. Comp. 686 (2016) 489−495, https://doi.org/10.1016/j.jallcom.2016.06.019.
[41] B. Li, X. Huang, H. Guo, Y. Zeng, Energy transfer and tunable photoluminescence of $LaBWO_6$:Tb^{3+},Eu^{3+} phosphors for near-UV white LEDs, Dyes Pigments 150 (2018) 67−72, https://doi.org/10.1016/J.DYEPIG.2017.11.003.
[42] K.-I. Machida, G.-Y. Adachi, J. Shiokawa, Structure of europium(II) tetraborate, Acta Crystallogr. Sect. B Struct. Crystallogr. Cryst. Chem. 36 (2002) 2008−2011, https://doi.org/10.1107/s0567740880007820.

[43] P. ZENG, Z. CAO, Y. CHEN, M. YIN, Investigation of the temperature characteristic in $SrB_4O_7:Sm^{2+}$ phosphor-in-glass by analyzing the lifetime of 684 nm, J. Rare Earths 35 (2017) 783–786, https://doi.org/10.1016/S1002-0721(17)60976-1.

[44] G.L. Stamokostas, G.A. Fiete, Mixing of t_{2g} - e_g orbitals in 4d and 5d transition metal oxides, Phys. Rev. B. 97 (2018), 085150, https://doi.org/10.1103/PhysRevB.97.085150.

[45] C. Klixbüll Jørgensen, Electron Transfer Spectra, John Wiley & Sons, Ltd, 2007, pp. 101–158, https://doi.org/10.1002/9780470166130.ch2.

[46] L. Chunxu, L. Junye, D. Kai, Judd-ofelt intensity parameters and spectral properties of $Gd_2O_3:Eu^{3+}$ nanocrystals, J. Phys. Chem. B 110 (2006) 20277–20281, https://doi.org/10.1021/jp063075j.

[47] P. Ghosh, S. Sadhu, A. Patra, Preparation and photoluminescence properties of $Y_2SiO_5:Eu^{3+}$ nanocrystals, Phys. Chem. Chem. Phys. 8 (2006) 3342–3348, https://doi.org/10.1039/b603273g.

[48] J. Zhong, D. Chen, H. Xu, W. Zhao, J. Sun, Z. Ji, Red-emitting $CaLa_4(SiO_4)_3O:Eu^{3+}$ phosphor with superior thermal stability and high quantum efficiency for warm w-LEDs, J. Alloy. Comp. 695 (2017) 311–318, https://doi.org/10.1016/J.JALLCOM.2016.10.211.

[49] X. Liu, W. Xie, Y. Lü, J. Feng, X. Tang, J. Lin, Y. Dai, Y. Xie, L. Yan, Multichannel luminescence properties of mixed-valent Eu^{2+}/Eu^{3+} coactivated $SrAl_3BO_7$ nanocrystalline phosphors for near-UV LEDs, Inorg. Chem. 56 (2017) 13829–13841, https://doi.org/10.1021/acs.inorgchem.7b01938.

[50] M. Runowski, N. Stopikowska, S. Goderski, S. Lis, Luminescent-plasmonic, lanthanide-doped core/shell nanomaterials modified with Au nanorods – up-conversion luminescence tuning and morphology transformation after NIR laser irradiation, J. Alloy. Comp. 762 (2018) 621–630, https://doi.org/10.1016/J.JALLCOM.2018.05.211.

[51] P. Woźny, M. Runowski, S. Lis, Emission color tuning and phase transition determination based on high-pressure up-conversion luminescence in $YVO_4:Yb^{3+}$, Er^{3+} nanoparticles, J. Lumin. 209 (2019) 321–327, https://doi.org/10.1016/J.JLUMIN.2019.02.008.

[52] A.R. Allu, S. Das, S. Som, H.V.R. Maraka, S. Balaji, L.F. Santos, I. Manek-Hönninger, V. Jubera, J.M.F. Ferreira, Dependence of Eu^{3+} photoluminescence properties on structural transformations in diopside-based glass-ceramics, J. Alloy. Comp. 699 (2017) 856–865, https://doi.org/10.1016/j.jallcom.2016.12.438.

[53] M. Runowski, T. Grzyb, A. Zep, P. Krzyczkowska, E. Gorecka, M. Giersig, S. Lis, Eu^{3+} and Tb^{3+} doped $LaPO_4$ nanorods, modified with a luminescent organic compound, exhibiting tunable multicolour emission, RSC Adv. 4 (2014) 46305–46312, https://doi.org/10.1039/c4ra06168c.

[54] G. Fan, C. Lin, W. Yang, Y. Guan, Y. Liu, L. Wang, Concentration induced site symmetry transformation of Eu^{3+} luminescence center in β-$Ca_2P_2O_7$, Mater. Res. Bull. 80 (2016) 64–71, https://doi.org/10.1016/j.materresbull.2016.03.016.

[55] P. Manasa, C.K. Jayasankar, Luminescence and phonon side band analysis of Eu^{3+}-doped lead fluorosilicate glasses, Opt. Mater. 62 (2016) 139–145, https://doi.org/10.1016/j.optmat.2016.09.006.

[56] G. Blasse, B.C. Grabmaier, G. Blasse, B.C. Grabmaier, How does a luminescent material absorb its excitation energy?, in: Lumin. Mater Springer Berlin Heidelberg, Berlin, Heidelberg, 2011, pp. 10–32, https://doi.org/10.1007/978-3-642-79017-1_2.

[57] D.T. de Araujo, K.J. Ciuffi, E.J. Nassar, M.A. Vicente, R. Trujillano, P.S. Calefi, V. Rives, E.H. de Faria, Eu^{3+}- and Tb^{3+} -dipicolinate complexes covalently grafted into kaolinite as luminescence-functionalized clay hybrid materials, J. Phys. Chem. C 121 (2017) 5081–5088, https://doi.org/10.1021/acs.jpcc.6b12308.

[58] S.L. Yefimova, T.N. Tkacheva, P.O. Maksimchuk, I.I. Bespalova, K.O. Hubenko, V.K. Klochkov, A.V. Sorokin, Y.V. Malyukin, $GdVO_4:Eu^{3+}$ nanoparticles - methylene Blue complexes for PDT: electronic excitation energy transfer study, J. Lumin. 192 (2017) 975–981, https://doi.org/10.1016/J.JLUMIN.2017.08.044.

Influence of matrix on the luminescence properties of Eu^{2+}/Eu^{3+} doped strontium borates SrB_4O_7, SrB_2O_4 and $Sr_3(BO_3)_2$, exhibiting multicolor tunable emission

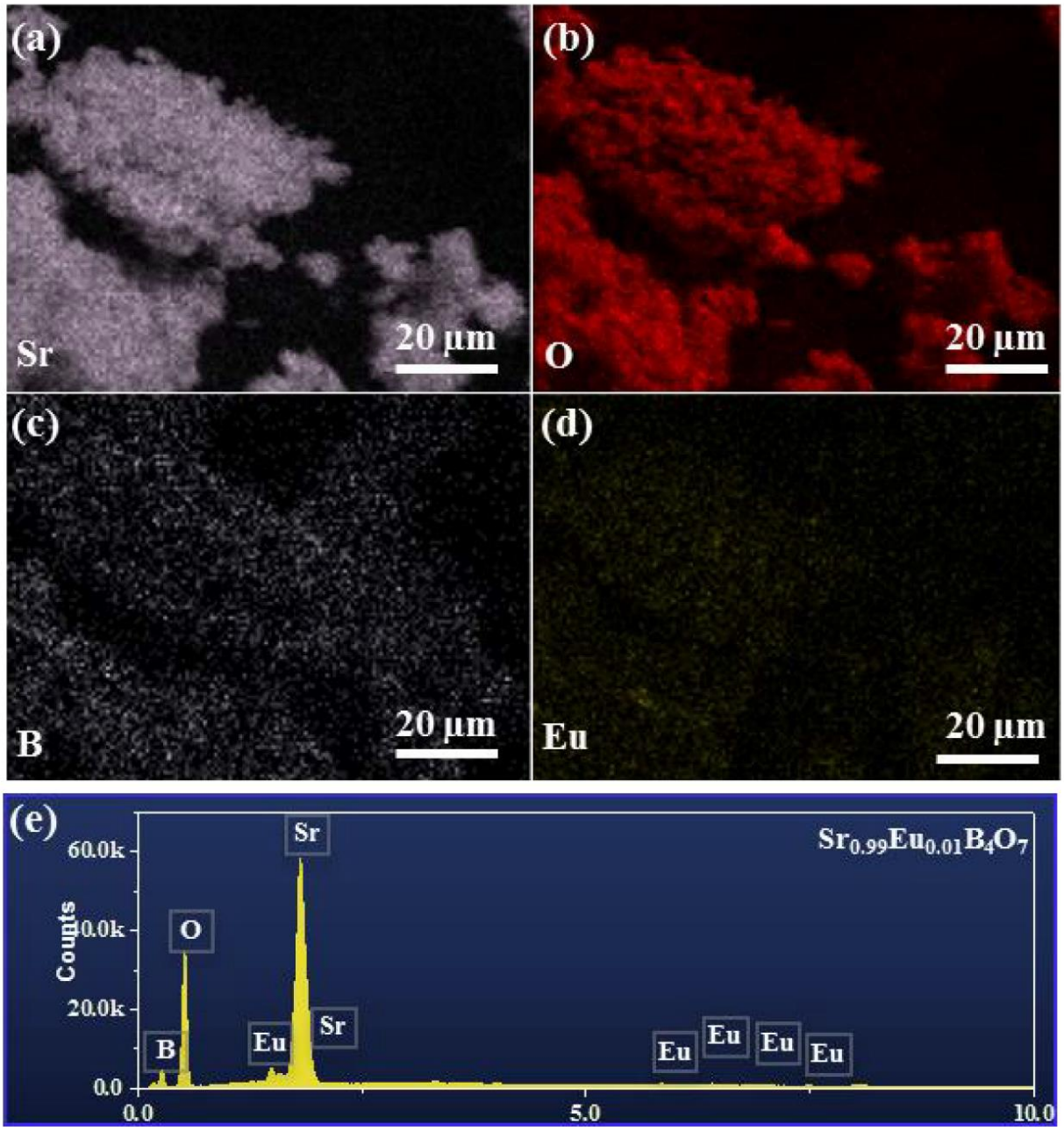

Fig. S1. Elemental mapping(a, b, c and d) and EDX spectra of the $Sr_{0.99}Eu_{0.01}B_4O_7$ phosphors**.**

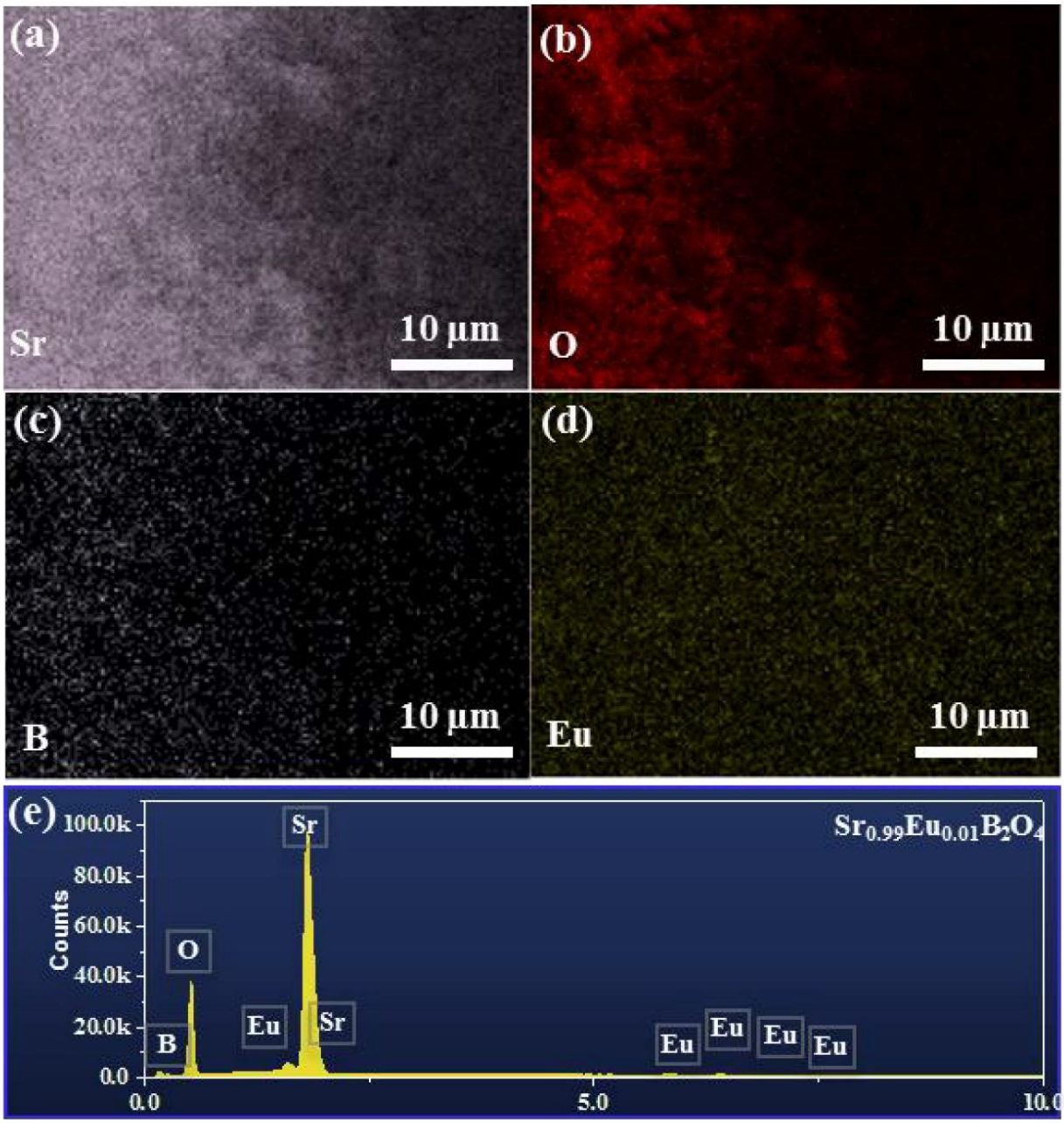

Fig. S2. Elemental mapping(a, b, c and d) and EDX spectra of the $Sr_{0.99}Eu_{0.01}B_2O_4$ phosphors**.**

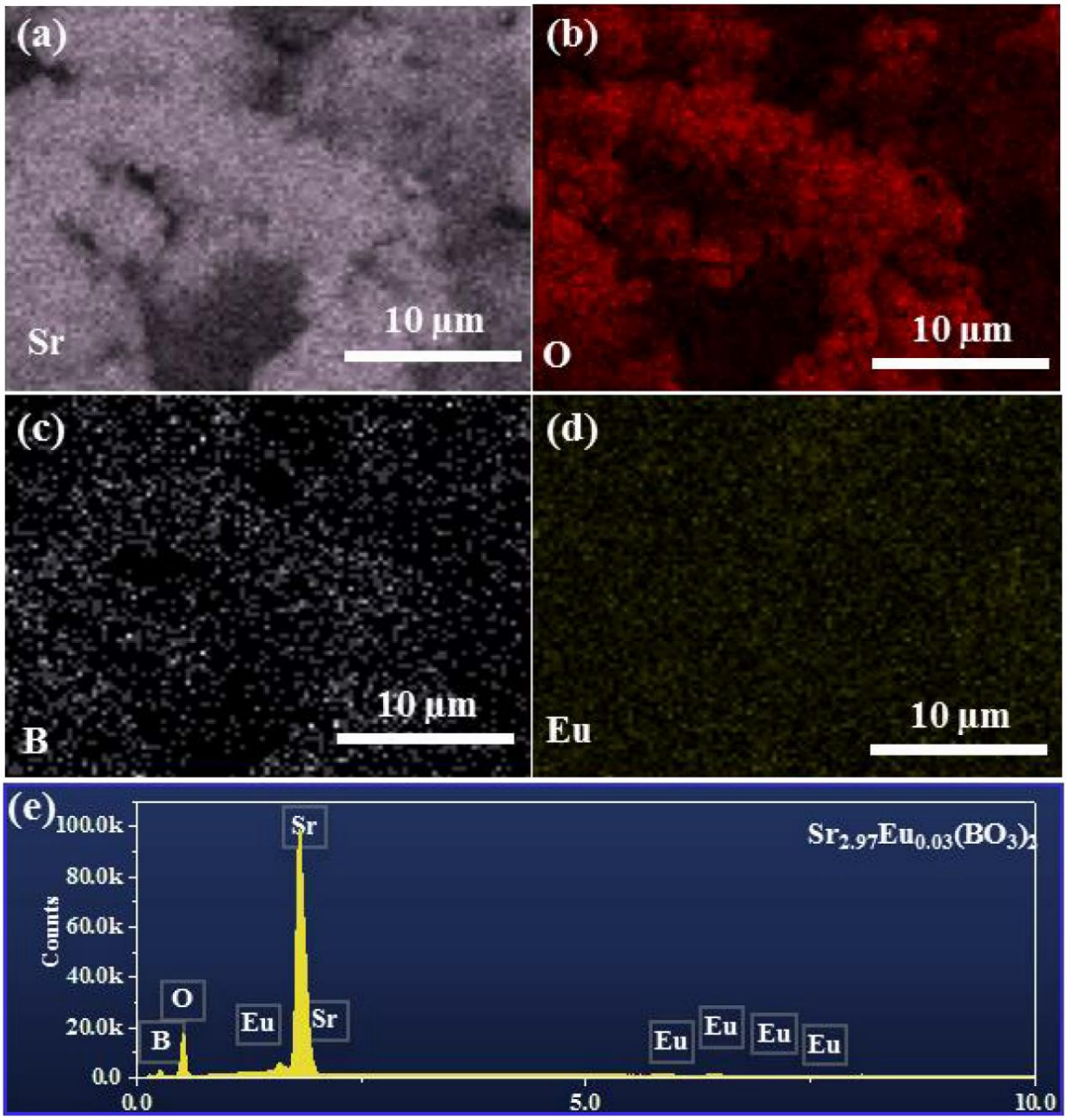

Fig. S3. Elemental mapping(a, b, c and d) and EDX spectra of the $Sr_{2.97}Eu_{0.03}(BO_3)_2$ phosphors.

Table S1. The calculated Eu^{2+}/Eu^{3+} integrated intensity ratio values at different excitation wavelength.

Compounds	240 nm	250 nm	260 nm	270 nm	280 nm	290 nm	300 nm
$Sr_{0.99}Eu_{0.01}B_4O_7$	137.2	739.2	5553.0	10569.1	11426.7	22777.0	22014.9
$Sr_{0.99}Eu_{0.01}B_2O_4$	4.02	0.54	0.17	0.11	0.11	0.19	0.30
$Sr_{2.97}Eu_{0.03}(BO_3)_2$	6.39	0.25	0.04	0.02	0.02	0.02	0.03

5.2. Huge enhancement of Sm^{2+} emission: via Eu^{2+} energy transfer in a SrB_4O_7 pressure sensor

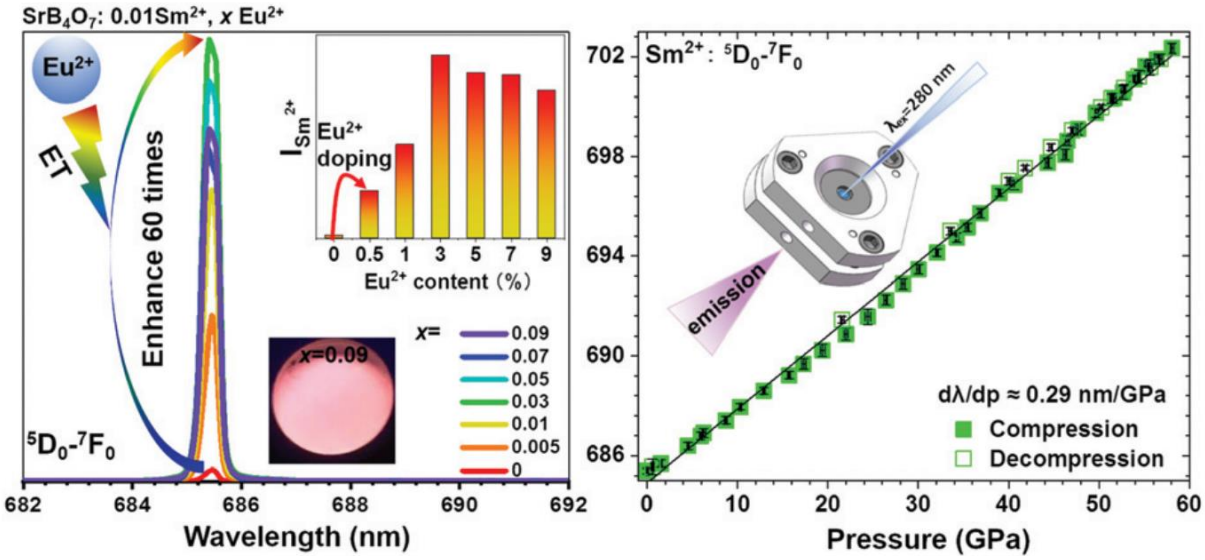

The result in this section were published in: Teng Zheng, Marcin Runowski, Przemysław Woźny, Stefan Lis, Victor Lavin, Huge enhancement of Sm^{2+} emission via Eu^{2+} energy transfer in a SrB_4O_7 pressure sensor, Journal of Materials Chemistry C, 2020, 8, 4810-4817(8).

Abstract of the section: Based on the last section, the main aim of the work: "Huge enhancement of Sm^{2+} emission via Eu^{2+} energy transfer in a SrB_4O_7 pressure sensor" is, taking advantage of the typical pressure-sensing performances of the Sm^{2+} ion in the SrB_4O_7 crystal, to explore the improvement of the emission intensity of Sm^{2+} ions via the strategy of Eu^{2+}-to-Sm^{2+} ET process. When Eu^{2+} ions are also incorporated into the crystalline structure, an enormous enhancement of about 60 times was observed in the $^5D_0$ - $^7F_0$ emission line. The spectral position of the ultra-narrow and most intense $^5D_0$ - $^7F_0$ emission line in the material was correlated with pressure and was successfully calibrated up to about 58 GPa. The developed sensor is characterized by favourable pressure-sensing features, i.e., a pressure sensitivity of ~0.29 $nmGPa^{-1}$, excellent temperature independence, sharp and single emission lines, and an intense luminescence signal. Depending on the excitation wavelength used and the content of dopants in the matrix, the samples also exhibit multicolour tuneable luminescence from orange-red to amaranth, and to warm-white light, which allows their potential application in white light emitting diode devices.

Contribution of Ph.D. student in this work: Conceptualization, material synthesis, structural and morphological characterization, conduction of the spectroscopic measurements, visualization, data analysis and curation, formal analysis, writing original draft and writing review & editing.

Journal of Materials Chemistry C

ROYAL SOCIETY OF CHEMISTRY

PAPER

View Article Online
View Journal | View Issue

Cite this: J. Mater. Chem. C, 2020, 8, 4810

Huge enhancement of Sm^{2+} emission *via* Eu^{2+} energy transfer in a SrB_4O_7 pressure sensor†

Teng Zheng, [a] Marcin Runowski, *[a] Przemysław Woźny, [a] Stefan Lis [a] and Víctor Lavín [b]

Received 27th January 2020,
Accepted 29th February 2020

DOI: 10.1039/d0tc00463d

rsc.li/materials-c

Taking advantage of the excellent pressure-sensing properties of the Sm^{2+} ion in the SrB_4O_7 crystal, we demonstrate an enormous enhancement of about 60 times in the emission intensity of Sm^{2+} ions when Eu^{2+} ions are also incorporated into the crystalline structure. This enhancement is induced by the energy transfer from Eu^{2+} to Sm^{2+} ions. The spectral position of the ultra-narrow and most intense $^5D_0 \rightarrow {}^7F_0$ emission line in the material was correlated with pressure and successfully calibrated up to about 58 GPa. The material exhibits favorable pressure-sensing features, *i.e.* $d\lambda/dp \approx 0.29$ nm GPa^{-1}, negligible temperature-dependent shift, narrow and well-separated emission lines, and a strong luminescence signal. The samples also exhibit multicolor tunable luminescence from orange-red to amaranth, and to warm-white light, depending on the excitation wavelength used and dopant content in the matrix, allowing their potential application in white light emitting diode (LED) devices.

Introduction

Pressure shapes stars and planets, continents and oceans, and affects all aspects of our lives.[1] Pressure also has a crucial influence on the physicochemical properties of materials. Compression of materials under high-pressure conditions has been widely utilized for the study of pressure-induced changes of physicochemical characteristics of substances, formations of new phases or materials under extreme conditions, spectroscopic and structural variation of the chemical compounds, *etc.*[2–10] When trying to mimic these processes for scientific and industrial purposes in the laboratory using a high pressure anvil cell, a quick and precise determination of pressure is of paramount importance and, thanks to the transparency of diamonds and other gems in the visible range, optical pressure calibrants are often used.[11]

In the case of a static high pressure experiment, the combination of a sample with a variety of hydrostatic pressure transmitting media (PTM) is a typical assemblage for diamond anvil cell (DAC) system, using the calibration of the line shift of the fluorescence at around 694 nm of Cr^{3+} ion in ruby, *i.e.* $d\lambda/dp \approx 0.35$ nm GPa^{-1}, for the pressure determination.[12–15] However, due to the pressure-induced solidification of most of the commonly used PTMs and the subsequent loss of hydrostaticity in the sample's chamber,[15–18] a large error occurs in the ruby spectral data analysis that significantly reduces the accuracy of the pressure determination under very high pressure conditions. This is because of the relatively broad ($\approx$0.8 nm at ambient condition) emission bands of ruby and the strong overlapping of the ruby peaks (R_1 and R_2) under non-hydrostatic, high-pressure conditions. Moreover, the fluorescence line shift of ruby is strongly temperature-dependent, *i.e.* $d\lambda/dT \approx 0.007$ nm K^{-1}, which limits its pressure-sensing capability to the low-temperature range.

The SrB_4O_7:Sm^{2+} compound has been reported in many works as a splendid alternative to ruby as pressure gauge,[18–21] thanks to its favorable features such as: (I) an isolated, narrow ($\approx$0.2 nm) and intense $^5D_0 \rightarrow {}^7F_0$ emission band (0–0 line) located at around 685 nm; (II) a large pressure-induced shift of the 0–0 line ($\approx$0.25 nm GPa^{-1}), comparable to that of Cr^{3+} in ruby, (III) a negligible temperature coefficient (10^{-4} nm K^{-1}), and (IV) excellent thermal, chemical and structural stabilities. However, despite these benefits, and as it also happens to ruby, the inevitable decrease of Sm^{2+} luminescence intensity under pressure may limit the measurable pressure range and also may diminish the sensing accuracy.

The divalent lanthanide (Ln) ions are interesting luminescent centers because of the smaller energy gap between the $4f^n$ ground and the first excited $4f^{n-1}5d$ configurations compared to the Ln^{3+} ions.[22–29] This smaller energy difference increases the mixing of wavefunctions of the different configurations, *i.e.* increasing the 5d state opposite parity character of the 4f wavefunctions,

[a] Adam Mickiewicz University, Faculty of Chemistry, Uniwersytetu Poznańskiego 8, 61-614 Poznań, Poland. E-mail: runowski@amu.edu.pl; Tel: +48618291778
[b] Departamento de Física, MALTA Consolider Team and IUdEA, Universidad de La Laguna, Apdo. Correos 456, E-38200 San Cristóbal de La Laguna, Santa Cruz de Tenerife, Spain

† Electronic supplementary information (ESI) available: Experimental details; XRD data; SEM images; EDX mapping and spectra; emission spectra; FWHM in pressure; temperature shift; luminescence decay curves and luminescence lifetime; CIE diagram. See DOI: 10.1039/d0tc00463d

that shorten the lifetime and increases the intensity of the luminescence of Ln^{2+} ions.[30] The divalent europium ion (Eu^{2+}) has many advantages, such as intense broad excitation and emission bands corresponding to the allowed $4f^65d \leftrightarrow 4f^7$ transitions, relatively low reduction potential, relatively high stability, *etc.*[31–35] Thanks to the large absorption in the UV region of Eu^{2+} in many host materials, this ion may exhibit excellent sensitization effects to other lanthanide ions.[36–40] According to energy transfer (ET) mechanism,[41–43] such a process occurring from sensitizer (Eu^{2+}) to activator ions can effectively enhance emission of the luminophore. A host material based on the SrB_4O_7 crystal structure is a good choice for effective combination of sensitizing properties of Eu^{2+} ions with the targeted Sm^{2+} activator ions, to enhance luminescence performance of the system. This is because SrB_4O_7 host reveals excellent stabilization of both Eu^{2+} and Sm^{2+}, even at high temperature in an oxidizing atmosphere. Moreover, the similar ionic radii of the dopant and host ions ($R_{Eu^{2+}}$ = 1.39 Å, $R_{Sm^{2+}}$ = 1.41 Å and $R_{Sr^{2+}}$ = 1.40 Å) provide less lattice distortion of the synthesized crystals.[44–47]

Many works have focused on the synthesis of different compounds doped with Sm^{2+} and other trivalent lanthanide ions, *i.e.* Ce^{3+}, Er^{3+}, Tm^{3+}, *etc.*, and their use for pressure sensing applications.[25,26,48–53] However, there are no reports concerning signal enhancement of pressure sensors *via* the ET processes from Eu^{2+} to other $Ln^{2+/3+}$ ions, which may significantly increase the emission intensity of various co-doped optical sensors, working under high pressure conditions. Herein, we report a huge enhancement of about 60 times in the emission intensity of Sm^{2+} caused by the $Eu^{2+} \rightarrow Sm^{2+}$ ET in the co-doped SrB_4O_7 compound synthesized by a simple solid-state method in air, and its application as a well-calibrated and accurate optical pressure sensor, which can work simultaneously under extreme conditions of pressure and temperature. In addition, we also demonstrate multi-color tunable emission from orange-red to warm white, depending on the concentration of Sm^{2+} and Eu^{2+} ions in the host and the excitation wavelength used.

Results and discussions

Structural and morphological properties

Information concerning the raw material used, synthesis and characterization are available in the ESI.† The powder X-ray diffraction (XRD) patterns (Fig. S1 in ESI†) of the SrB_4O_7:0.01Sm^{2+},$x$$Eu^{2+}$ (x = 0, 0.005, 0.01, 0.03, 0.05, 0.07 and 0.09) micro-particles fit well with the reference patterns (card no. 071-2191) from the ICDD standards database: orthorhombic SrB_4O_7 phase with space group $Pmn2_1$. The graphical representation of crystal structure is shown in Fig. 1a, where it is indicated that only one Sr^{2+} site exists in the structure of SrB_4O_7 host occupying a nonahedron (coordination number: 9) with local

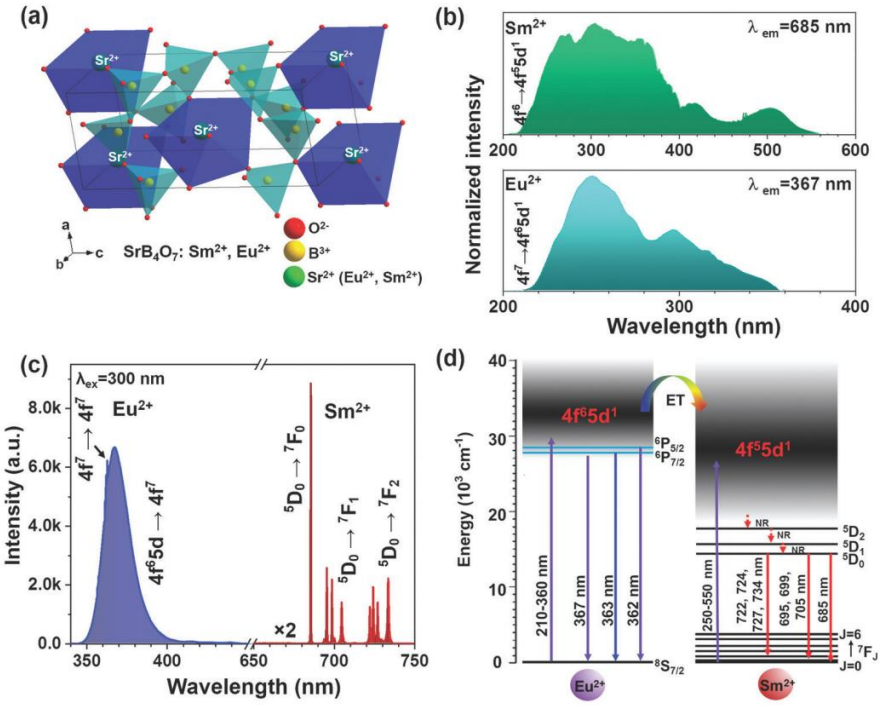

Fig. 1 (a) Graphical representation of the crystal structure of orthorhombic SrB_4O_7 matrix ($Pmn2_1$ space group). (b) The excitation spectra monitoring the emission at 685 nm for Sm^{2+} (top) and λ_{em} = 367 nm for Eu^{2+} (bottom) and (c) the emission spectrum at λ_{ex} = 300 nm of the SrB_4O_7:0.01Sm^{2+},0.03Eu^{2+} compound. (d) Simplified energy level diagram for the Sm^{2+} and Eu^{2+} ions and emission processes in the co-doped SrB_4O_7 system with the possible $Eu^{2+} \rightarrow Sm^{2+}$ ET process.

point symmetry C_{2v}, and the cell parameters are: a = 4.431(4) Å, b = 10.707(10) Å, c = 4.237(4) Å, V = 200.810 Å^3.

The morphology of the synthesized products was inspected by a scanning electron microscopy (SEM), and the representative SEM images of SrB_4O_7:0.01Sm^{2+},xEu^{2+} samples (x = 0, 0.01, 0.03, 0.05) are shown in Fig. S2 (ESI†). The synthesized products are composed of irregular, nearly-spherical micro-particles (typical of inorganic borates), whose sizes range from approximately ~0.2 to 2.0 μm. With increasing content of Eu^{2+}, from 0 to 5 mol% (x = 0–0.05), the particle sizes vary slightly, which can be attributed to the similar ionic radii between the host and dopant ions.[54–56] In Fig. S2e–k (ESI†), the representative elemental mapping results and the EDX spectrum of the SrB_4O_7:0.01Sm^{2+},0.03Eu^{2+} compound revealed that the obtained phosphor consist of Sr, B, O, Eu and Sm, and these elements are uniformly distributed in the prepared product over the whole particle volume.

Optical properties at ambient conditions

The photoluminescence (PL) emission and excitation spectra, as well as luminescence decay curves, of the samples obtained were recorded under the same experimental conditions, and were corrected for the apparatus response. In Fig. 1b, the excitation spectra are given for the SrB_4O_7:0.01Sm^{2+},0.03Eu^{2+} compound recorded monitoring the emission at 685 nm for Sm^{2+} (top) and 367 nm for Eu^{2+} (bottom). It was found that the excitation spectra of both Sm^{2+} and Eu^{2+} consist of two overlapped broad peaks with maxima at around ≈250 nm and ≈300 nm, which are due to the splitting of 5d orbital into the t_{2g} and e_g components.[57] Upon UV light excitation at 300 nm (the highest peak in excitation spectra of Sm^{2+} in Fig. 1b), the PL emission spectrum of the SrB_4O_7:0.01Sm^{2+},0.03Eu^{2+} compound was examined. As shown in Fig. 1c, the emission spectrum consists of UV-violet and red bands. In the UV-violet region, the detected emission band can be deconvoluted into two peaks, *i.e.* the characteristic $4f^65d \rightarrow 4f^7$ transition of Eu^{2+} centered at 367 nm (broad band) and the rarely observed $4f^7$–$4f^7$ line-type (narrow) transitions of Eu^{2+} centered at ≈362.1 and ≈362.7 nm.[58–61] On the other hand, the red emissions of Sm^{2+}, located in the range of ≈680–750 nm, correspond to $^5D_0 \rightarrow {}^7F_0$ (685.4 nm), $^5D_0 \rightarrow {}^7F_1$ (695.4, 698.6, 704.6 nm), $^5D_0 \rightarrow {}^7F_2$ (722.1, 724.2, 727.0 and 733.5 nm) and they are associated with $4f^6$–$4f^6$ intra-configurational transitions of Sm^{2+} ions. It is clearly seen that the $^5D_0 \rightarrow {}^7F_0$ transition of Sm^{2+} exhibits its characteristic isolated, narrow and intense singlet band located at 685.4 nm. In the case of inevitable broadening of emission peaks under high pressure conditions, such a characteristic intensive, singlet and narrow 0–0 line of Sm^{2+} in a co-doped SrB_4O_7, reveals its superiority for high-pressure measurements, in comparison with the emissions bands of other transition metal ions (*e.g.* Mn^{4+}, Ce^{3+}, Er^{3+}).[53,62–64] This is attributed to the fact that the lowest emitting level and the ground state of the Sm^{2+} ion are singlets, *i.e.* non-degenerated multiplets with a total angular quantum momentum (J number) equal to zero. In addition, the $^5D_0 \rightarrow {}^7F_1$ band presents three sharp peaks, while the $^5D_0 \rightarrow {}^7F_2$ band presents only four out of five peaks. Hence, all the observed Sm^{2+} bands are split in a maximum of $2J + 1$ Stark components, which further confirms only one Sm^{2+} local symmetry site (local point symmetry C_{2v}) existing in the SrB_4O_7 structure.

To better comprehend the feasible ET process and the luminescence mechanisms governing the generation of UV-violet and red emissions, the simplified energy level diagram of Eu^{2+} and Sm^{2+} ions is illustrated in Fig. 1d. With the excitation of UV light (from 210 to 360 nm), the Eu^{2+} ions can be excited from their ground $^8S_{7/2}$ level to the excited $4f^65d^1$, as well as $^6P_{5/2}$ and $^6P_{7/2}$ levels, and then radiatively relax to the ground state, accompanied with a broad UV-violet emission (5d → 4f) overlapping with line-type emission ($4f^7 \rightarrow 4f^7$) of Eu^{2+}. Meanwhile, the Sm^{2+} ions populating the $^7F_0$ ground state can be excited to the $4f^55d^1$ first excited configuration of Sm^{2+} when pumping at λ_{ex} = 250–550 nm. Afterward, non-radiative (NR) decays occur, populating the lowest excited level $^5D_0$, finally leading to a series of radiative $^5D_0 \rightarrow {}^7F_J$ transitions, giving rise to the characteristic narrow bands of the red emission of Sm^{2+} ions. We assume that there is an energy transfer (ET) process between the Eu^{2+} and Sm^{2+} ions in the SrB_4O_7 host, which will be discussed in detail in the following paragraphs.

In order to explore the influence of Eu^{2+} ion concentration on the emission properties of the synthesized samples, the emission

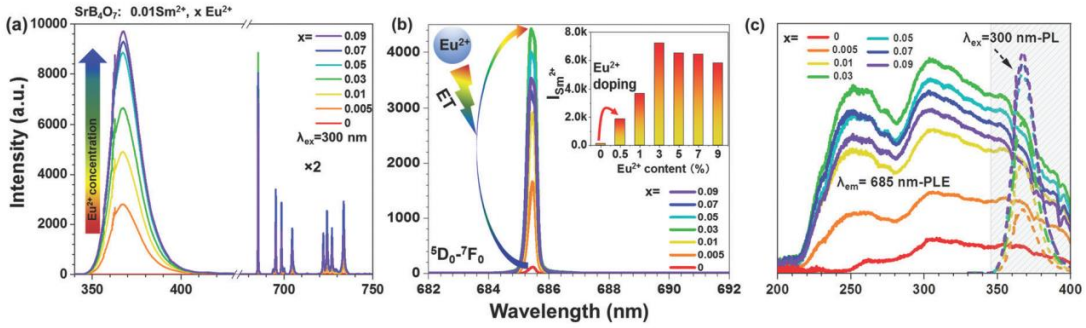

Fig. 2 (a) Emission spectra of the SrB_4O_7:0.01Sm^{2+},xEu^{2+} (x = 0, 0.005, 0.01, 0.03, 0.05, 0.07 and 0.09) compounds, using λ_{ex} = 300 nm at ambient condition. (b) Magnified emission spectra showing the 0–0 line of Sm^{2+} as a function of Eu^{2+} content x. (c) Excitation spectra for Sm^{2+} ions monitoring the emission at 685 nm (solid lines) and their overlapping part (shaded area) with Eu^{2+} emission (dashed lines) of the samples.

spectra exciting at λ_{ex} = 300 nm of the samples as a function of the Eu^{2+} ion content are shown in Fig. 2a. It is clearly seen that all the emission spectra consist of UV-violet emission bands of Eu^{2+} ions and red emission lines from Sm^{2+} ions, except of the sample without Eu^{2+} ions (SrB_4O_7:0.01Sm^{2+}) that only shows Sm^{2+} emission lines. With increasing the Eu^{2+} ion content from 0.5 to 9 mol% (x = 0.05–0.9), the shape of emission peaks scarcely varies, whereas the emission intensity and the Eu^{2+}/Sm^{2+} band intensity ratios are greatly dependent on the Eu^{2+} doping content. In the UV-violet region, the emission intensity of Eu^{2+} maintains an upward tendency with increasing the Eu^{2+} doping content from 0 to 9 mol%. For detailed investigation of the sensitization effect of Eu^{2+} in the synthesized samples, the magnified emission spectra of the Sm^{2+}: 0–0 line (in a narrow range) as a function of the Eu^{2+} doping content are shown in Fig. 2b. As disclosed, the Sm^{2+} emission intensity of the samples is highly dependent on the Eu^{2+} concentration and the best enhancement occurs for x = 0.03 (inset in Fig. 2b). Based on the integrated emission intensity of Sm^{2+} in the SrB_4O_7:0.01Sm^{2+},$x$$Eu^{2+}$ samples (see Table S1 in ESI†), it is clearly seen that the addition of even 0.5 mol% of Eu^{2+} results in the ≈16-times enhancement in emission intensity of Sm^{2+} compared to the sample without Eu^{2+} ions. As the Eu^{2+} content further increases, the enhancement demonstrates an upward tendency, exhibiting its optimal value, *i.e.* about 60 times enhancement, with 3 mol% of Eu^{2+}. Afterwards, the emission intensity of Sm^{2+} ions starts to decrease when the doping concentration is over 3 mol%, probably due to the concentration quenching effects. Such a large increase in the intensity of Sm^{2+} emission in this material may be attributed to the ET phenomenon, occurring from Eu^{2+} to Sm^{2+} ions.

For the sake of studying the possible ET process from the Eu^{2+}–Sm^{2+} ions, the emission spectra recorded at λ_{ex} = 300 nm (Eu^{2+}) and the excitation spectra at λ_{em} = 685 (Sm^{2+}) of SrB_4O_7:0.01Sm^{2+},$x$$Eu^{2+}$ (x = 0–0.09) are shown in Fig. 2c, emphasizing their overlapping parts. It can be clearly seen that all the obtained samples have a very broad excitation band from 200 to over 400 nm, with the highest peak at around 300 nm, associated with Sm^{2+} ions that overlaps the Eu^{2+} emission band, located in the range from 345 to 400 nm. In fact, Eu^{2+} begins to emit even at lower wavelengths, however, due to the technical reasons, *i.e.* the necessity of using a long-pass (350 nm) filter, this emission is partially cutoff. The overlapping area indicates the resonant channel for ET from Eu^{2+} to Sm^{2+} ions, which occurs in the Sm^{2+}–Eu^{2+} co-doped SrB_4O_7 system, leading to the enhancement of Sm^{2+} emission.[65]

The Commission Internationale de l'Eclairage (CIE) chromaticity diagram for the SrB_4O_7:0.01Sm^{2+},$x$$Eu^{2+}$ (x = 0–0.09) samples and the corresponding photographs of the samples under irradiation with a 254 nm UV lamp are shown in Fig. 3a. All the samples obtained are white powders in daylight. The presented colors in the CIE diagram (based on the emission spectra characteristics) agree with the luminescence photographs. As disclosed, the samples obtained exhibit multi-color tunable emission from orange-red to warm white, depending on the Eu^{2+} content in

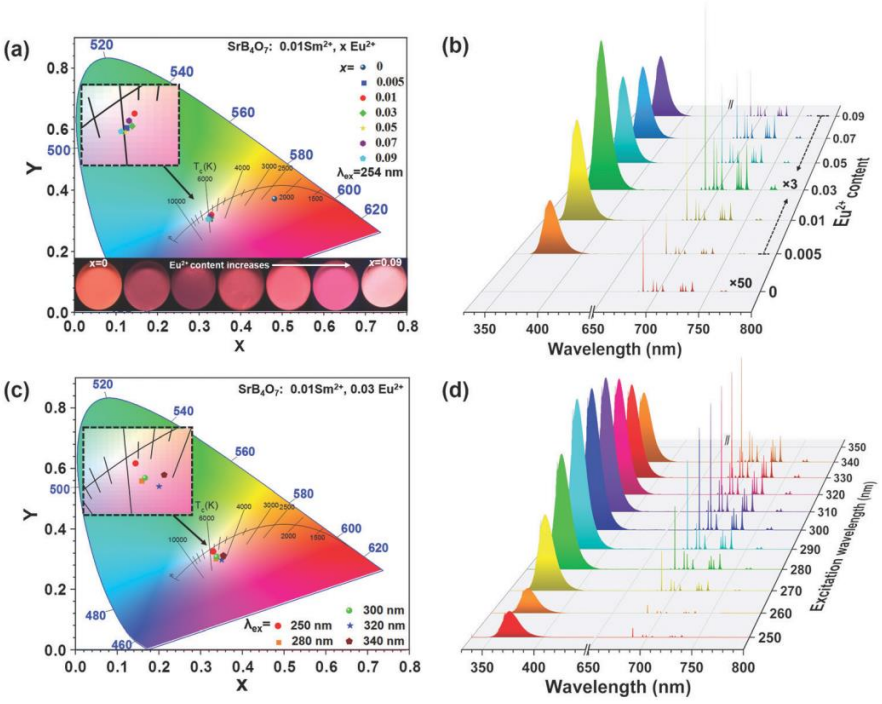

Fig. 3 (a) CIE chromaticity diagram and luminescence images of the SrB_4O_7:0.01Sm^{2+},$x$$Eu^{2+}$ (x = 0–0.09) phosphors, excited at 254 nm, and (b) the corresponding emission spectra. (c) CIE chromaticity diagram of SrB_4O_7:0.01Sm^{2+},0.03Eu^{2+} as a function of representative excitation wavelengths, and (d) the corresponding emission spectra.

the phosphor. The corresponding emission spectra excited at 254 nm are shown in Fig. 3b. Moreover, as shown in Fig. 3c and d, the emission color of the best-enhanced sample (SrB_4O_7:0.01Sm^{2+},0.03Eu^{2+}) can also be tuned depending on the excitation wavelength used. Noteworthy, the determined color coordinates of the Sm^{2+}–Eu^{2+} co-doped SrB_4O_7 are very close to the white illumination (0.310, 0.316), *e.g.* 0.322, 0.306 (9 mol% of Eu^{2+}) and 0.330, 0.325 (3 mol% of Eu^{2+}), indicating that the phosphors obtained have potential application in white LED. All determined color coordinates as a function of the Eu^{2+} doping concentration and the excitation wavelength used are shown in Tables S2 and S3 in ESI,† respectively.

Optical properties at high pressure

To investigate the pressure-sensing abilities of Sm^{2+} in the Eu^{2+} co-doped SrB_4O_7 material, the best-enhanced sample, *i.e.* SrB_4O_7:0.01Sm^{2+},0.03Eu^{2+}, was used in high-pressure measurements from ambient pressure up to about 58 GPa. The experimental setup used for the measurements of high-pressure luminescence is schematically presented in Fig. 4a. Due to technical reasons (availability of a high-power, focusable light source), the sample was excited at 280 nm, which is close to the optimal excitation wavelength. Technical details concerning measurements under high-pressure and sample preparation for DAC are presented in ESI.†

The normalized emission spectra of the SrB_4O_7:0.01Sm^{2+},0.03Eu^{2+} material under pressure are shown in Fig. 4b. It can be clearly seen that, when the pressure increases, the red-shifts of the $^5D_0 \rightarrow {}^7F_0$ and $^5D_0 \rightarrow {}^7F_1$ emission peaks are observed. These shifts to lower energies under pressure are caused by an overall contraction of the $4f^N$ ground configuration leading to a reduction in the energy difference between the ground state and the excited state of the $^{2S+1}L_J$ multiplets.[11,51] This phenomenon is related to decreasing coulomb and spin–orbit interactions under pressure, and it is called nephelauxetic effect,[66] which can be accounted by a reduction of the free-ion parameters due to the increasing covalent character of the lanthanide–oxygen bonds, when interatomic distances decrease along with decreasing volume. Superimposed on the reduction in multiplets splitting, there is an increase in the splitting of the multiplets, ascribed to an increase of the crystal field interaction between the 4f electron of the lanthanide ion and the valence electrons of the oxygen anions of the first coordination shell, when interatomic distances decrease with pressure.[10] This can be clearly observed in the splitting of the $^5D_0 \rightarrow {}^7F_1$ emission peaks that increases from ≈9.2 nm (≈188 cm^{-1}) at ambient pressure to ≈11.8 nm (≈230 cm^{-1}) at 58.07 GPa. The emission spectra for all recorded pressure values are shown in Fig. S3(a–c) (ESI†).

The calibration curve for the spectral position of the Sm^{2+} 0–0 line as a function of pressure, in the compression and decompression cycles is presented in Fig. 4c. The peak centroid reversibly shifts from about 685.4 nm at ambient pressure to 702.3 nm at 58.07 GPa, which can be well fitted (R^2 = 0.998) to a linear function. The calculated shift rate for this band is $d\lambda/dT \approx 0.29$ nm GPa^{-1}, which is close to the shifts of the SrB_4O_7:Sm^{2+} reported previously[18–21,45] and also to that

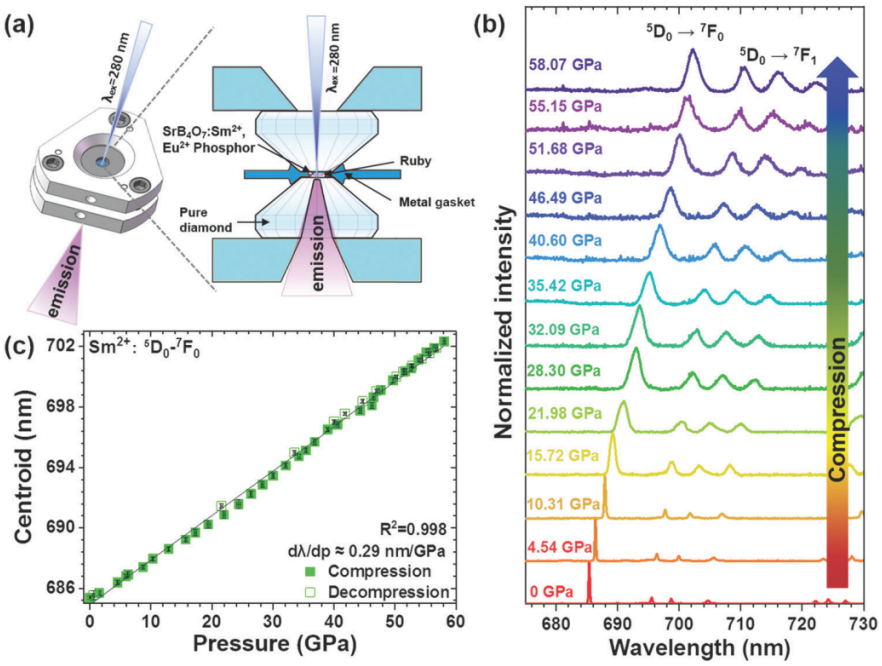

Fig. 4 (a) Schematic configuration of the setup used for high-pressure luminescence measurements. (b) The normalized emission spectra of the SrB_4O_7:0.01Sm^{2+},0.03Eu^{2+} material as a function of pressure; λ_{ex} = 280 nm. (c) Spectral positions (peak centroids) of the $^5D_0 \rightarrow {}^7F_0$ emission peak as a function of pressure. The filled symbols represent the compression and the empty ones decompression data.

Table 1 Determined decay times for the Eu^{2+} $4f^65d^1 \rightarrow 4f^7$ transition in the SrB_4O_7:ySm^{2+},0.05Eu^{2+} (y = 0.005, 0.01, 0.02, 0.03 and 0.05) compounds synthesized

Sample (% Sm^{2+})	Eu^{2+} ($4f^65d^1 \rightarrow 4f^7$)					
	τ_1 (μs)	A_1 (%)	τ_2 (μs)	A_2 (%)	τ (μs)	R^2
0.5	0.668 ± 0.006	0.117	2.616 ± 0.002	0.883	2.388	>0.999
1	0.570 ± 0.006	0.142	2.500 ± 0.004	0.858	2.226	>0.999
2	0.559 ± 0.002	0.189	2.326 ± 0.002	0.811	1.992	>0.999
3	0.461 ± 0.002	0.249	2.227 ± 0.002	0.751	1.787	>0.999
5	0.398 ± 0.002	0.272	2.117 ± 0.003	0.728	1.649	>0.999

reported for ruby.[12,15] All the exact $d\lambda/dP$ values, and the initial and final spectral positions of the peak centroids ($^5D_0 \rightarrow {}^7F_0$ and $^5D_0 \rightarrow {}^7F_1$ transitions) are presented in Table S4 in ESI.† The 0–0 line of Sm^{2+} in the SrB_4O_7:Eu^{2+}–Sm^{2+} material is almost temperature-independent showing a relatively low thermal-quenching effect of $d\lambda/dT \approx -2.8 \times 10^{-4}$ nm K^{-1}, as reported for SrB_4O_7:Sm^{2+} in several papers,[18–21,45] which we additionally confirmed for our compound (see Fig. S4 in ESI†). The low thermal-quenching effect presented, *i.e.* ≈75% of the initial emission intensity at 420 K (working temperature of LED devices), is beneficial not only for pressure sensing, but also for potential use in lighting applications.[67,68]

The broadening of the $^5D_0 \rightarrow {}^7F_0$ and $^5D_0 \rightarrow {}^7F_1$ band profiles together with the increase in pressure (volume reduction) is clearly seen in the presented emission spectra (Fig. 4b). At ambient conditions, the 0–0 line is extremely narrow, *i.e.* the full width at half maximum $\Gamma \approx 0.23$ nm. It keeps an upward tendency with increasing pressure (see Fig. S3d, ESI†) and increases to ≈1.81 nm at 26.42 GPa, which is mainly due to the increasing non-hydrostaticity of the pressure transmitting medium used. Then, this peak undertakes a slower broadening, up to ≈2.27 nm at 58.07 GPa, with an average $d\Gamma/dP \approx 14.5 \times 10^{-3}$ nm GPa^{-1}.

Confirmation of ET from Eu^{2+} to Sm^{2+} in co-doped SrB_4O_7

In order to fully confirm the ET from Eu^{2+} to Sm^{2+}, a series of SrB_4O_7 doped with a constant amount of Eu^{2+} and varied content of Sm^{2+} were synthesized. As shown in Fig. S5a (ESI†), the XRD patterns of the SrB_4O_7:ySm^{2+},0.05Eu^{2+} (y = 0.005, 0.01, 0.02, 0.03 and 0.05) micro-particles indicated that all phosphors were successfully synthesized. In Fig. S5b (ESI†), the emission spectra are shown for the excitation wavelength λ_{ex} = 254 nm, indicating a gradual increase in the Sm^{2+} emission intensity and a deterioration of Eu^{2+} emission, as the Sm^{2+} doping content increases. In the inset in Fig. S5(b) (ESI†), the integrated emission intensity ratio of Sm^{2+}/Eu^{2+} as a function of Sm^{2+} concentration shows an upward tendency. The CIE diagram for the synthesized phosphors at λ_{ex} = 254 nm, *i.e.* the comparison of the emission color between different doping content of Sm^{2+} is shown in Fig. S5c (ESI†). The colors presented in this CIE diagram agree with the luminescence photographs. The corresponding color coordinates are listed in Table S5 (ESI†). Accordingly, the corresponding emission color can be tuned from orange-red to amaranth depending on the Sm^{2+} content in the SrB_4O_7:ySm^{2+},0.05Eu^{2+} samples.

The photoluminescence decay curves of the as-prepared SrB_4O_7:ySm^{2+},0.05Eu^{2+} (y = 0.005–0.05) samples are presented in Fig. S5d (ESI†). The luminescence decay curves of these phosphors were recorded at λ_{em} = 367 nm for the Eu^{2+} ion after the excitation at 300 nm. The decay curves of Eu^{2+} emission show a non-exponential character (due to the high doping concentration). However, to analyze the tendency of luminescence lifetimes as a function of Sm^{2+} content, and confirm the $Eu^{2+} \rightarrow Sm^{2+}$ ET phenomenon, the decay profiles were fitted ($R^2 > 0.999$) to the bi-exponential function:

$$I = A_1 \exp(-x/\tau_1) + A_2 \exp(-x/\tau_2) \quad (1)$$

where I is the luminescence intensity at time x, A is the amplitude, and τ is the emission lifetime. It is indicated that, in the recorded decay profiles, there are at least two components (τ_1 and τ_2), which are associated with the ET process from Eu^{2+} to Sm^{2+} in the crystal lattice. The determined emission lifetime values of Eu^{2+} ion as a function of Sm^{2+} content are presented in Table 1. Clearly, the average lifetime (τ) of Eu^{2+} decreases monotonically from 2.388 to 1.649 μs as the content of Sm^{2+} increases, which further confirms the efficient ET from Eu^{2+} to Sm^{2+} occurring in the Sm^{2+}–Eu^{2+} co-doped SrB_4O_7 system, in which the Eu^{2+} ions act as sensitizers and the Sm^{2+} ions act as activators. Additionally, the luminescence decay curves for all Stark sublevels of $^5D_0 \rightarrow {}^7F_0$, $^5D_0 \rightarrow {}^7F_1$ and $^5D_0 \rightarrow {}^7F_2$ transitions of Sm^{2+} ions, in the SrB_4O_7:0.01Sm^{2+},0.03Eu^{2+} system were measured and analyzed (see Fig. S6 in the ESI†). As shown in Table S6 in the ESI,† all the determined luminescence lifetimes for Sm^{2+} are similar, *i.e.* around 4 ms, because for all bands the emission occurs from the same excited state ($^5D_0$).

Conclusions

Incorporating Eu^{2+} ions into the crystal structure of the commonly used optical pressure sensor SrB_4O_7:Sm^{2+} (temperature-independent gauge), we have demonstrated a huge enhancement of about 60 times on the Sm^{2+} emission, induced by energy transfer processes from Eu^{2+} to Sm^{2+} in the co-doped material. The samples obtained exhibit color-tunable luminescence from orange-red to amaranth, and to warm white depending on the Sm^{2+} and Eu^{2+} concentrations in the matrix and the excitation wavelength. The most intense and extremely narrow (≈0.2 nm) 0–0 line of the Sm^{2+} (around 685 nm) in the best-enhanced sample (SrB_4O_7: 1 mol% Sm^{2+}, 3 mol% Eu^{2+}) was correlated with pressure and successfully calibrated up to about 58 GPa.

The emission line used for pressure sensing exhibit a large and linear red-shift under pressure, *i.e.* $d\lambda/dp \approx 0.29$ nm GPa^{-1}, a negligible temperature-induced band-shift and relatively low thermal quenching of luminescence. The energy transfer processes from Eu^{2+} to Sm^{2+} ions were confirmed by luminescence spectroscopy. Such favorable features can significantly extend the measurable pressure range, along with very high accuracy of pressure determination, even under high temperature conditions, and the material can be applied in white light emitting diode (LED) devices.

Conflicts of interest

The authors declare no competing financial interest.

Acknowledgements

This work was supported by the Polish National Science Centre, grant no. 2016/23/D/ST4/00296 and 2016/21/B/ST5/00110, The Ministerio de Economía y Competitividad (MINECO) under the Spanish National Program of Materials (MAT2016-75586-C4-4-P), The Agencia Canaria de Investigación, Innovación y Sociedad de la Información (ACIISI) (ProID2017010078), and grant no. POWR.03.02.00-00-I023/17 and POWR.03.02.00-00-i020/17 co-financed by the European Union through the European Social Fund under the Operational Program Knowledge Education Development, and by The EU-FEDER funds. M. R. is a recipient of the Bekker Programme scholarship supported by the Polish National Agency for Academic Exchange.

References

1 *An Introduction to High-Pressure Science and Technology*, ed. J. M. Recio, J. M. Menendez and A. Otero de la Roza, CRC Press, Boca Raton, 2016.
2 M. Runowski, S. Sobczak, J. Marciniak, I. Bukalska, S. Lis and A. Katrusiak, *Nanoscale*, 2019, **11**, 8718–8726.
3 F. Bai, K. Bian, X. Huang, Z. Wang and H. Fan, *Chem. Rev.*, 2019, **119**, 7673–7717.
4 M. Somayazulu, P. Dera, A. F. Goncharov, S. A. Gramsch, P. Liermann, W. Yang, Z. Liu, H. K. Mao and R. J. Hemley, *Nat. Chem.*, 2010, **2**, 50–53.
5 A. Cantaluppi, M. Buzzi, G. Jotzu, D. Nicoletti, M. Mitrano, D. Pontiroli, M. Riccò, A. Perucchi, P. Di Pietro and A. Cavalleri, *Nat. Phys.*, 2018, **14**, 837–841.
6 Z. Ma, Z. Liu, S. Lu, L. Wang, X. Feng, D. Yang, K. Wang, G. Xiao, L. Zhang, S. A. T. Redfern and B. Zou, *Nat. Commun.*, 2018, **9**, 4506.
7 W. Kim, M. S. Jung, S. Lee, Y. J. Choi, J. K. Kim, S. U. Chai, W. Kim, D. G. Choi, H. Ahn, J. H. Cho, D. Choi, H. Shin, D. Kim and J. H. Park, *Adv. Energy Mater.*, 2018, **8**, 1702369.
8 J. Song, G. Fabbris, W. Bi, D. Haskel and J. S. Schilling, *Phys. Rev. Lett.*, 2018, **121**, 037004.
9 L. Zhang, C. Liu, L. Wang, C. Liu, K. Wang and B. Zou, *Angew. Chem., Int. Ed.*, 2018, **57**, 11213–11217.
10 T. Yin, Y. Fang, W. K. Chong, K. T. Ming, S. Jiang, X. Li, J. L. Kuo, J. Fang, T. C. Sum, T. J. White, J. Yan and Z. X. Shen, *Adv. Mater.*, 2018, **30**, 1705017.
11 Th. Tröster, in *Handbook on the Physics and Chemistry of Rare Earths*, ed. K. A. Gschnidner, Jr., J.-C. G. Bünzli and V. K. Pecharsky, Elsevier, North-Holland, 2003, vol. 33, pp. 515–589.
12 P. M. Bell, H. K. Mao and K. Goettel, *Science*, 1984, **226**, 542–544.
13 J. A. Xu, H. K. Mao and P. M. Bell, *Science*, 1986, **232**, 1404–1406.
14 K. Syassen, *High Press. Res.*, 2008, **28**, 75–126.
15 G. J. Piermarini, S. Block, J. D. Barnett and R. A. Forman, *J. Appl. Phys.*, 1975, **46**, 2774–2780.
16 R. J. Angel, M. Bujak, J. Zhao, G. D. Gatta and S. D. Jacobsen, *J. Appl. Crystallogr.*, 2007, **40**, 26–32.
17 R. J. Angel, *Transformation Processes in Minerals*, De Gruyter, Mouton, 2019, vol. 39, pp. 85–104.
18 F. Datchi, R. LeToullec and P. Loubeyre, *J. Appl. Phys.*, 1997, **81**, 3333–3339.
19 C. Zhao, H. Li, Y. Wang, J. Jiang and Y. He, *High Press. Res.*, 2017, **37**, 18–27.
20 S. V. Rashchenko, A. Kurnosov, L. Dubrovinsky and K. D. Litasov, *J. Appl. Phys.*, 2015, **117**, 2–7.
21 Q. Jing, Q. Wu, L. Liu, J. Xu, Y. Bi, Y. Liu, H. Chen, S. Liu, Y. Zhang, L. Xiong, Y. Li and J. Liu, *J. Appl. Phys.*, 2013, **113**, 023507.
22 T. Zheng, L. Luo, P. Du, A. Deng and W. Li, *J. Eur. Ceram. Soc.*, 2018, **38**, 575–583.
23 Q. Dong, J. Cui, Y. Tian, F. Yang, H. Ming, F. Du, J. Peng and X. Ye, *J. Lumin.*, 2019, **212**, 146–153.
24 T. Zheng and L. Luo, *Ceram. Int.*, 2018, **44**, 12670–12675.
25 M. Runowski, *Handbook of Nanomaterials in Analytical Chemistry*, Elsevier, 2020, pp. 227–273.
26 M. Runowski, P. Woźny, S. Lis, V. Lavín and I. R. Martín, *Adv. Mater. Technol.*, 2020, 1901091.
27 H. Li, Q. Li and Z. Xu, *J. Mater. Chem. C*, 2019, **7**, 2880–2885.
28 H. Ji, L. Wang, M. S. Molokeev, N. Hirosaki, R. Xie, Z. Huang, Z. Xia, O. M. Ten Kate, L. Liu and V. V. Atuchin, *J. Mater. Chem. C*, 2016, **4**, 6855–6863.
29 V. V. Atuchin, A. S. Aleksandrovsky, O. D. Chimitova, T. A. Gavrilova, A. S. Krylov, M. S. Molokeev, A. S. Oreshonkov, B. G. Bazarov and J. G. Bazarova, *J. Phys. Chem. C*, 2014, **118**, 15404–15411.
30 Y. Shen and K. L. Bray, *Mater. Sci. Forum*, 1999, **315–317**, 243–248.
31 H. Fang, G. Qiu, J. Li and X. Wang, *J. Alloys Compd.*, 2018, **763**, 267–272.
32 W. J. Evans, *Coord. Chem. Rev.*, 2000, **206–207**, 263–283.
33 R. Shi, L. Ning, Y. Huang, Y. Tao, L. Zheng, Z. Li and H. Liang, *ACS Appl. Mater. Interfaces*, 2019, **11**, 9691–9695.
34 Z. Xia, Y. Zhang, M. S. Molokeev and V. V. Atuchin, *J. Phys. Chem. C*, 2013, **117**, 20847–20854.
35 Z. Wang, Z. Xia, M. S. Molokeev, V. V. Atuchin and Q. Liu, *Dalton Trans.*, 2014, **43**, 16800–16804.
36 H. Lai, J. Zhang, D. Hou, H. Guan and X. Ye, *Ceram. Int.*, 2018, **44**, 15072–15078.

37 L. Dong, L. Zhang, W. Lü, B. Shao, S. Zhao and H. You, *Dalton Trans.*, 2019, **48**, 3028–3037.
38 D. Liu, Y. Jin, Y. Lv, G. Ju, C. Wang, L. Chen, W. Luo and Y. Hu, *J. Am. Ceram. Soc.*, 2018, **101**, 5627–5639.
39 M. Shi, C. Zhu, M. Lu, X. Meng and M. Wei, *J. Am. Ceram. Soc.*, 2018, **101**, 5461–5468.
40 W. Wolszczak, K. W. Krämer and P. Dorenbos, *J. Lumin.*, 2020, **222**, 117101.
41 H. Dong, L. D. Sun and C. H. Yan, *Chem. Soc. Rev.*, 2015, **44**, 1608–1634.
42 S. Ye, F. Xiao, Y. X. Pan, Y. Y. Ma and Q. Y. Zhang, *Mater. Sci. Eng., R*, 2010, **71**, 1–34.
43 J. Xue, X. Wang, J. H. Jeong and X. Yan, *Phys. Chem. Chem. Phys.*, 2018, **20**, 11516–11541.
44 T. Zheng, M. Runowski, P. Woźny and S. Lis, *J. Alloys Compd.*, 2020, **822**, 1–9.
45 Z. Cao, X. Wei, L. Zhao, Y. Chen and M. Yin, *ACS Appl. Mater. Interfaces*, 2016, **8**, 34546–34551.
46 J. Sun, J. Zhu, X. Liu and H. Du, *J. Rare Earths*, 2012, **30**, 1084–1087.
47 P. Solarz, M. Karbowiak, M. Głowacki, M. Berkowski, R. Diduszko and W. Ryba-Romanowski, *J. Alloys Compd.*, 2016, **661**, 419–427.
48 S. Kobyakov, A. Kamińska, A. Suchocki, D. Galanciak and M. Malinowski, *Appl. Phys. Lett.*, 2006, **88**, 234102.
49 Q. Jing, Q. Wu, L. Liu, J. Xu, Y. Bi, Y. Liu, H. Chen, S. Liu, Y. Zhang, L. Xiong, Y. Li and J. Liu, *J. Appl. Phys.*, 2013, **113**, 023507.
50 M. Runowski, A. Shyichuk, A. Tymiński, T. Grzyb, V. Lavín and S. Lis, *ACS Appl. Mater. Interfaces*, 2018, **10**, 17269–17279.
51 M. Runowski, P. Woźny, V. Lavín and S. Lis, *Sens. Actuators, B*, 2018, **273**, 585–591.
52 P. Woźny, M. Runowski and S. Lis, *J. Lumin.*, 2019, **209**, 321–327.
53 M. Runowski, J. Marciniak, T. Grzyb, D. Przybylska, A. Shyichuk, B. Barszcz, A. Katrusiak and S. Lis, *Nanoscale*, 2017, **9**, 16030–16037.
54 X. Feng, D. C. Sayle, Z. L. Wang, M. S. Paras, B. Santora, A. C. Sutorik, T. X. T. Sayle, Y. Yang, Y. Ding, X. Wang and Y. Her, *Science*, 2006, **312**, 1504–1507.
55 X. Wang, Y. Wang, J. Yu, Y. Bu and X. Yan, *Opt. Express*, 2018, **26**, 21950.
56 D. Chen, Y. Yu, F. Huang, P. Huang, A. Yang and Y. Wang, *J. Am. Chem. Soc.*, 2010, **132**, 9976–9978.
57 R. Stefani, A. D. Maia, E. E. S. Teotonio, M. A. F. Monteiro, M. C. F. C. Felinto and H. F. Brito, *J. Solid State Chem.*, 2006, **179**, 1086–1092.
58 W. Liu, L. Liu, Y. Wang, L. Chen, J. A. McLeod, L. Yang, J. Zhao, Z. Liu, J. Diwu, Z. Chai, T. E. Albrecht-Schmitt, G. Liu and S. Wang, *Chem. – Eur. J.*, 2016, **22**, 11170–11175.
59 R. A. Hewes and M. V. Hoffman, *J. Lumin.*, 1971, **3**, 261–280.
60 M. V. Hoffman, *J. Electrochem. Soc.*, 1972, **119**, 905–909.
61 S. G. Jantz, F. Pielnhofer, L. van Wüllen, R. Weihrich, M. J. Schäfer and H. A. Höppe, *Chem. – Eur. J.*, 2018, **24**, 443–450.
62 R. Verstraete, H. F. Sijbom, J. J. Joos, K. Korthout, D. Poelman, C. Detavernier and P. F. Smet, *ACS Appl. Mater. Interfaces*, 2018, **10**, 18845–18856.
63 P. Cai, X. Wang and H. J. Seo, *Phys. Chem. Chem. Phys.*, 2018, **20**, 2028–2035.
64 M. Runowski, P. Woźny, N. Stopikowska, Q. Guo and S. Lis, *ACS Appl. Mater. Interfaces*, 2019, **11**, 4131–4138.
65 S. Stojadinović and R. Vasilić, *Mater. Lett.*, 2019, **234**, 9–12.
66 R. Reisfeld and C. K. Jørgensen, *Lasers and Excited States of Rare Earths*, 2012.
67 Q. Guo, Q. Wang, L. Jiang, L. Liao, H. Liu and L. Mei, *Phys. Chem. Chem. Phys.*, 2016, **18**, 15545–15554.
68 Q. Guo, C. Zhao, L. Liao, S. Lis, H. Liu, L. Mei and Z. Jiang, *J. Am. Ceram. Soc.*, 2017, **100**, 2221–2231.

Supporting information for:

Huge Enhancement of Sm^{2+} Emission via Eu^{2+} Energy Transfer in SrB_4O_7 pressure sensor

Teng Zheng,[1] Marcin Runowski,[1]* Przemysław Woźny,[1] Stefan Lis,[1] Víctor Lavín[2]

[1]*Adam Mickiewicz University, Faculty of Chemistry, Uniwersytetu Poznańskiego 8, 61-614 Poznań, Poland*
[2]*Departamento de Física, MALTA Consolider Team and IUdEA, Universidad de La Laguna, Apdo. Correos 456, E-38200 San Cristóbal de La Laguna, Santa Cruz de Tenerife, Spain*

Experimental Section

Materials

All chemicals were used as received without further purification. Strontium carbonate - $SrCO_3$ (pure p.a.; 99.9%) was purchased from Sigma-Aldrich; boric acid - H_3BO_3 (pure p.a) was purchased from Chempur; europium oxide (Eu_2O_3) (99.99%) and samarium oxide (Sm_2O_3) (99.99%) were purchased from Stanford Materials.

Synthesis

The SrB_4O_7:0.01 Sm^{2+}, *x* Eu^{2+} (*x*=0, 0.005, 0.01, 0.03, 0.05, 0.07 and 0.09) and SrB_4O_7: 0.05 Eu^{2+}, y Sm^{2+} (y=0.005, 0.01, 0.02, 0.03 and 0.05) micro-particles were synthesized by means of a facile, reproducible and cheap method, i.e. a solid-state method in the air. Stoichiometric amounts of Eu_2O_3, Sm_2O_3, H_3BO_3 and $SrCO_3$ were weighted and ground together in an agate mortar. Then the mixtures were transferred to porcelain crucibles covered with a lid, then heat-treated at 700 °C for 5 h and then ground, subsequently further heat-treated at 850°C for 5 h. Then they were ground again in a mortar, and then heat-treated at 850 °C for another 5 h. All grinding must last more than 15 minutes to ensure that the powder is evenly mixed. It is crucial to cover the crucibles with lids to limit the amount of oxygen from the air in the system.

Characterization

X-ray diffraction patterns (XRD) were recorded using a Bruker AXS D8 Advance diffractometer in Bragg-Brentano geometry, with Cu Kα1 radiation (λ=1.5406 Å) in the 2θ range from 6°to 60°, with 0.05° step scan mode. The reference data for XRD were taken from ICDD (International Centre for Diffraction Data). Scanning electron microscopy (SEM) and energy-dispersive X-ray analysis (EDX) were obtained with a scanning electron microscope FEI Quanta 250 FEG, using an EDAX detector. The excitation spectra of the prepared samples were collected using a Hitachi F-7000 spectrofluorometer, at ambient conditions. The studies of the emission properties in ambient (in quartz holder) and under high-pressure conditions (in the DAC, with methanol/ethanol/water medium) were carried out by using Andor Shamrock 500i spectrograph

with iDus CCD camera as a detector. The excitation source for high-pressure luminescence measurements was a focusable, 280 nm LED device.

DAC loading procedure

High-pressure measurements were performed in a Merrill-Bassett diamond anvil cell (DAC), modified by mounting the anvils directly on steel supporting plates. The pressure in DAC was adjusted by the use of three metal screws. The gaskets used were made of stainless-steel sheets 250 μm thick, with the aperture of ≈150 μm (hole size). The gaskets were pre-indented to ≈70 μm thick (sample thickness). The DAC chamber was loaded with sample (white powder), one small ruby sphere (<10 μm diameter) and filled with methanol/ethanol/water (16:3:1 vol.) solvent system (pressure transmitting medium), to provide hydrostatic or quasi-hydrostatic conditions, in the whole range of measurements.

Pressure calibration

Pressure in the system was determined monitoring the ruby R_1 fluorescence line shift, using Andor Shamrock 500i spectrograph with iDus CCD camera as a detector, and a 100 mW 532 nm laser, as an excitation source. The pressure values in DAC were determined using the standard ruby calibration curve, available at: http://kantor.50webs.com/ruby.htm.

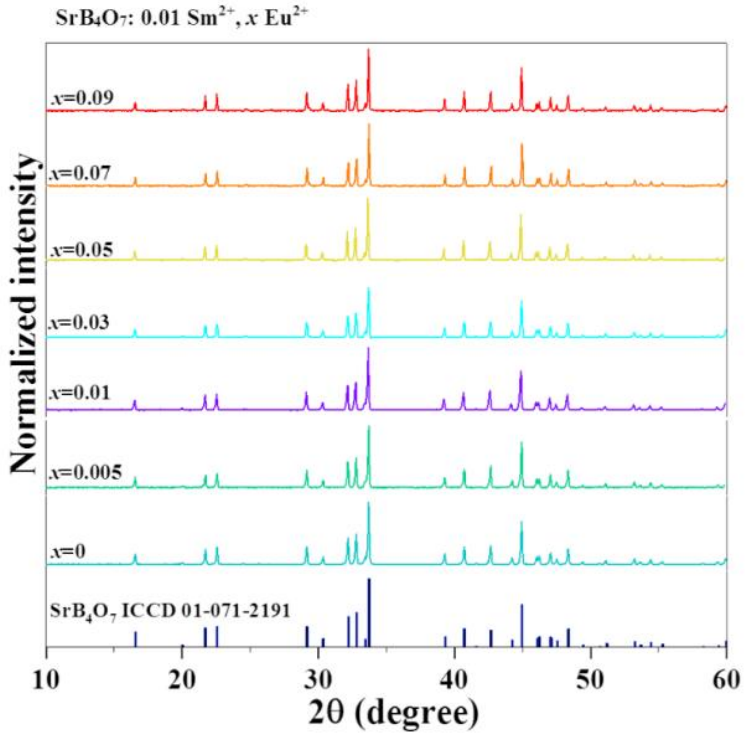

Figure S1 (a) XRD patterns of the SrB_4O_7:0.01 Sm^{2+}, *x* Eu^{2+} (*x*=0, 0.005, 0.01, 0.03, 0.05, 0.07 and 0.09) micro-particles.

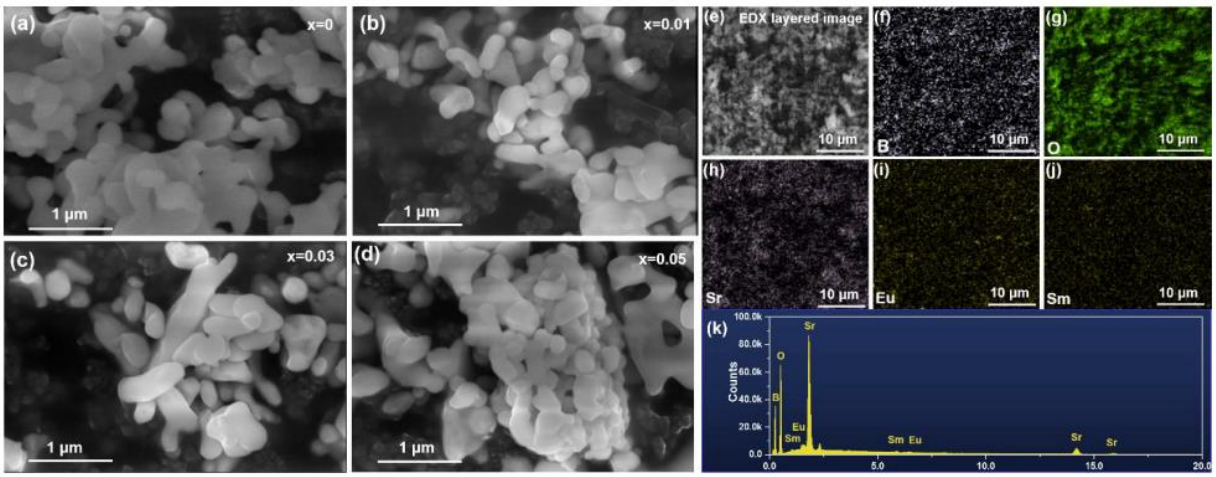

Figure S2. SEM images of SrB_4O_7:0.01 Sm^{2+}, *x* Eu^{2+} micro-particles obtained: (a) *x* = 0, (b) *x* = 0.01, (c) *x* = 0.03 and (d) *x* = 0.05. (e)–(j) Elemental mappings and (k) EDX spectrum of the SrB_4O_7:0.01 Sm^{2+}, 0.03 Eu^{2+} micro-particles.

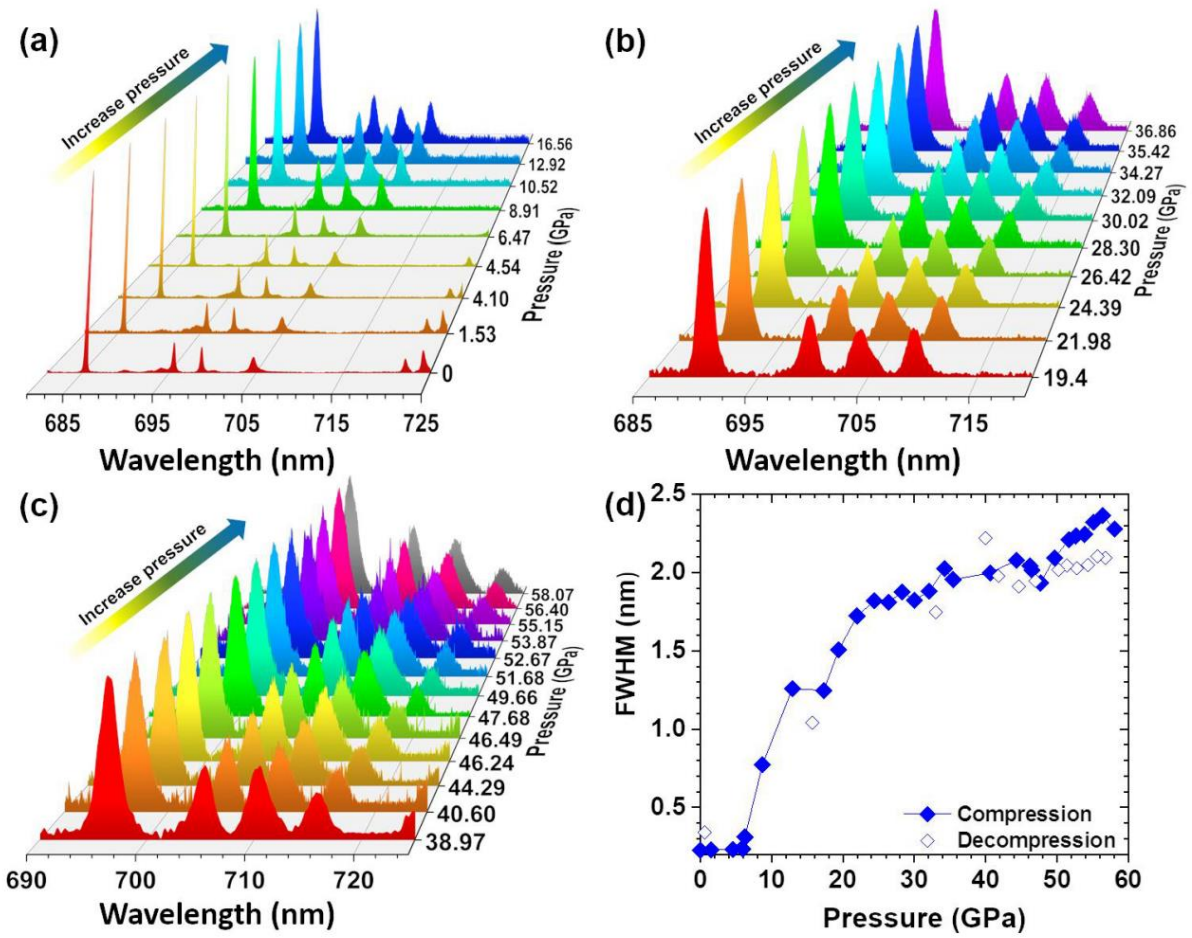

Figure S3. The emission spectra of SrB_4O_7: $0.01Sm^{2+}$, $0.03Eu^{2+}$ micro-particles at every measured pressure (a) 0 - 16.56 GPa, (b) 19.40 - 36.86 GPa and (c) 38.97 - 58.07 GPa normalized at 0-0 line of Sm^{2+}. (d) The linewidth Γ (FWHM) of $^5D_0 \rightarrow {}^7F_0$ emission peaks as a function of pressure. The filled symbols represent the compression and the empty ones decompression data.

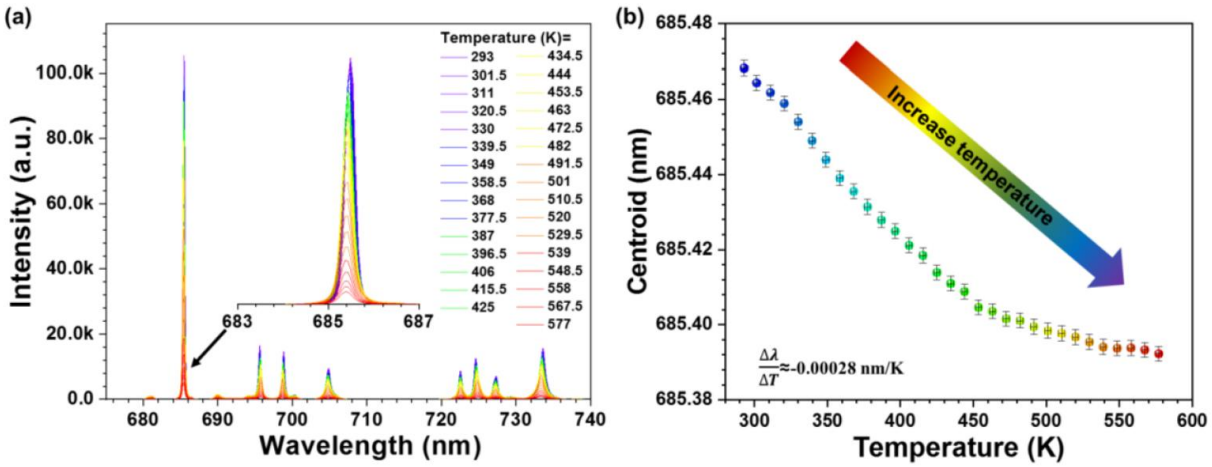

Figure S4 (a) non-normalized emission spectra of Sm^{2+} the SrB_4O_7: $0.03Eu^{2+}$, $0.01Sm^{2+}$ micro-particles at high temperature. The inset of (a) shows the magnified emission spectra of 0-0 line at various temperatures; (b) Peak centroid of 0-0 line of the sample as a function of temperature.

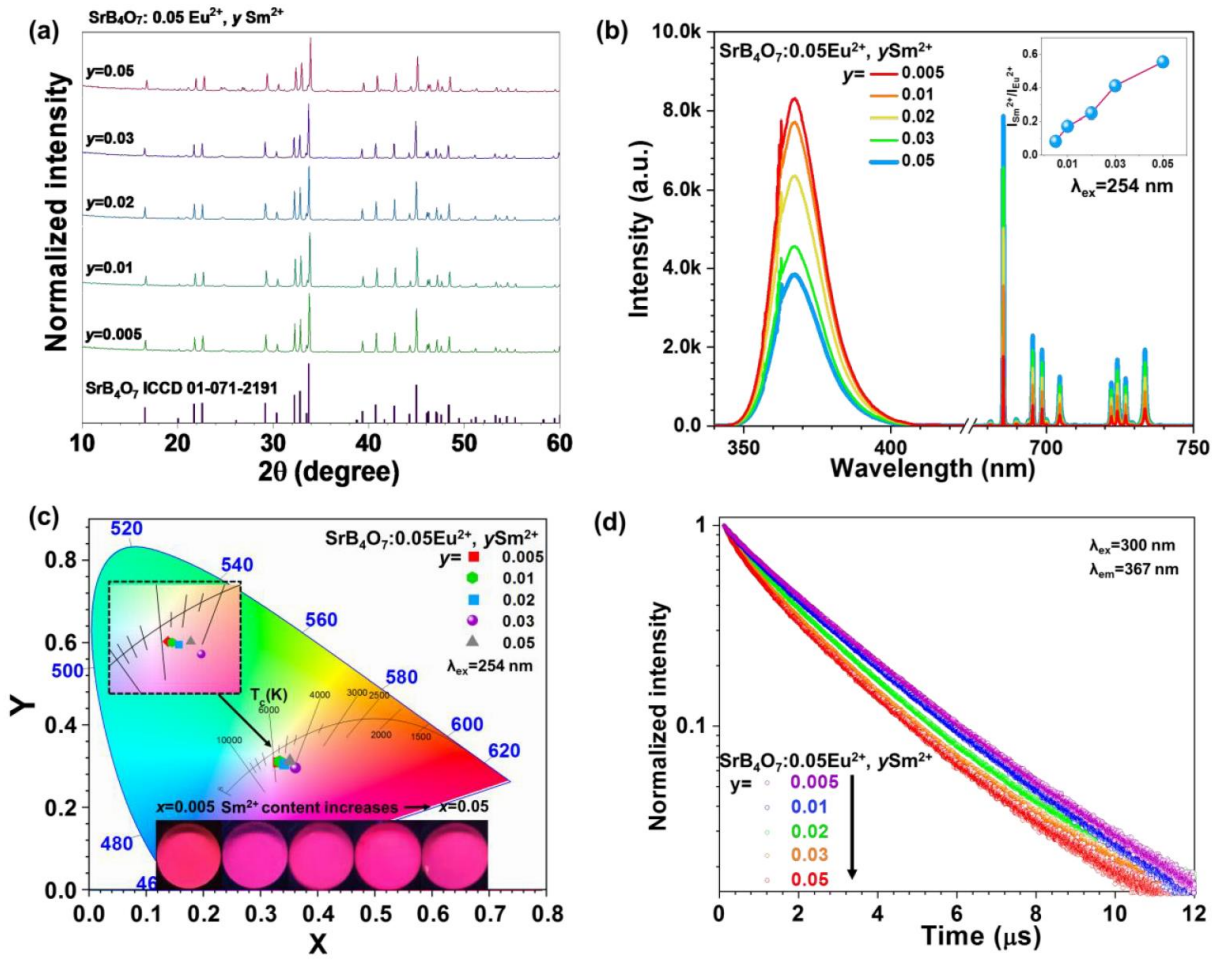

Figure S5 (a) XRD patterns of the SrB_4O_7: y Sm^{2+}, 0.005 Eu^{2+} (y=0.005, 0.01, 0.02, 0.03 and 0.05) micro-particles. (b)The emission spectra with excitation wavelength λ_{ex}=254 nm. The inset of (b) shows the corresponding Sm^{2+}/Eu^{2+} integrated intensity ratio as a function of Sm^{2+} content. (c) CIE chromaticity diagram and luminescent images excited at 254 nm LED light. These samples are white powders at daylight. (d) The luminescence decay curves recorded for the Eu^{2+} ($4f^6 5d \rightarrow 4f^7$ transition) of obtained samples.

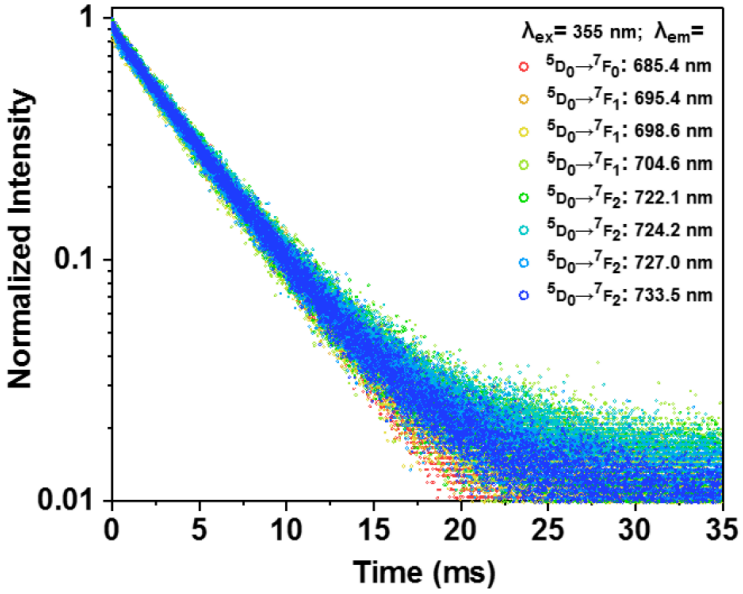

Figure S6. The luminescence decay curves recorded for the Sm^{2+} ($^5D_0 \rightarrow {}^7F_0$, $^5D_0 \rightarrow {}^7F_1$, $^5D_0 \rightarrow {}^7F_2$ transitions) of obtained samples.

Table S1. The integrated emission intensity of Sm^{2+} ($I_{Sm}{}^{2+}$) and Eu^{2+} ($I_{Eu}{}^{2+}$), corresponding multiples of the increase in Sm^{2+} emission at different Eu^{2+} concentration and the integrated intensity ratio of Eu^{2+}/Sm^{2+} ($I_{Eu}{}^{2+}/ I_{Sm}{}^{2+}$) of the SrB_4O_7:0.01 Sm^{2+}, x Eu^{2+} (x=0, 0.005, 0.01, 0.03, 0.05, 0.07 and 0.09) micro-particles.

Eu^{2+} content	0	0.005	0.01	0.03	0.05	0.07	0.09
I_{Eu}^{2+}	0	60241.7	104373.6	140794.4	184633.8	192050.6	200760.0
I_{Sm}^{2+}	119.5	1870.3	3694.5	7211.2	6502.0	6427.7	5808.9
Enhancement	-	15.7	30.9	60.4	54.4	53.8	48.6
I_{Eu}^{2+}/ I_{Sm}^{2+}	-	3.6	3.8	4.2	4.3	4.7	4.3

Table. S2. The determined color coordinates of the SrB_4O_7:0.01 Sm^{2+}, *x* Eu^{2+} (*x*=0, 0.005, 0.01, 0.03, 0.05, 0.07 and 0.09) micro-particles under 254 nm excitation.

Eu^{2+} doping concentration	Color coordinates (x,y)
0	(0.48158, 0.37176)
0.005	(0.32549, 0.30865)
0.01	(0.33005, 0.32013)
0.03	(0.32868, 0.31012)
0.05	(0.32469, 0.3051)
0.07	(0.32691, 0.31423)
0.09	(0.32218, 0.30554)

Table. S3. The determined color coordinates of the SrB_4O_7:0.01 Sm^{2+}, 0.03Eu^{2+} micro-particles under excitation wavelength from 250-350 nm.

excitation wavelength (nm)	Color coordinates (x,y)
250	(0.33001, 0.32544)
280	(0.33547, 0.30388)
300	(0.33822, 0.30787)

320	(0.35061, 0.29726)
340	(0.35453, 0.31118)

Table S4. Calculated spectral positions (peak centroids) of the $^5D_0 \rightarrow {}^7F_0$ and $^5D_0 \rightarrow {}^7F_1$ emission peaks, and the corresponding pressure-induced wavelength shift rates.

	Peak centroid (nm) ambient conditions	Peak centroid (nm) at 58.07 GPa	$d\lambda/dP$ (nm/GPa)
$^5D_0 \rightarrow {}^7F_0$	685.3784	702.3325	0.291959
$^5D_0 \rightarrow {}^7F_1$	695.4777	710.5647	0.259807
	698.7308	716.3253	0.302988
	704.6798	722.3945	0.305058

Table. S5. The determined color coordinates of the SrB_4O_7: y Sm^{2+}, *x* Eu^{2+} (*x*=0.005, 0.01, 0.02, 0.03 and 0.05) micro-particles under 254 nm excitation.

Sm^{2+} doping concentration	Color coordinates (x,y)
0.005	(0.32933, 0.31220)
0.01	(0.33337, 0.31083)
0.02	(0.33986, 0.30815)
0.03	(0.36112, 0.29559)
0.05	(0.35130, 0.31231)

Table. S6. Determined luminescence lifetimes for the emission bands (Stark sublevels) of Sm^{2+}:$^5D_0 \rightarrow {}^7F_0$, $^5D_0 \rightarrow {}^7F_1$ and $^5D_0 \rightarrow {}^7F_2$ transitions in the SrB_4O_7: 0.01 Sm^{2+}, 0.03 Eu^{2+} system, obtained under λ_{ex} = 355 nm.

λ_{em} (nm)	*Transitions*	τ (ms)	R^2
685.4	$^5D_0 \rightarrow {}^7F_0$	4.17 5± 0.009	0.998
695.4	$^5D_0 \rightarrow {}^7F_1$	4.236 ± 0.013	0.996
698.6	$^5D_0 \rightarrow {}^7F_1$	4.243 ± 0.013	0.995
704.6	$^5D_0 \rightarrow {}^7F_1$	4.227 ± 0.006	0.995
722.1	$^5D_0 \rightarrow {}^7F_2$	4.294 ± 0.006	0.996
724.2	$^5D_0 \rightarrow {}^7F_2$	4.342 ± 0.005	0.997
727.0	$^5D_0 \rightarrow {}^7F_2$	4.278 ± 0.006	0.996
733.5	$^5D_0 \rightarrow {}^7F_2$	4.286 ± 0.004	0.998

5.3. Pressure-driven configurational crossover between $4f^7$ and $4f^65d^1$ States – Giant enhancement of narrow Eu^{2+} UV-Emission lines in SrB_4O_7 for luminescence manometry

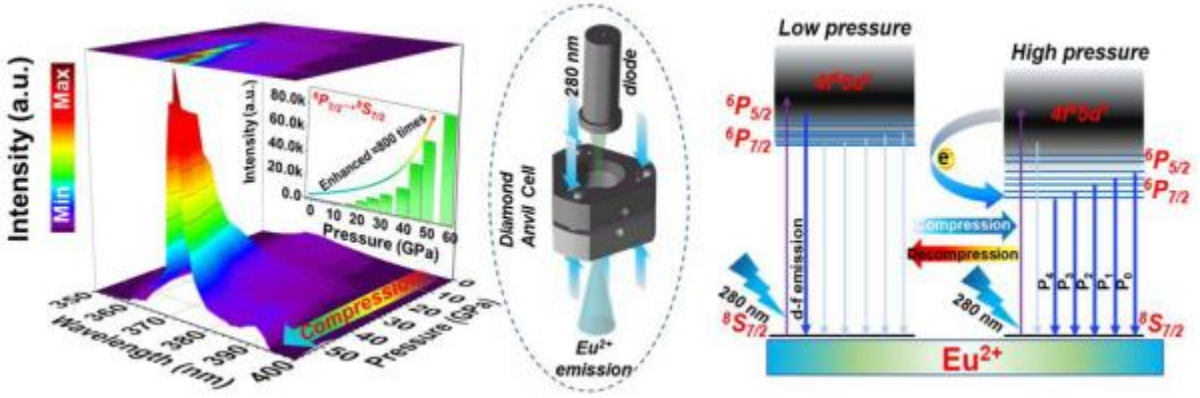

The result in this section were published in: **Teng Zheng**, Marcin Runowski, Plácida Rodríguez-Hernández, Alfonso Muñoz, Francisco J. Manjón, Małgorzata Sójka, Markus Suta, Eugeniusz Zych, Stefan Lis and Víctor Lavín, Pressure-driven configurational crossover between $4f^7$ and $4f^65d^1$ states – Giant enhancement of narrow Eu^{2+} UV-Emission lines in SrB_4O_7 for luminescence manometry, Acta Materialia, 231 (2022) 117886.

Abstract of the section: Accurate, fast, and non-invasive determination of pressure is very important for scientific research concerning the physical and chemical behaviour of materials under high pressure conditions. Luminescence manometry is a promising method for the remote operando pressure determination. However, the limiting bottleneck for high-pressure sensing is the usually occurring quenching of the emission signal of the luminescent sensor material upon compression. In this section, the pressure-triggered intensity enhancement (by 3 orders of magnitude) of the $4f^7$ ($^6P_{7/2}$) $\rightarrow 4f^7$ ($^8S_{7/2}$) emission line of Eu^{2+}, originated from the pressure-induced configurational crossover between the excited $4f^65d^1$ and $4f^7$ energy levels in the SrB_4O_7 host, is shown for the first time. Moreover, the developed pressure sensor shows many excellent pressure sensing performances, i.e., a significant red-shift (~ -12.84 $cm^{-1}GPa^{-1}$; 0.17 nm GPa^{-1}) based on a narrow $4f^7 \rightarrow 4f^7$ transition, great temperature independence of the line position ($4.8 \cdot 10^{-4}$ nm K^{-1}). This novel pressure gauge may significantly increase the accuracy of non-invasive pressure determination and open new horizons for materials science research in an even higher-pressure range.

Contribution of Ph.D. student in this work: Conceptualization, material synthesis, structural and morphological characterization, conduction of the spectroscopic measurements, visualization, data analysis and curation, formal analysis, writing original draft and writing review & editing

Acta Materialia 231 (2022) 117886

Contents lists available at ScienceDirect

Acta Materialia

journal homepage: www.elsevier.com/locate/actamat

Pressure-driven configurational crossover between $4f^7$ and $4f^65d^1$ States – Giant enhancement of narrow Eu^{2+} UV-Emission lines in SrB_4O_7 for luminescence manometry

Teng Zheng[a], Marcin Runowski[a,f,*], Plácida Rodríguez-Hernández[b], Alfonso Muñoz[b], Francisco J. Manjón[c], Małgorzata Sójka[d], Markus Suta[e], Eugeniusz Zych[d], Stefan Lis[a], Víctor Lavín[f,*]

[a] Adam Mickiewicz University, Faculty of Chemistry, Uniwersytetu Poznańskiego 8, 61-614 Poznań, Poland
[b] Departamento de Física, MALTA Consolider Team, and Instituto de Materiales y Nanotecnología, Universidad de La Laguna, Apartado de Correos 456, E-38200 San Cristóbal de La Laguna, Santa Cruz de Tenerife, Spain
[c] Instituto de Diseño para la Fabricación y Producción Automatizada, and MALTA Consolider Team, E.T.S. Ingeniería del Diseño, Universitat Politècnica de València, Cno. de Vera s/n, 46022 València, Spain.
[d] University of Wrocław, Faculty of Chemistry, F. Joliot-Curie 14, 50-383 Wrocław
[e] Inorganic Photoactive Materials, Institute of Inorganic Chemistry, Heinrich Heine University Düsseldorf, Universitätsstr. 1, D-40225 Düsseldorf, Germany
[f] Departamento de Física, MALTA Consolider Team, and IUdEA, Universidad de La Laguna, Apartado de Correos 456, E-38200 San Cristóbal de La Laguna, Santa Cruz de Tenerife, Spain

ARTICLE INFO

Article history:
Received 7 December 2021
Revised 18 February 2022
Accepted 23 March 2022
Available online 25 March 2022

Keywords:
Pressure-enhanced emission
$4f^7 \rightarrow 4f^7$ emission of Eu^{2+}
Strontium tetraborate
optical pressure gauge
luminescent manometer
pressure-induced crossover

ABSTRACT

Accurate, fast, and non-invasive methods for the determination of the local pressure magnitude are crucial for the investigation of the physical and chemical behavior of materials at the extreme conditions of high pressure. A promising method for remote *operando* pressure measurements is luminescence manometry. However, a limiting bottleneck for high-pressure readout is the usually occurring quenching of the emission signal of the luminescent sensor material upon compression. In this work, we reported for the first time the pressure-induced intensity enhancement (by 3 orders of magnitude) of the $4f^7(^6P_{7/2}) \rightarrow 4f^7(^8S_{7/2})$ emission line of Eu^{2+} in the UV range due to pressure-induced configurational crossover between the excited $4f^65d^1$ and $4f^7$ energy levels in SrB_4O_7 host. The peak centroid of the narrow $4f^7 \rightarrow 4f^7$ transition exhibits a significant red-shift ($\sim$ -12.84 cm^{-1} GPa^{-1}; 0.17 nm GPa^{-1}) with simultaneous temperature independence of the line position ($4.8 \cdot 10^{-4}$ nm K^{-1}). The pressure sensitivity of the proposed system is competitive to the so far well-established luminescent pressure sensors based on $Al_2O_3:Cr^{3+}$ (ruby) and $SrB_4O_7:Sm^{2+}$ with characteristic narrow line emission in the red range, and offers an alternative spectral range in parallel with an intensity enhancement at higher pressures. This novel pressure gauge may significantly improve the accuracy of the remote pressure measurements and open up new horizons for materials science research at even higher pressures.

1. Introduction

In recent decades, the implementation of high pressure (HP) in scientific research in many laboratories worldwide led to the discovery of new phenomena, *e.g.*, phase transformations and formation of new materials, as well as an in-depth insight into the intriguing and conclusive mechanisms that have generated great progress in solid-state physics/chemistry, material science, and geophysics [1–3]. In response to external mechanical stimuli such as pressure, considerable changes occur in the material related to a change in the interatomic distances [4], alteration of electronic orbitals [5], *etc* [6,7]. These changes are usually accompanied by alterations in the nature of the chemical bonds and coordination numbers thus leading to other structure types with different electronic properties at HP [8–12]. In this context, the fast and precise monitoring of the locally present pressure is of utmost importance.

In order to precisely monitor pressure values at HP conditions in laboratory and industrial processes, optical pressure gauges, typically based on Cr^{3+} (mostly ruby; $Al_2O_3:Cr^{3+}$) and various lanthanide-doped (mostly Sm^{2+}) materials, have gained great attention, mainly due to their low electronic noise, rapid and non-

* Corresponding authors.
E-mail addresses: runowski@amu.edu.pl, mrunowsk@ull.edu.es (M. Runowski), vlavin@ull.edu.es (V. Lavín).

https://doi.org/10.1016/j.actamat.2022.117886
1359-6454/

invasive detection and chemical durability [13–15]. Most of the established luminescent pressure sensors, including the two previous examples, emit in the red or near infrared range. However, there is still a bottleneck in experimental pressure-sensing techniques based on photoluminescence to significantly improve the accuracy of pressure measurements and widen the pressure sensing range covered by these techniques. The bottleneck is the ubiquitous and progressive compression-induced quenching of emission of lanthanide ($Ln^{3+}/^{2+}$) and transition metal ions (including Cr^{3+} in ruby) accommodated in a host lattice. To the best of our knowledge, this is a notoriously observed effect in all luminescence pressure sensors reported so far [4,16,17].

Among other Ln^{2+} ions, the divalent europium ion (Eu^{2+}) is particularly attractive for its important role in light-emitting diodes (LED) and optical displays, due to its largely tunable, broad $4f^6 5d \leftrightarrow 4f^7$ emission band leading to good color rendering properties. The high sensitivity of the 5d orbitals to the nature of the chemical bond to the surrounding ligands in a host compound makes the photoluminescence of Eu^{2+} highly tunable [18–20] with known examples for emission in the UV-violet [21], blue [22], red [23], and even NIR regions depending on the host matrix [23–27]. Aside from that, the emission of Eu^{2+} associated with the alternatively possible intra-configurational $4f^7$ ($^6P_{7/2}$)→ $4f^7$ ($^8S_{7/2}$) transitions characterized by several sharp, narrow (≈ 1-2 nm width in the wavelength domain) emission lines in the UV range at around 360 nm is only occasionally reported and typically observed in highly ionic host compounds [28–30]. Understanding the control mechanisms of the appearance of this unusual type of luminescence of Eu^{2+} is not only relevant from a fundamental perspective but also important for potential industrial applications [18–23].

Borates, which are naturally deposited in the sediments of ancient lakes or in hydrothermal solutions in the products of the hervidero hotbed, play an irreplaceable role in industrial and scientific fields [31]. Strontium tetraborate (SrB_4O_7) is a well-known material in non-linear optics and luminescence pressure sensing. Its superiority lies mainly in its high non-linear optical coefficients, high optical damage thresholds, neutron sensitivity, wide optical transparency in the UV-vacuum range, with the fundamental absorption edge below 120 nm (∼83 333 cm^{-1}), that extends towards ∼ 3250 nm (∼ 3077 cm^{-1}) in the IR range [32–35]. Due to the rigid three-dimensional network of the corner-linked tetrahedral $(BO_4)^{5-}$ anion structure groups of the boron-oxygen framework, SrB_4O_7 shows excellent stabilization of the divalent lanthanide ions even in air [21]. Huppertz *et al.* reported a HP β-CaB_4O_7 phase, which crystallizes isotypically to SrB_4O_7 in the space group $Pnm2_1$ (no. 31) [36]. Upon doping of Eu^{2+} ions into the SrB_4O_7 crystal structure, Machida *et al.* observed a very efficient broad luminescence band at around 367 nm at room temperature (RT), which is assigned to the $4f^6 5d \rightarrow 4f^7(^8S_{7/2})$ transition of Eu^{2+} [37]. On the other hand, Meijerink *et al.* observed sharp lines caused by the transitions within the $4f^7$ ground configuration at low temperatures [38] and showed that a configuration crossover between the $4f^7$ and $4f^6 5d^1$ configuration of Eu^{2+} can be stimulated by temperature variation, which was confirmed by some of us recently [33]. However, detailed HP studies of Eu^{2+}-doped SrB_4O_7 have never been performed before and offer additional insights into this configuration crossover and its potential use for remote sensing applications.

In this work, we regard the influence of high pressure on the photoluminescence properties of Eu^{2+} in SrB_4O_7. Moreover, we consider the potential of SrB_4O_7 for applications at higher pressures by evaluation of the elastic and mechanical properties of this compound. For that purpose, we performed density functional theory (DFT) calculations under periodic boundary conditions and related the computational results to vibrational spectra at varying pressure. We observed a so far not reported pressure-induced enhancement of the narrow $4f^7$ ($^6P_{7/2}$) → $4f^7$ ($^8S_{7/2}$) emission lines of Eu^{2+}, exhibiting a linear red-shift of ∼ -12.84 cm^{-1} GPa^{-1} (∼ 0.17 nm GPa^{-1}) within the pressure range of ∼ 0 - 60 GPa. The observed pressure-induced enhancement of the emission is beneficial for applications as a pressure gauge, as the UV emission of Eu^{2+} doped into SrB_4O_7 is robust towards quenching effects. Moreover, it does not interfere with the luminescence of most conventional phosphors upon usage as an internal pressure sensor. Overall, the investigation of the pressure-dependent luminescence properties of SrB_4O_7:Eu^{2+} could offer a first step towards the development of an alternative concept in sensitive luminescence manometry.

2. Experimental

2.1. Synthesis and characterization at ambient condition

Details of the synthesis protocol, structural and spectroscopic characterization including X-ray diffraction (XRD) patterns, scanning electronic microscopy (SEM), energy dispersive X-ray (EDX) analysis, as well as luminescence spectroscopy studies at ambient conditions of the SrB_4O_7: Eu^{2+}, Sm^{2+} samples can be found in our previous work [39].

2.2. DAC loading procedure

For high-pressure measurements, we applied a typical Merrill-Bassett diamond anvil cell (DAC), equipped with high-purity IIas diamond anvils (for Raman and fluorescence spectroscopy), purchased from Almax easyLab. The pressure values inside the DAC chamber are adjusted with three metal screws. Stainless-steel sheets (thickness: 250 µm) with an aperture of ∼150 µm (hole size) were applied as gaskets, used for high-pressure experiments in DAC. Before loading the sample, the gaskets were pre-indented down to ∼80 µm (sample thickness). Using a stereo microscope, the sample and a single ruby ball (< 10 µm diameter) was loaded into the DAC chamber, and, subsequently the pressure transmitting medium composed of a solvent system of methanol/ethanol/water (at a volume ratio 16:3:1) was filled in the DAC chamber for maintaining hydrostatic and quasi-hydrostatic conditions during the compression process.

2.3. High-pressure Raman scattering characterization

Raman spectra were recorded in backscattering geometry with a Renishaw InVia confocal micro-Raman system, using a grating with 1800 grooves/mm and a power-controlled 785 nm laser diode. The laser beam was focused using an Olympus x20 SLMPlan N long working distance objective.

2.4. High-pressure Photoluminescence characterization

The photoluminescence characterization at high pressure conditions was performed by measuring the emission spectra (with a resolution of ≈0.1 nm) of the samples placed in the DAC chamber, using an Andor Shamrock 500i spectrometer, equipped with a detector of iDus 420 CCD camera. The applied excitation light source was a 280 nm UV diode, which was focused on the sample in the gasket hole of DAC. The photoluminescence signal was collected in an optimized configuration with 180° detection geometry (back illuminated configuration). The pressure calibration of the system in the DAC chamber was based on the monitored shift of the ruby R_1 fluorescence line, using the standard ruby calibration curve from http://kantor.50webs.com/ruby.htm.

2.5. Low-temperature Photoluminescence characterization

Low-temperature photoluminescence characterization was performed using an FLS1000 Fluorescence spectrometer (Edinburgh Instruments Ltd) with a 450-W xenon arc lamp (excitation light source) and a Hamamatsu R928P high-gain photomultiplier (cooled -20°C). Emission spectra were collected in the temperature range of 11 – 300 K, with a 10 K step. The decay curves were recorded using an EPLED285 (285 nm) picosecond pulsed light-emitting diode and the same FLS1000 spectrometer. The sample for low-temperature measurements was mounted on a Cu-holder of a closed-cycle helium cryostat (Lake Shore Cryotronics, Inc.) using Silver Adhesive 503 (Electron Microscopy Sciences).

3. Overview of the calculations

Ab initio simulations of bulk SrB_4O_7 were performed within the framework of DFT [40], as implemented in the Vienna Simulation package (VASP) [41]. The projector-augmented wave pseudopotential (PAW) [42] was employed to describe the atomic species. Due to the presence of oxygen atoms, a plane-wave energy cutoff of 540 eV was used to obtain accurate results. The exchange-correlation energy was described within the generalized gradient approximation (GGA) with the Perdew-Burke-Ernzenhof prescription for solids (PBEsol) [43]. Integrations over the Brillouin zone (BZ) were carried out with (6×6×2) meshes of Monkhorst-Pack special k-points [44]. Thanks to this procedure, the convergence achieved in the energy was better than 1 meV per formula unit and for a set of selected volumes, the cell parameters, and atomic positions were fully optimized by calculating the forces on atoms and the stress tensor. In the optimized configurations, the forces on atoms were less than 0.002 eV/ Å and the deviation of stress tensor components from the diagonal hydrostatic form - lower than 0.1 GPa. For completeness, electronic band structure calculations were carried out along high-symmetry directions in the first Brillouin zone.

The direct force-constant method was employed to study the lattice vibrations, which is available in http://wolf.ifj.edu.pl/phonon. Lattice dynamic calculations were carried out under pressure at the zone center (Γ point) of the BZ. These calculations also allow identifying the symmetry and eigenvectors of the vibration modes of the considered structures at the Γ point. The supercell method was used to obtain the phonon dispersion and the projected phonon density of states (DOS) using a (2×2×2) supercell.

The elastic constants were evaluated by computing the macroscopic stress for a small strain applying the stress theorem [45,46], as implemented in the VASP code [47]. The mechanical stability and elastic properties of SrB_4O_7 were also studied, since the elastic moduli can be obtained from the calculated elastic stiffness constants.

4. Results and discussion

4.1. Properties at ambient conditions

4.1.1. Structural properties

All details about the conducted experiments are presented in the supporting information (SI) file. As shown in **Fig. S1a-c** in SI, the emission bands of both the $4f^65d \leftrightarrow 4f^7$ and $4f^7 \rightarrow 4f^7$ transitions of Eu^{2+} are clearly observed in the UV range of the emission spectra of SrB_4O_7:$0.01Eu^{2+}$ (without Sm^{2+}) and SrB_4O_7: xEu^{2+}, $0.01Sm^{2+}$ (x=0.005, 0.01, 0.03, 0.05, 0.07 and 0.09) materials. The presence of a small amount of Sm^{2+} ions in the phosphors is related to our previous work on the investigation of the pressure sensing performance of Sm^{2+} in these materials in the visible range upon exploitation of an energy transfer from Eu^{2+} ones [39]. The obtained samples are composed of microcrystalline SrB_4O_7 powder that can be synthesized reproducibly [39]. The morphology of the material was checked by SEM at various magnifications, as shown in Figure S2a-c, confirming the phosphor material is composed of micron-sized particles. First, an additional detailed structural analysis of a representative powder sample SrB_4O_7: $0.03Eu^{2+}$, $0.01Sm^{2+}$ was performed here, as this sample shows a strong emission signal. The structure of SrB_4O_7: $0.03Eu^{2+}$, $0.01Sm^{2+}$ was refined with the Rietveld (whole profiled) method based on the experimental powder X-ray diffraction pattern using the structural model according to diffraction data from the ICDD (card. no. 071-2191) as an input (see Fig. 1**a**) [48]. No traces of additional phases are found. It crystallizes in an orthorhombic structure with the space group $Pmn2_1$ (no. 31) and the Rietveld refinement allows obtaining the following cell parameters and unit-cell volume values: a = 10.7148 Å, b = 4.4428 Å, c = 4.2362 Å, V=201.00 Å^3, and a density of 4.055 g•cm^{-3}, with (R_{wp} = 8.59%; R_{exp} = 3.91%; R_p = 6.45%; g_{of} = 2.2). The error for the determined unit cell parameters (a, b and c) is about ±0.0001 Å. These values are comparable with those found for the bulk crystal (a = 10.724 Å, b = 4.447 Å, c = 4.239 Å, and V = 202.16 Å^3) [49] and those obtained from *ab initio* calculations (see **Table S1** in SI). The collected data are even comparable to those found in the stoichiometric EuB_4O_7 crystal, *i.e.*, (a = 10.731 Å, b = 4.435 Å, c = 4.240 Å, and V = 201.8 Å^3) [50], which is considered due to the similar ionic radii between Eu^{2+} and Sr^{2+}. Additionally, the indexed experimental XRD pattern, clearly showing the matching with the reference ICDD pattern (071-2191), is given in Figure S2d.

According to the Krogh–Moe theory [51], the structure of strontium tetraborate is not a random distribution of BO_4 tetrahedra. Instead, these units are assembled to form well-defined, condensed [B_4O_7] tetraborate groups, building a rigid three-dimensional network with channels parallel to the short crystallographic axes b and c, which leads to the formation of large cavities. All these tetrahedra are distorted and there are two kinds of borate units, [B(1)O_4] and [B(2)O_4], with mean B-O distances of 1.478 Å and 1.486 Å, respectively. In this structure, four independent positions of the O atoms can be found and they can be divided into two groups: O(1), O(2), and O(3) are linked to two B atoms with shorter B-O bonds (< 1.47 Å), while O(4) is linked to three B atoms with longer B-O bonds (> 1.53 Å). The latter is an original motif within the structure compared to other borates. Consequently, it is characterized by considerably elongated, much weaker bonds, *i.e.*, the average B–O(4) distance is 1.55 Å, while the B–O distances for the remaining oxygen atoms range from 1.36 to 1.47 Å.

There are six-membered B–O rings in the borate network parallel to the b axis. The Sr^{2+} cation occupies large cavities formed by these channels and it has only one crystallographically independent site coordinated by nine oxygen atoms, with distances varying from ∼ 2.54 Å to ∼ 2.83 Å. This gives rise to a [SrO_9] capped cube nonahedron with C_S local point symmetry. As mentioned above, the real site symmetry on the Sr sites in SrB_4O_7 is C_s. However, for a luminescent ion with extended and diffuse 5d orbitals such as Eu^{2+}, usually the "experienced" site symmetry of the dopant is somewhat higher. Upon regarding the nine-fold coordinated Sr site in SrB_4O_7, eight oxygen ligands form a slightly distorted cube, while the other oxygen ligand is on the tip and lies on a four-fold rotation axis. This allows an effective C_{4v} site symmetry as the approximation for the doped lanthanide ion [52].

It is noteworthy that the BO_4 tetragonal units surround the channel forming a cage that isolates the divalent lanthanide ions, which is usually considered as the reason for the high stability of the otherwise reactive divalent oxidation state of the lanthanides in this structure [53]. In addition, similar ionic radii values for coordination 6, of Eu^{2+}, Sm^{2+} and Sr^{2+} (R(Sr^{2+}) = 1.18 Å; R(Eu^{2+}) = 1.17 Å; R(Sm^{2+}) = 1.17 Å) [54], facilitate the incorpo-

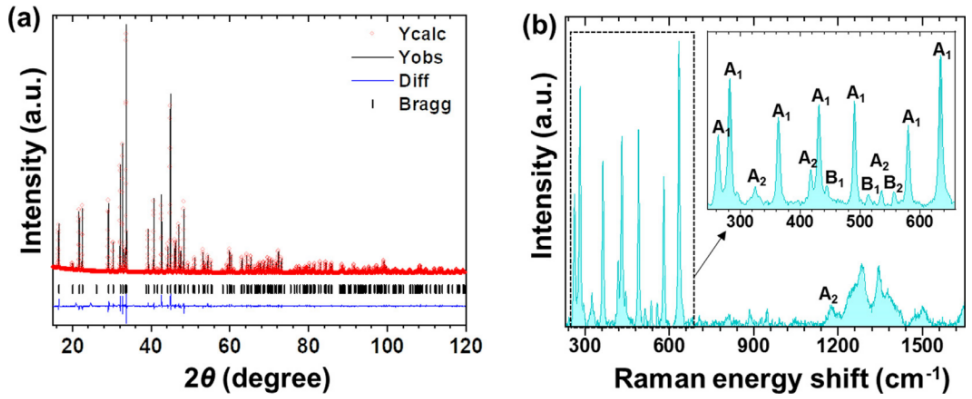

Fig. 1. a) Experimental (black) powder XRD pattern of SrB_4O_7: $0.03Eu^{2+}$, $0.01Sm^{2+}$ and corresponding theoretical (red) XRD pattern. b) Experimental Raman spectrum of the SrB_4O_7: $0.03Eu^{2+}$, $0.01Sm^{2+}$ sample measured at ambient conditions.

ration of the Eu^{2+} and Sm^{2+} into the network substituting Sr^{2+} ions in the nonahedron, without the need for charge compensation [49,50]. Machida *et al.* suggest that the rigid 3D-network of tetrahedral $[BO_4]^{5-}$ ions isolates the Eu^{2+} ions from one another, *i.e.*, it acts as a shield of the Eu^{2+}-Eu^{2+} non-radiative energy transfer processes, and is one of the reasons for the strong Eu^{2+} luminescence in the borate host matrices [37]. Moreover, the high emission energy in the UV range makes non-radiative quenching highly improbable in favor of a high radiative transition probability. Besides, the band gap in a very ionic compound like SrB_4O_7 is expectedly high, which also minimizes the probability for thermally assisted delocalization of the excited 5d electron into the conduction band.

4.1.2. Elastic properties

The elastic properties of SrB_4O_7 were analyzed at ambient pressure based on *ab initio* calculations in order to evaluate its potential as a host compound of luminescent ions for high-pressure applications. SrB_4O_7 crystallizes in an orthorhombic crystal system, which gives rise to 9 independent elastic constants [55]. As presented in **Table S2** in SI, the calculated values of the elastic constants are in better agreement with the experimental values than the calculations based on the non-empirical ionic-crystal model [56,57]. The bulk modulus (B), shear modulus (G), Young modulus (E) and Poisson's ratio (ν), which describe the main elastic properties of a material, can be obtained by analytical expressions from the reference [58] in the Voigt and Reuss approximations assuming uniform stress or strain throughout a polycrystalline compound [59,60]. Hill indicated that the Voigt and Reuss approximations have limitations and pointed out that the actual elastic moduli can be estimated by the arithmetic mean of the two bounds [61]. The elastic moduli of the orthorhombic SrB_4O_7 at 0 GPa are compiled in **Table S3** in SI. The value of the Hill bulk modulus, B_H = 149.33 GPa, agrees well with the value obtained from the theoretical data with the Birch-Murnaghan equation of state [62], *i.e.*, B_0 = 150.17 GPa. This fact indicates a high reliability of the calculated elastic constant values and the consistency of calculations.

The bulk modulus (B =149.33 GPa) can be considered as a measure of the resistance to volume changes and the shear modulus (G = 123.22 GPa) - as a measure of resistance to reversible deformations upon shear stress. Therefore, this material is more resistant to compression than to shear stress. The B/G ratio introduced by Pugh describes the relationship between the plastic properties and the elastic moduli of materials [63]. If $B/G > 1.75$, the material exhibits ductility. Otherwise, the material is classified as brittle. At 0 GPa, the B/G ratio of SrB_4O_7 is around 1.2 and would thus, be classified as brittle at ambient conditions. Poisson ratio provides information about the characteristics of the bonding forces, and the value of $\nu = 0.25$ is considered as the lower limit of the central forces in the solid [62]. The investigated compound has a Poisson ratio of $\nu = 0.176$ that agrees with the previously described brittle nature of the solid. It indicates a low degree of elasticity of crystalline SrB_4O_7, which is a consequence of the very strong ionic bonds and highly condensed network of $[BO_4]^{5-}$ tetrahedra within the crystal structure. The elastic anisotropy is one of the most important elastic properties of materials for both engineering and crystal physics, since it is related to the possibility of inducing micro-cracks in materials [64]. This property is quantified by the universal elastic anisotropy index A_U. The more this index differs from 0, the more elastically anisotropic the structure is [65]. The A_U at 0 GPa is 0.071, further indicating that SrB_4O_7 is slightly anisotropic, in agreement to the orthorhombic crystal system it crystallizes in at ambient pressure.

To conclude this section, the average sound wave velocity (v_m= 6110.63 m s^{-1}) within the Debye approximation was calculated. From the shear modulus G and the bulk modulus B, longitudinal (v_l = 8851.89 m s^{-1}) and transverse (v_t = 5548.85 m s^{-1}) elastic wave velocities can be obtained [66]. The Debye temperature (θ_D), a fundamental parameter that correlates with the mechanical and thermodynamic properties of a solid such as specific heat capacity and melting temperature, can be estimated from the average wave velocity [67]. For SrB_4O_7, we find a value of θ_D = 895.11 K, which is perfectly well related to the previously indicated rigid structure with the highly condensed $[BO_4]$-based network. A high Debye temperature is a usually beneficial material property [68] for a host compound for luminescent ions, as is e.g., demonstrated by the thermally stable red-emitting phosphors $Sr[LiAl_3N_4]:Eu^{2+}$ (SLA:Eu^{2+}) [20] and $Sr[Li_2Al_2O_2N_2]:Eu^{2+}$ (SALON:Eu^{2+}) [19].

4.1.3. Vibrational properties

The unit cell of SrB_4O_7 gives rise to 72 normal vibrational modes in the center of the Brillouin zone (19 A_1 + 17 A_2 + 17 B_1 + 19 B_2), which are all Raman-active. Since A_1, B_1, and B_2 are polar modes, they are also IR-active and can exhibit a transversal optical – longitudinal optical (TO-LO) splitting of vibrational modes in the Raman and IR spectra. Therefore, 69 TO modes and 52 LO modes could potentially appear in the Raman spectrum. Fig. 1**b** depicts the Raman spectrum at RT measured in backscattering geometry, and it mainly contains lines due to the A_1 and A_2 modes by means of the Raman selection rules. It exhibits 13 Raman-active modes in the lower-energy range, from 200 to 700 cm^{-1}, *i.e.*, the modes at around 263, 283, 325, 364, 417, 431, 445, 491, 514, 536, 557, 580 and 635 cm^{-1}. These modes agree well with

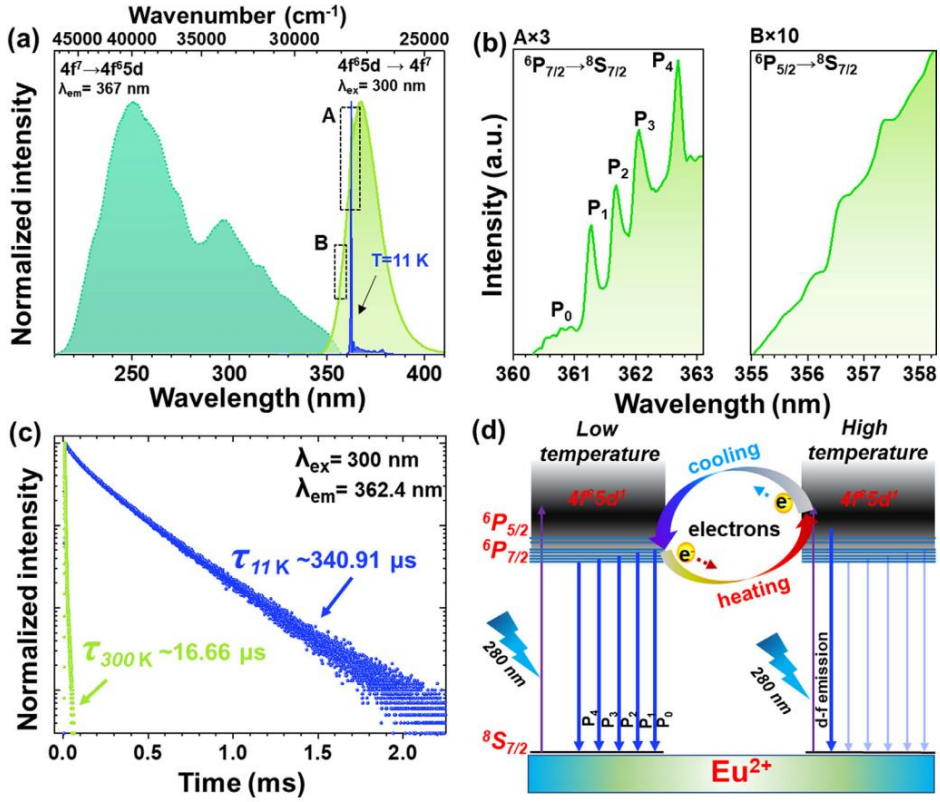

Fig. 2. a) Photoluminescence excitation (dark green area) and emission (light green area) spectra of Eu^{2+} in the SrB_4O_7 matrix at ambient conditions. For comparison, the emission spectrum (blue) measured at 11 K is also included. b) The magnified fine structure of the emission bands (at RT) attributed to the $4f^7 \rightarrow 4f^7$ transitions of Eu^{2+}, *i.e.*, $^6P_{7/2} \rightarrow {}^8S_{7/2}$ (left) and $^6P_{5/2} \rightarrow {}^8S_{7/2}$ (right). c) Luminescence decay curves measured at 11 K and 300 K, at λ_{ex} = 300 nm, λ_{em} = 362.4 nm. d) A simplified diagram of the energy levels for Eu^{2+} in the SrB_4O_7 matrix, at low- and high-temperature conditions.

the A_1 and A_2 modes reported in ref. [69], except for the mode at 445 cm^{-1} that could be assigned to a B_1 mode. In fact, most of the Raman modes of high (low) intensity can be ascribed to modes transforming like A_1 (A_2) [57,69], with A_2 modes only allowed for backscattering configuration with crossed polarization. However, taking into account our theoretical calculations, the modes at 445, 514 and 557 cm^{-1} may be correspondent to B_1, B_1, and B_2 modes, respectively (see **Table S4**). In isostructural PbB_4O_7, three similar modes have been associated with the bending mode (ν_4) of free tetrahedral [BO_4] units, the stretching mode (ν_5) of metaborate ring groups, and the stretching mode (ν_1) of the [BO_4] units [70]. In addition, Raman spectra in the 1100-1750 cm^{-1} range consist of 5 broad bands centered at 1172, 1282, 1346, 1498, and 1651 cm^{-1}, respectively. Only the first one is close to the A_2 mode reported at 1167 cm^{-1} in ref. [69], and this is attributed to the B-O stretching vibration [71].

Fig. S3 in SI shows the calculated total one-phonon density of states (1-PDOS) and the partial 1-PDOS for each atom. It can be observed that low-frequency modes below 200 cm^{-1} are dominated by the movement of Sr atoms. Mid-frequency modes, between 200 and 800 cm^{-1}, are dominated by the vibration of O atoms with some contribution of B atoms above 500 cm^{-1}. Finally, the high-frequency modes above 800 cm^{-1} are dominated by vibrations of B atoms, with some contribution of O atoms. The vibrational modes of AMO_4 compounds were discussed in terms of internal and external modes of rigid [MO_n] polyhedra [72,73]. Similarly, $A_xB_4O_7$ borates could be discussed in terms of internal and external modes of [B_2O_7] units or in terms of the internal and external modes of [BO_4] units, since [BO_4] polyhedra constitute the rigid units of these compounds [74–76].

4.1.4. Photoluminescence Properties

The optically active Eu^{2+} ion is isoelectronic to Gd^{3+} and has an $^8S_{7/2}$ ground level arising from the $4f^7$ configuration. The main difference between them is the lower charge of the Eu^{2+}, which makes it more covalent and, hence, leads to a smaller energy gap between the first excited $4f^65d^1$ and the $^8S_{7/2}$ ground level than for the Gd^{3+} ion. The energy level diagram of the Eu^{2+} is quite simple, *i.e.*, the $^8S_{7/2}$ ground level with a large energy gap of around 27000 cm^{-1} to the lowest excited level, and the ^6P_J, ^6I_J, and ^6D_J excited multiplets of the $4f^7$ ground configuration. The $4f^7 \rightarrow 4f^7$ emissions are characterized by typical decay times ranging from hundreds of microseconds to several milliseconds [77,78]. The $4f^65d^1$ levels, often obscuring the excited levels of the 4f configuration (because the lowest energy of the $4f^65d$ configuration in Eu^{2+} is usually lower than the energy of the ^6P_J levels), give rise to $4f^65d^1 \rightarrow 4f^7(^8S_{7/2})$ emission, which shows much faster decay times in the order of 1 μs. A detailed discussion of the Eu^{2+} energy level diagram can be found in ref. [79].

The Eu^{2+} excitation spectra at RT typically consist of broad bands associated to parity-allowed, inter-configurational electronic transitions between the $^8S_{7/2}$ ground level of the $4f^7$ configuration and the multiplets of the $4f^65d^1$ excited configuration [80,81]. In the emission spectrum recorded at RT, a single broad band corresponding to the $4f^65d^1 \rightarrow 4f^7(^8S_{7/2})$ transition is observed (see

Fig. 2**a**) [21]. While energies of the $4f^7$ levels are hardly influenced by the matrix, as these electrons are shielded by the 5s and 5p electrons, the energies of the $4f^65d^1$ levels are highly sensitive to the magnitude of the crystal-field interaction experienced by the Eu^{2+} ions in the host lattice and the degree of bond covalency [82]. Thus, the emission energy associated with the parity-allowed $4f^65d^1 \rightarrow 4f^7(^8S_{7/2})$ transitions may vary, for example, from 367 nm in SrB_4O_7 [37,38] to e.g., 733 nm in CaO [83].

The excitation spectrum of Eu^{2+} ions in SrB_4O_7 tetraborate is presented in Fig. 2**a**. In the excitation spectrum, two components can be distinguished as two intense, broad bands in the UV range, starting from about 210 nm ($\sim$ 47619 cm^{-1}) to 355 nm ($\sim$ 28169 cm^{-1}) and peaked at around 251 and 297 nm [37,38,84], in agreement to the pioneering findings by Meijerink *et al.*[38]. Given the low approximate C_{4v} site symmetry at the Sr sites in SrB_4O_7, which leads to a splitting of the 5d orbitals into four components (transforming like $a_1(z^2) + b_1(x^2\text{-}y^2) + b_2(xy) + e(xz, yz)$), which additionally couple to the six 4f electrons in the excited configuration, the excited energy level landscape of Eu^{2+} in this compound is very dense and does not readily allow unambiguous assignments of the excitation bands.

Concerning the luminescence, if the lowest states of the excited $4f^65d^1$ configuration are at the higher energies than the excited $4f^7$ multiplets, narrow intra-configurational $4f^7 \rightarrow 4f^7$ emission lines from the $^6P_{7/2}$ [30,85–92], $^6P_{5/2}$ [30,88,93] and $^6I_{7/2}$ [94] multiplets to the $^8S_{7/2}$ ground state can be observed. According to Blasse [87], such a situation can be easily found in host matrices with hard anions giving rise to ionic Eu-ligand bonds, such as fluorides. However, other conditions must also be fulfilled, *i.e.*, a small crystal-field splitting of the 5d orbitals of Eu^{2+}, and a small Stokes shift of the broad band emission, associated with the slight difference between the equilibrium positions of the $^8S_{7/2}$ ground state and the lowest $4f^65d$ state in the configuration coordinate model. In addition, Ryan *et al.* also considered the existence of a small exchange interaction between the six 4f electrons and the 5d one of the excited configurations as another condition to be taken into account [79]. As already mentioned, these conditions usually occur in fluoride matrices [95], but some oxide hosts, such as $SrBe_2Si_2O_7$, $BaBe_2Si_2O_7$, SrB_4O_7, and $SrAl_{12}O_{19}$ [38,96,97], also show these characteristics. In the case of SrB_4O_7, it is worth noting that the formally trivalent B^{3+} ions located in the neighborhood of the Eu^{2+} ions, are small ions with a high charge density and, thus, additionally withdraw electron density from the O^{2-} ligands. Due to the high B:Sr ratio in SrB_4O_7, the Eu-O bond has an overall high ionic character, which is connected to a small exchange interaction between 4f and 5d electrons [38]. Moreover, the rigid network in the crystal structure (also leading to the high Debye temperature) renders the Stokes shift of the $4f^65d^1 \rightarrow 4f^7(^8S_{7/2})$-related emission small [87,98].

It is essential to mention that although these calculations give values for the crystal-field strength and the splitting of the multiplets are more significant than those found in fluoride host matrices, they are still lower than those typically found in oxide hosts. Thus, the Eu^{2+} ions replace the Sr^{2+} ones located in the large cavities formed by the interconnected $[BO_4]$ tetrahedra, and the crystal-field interaction by the lanthanide ion is weak given the large coordination number of 9. This results in low splitting of the multiplets of the $4f^7$ ground and the $4f^65d$ excited configurations. In addition, the highly condensed borate network in SrB_4O_7 and the electron-withdrawing nature of the various B^{3+} ions make the oxygen ligands chemically hard and lead to a rather ionic Eu-O bond. With decreasing Sr/B ratio such as in $Sr_3(BO_3)_2$:Eu^{2+} (emission at 590 nm) or the extreme case of SrO:Eu^{2+} (emission at 625 nm), the $4f^65d^1 \rightarrow 4f^7$ transition of Eu^{2+} systematically shifts to lower energies in agreement with the expectation of a more covalent Eu-O bond. Meijerink *et al.* found in Eu^{2+}-doped SrB_4O_7 that the lowest state of the $4f^65d$ first excited configuration is only $\sim$ 130 cm^{-1} above the lowest Stark state of the $^6P_{7/2}$ level [38]. This low value offers the possibility to investigate a stimuli-induced configuration crossover.

The photoluminescence spectrum in the UV region from $\sim$ 345 to $\sim$ 410 nm upon the excitation at 300 nm is depicted in Fig. 2**a, b** and supports the above argument. At 11 K, it consists of a single sharp line at 362.4 nm (Fig. 2**a**; blue area), at a similar wavelength reported by Meijerink *et al.*, [38] and can be assigned to the $4f^7 \rightarrow 4f^7$ intra-configurational transitions between the two lowest Stark levels of the $^6P_{7/2}$ and $^8S_{7/2}$ multiplets of the Eu^{2+} ions. In addition, this peak is accompanied by vibronic sidebands on the low energy (long wavelength) side (see **Fig. S4** in SI). These bands simultaneously involve the emission of the $^6P_{7/2} \rightarrow ^8S_{7/2}$ electronic transition of the Eu^{2+} ion and vibronic replicas based on coupling to vibrational modes of the host [99]. The luminescence decay curve depicted in Fig. 2**c** additionally proves the expected forbidden nature of this sharp line for a $4f^7 \rightarrow 4f^7$ transition based on the large effective lifetime ($\tau_{eff} = \int t \cdot I \, dt / \int I dt$), of $\tau_{11\ K} \approx$ 340.9 µs compared to the otherwise shorter decay time of the $4f^65d^1 \rightarrow 4f^7(^8S_{7/2})$ broad-band emission of $\tau_{300\ K} \approx$ 16.66 µs.

In order to better understand the mechanism of the Eu^{2+} emission at RT, the normalized emission spectra with increasing temperature values from 11 K to 200 K were acquired and are shown in **Fig. S5a** in SI. The Eu^{2+} emission spectrum changes strongly with temperature. Just above 20 K, one can observe not only a sharp peak at 362.4 nm, but also new sharp features at higher energies (shorter wavelengths) together with the underlying broad-band peak at $\sim$ 367 nm, due to the thermally induced population of the upper $^6P_{7/2}$ Stark states and the lowest levels of the $4f^65d$ excited configuration, respectively, as shown in the simplified energy level diagram in Fig. 2**d**. The relative intensity of this broad band dramatically increases with temperature, not only masking the vibronic sidebands but also partially the other sharp peaks ($4f^7 \rightarrow 4f^7$ emission lines). That is why the emission spectrum at RT is the result of a convolution of Eu^{2+}-related radiative transitions of different nature, *i.e.*, the intense $4f^65d^1 \rightarrow 4f^7(^8S_{7/2})$ inter-configurational, broad-band emission, with a maximum at around 367 nm ($\sim$ 27248 cm^{-1}), and a group of five superimposed narrow and weak $4f^7(^6P_{7/2}) \rightarrow 4f^7(^8S_{7/2})$ intra-configurational emission lines in the range from 360 to 363 nm. In addition, there are emission peaks observed at around 357 nm, which are plausibly related to the $4f^7(^6P_{5/2}) \rightarrow 4f^7(^8S_{7/2})$ transition. The difference in energy between the vibronic bands and the sharp line corresponds to the energy of one phonon and range from 200 to 1200 cm^{-1}, *i.e.* they cover almost all vibrational modes analyzed in this matrix [38]. Fig. 2**b** presents the magnified A and B area marked in Fig. 2**a**, and shows the detailed structure of this emission represented by five sharp lines. They center at 360.9 nm ($\sim$ 27708 cm^{-1}), 361.4 ($\sim$ 27670 cm^{-1}), 361.8 ($\sim$ 27639 cm^{-1}), 362.1 ($\sim$ 27616 cm^{-1}) and 362.7 nm ($\sim$ 27571 cm^{-1}), labelled as P_0 to P_4, respectively. The P_0 peak corresponds to the zero-phonon line of the broad band $4f^65d^1 \rightarrow 4f^7(^8S_{7/2})$ inter-configurational emission, whereas P_1 to P_4 are associated with the transitions from the four crystal-field (Stark) sublevels of the $^6P_{7/2}$ multiplet to the $^8S_{7/2}$ ground level. The total splitting is in the order of $\sim$100 cm^{-1}. The $^8S_{7/2}$ level only shows negligible crystal field splitting (< 1 cm^{-1}) based on its single orbital degeneracy ($2L + 1 = 1$) and the solely intermediate degree of spin-orbit coupling that makes L still a well-defined quantum number [100]. Meijerink *et al.* have presented a schematic configurational coordinate diagram for Eu^{2+} in SrB_4O_7, justifying the presence of emission peaks at low temperature and showing the energy difference between the high-

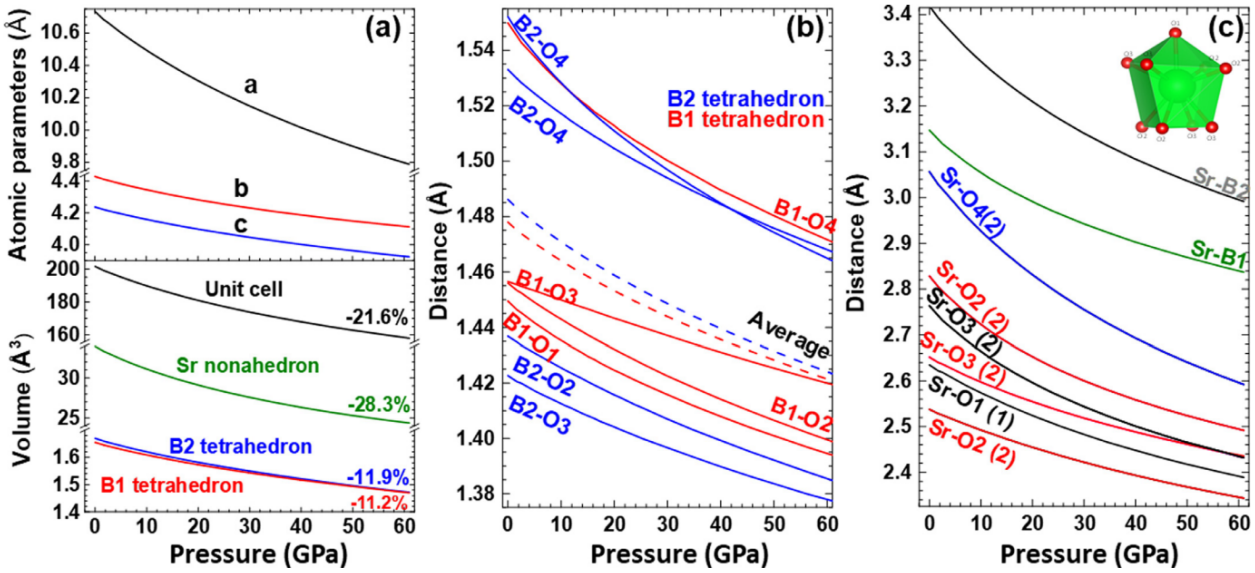

Fig. 3. Pressure dependence of a) cell parameters (top); unit cell volume, [SrO_9] polyhedron and [BO_4] tetrahedra (bottom) of SrB_4O_7 based on *ab initio* calculations. b, c) Evolution of atomic bonds in the polyhedral units based on *ab initio* calculations. The [SrO_9] coordination unit is displayed as an inset at the top of c).

est $^6P_{7/2}$ Stark level and the ground state of the $4f^65d$ configuration of 130 cm^{-1} [38]. They also determined a Stokes shift of 750 cm^{-1} for the $4f^65d^1 \rightarrow 4f^7$transition. Another interpretation could be that the $P_{0\text{-}4}$ lines are related to the one-phonon repetition of the zero-phonon line [90,92]. However, the theoretical calculations of the lowest phonon energies showed only six Raman and IR active phonon modes ranging from 95 to 150 cm^{-1} (see **Table S5**), which do not match well the (P_1-P_0=) 38 cm^{-1}, (P_2-P_0=) 69 cm^{-1}, (P_3-P_0=) 92 cm^{-1}, and (P_4-P_0=) 137 cm^{-1} energy differences found in the emission spectrum. Hence, this assignment is doubtful.

As a conclusion, SrB_4O_7 tetraborate fulfills all the requirements formulated by Blasse to allow emitting both inter- and intra-configurational electronic transitions [87]. At low temperature and under direct excitation, the $4f^7(^6P_{7/2}) \rightarrow 4f^7(^8S_{7/2})$ emission peaks are dominant, while a broad-band emission due to the $4f^65d^1 \rightarrow 4f^7$ transition is observed at higher temperatures [38]. Furthermore, no emission from Eu^{3+} ions above 580 nm was observed, but features related to the additionally present Sm^{2+} ions appeared above ~ 685 nm, which were already presented and discussed in our previous work [39].

4.2. Properties at high pressure

4.2.1. Structural and elastic properties

In order to definitively clarify the impact of high pressure on the crystal structure, mechanical and vibrational properties of orthorhombic SrB_4O_7, we have carried out *ab initio* calculations. In this system, the strontium atoms are positioned in the nine-fold coordinated polyhedron in a rigid three-dimensional [B_4O_7] network of vertex-sharing [BO_4] tetrahedra. The *ab initio* atomic coordinates and cell parameters at 61 GPa pressure are compared to the values at zero pressure in **Table S1**. The evolution of the unit cell parameters and volume as a function of pressure in the $Pmn2_1$ structure of SrB_4O_7 is displayed in Fig. 3**a (top)**. All the cell parameters decrease with increasing pressure from 0 to 60 GPa, although the *a* axis is more compressible than the other two axes, indicating that compression of the structure is anisotropic under hydrostatic pressure. The linear axial compressibility (K_i) of the crystal axis can be calculated using the following equations:

$$K_a = \frac{-1}{a_0}\frac{da}{dp};\ K_b = \frac{-1}{b_0}\frac{db}{dp};\ K_c = \frac{-1}{c_0}\frac{dc}{dp} \quad (1)$$

Using equations (1), we obtained K_a=2.15·10^{-3} GPa, K_b =1.77·10^{-3} GPa and K_c=1.75·10^{-3} GPa. The evolution of the unit cell volume and the polyhedral units under pressure is shown in Fig. 3**a (bottom)**. It was found that there is a decreasing tendency and no volume discontinuity during compression. The compression of the unit cell is dominated by the softer polyhedral unit, in this case, the strontium nonahedron, which decreases its volume by ~ 28.3% in the studied pressure range. This is a consequence of the continuous decrease of the bond lengths (B-O, Sr-O, and Sr-B) upon compression (see Fig. 3**b** and **c**).

In addition, we investigated the evolution of the electronic bandgap under pressure by DFT calculations. The *ab initio* calculated electronic band structures along the high symmetry directions in the first Brillouin zone at 0 GPa and 54 GPa are displayed in Fig. 4**a and** 4**b**, respectively. The band structures show a typical semiconductor-like distribution. The bands are very flat with little dispersion, which agrees with the very ionic nature of the chemical bonds in SrB_4O_7 that lead to highly localized and polarized states in real space and consequently, no covalent and extended bond formation within the periodic structure of the crystal. The edge of the conduction band (CB) changes with pressure, while the one of the valence band (VB) negligibly alters at the Γ point within the whole pressure range studied.

At zero pressure, the VB maximum is located at the R point, giving rise to a wide indirect band gap (R-Γ) of 7.16 eV. With increasing pressure, this gap increases linearly until approximately 9 GPa (see Fig. 4**c**). The maximum value of band gap, 7.49 eV, is achieved at 26.2 GPa where the maximum VB is shifted to the U point, and, then, it slowly decreases with increasing pressure. Interestingly, the band structure becomes even less dispersive in reciprocal space at high pressures, which formally implies an even more ionic nature of the chemical bonds in the compound and perfectly agrees with the generally increasing band gap.

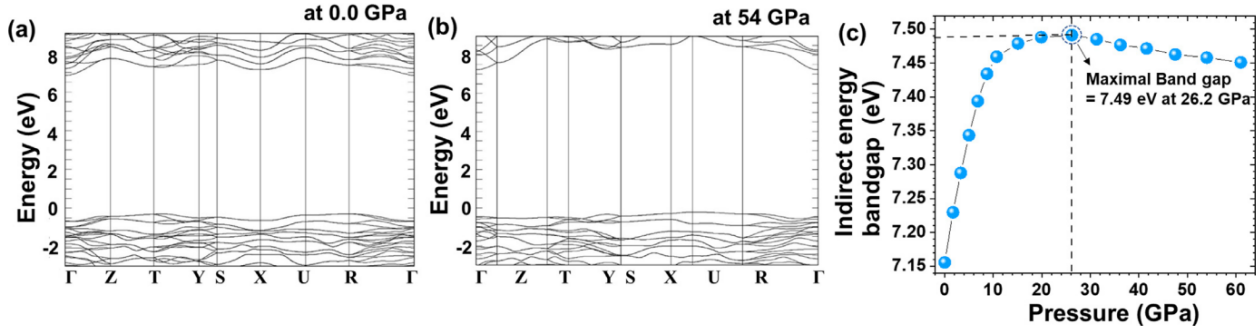

Fig. 4. Electronic band structure of SrB_4O_7 at a) 0 GPa and b) 54 GPa. c) Pressure evolutions of the electronic bandgap

For the sake of completeness, we also analyzed the elastic properties of SrB_4O_7 under pressure. When a non-zero uniform stress is applied to a crystal, the relevant magnitudes describing its elastic properties are no longer the elastic constants (C_{ij}). Instead, the elastic stiffness coefficients (B_{ij}) should be used [101]. In the special case of the hydrostatic pressure, P, applied to the orthorhombic crystal, the elastic stiffness coefficients are related to the elastic constants by the following expressions [101,102]:

$$B_{ii} = C_{ii} - P \quad \text{for } i = 1 \text{ to } 6 \tag{2}$$

$$B_{ij} = C_{ij} + P \quad \text{for } i \neq j \text{ and } i, j = 1 \text{ to } 3 \tag{3}$$

$$B_{ij} = C_{ij} \quad \text{for } i \neq j \text{ and i, } j = 4 \text{ to } 6 \tag{4}$$

with C_{ii} being the elastic constants evaluated at the current stressed state. It should be noted that for zero applied pressure, the B_{ij} values are reduced to the conventional constants C_{ij}.

Fig. 5**a** shows the pressure dependence of the elastic stiffness coefficients, B_{ij}. They increase rapidly with pressure, except of B_{55}, B_{66}, and B_{44}. The coefficients B_{55}, and B_{66} have similar values, while B_{44} remains almost constant in the whole pressure range studied. If the crystal is mechanically stable at zero pressure, the Born stability criteria involving the elastic constants are fulfilled [103]. However, if the crystal is subjected to hydrostatic pressure, the previous criteria should be modified by means of the elastic stiffness coefficients, which leads to a modification of the Born stability criteria. A crystal at elevated pressures is considered mechanically stable if the representation matrix of the elastic stiffness tensor, (B_{ij}), is positive-definite [104]. Our study shows that all the eigenvalues of the matrices B_{ij} are positive; therefore the orthorhombic SrB_4O_7 is mechanically stable up to the maximum pressure (61 GPa) regarded in the present study.

The elastic stiffness constants allow to obtain the elastic properties of the material at any hydrostatic pressure. All the relationships of the theory of elasticity employed at zero pressure can be applied to a crystal subjected to high-pressure compression using the elastic stiffness coefficients B_{ij} [105,106]. The pressure dependences of the B, G, E elastic moduli, Poisson's ratio ν, and the B/G ratio for SrB_4O_7 are shown in Fig. 5**b-d**. The bulk modulus (B) increases rapidly with pressure, while the shear modulus increases only slightly. The B/G ratios are all over 1 from 0 to 61 GPa, which indicates that strontium tetraborate is more resistant to volume compression than to shear deformation. Moreover, the B/G ratio increases rapidly with pressure. At 30 GPa, it is $B/G = 1.77$, and, therefore, the material becomes ductile. Poissonś ratio (ν) corroborates this behavior change. Around 24 GPa, it is $\nu = 0.25$, which appears reasonable since successively higher pressures enforce smaller distances between the different ions, which is partially released by a successive release of strain in the directions orthogonal to the direction of compression. A higher Poisson ratio at elevated pressures indicates that a compound becomes more elastic then, which agrees with the findings on the elastic moduli.

4.2.2. Vibrational properties

We have carried out HP Raman scattering experiments up to ~ 17 GPa, and the Raman spectra at selected pressures are shown in **Fig. S6a**. The signal/noise ratio decreases as the pressure increases, which is a commonly encountered phenomenon. We were able to trace the experimental pressure dependence of the six most intense Raman-active modes of A_1 symmetry during the compression and decompression processes (see Figs. 6, **S6b and S7** in SI). The six observed Raman-active modes of SrB_4O_7 shift monotonously, suggesting no phase transition as the pressure increases up to 16.6 GPa. This agrees with the emission spectra and other reports on SrB_4O_7 under pressure [107,108]. Due to the bond shortening caused by the compression, all the observed Raman peaks show a shift towards the high wavenumbers. As shown in the pressure dependences of the experimental (symbols) and theoretical (lines) Raman-active mode frequencies (see Fig. 6), the experimental data agrees with theoretical calculations up to 16 GPa, *i.e.*, show that all Raman modes have a positive frequency-pressure coefficient (see **Table S5**). As shown in **Fig. S7**, the evolution of the theoretical Raman-active mode frequencies in SrB_4O_7 shows a sublinear pressure dependence up to 25 GPa, which is also confirmed by our experiments up to 16 GPa. However, for the sake of simplicity, in **Table S5** we have included the theoretical zero-pressure linear coefficients obtained from fits to 5 GPa. Similarly, the zero-pressure linear coefficients of the experimental modes centered at 283, 364, 431, 491, 580 and 635 cm^{-1} are 2.8, 2.2, 2.3, 2.3, 1.9 and 2.6 cm^{-1}/GPa, respectively. These pressure coefficients are in good agreement with those of the theoretical $A_1{}^3$, $A_1{}^5$, $A_1{}^6$, $A_1{}^7$, $A_1{}^8$ and $A_1{}^9$ modes (see **Table S5**). It is observed that the modes with smaller pressure coefficients are those with wavenumbers below 640 cm^{-1}, and the modes with the largest pressure coefficients are those with wavenumbers above 740 cm^{-1}.

4.2.3. Photoluminescence properties and pressure sensing performance

The appearance of the emission spectrum of Eu^{2+} in SrB_4O_7 based on dominant emission from the excited $4f^65d^1$ or $4f^7$ configurations depends on different stimuli. As for other divalent lanthanide ions, the most important ones are: I) a temperature-induced excitation from the excited emitting $4f^7$ states to the lowest states of the $4f^65d$ configuration, which may lead to enhancement of the $4f^65d^1 \rightarrow 4f^7$ emission at the expense of the $4f^7 \rightarrow 4f^7$ luminescence, as already observed for the luminescence

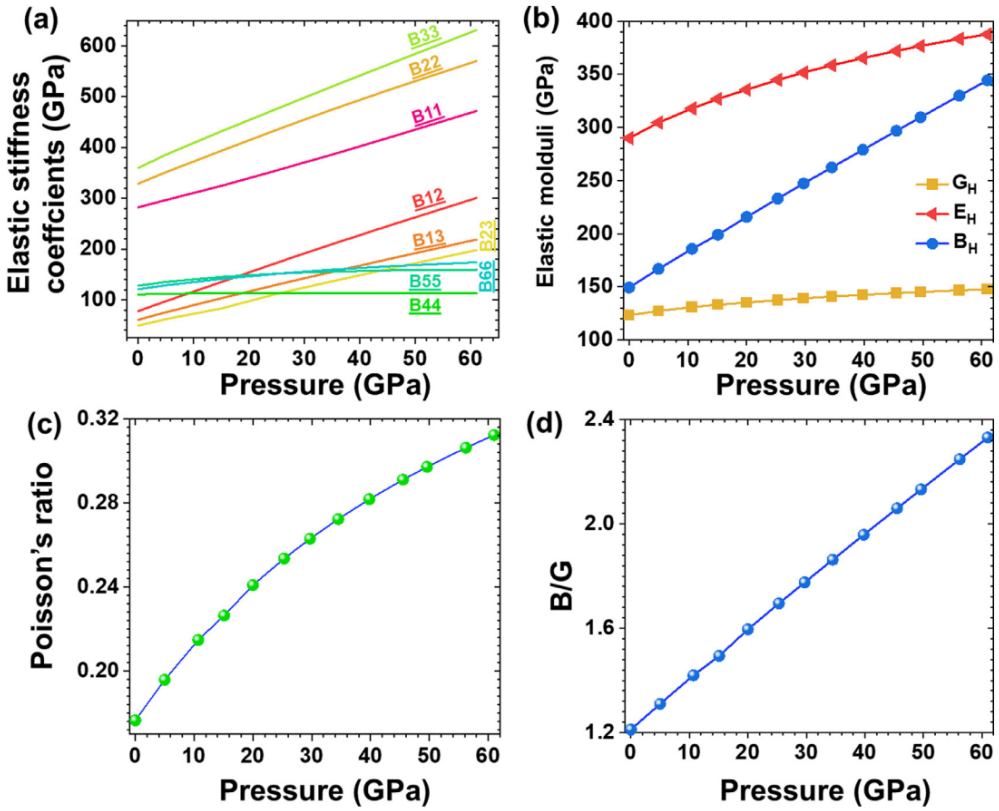

Fig. 5. a) elastic stiffness coefficients (B_{ij}) in SrB_4O_7. b-d) Pressure dependences of *B, E, G* (b), *ν* (c), and *B*/*G* (d) parameters in SrB_4O_7 according to *ab initio* calculations.

in SrB_4O_7:Eu^{2+} above 11 K (see **Fig. S5a, b** in SI) [101]; and II) a pressure-induced tuning of the energy separation between configurations and their respective levels.[109,110] Thus, pressure can increase the mixing of $4f^6 5d$ to $4f^7$ wave functions, with clear impact on the emission probabilities and intensities. However, the specific response of the electronic state to pressure, *i.e.*, the changes in its energy and the probability of absorption, emission, or non-radiative relaxation, depends on the extension of the involved orbitals in the excited states and thus, also the magnitudes of the crystal-field and covalency effects [110].

By focusing on the optical properties of Eu^{2+}, as the pressure increases, the different polyhedral volumes of the matrix decrease, especially the [EuO_9] and [SrO_9] polyhedra that show the largest compression rate, *i.e.*, 28.3 % at 60 GPa with respect to the volume at ambient pressure, as already mentioned. Consequently, the interactions between the seven *f*-electrons, *i.e.*, the free-ion interactions, are affected by the valence electrons of the nine oxygen ligands. In general, the major free-ion interactions, *i.e.*, the Coulomb interelectronic repulsion and the spin-orbit coupling decrease with pressure due to a generally increasing covalency, while the magnitude of the crystal-field interaction increases, albeit with a lower rate. Typical consequences are the decrease of the transition energy (red-shift), due to the overall contraction of the configurations, and the simultaneous increase of the splitting of the multiplets. However, different rates of change are expected for the multiplets of the excited and ground configurations. This is because the variations in the energies of the 4f multiplets are relatively small [109,111], on the order of a few cm^{-1}/GPa, whereas they can be very large for the multiplets of the excited configuration involving *5d* states. These may range from tens to hundreds of cm^{-1}/GPa, as shown in **Table S6** in SI.

In order to investigate the effect of lattice compression on the UV emissions of Eu^{2+} ions in the synthesized micron-sized SrB_4O_7 material, high-pressure photoluminescence experiments were conducted in a diamond anvil cell (DAC) up to ~ 58 GPa at RT. The schematic configuration of the applied DAC and a simplified scheme of the experimental setup used for high-pressure luminescence measurements are presented in Fig. 7**a**. The pressure-induced variations of the relative luminescence intensities of the inter- and intra-configurational transitions of Eu^{2+}, upon the 280 nm light excitation are shown in Fig. 7**b**. The use of 280 nm excitation light (close to the optimal excitation wavelength) is due to the availability of a high-power, focusable light source. The intensity of the broad emission band $4f^6 5d^1 \rightarrow 4f^7(^8S_{7/2})$ gradually decreases up to ~ 35 GPa, above which the band is no longer clearly observed as its intensity is close to the noise level. Inversely, the $4f^7(^6P_{7/2}) \rightarrow 4f^7(^8S_{7/2})$ intra-configurational emission starts to increase in intensity, almost abruptly, above ~ 20 GPa and become the only emissions above ~ 30 GPa, together with broad vibronic bands, already observed in the normalized emission spectra at low temperature in **Fig. S5a, b** in the SI. The emission intensities of the $4f^7(^6P_{7/2}) \rightarrow 4f^7(^8S_{7/2})$ peaks (P_4 peak) were estimated by Gaussian deconvolution (Gaussian fitting) using the integrated peak area of the Gauss bands with abscissa of wavelength (in nm) as a measure for that. Over the entire measured high-pressure range, the intensity enhancement of the $4f^7(^6P_{7/2}) \rightarrow 4f^7(^8S_{7/2})$ peak is estimated to be about three orders of magnitude (~800 times), as depicted in Fig. 7**d** and the histogram in the inset of Fig. 7**d**. In addition, as shown in **Fig. S8** in SI, the Eu^{2+} emission band changes back to its initial shape, and the $4f^7 \rightarrow 4f^7$ emission intensity also returns to its initial intensity upon compression, confirming that the tendency in the intensity change of both $4f^7 \rightarrow 4f^7$ and $4f^6 5d^1 \rightarrow 4f^7$

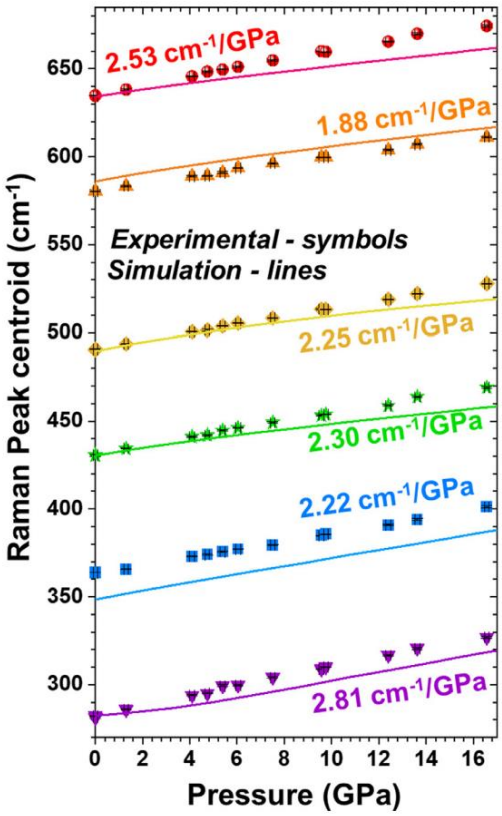

Fig. 6. Pressure dependences of the experimental (symbols) and theoretical (solid lines) Raman-active mode wavenumbers.

emissions of Eu^{2+} in the sample is reversible in compression and decompression cycles.

The $4f^7 \rightarrow 4f^7$ emission peaks also show a fully reversible red-shift under pressure (see Fig. 7**c**), due to the overall contraction of the $4f^7$ ground configuration, which results in a reduction of the energetic separation between the ground state and the excited $^{2S+1}L_J$ multiplets, as shown in the simplified energy level diagram in Fig. 7**e**. The peak centroid of the Eu^{2+} transition $^6P_{7/2} \rightarrow {}^8S_{7/2}$ (P_4) reversibly shifts from 362.1 nm at ambient conditions to ~372.4 nm at 58.7 GPa, with a rate of -12.84 cm^{-1}/GPa (or 0.17 nm/GPa), being comparable to the pressure sensitivity of the wavelength of the $^5D_0 \rightarrow {}^7F_0$ transition of Sm^{2+} in this matrix [39]. It is of great importance that the position of the peak centroid of the $^6P_{7/2} \rightarrow {}^8S_{7/2}$ transition as a function of temperature (see **Fig. S5c**) shows an extremely weak temperature dependence, *i.e.*, $|d\lambda/dT| = 4.8 \times 10^{-4}$ nm K^{-1} (~ -0.037 cm^{-1}/K). The combination of the huge pressure-induced intensity enhancement accompanied by the significant red-shift of the Eu^{2+} $4f^7 \rightarrow 4f^7$ emission lines, and negligible temperature dependence of the corresponding $^6P_{7/2} \rightarrow {}^8S_{7/2}$ transition peak centroid, make the Eu^{2+}-doped SrB_4O_7 material an excellent pressure gauge for high pressures.

In order to examine the validity/reliability of the discussed signal enhancement and explore the influence of different Eu^{2+} contents on the enhancement and red-shift of the P_4 peak, a series of high-pressure photoluminescence experiments were performed using SrB_4O_7 with a higher Eu^{2+} content, *i.e.* 0.09 Eu^{2+} (9 mol.%). As expected, the normalized emission spectra recorded in the pressure range from ~ 1.3 to 34.6 GPa (see Fig. 8**a**) also exhibit a pressure-induced increase in the relative intensity of the $^6P_{7/2} \rightarrow {}^8S_{7/2}$-related peak and decrease in intensity of the $4f^6 5d^1 \rightarrow 4f^7(^8S_{7/2})$ band. As depicted in Fig. 8**b,** the peak centroid of the $^6P_{7/2} \rightarrow {}^8S_{7/2}$ transition continuously shifts to red with increasing pressure at the same rate (0.17 nm/GPa) as in the case of lower Eu^{2+} doping concentrations. Hence, the dopant concen-

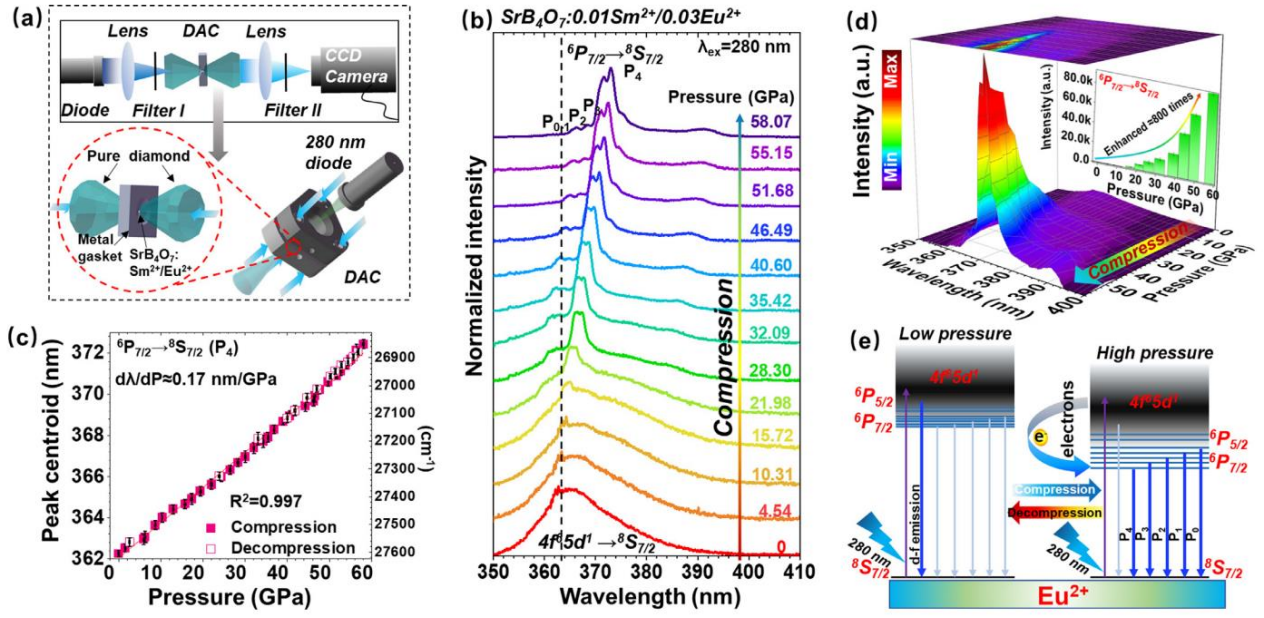

Fig. 7. a) Schematic configuration of a diamond anvil cell (DAC) and the experimental setup used for high-pressure luminescence measurements. Filter *I* and *II* is the optical short pass filter and long pass filter, respectively. b) Selected, normalized UV emission spectra of the SrB_4O_7: 0.03Eu^{2+}, 0.01Sm^{2+} material, measured with increasing pressure values. c) Spectral position (peak centroid) of the P_4 component of $4f^7 \rightarrow 4f^7$ transition of Eu^{2+}. d) Non-normalized UV emission spectra measured at increasing pressure values; the inset presents the integrated intensity of the $4f^7(^6P_{7/2}) \rightarrow 4f^7(^8S_{7/2})$ emission as a function of pressure. e) A simplified diagram of the energy levels for Eu^{2+} in the SrB_4O_7 matrix at low and high pressure conditions.

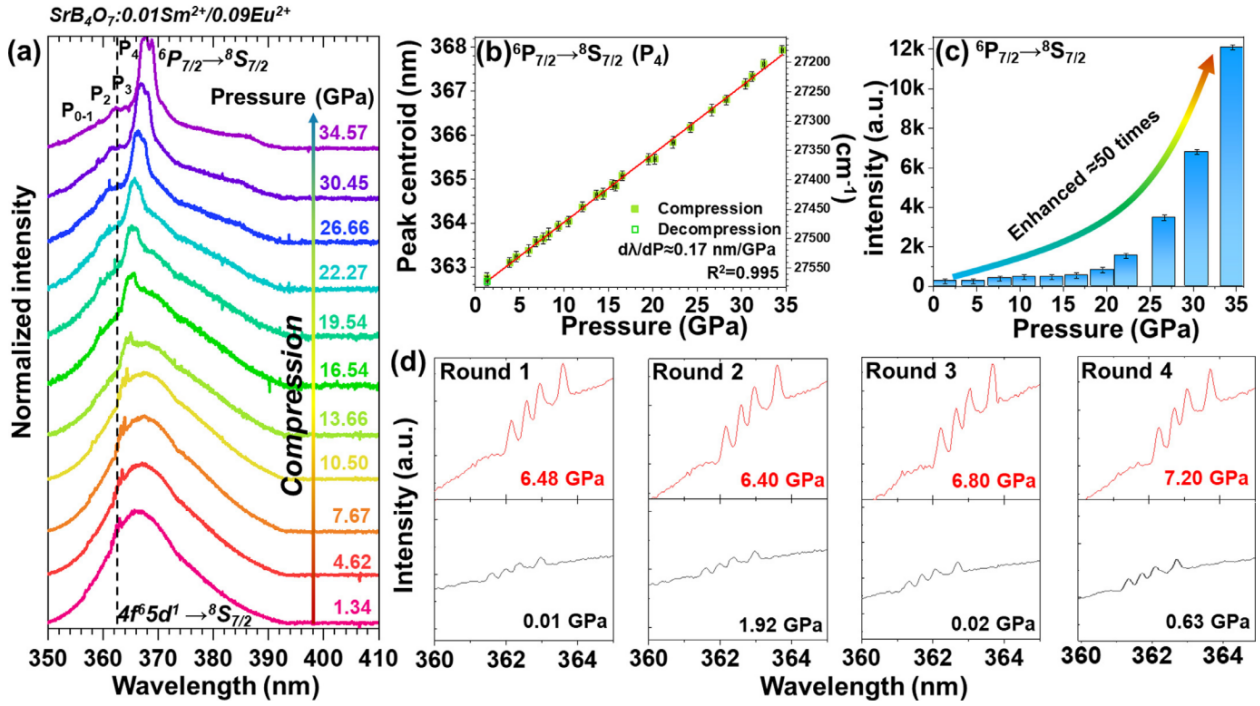

Fig. 8. (a) Selected, normalized UV emission spectra of SrB_4O_7: 0.09 Eu^{2+}, 0.01Sm^{2+} measured at increasing pressure values and room temperature. (b) Spectral position (peak centroid) of the P_4 components of the $4f^7(^6P_{7/2})$- $4f^7(^8S_{7/2})$ transition of Eu^{2+}. (c) Integrated intensity of the $^6P_{7/2} \rightarrow {}^8S_{7/2}$ ($4f^7 \rightarrow 4f^7$) emission as a function of pressure. (d) Magnified emission spectra, emphasizing the $^6P_{7/2} \rightarrow {}^8S_{7/2}$ transition, recorded during four different compression cycles.

tration has a negligible influence on the shift rate of this narrow emission band. If the pressure is higher than 20 GPa, the $4f^65d^1 \rightarrow 4f^7(^8S_{7/2})$ broad-band emission practically disappears, and the $4f^7(^6P_{7/2}) \rightarrow 4f^7(^8S_{7/2})$ luminescence completely dominates the luminescence spectrum. As shown in Fig. 8**c**, the absolute intensity of the P_4 peak of the $4f^7(^6P_{7/2}) \rightarrow 4f^7(^8S_{7/2})$ emission at 34.6 GPa is about 50 times higher than at 1.3 GPa. It is important to mention that these effects were observed in four independent compression-decompression experiments (cycles), as shown in Fig. 8**d**, confirming the reliability of our experiments and the reversibility of the observed effects.

These results show that pressure acts inversely to temperature, *i.e.*, deteriorating the intensity of the $4f^65d^1$-$4f^7$ emission and enhancing the $4f^7(^6P_{7/2}) \rightarrow 4f^7(^8S_{7/2})$ luminescence. Due to the fact that the Eu^{2+} emission intensity is higher in the sample with 9 mol% of Eu^{2+} (see **Fig. S1a),** we calculated the pressure shift rate of the $4f^65d^1 \rightarrow 4f^7(^8S_{7/2})$ band for this sample. As shown in **Fig. S9** in the SI, the pressure-induced shift of the interconfigurational, parity-allowed $4f^65d^1 \rightarrow 4f^7(^8S_{7/2})$ transition is estimated to be around -8.5 cm^{-1}/GPa (0.11 nm/GPa), which is lower compared to the shift of the $4f^7(^6P_{7/2}) \rightarrow 4f^7(^8S_{7/2})$ emission (-12.84 cm^{-1}/GPa; 0.17 nm/GPa). That is why the energy separation of the excited $4f^65d$ configuration and the $^6P_{7/2}$ emitting levels appears to change with pressure, leading to a decreasing intensity of the $4f^65d^1 \rightarrow 4f^7(^8S_{7/2})$ broad band with increasing pressure and complete quenching above ≈ 35GPa. Phonon energies and electron-phonon coupling increase with pressure, which can be observed in the Raman spectra and the vibronic bands at the high energy side of the $4f^7(^6P_{7/2}) \rightarrow 4f^7(^8S_{7/2})$ emission peaks. However, these two effects do not have a dominant impact on the intensity of the discussed $4f^7 \rightarrow 4f^7$ transitions of Eu^{2+}, which is significantly enhanced with increasing pressure.

The centroid red-shift of the $^6P_{7/2} \rightarrow {}^8S_{7/2}$ can be additionally explained by an increase in the nephelauxetic effect: the interelectronic repulsion decreases as the shorter Eu-O bond lengths also lead to a higher covalent nature of the bond. Correspondingly, the Slater-Condon-Shortley parameters expectedly decrease, which determine the energy of the excited $4f^7$ states relative to the ground level in general. As the mutual electron repulsion among the 4f electrons is reduced in the more extended, lower valent Eu^{2+} ion, the energy of the higher excited $^6P_{7/2}$ levels is reduced. Concerning the fact that the narrow $4f^7 \rightarrow 4f^7$-related luminescence becomes dominant at elevated pressures, it is actually an indication that the bond length in the lowest excited $4f^65d^1$ state must be smaller than in the $^8S_{7/2}$ ground level. The concept is demonstrated schematically in Fig. 9. It turns out that for a bond-contracted $4f^65d^1$ state, elevation of pressure will lead to a higher thermal activation barrier to thermally populate the lowest excited $4f^65d^1$ state. Such a bond contraction in the lowest excited $4f^65d^1$ level has been consistently proven for several trivalent and divalent lanthanides [112–114]. In contrast, an elongated bond in the excited $4f^65d^1$ state would actually lead to an even more dominant $4f^65d^1 \rightarrow 4f^7$ broad-band emission at higher pressure. The significant enhancement in the narrow $4f^7 \rightarrow 4f^7$-related luminescence is thus a consequence of the reduced non-radiative thermal crossover to the excited $4f^65d^1$ state (see Fig. 9**a and b**).

As shown in Figs. 7**b and** 8**a**, in the initial pressure stages, the $4f^7 \rightarrow 4f^7$ emission lines broaden and overlap, and, at HP, the splitting of the peaks increases with increasing pressure, indicating a stronger magnitude of the crystal-field interaction acting on the Eu^{2+} ions when the volume of the [EuO_9] polyhedron decreases with pressure. However, as already indicated above, the Eu^{2+} ion in the SrB_4O_7 structure is only prone to a rather weak crystal field and very ionic bonds to the surrounding oxygen atoms.

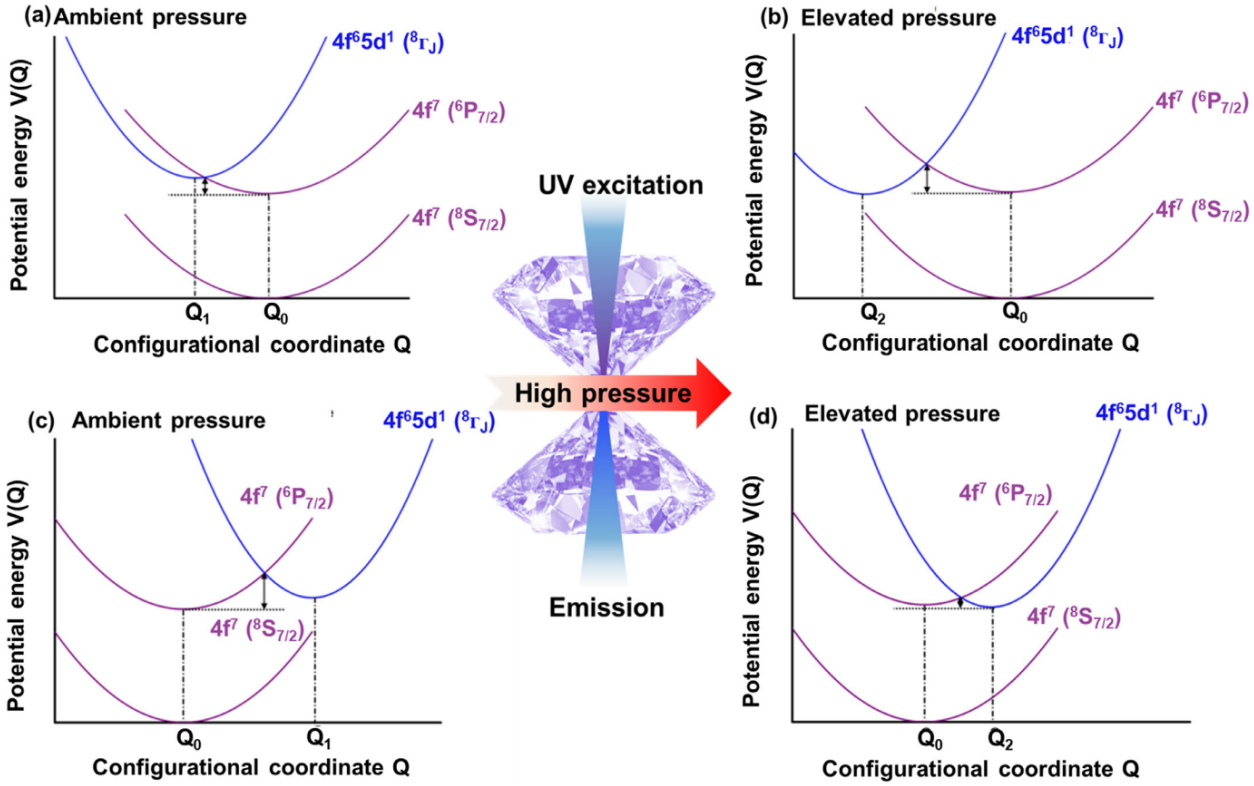

Fig. 9. (a) Impact of the position of the lowest excited $4f^65d^1$ state relative to the $^6P_{7/2}$ level of Eu^{2+} in the configurational coordinate space on the appearance of the respective luminescence spectrum; (b) shows the case of a bond contraction upon excitation into the $4f^65d^1$ state; while (c) and (d) show the pressure dependence if the excited $4f^65d^1$ state has higher equilibrium bond distances.

Since the pressure strongly reduces the volume of the $[EuO_9]$ entity, the crystal-field interaction should increase. Anyway, the large volume changes of the $[EuO_9]$ polyhedron may be responsible for relatively large changes in the red-shift of the luminescence. When Eu^{2+} is incorporated in the SrB_4O_7 network, the contraction of energy differences between multiplets is more important than the increase in individual splitting of each multiplet due to crystal-field interaction, indicating the importance of pressure-induced changes in the covalency nature of the Eu^{2+} local environment [109,110]. The quantum efficiency of the emission from the $^6P_{7/2}$ multiplet is practically 100% given the large gap to the ground multiplet that makes multiphonon relaxation improbable. The proximity of the $^6P_{7/2}$ Stark levels and the lowest $4f^65d^1$ multiplets of the excited configuration and the increasing odd part of the crystal-field interaction with the pressure favor this mixing. This, in turn, gives rise to an increase of the parity-allowed components of the $^6P_{7/2}$ levels and, thus, increasing the spontaneous emission probabilities of the $4f^7(^6P_{7/2}) \rightarrow 4f^7(^8S_{7/2})$ transitions over the inter-configurational emission. Since vibronic transitions involve electronic and phonon states, they are also enhanced by pressure.

In Table S7, we summarize and compare the extraordinary pressure sensing performance of the studied material with the other optical pressure gauges reported. The Eu^{2+} and Sm^{2+} co-doped SrB_4O_7 pressure sensor shows its superiority as a high-accuracy and high-precision, reversible pressure gauge, operating within a very wide pressure range. The spectral shift of the narrow $4f^7(^6P_{7/2}) \rightarrow 4f^7(^8S_{7/2})$ emission line can be applied as a manometric parameter, when experiments require compression under very high pressure conditions (*i.e.*, above $\approx$ 30 GPa). This is due to the great advantage of its pressure-enhanced signal intensity, narrow emission line, and significant and reversible spectral shift, as well as negligible temperature dependence.

5. Conclusions

A strong pressure-induced enhancement of the $4f^7(^6P_{7/2}) \rightarrow 4f^7(^8S_{7/2})$ emission intensity of Eu^{2+} was recorded in SrB_4O_7 for the first time. In order to investigate and support the proposed mechanism underlying the pressure-dependent photoluminescence, a combination of theoretical and experimental studies of the structural, vibrational, elastic, and luminescence properties was systematically performed on SrB_4O_7:Eu^{2+} at varying pressure and temperature. It could be established that the strong enhancement of the intensity of the $4f^7(^6P_{7/2}) \rightarrow 4f^7(^8S_{7/2})$ emission intensity is a pressure-induced configuration crossover between the energetically close $4f^7(^6P_{7/2})$ and $4f^65d^1$ excited configurations. It turns out that elevated pressure has the opposite effect on the appearance of the luminescence spectra to temperature and favors the narrow line emission. In contrast to the currently applied sensors, usually showing a significant luminescence quenching (signal deterioration) under high-pressure conditions, the narrow emission lines of Eu^{2+} show a strong increase in the intensity of the obtained material, as well as a significant spectral shift ($\sim$ -12.84 cm^{-1}/GPa) alongside with negligible temperature dependence. Such a co-doped (Eu^{2+}/Sm^{2+}) luminescent material SrB_4O_7 can be applied as a multi-mode, pressure-enhanced gauge, which offers new perspectives for research under high-pressure conditions.

Data availability

The original data for this study are available from the corresponding authors upon request.

Fourier transform infrared (FTIR) spectrpscopy of these catalysts were conducted on a Thermo Scientific Nicolet Is5 spectrometer using KBr pellet technique.

Declaration of Competing Interest

The authors declare that they have no known competing financial interests or personal relationships that could have appeared to influence the work reported in this paper.

Acknowledgements

This work was supported by the Polish National Science Centre (2016/23/D/ST4/00296), Ministerio de Economía y Competitividad (MINECO) under the National Program of Sciences and Technological Materials (PID2019-106383GB-42, PID2019-106383GB-43, and PID2019-106383GB-44), by the Spanish Research Agency (AEI) under projects MALTA Consolider Team network (RED2018-102612-T), by Agencia Canaria de Investigación, Innovación y Sociedad de la Información (ACIISI) (ProID2017010078), by Generalidad Valenciana under Project PROMETEO/2018/123 (EFIMAT) and by EU-FEDER funds. M. Runowski acknowledges support from Fondo Social Europeo and Agencia Estatal de Investigación (RYC2020-028778-I). T.Z. is grateful to grant No. POWR.03.02.00–00-i020/17 financed by European Union through the European Social Fund under the Operational Program Knowledge Education Development. The authors also acknowledge the computational resource time provide by the MALTA cluster and the Red Española de Supercomputación.

Supplementary materials

Supplementary material associated with this article can be found, in the online version, at doi:10.1016/j.actamat.2022.117886.

References

[1] S. Liu, S. Sun, C.K. Gan, A.G. Del Águila, Y. Fang, J. Xing, T.Thu Ha Do, T.J. White, H. Li, W. Huang, Q. Xiong, Manipulating efficient light emission in two-dimensional perovskite crystals by pressure-induced anisotropic deformation, Sci. Adv. 5 (2019) 1–11, doi:10.1126/sciadv.aav9445.

[2] J. Sun, Q. Li, H. Zhu, Z. Liu, K. Lin, N. Wang, Q. Zhang, L. Gu, J. Deng, J. Chen, X. Xing, Negative-pressure-induced large polarization in Nanosized $PbTiO_3$, Adv. Mater. 32 (2020) 1–6, doi:10.1002/adma.202002968.

[3] H. Liu, Y. Gu, Y. Dai, K. Wang, S. Zhang, G. Chen, B. Zou, B. Yang, Pressure-induced blue-shifted and enhanced emission: a cooperative effect between aggregation-induced emission and energy-transfer suppression, J. Am. Chem. Soc. 142 (2020) 1153–1158, doi:10.1021/jacs.9b11080.

[4] M. Runowski, P. Woźny, S. Lis, V. Lavín, I.R. Martín, Optical vacuum sensor based on lanthanide Upconversion—luminescence thermometry as a tool for ultralow pressure sensing, Adv. Mater. Technol. 5 (2020) 1901091, doi:10.1002/admt.201901091.

[5] X. Liu, W. Xie, Y. Lü, J. Feng, X. Tang, J. Lin, Y. Dai, Y. Xie, L. Yan, Multichannel luminescence properties of mixed-valent Eu^{2+}/Eu^{3+} coactivated $SrAl_3BO_7$ nanocrystalline phosphors for Near-UV LEDs, Inorg. Chem. 56 (2017) 13829–13841, doi:10.1021/acs.inorgchem.7b01938.

[6] J.A. Sans, V. Monteseguro, G. Garbarino, M. Gich, V. Cerantola, V. Cuartero, M. Monte, T. Irifune, A. Muñoz, C. Popescu, Stability and nature of the volume collapse of ε-Fe_2O_3 under extreme conditions, Nat. Commun. 9 (2018) 4554, doi:10.1038/s41467-018-06966-9.

[7] D. Santamaria-Perez, C. McGuire, A. Makhluf, A. Kavner, R. Chuliá-Jordan, J.L. Jorda, F. Rey, J. Pellicer-Porres, D. Martinez-García, P. Rodriguez-Hernández, A. Muñoz, Correspondence: strongly-driven Re+CO_2 redox reaction at high-pressure and high-temperature, Nat. Commun. 7 (2016) 4–6, doi:10.1038/ncomms13647.

[8] D.A. Davis, A. Hamilton, J. Yang, L.D. Cremar, D. Van Gough, S.L. Potisek, M.T. Ong, P.V. Braun, T.J. Martínez, S.R. White, J.S. Moore, N.R. Sottos, Force-induced activation of covalent bonds in mechanoresponsive polymeric materials, Nature 459 (2009) 68–72, doi:10.1038/nature07970.

[9] Y. Wang, X. Tan, Y.M. Zhang, S. Zhu, I. Zhang, B. Yu, K. Wang, B. Yang, M. Li, B. Zou, S.X.A. Zhang, Dynamic behavior of molecular switches in crystal under pressure and its reflection on tactile sensing, J. Am. Chem. Soc. 137 (2015) 931–939, doi:10.1021/ja511499p.

[10] X. Jiang, Y. Yang, M.S. Molokeev, P. Gong, F. Liang, S. Wang, L. Liu, X. Wu, X. Li, Y. Li, S. Wu, W. Li, Y. Wu, Z. Lin, Zero linear compressibility in Non-dense borates with a "Lu-Ban Stool"-Like structure, Adv. Mater. 30 (2018) 1–7, doi:10.1002/adma.201801313.

[11] X. Jiang, M.S. Molokeev, L. Dong, Z. Dong, N. Wang, L. Kang, X. Li, Y. Li, C. Tian, S. Peng, W. Li, Z. Lin, Anomalous mechanical materials squeezing three-dimensional volume compressibility into one dimension, Nat. Commun. 11 (2020) 1–7, doi:10.1038/s41467-020-19219-5.

[12] Y.N. Zhuravlev, V.V. Atuchin, First-principle studies of the vibrational properties of carbonates under pressure, Sensors 21 (2021), doi:10.3390/s21113644.

[13] M.A. Antoniak, S.J. Zelewski, R. Oliva, A. Żak, R. Kudrawiec, M. Nyk, Combined Temperature and Pressure Sensing Using Luminescent $NaBiF_4$:Yb,Er Nanoparticles, ACS Appl. Nano Mater. 3 (2020) 4209–4217, doi:10.1021/acsanm.0c00403.

[14] R.A. Forman, G.J. Piermarini, J.Dean Barnett, S. Block, Pressure measurement made by the utilization of ruby sharp-line luminescence, Science 80 (176) (1972) 284–285, doi:10.1126/science.176.4032.284.

[15] A. Lacam, C. Chateau, High-pressure measurements at moderate temperatures in a diamond anvil cell with a new optical sensor: $SrB_4O_7:Sm^{2+}$, J. Appl. Phys. 66 (1989) 366–372, doi:10.1063/1.343884.

[16] Z. Dai, J. Xie, W. Liu, X. Wang, L. Zhang, Z. Zhou, J. Li, X. Ren, Effective strategy to achieve excellent energy storage properties in Lead-Free $BaTiO^3$-based bulk ceramics, ACS Appl. Mater. Interfaces. 12 (2020) 30289–30296, doi:10.1021/acsami.0c02832.

[17] S. Goderski, M. Runowski, P. Woźny, V. Lavín, S. Lis, Lanthanide Upconverted luminescence for simultaneous contactless optical thermometry and manometry-sensing under extreme conditions of pressure and temperature, ACS Appl. Mater. Interfaces. 12 (2020) 40475–40485, doi:10.1021/acsami.0c09882.

[18] M. Zhao, Q. Zhang, Z. Xia, Structural engineering of Eu^{2+}-doped silicates phosphors for LED applications, Accounts Mater. Res. 1 (2020) 137–145, doi:10.1021/accountsmr.0c00014.

[19] G.J. Hoerder, M. Seibald, D. Baumann, T. Schröder, S. Peschke, P.C. Schmid, T. Tyborski, P. Pust, I. Stoll, M. Bergler, C. Patzig, S. Reißaus, M. Krause, L. Berthold, T. Höche, D. Johrendt, H. Huppertz, $Sr[Li_2Al_2O_2N_2]:Eu^{2+}$ —A high performance red phosphor to brighten the future, Nat. Commun. 10 (2019) 1–9, doi:10.1038/s41467-019-09632-w.

[20] P. Pust, V. Weiler, C. Hecht, A. Tücks, A.S. Wochnik, A.K. Henß, D. Wiechert, C. Scheu, P.J. Schmidt, W. Schnick, Narrow-band red-emitting $Sr[LiAl_3N_4]:Eu^{2+}$ as a next-generation LED-phosphor material, Nat. Mater. 13 (2014) 891–896, doi:10.1038/nmat4012.

[21] T. Zheng, M. Runowski, P. Woźny, S. Lis, Influence of matrix on the luminescence properties of Eu^{2+}/Eu^{3+} doped strontium borates: SrB_4O_7, SrB_2O_4 and $Sr_3(BO_3)_2$, exhibiting multicolor tunable emission, J. Alloys Compd. 822 (2020) 1–9, doi:10.1016/j.jallcom.2019.153511.

[22] J. Zhang, R. Li, Q. Chen, G. Zhao, J. Jia, Porous carbon-coated Li_2MoO_4 as high-performance anode materials for lithium-ion batteries, Mater. Lett. 233 (2018) 302–305, doi:10.1016/j.matlet.2018.09.032.

[23] J. Qiao, G. Zhou, Y. Zhou, Q. Zhang, Z. Xia, Divalent europium-doped near-infrared-emitting phosphor for light-emitting diodes, Nat. Commun. 10 (2019) 1–7, doi:10.1038/s41467-019-13293-0.

[24] G. Li, C.C. Lin, W.T. Chen, M.S. Molokeev, V.V. Atuchin, C.Y. Chiang, W. Zhou, C.W. Wang, W.H. Li, H.S. Sheu, T.S. Chan, C. Ma, R.S. Liu, Photoluminescence tuning via cation substitution in oxonitridosilicate phosphors: DFT calculations, different site occupations, and luminescence mechanisms, Chem. Mater. 26 (2014) 2991–3001, doi:10.1021/cm500844v.

[25] Z. Xia, Y. Zhang, M.S. Molokeev, V.V. Atuchin, Y. Luo, Linear structural evolution induced tunable photoluminescence in clinopyroxene solid-solution phosphors, Sci. Rep. 3 (2013) 1–7, doi:10.1038/srep03310.

[26] J. Ueda, T. Wylezich, N. Kunkel, S. Tanabe, Red luminescent Eu^{2+} in K_2MgH_4 and comparison with $KMgH_3$, J. Mater. Chem. C. 8 (2020) 5124–5130, doi:10.1039/c9tc06459a.

[27] H. Ji, Z. Huang, Z. Xia, M.S. Molokeev, V.V. Atuchin, M. Fang, Y. Liu, Discovery of new solid solution phosphors via cation substitution-dependent phase transition in $M_3(PO_4)_2:Eu^{2+}$ (M = Ca/Sr/Ba) quasi-binary sets, J. Phys. Chem. C. 119 (2015) 2038–2045, doi:10.1021/jp509743r.

[28] A. Baran, S. Mahlik, M. Grinberg, E. Zych, High pressure and time-resolved luminescence spectra of $Ca_3Y_2(SiO_4)_3$ doped with Eu^{2+} and Eu^{3+}, J. Phys. Condens. Matter. (2013) 25, doi:10.1088/0953-8984/25/2/025603.

[29] K. Winskiewski, S. Mahlik, M. Grinberg, H.J. Seo, Influence of high hydrostatic pressure on Eu^{2+}-luminescence in $KMgF_3:Eu^{2+}$ crystal, J. Lumin. 131 (2011) 306–309, doi:10.1016/j.jlumin.2010.10.020.

[30] R.A. Hewes, M.V Hoffman, G.E. Company, $4f^7$-$4f^7$ Emission from Eu^{2+} system MF_2•AlF_3, J. Lumin. 3 (2000) 261–280.

[31] C. Helvacı, Occurrence of rare borate minerals: Veatchite-A, tunellite, teruggite and cahnite in the Emet borate deposits, Turkey, Miner. Depos. 19 (1984) 217–226, doi:10.1007/BF00199788.

[32] M. Mohapatra, B. Rajeswari, R.M. Kadam, M. Kumar, T.K. Seshagiri, N.K. Porwal, S.V. Godbole, V. Natarajan, Investigation of uranium luminescence in SrB_4O_7 matrix by time resolved photoluminescence, thermally stimulated luminescence and electron spin resonance spectroscopy, J. Alloys Compd. 611 (2014) 74–81, doi:10.1016/j.jallcom.2014.05.096.

[33] J. Sun, J. Zhu, X. Liu, H. Du, Luminescence properties of SrB_4O_7:Sm^{2+} for light conversion agent, J. Rare Earths. 30 (2012) 1084–1087, doi:10.1016/S1002-0721(12)60183-5.

[34] C.B. Palan, N.S. Bajaj, S.K. Omanwar, Luminescence properties of Eu^{2+} doped SrB_4O_7 phosphor for radiation dosimetry, Mater. Res. Bull. 76 (2016) 216–221, doi:10.1016/j.materresbull.2015.12.027.

[35] V.V. Atuchin, V.G. Kesler, A.I. Zaitsev, M.S. Molokeev, A.S. Aleksandrovsky, A.A. Kuzubov, N.Y. Ignatova, Electronic structure of α-SrB_4O_7: experiment and theory, J. Phys. Condens. Matter. (2013) 25, doi:10.1088/0953-8984/25/8/085503.

[36] H. Huppertz, High-pressure preparation, crystal structure, and properties of $RE_4B_6O_{15}$ (RE = Dy, Ho) with an extension of the "fundamental building block"-descriptors, Zeitschrift Fur Naturforsch. - Sect. B J. Chem. Sci. 58 (2003) 278–290, doi:10.1515/znb-2003-0406.

[37] K. Machida, G. Adachi, J. Shiokawa, Luminescence properties of Eu(II)-borates and Eu^{2+}- activated Sr-Borates, J. Lumin. 21 (1979) 101–110, doi:10.1016/0022-2313(79)90038-3.

[38] A. Meijerink, J. Nuyten, G. Blasse, Luminescence and energy migration in (Sr,Eu)B_4O_7, a system with a $4f^7$-$4f^65d$ crossover in the excited state, J. Lumin. 44 (1989) 19–31, doi:10.1016/0022-2313(89)90017-3.

[39] T. Zheng, M. Runowski, P. Woźny, S. Lis, V. Lavín, Huge enhancement of Sm^{2+} emission: Via Eu^{2+} energy transfer in a SrB_4O_7 pressure sensor, J. Mater. Chem. C. 8 (2020) 4810–4817, doi:10.1039/d0tc00463d.

[40] P. Hohenberg, Inhomogeneous electron gas, Phys. Rev. 9 (1964) 864–871, doi:10.1007/BF01198136.

[41] G. Kresse, J. Hafner, Ab initio molecular dynamics for liquid metals, Phys. Rev. B. 47 (1993) 558–561, doi:10.1103/PhysRevB.47.558.

[42] D. Joubert, From ultrasoft pseudopotentials to the projector augmented-wave method, Phys. Rev. B - Condens. Matter Mater. Phys. 59 (1999) 1758–1775, doi:10.1103/PhysRevB.59.1758.

[43] J.P. Perdew, A. Ruzsinszky, G.I. Csonka, O.A. Vydrov, G.E. Scuseria, L.A. Constantin, X. Zhou, K. Burke, Restoring the density-gradient expansion for exchange in solids and surfaces, Phys. Rev. Lett. 100 (2008) 1–4, doi:10.1103/PhysRevLett.100.136406.

[44] K. Hu, M. Wu, S. Hinokuma, T. Ohto, M. Wakisaka, J.I. Fujita, Y. Ito, Boosting electrochemical water splitting: via ternary NiMoCo hybrid nanowire arrays, J. Mater. Chem. A. 7 (2019) 2156–2164, doi:10.1039/c8ta11250a.

[45] N. Chetty, A. Muoz, R.M. Martin, First-principles calculation of the elastic constants of AlAs, Phys. Rev. B. 40 (1989) 11934–11936, doi:10.1103/PhysRevB.40.11934.

[46] O.H. Nielsen, R.M. Martin, Quantum-mechanical theory of stress and force, Phys. Rev. B. 32 (1985) 3780–3791, doi:10.1103/PhysRevB.32.3780.

[47] Y.Le Page, P. Saxe, Symmetry-general least-squares extraction of elastic data for strained materials from ab initio calculations of stress, Phys. Rev. B - Condens. Matter Mater. Phys. 65 (2002) 1–14, doi:10.1103/PhysRevB.65.104104.

[48] A. Perloff, S. Block, The crystal structure of the strontium and lead tetraborates, $Sr_{0.2}B_2O_3$ and $Pb_{0.2}B_2O_3$, Acta Crystallogr 20 (1966) 274–279, doi:10.1107/s0365110x66000525.

[49] F. Pan, G. Shen, R. Wang, X. Wang, D. Shen, Growth, characterization and nonlinear optical properties of SrB_4O_7 crystals, J. Cryst. Growth. 241 (2002) 108–114, doi:10.1016/S0022-0248(02)00873-4.

[50] B.Y.K. Machida, G. Adachi, J. Shiokawa, Structure of Europium (II) Tetraborate, (2008) 2008–2011.

[51] D.L. Pye, D.V. Fréchette, N.J. Kreidl, Borate Glasses: Structure, Properties, Applications, Springer, 2021 n.d., doi:10.1007/978-1-4684-3357-9.

[52] G. Blasse, G.J. Dirksen, A. Meijerink, The luminescence of ytterbium(II) in Strontium tetraborate, Chem. Phys. Lett. 167 (1989) 41–44.

[53] Z. Pei, Q. Su, J. Zhang, The valence change from RE^{3+} SrB_4O_7: RE prepared in air and to RE^{2+} (RE = Eu, Sm, Yb) in the spectral properties of RE^{2+}, J. Alloys Compd. 198 (1993) 51–53.

[54] A.A.B.B. Baloch, S.M. Alqahtani, F. Mumtaz, A.H. Muqaibel, S.N. Rashkeev, F.H. Alharbi, Extending Shannon's ionic radii database using machine learning, Phys. Rev. Mater. 5 (2021) 1–10, doi:10.1103/PhysRevMaterials.5.043804.

[55] J.F. Nye, Physical properties of crystals: their representation by tensors and matrices, n.d. https://books.google.ie/books/about/Physical_Properties_of_Crystals.html?id=ugwql-uVB44C&redir_esc=y (accessed January 28, 2021).

[56] I. Martynyuk-Lototska, T. Dudok, O. Mys, R. Vlokh, Elastic, piezooptic and acoustooptic properties of SrB_4O_7 and PbB_4O_7 crystals, Opt. Mater. (Amst). 31 (2009) 660–667, doi:10.1016/j.optmat.2008.06.020.

[57] V.I. Zinenko, M.S. Pavlovskii, A.I. Zaitzev, A.S. Krylov, A.S. Shinkorenko, Vibrational spectra and elastic piezoelectric and polarization properties of the α-SrB_4O_7 crystal, J. Exp. Theor. Phys. 115 (2012) 455–461, doi:10.1134/S1063776112080195.

[58] K. Babesse, D. Hammoutène, P. Rodríguez-Hernández, A. Muñoz, K. Kassali, R. Nedjar, High pressure study of structural, electronic, elastic, and vibrational properties of $NaNb_3O_8$, J. Alloys Compd. 725 (2017) 773–782, doi:10.1016/j.jallcom.2017.07.231.

[59] W. Voigt, Lehrbuch der Kristallphysik, 1966. doi:10.1007/978-3-663-15884-4.

[60] A. Reuss, Berechnung der Fließgrenze von Mischkristallen auf Grund der Plastizitätsbedingung für Einkristalle. ZAMM - J. Appl. Math. Mech. /Zeitschrift Für Angew. Mat, h. Und Mech. 9 (1929) 49–58, doi:10.1002/zamm.19290090104.

[61] R. Hill, The elastic behaviour of a crystalline aggregate, Proc. Phys. Soc. Sect. A. 65 (1952) 349–354, doi:10.1088/0370-1298/65/5/307.

[62] F. Birch, Finite elastic strain of cubic crystals, Phys. Rev. 71 (1947) 809–824, doi:10.1103/PhysRev.71.809.

[63] S.F. Pugh XCII, Relations between the elastic moduli and the plastic properties of polycrystalline pure metals, London, Edinburgh, Dublin Philos. Mag. J. Sci. 45 (1954) 823–843, doi:10.1080/14786440808520496.

[64] V. Tvergaard, John W. Hutchinson, Microcracking in ceramics induced by thermal expansion or elastic anisotropy, J. Am. Ceram. Soc. 71 (1988) 157–166, doi:10.1111/j.1151-2916.1988.tb05022.x.

[65] S.I. Ranganathan, M. Ostoja-Starzewski, Universal elastic anisotropy index, Phys. Rev. Lett. 101 (2008) 3–6, doi:10.1103/PhysRevLett.101.055504.

[66] E. Schreiber, O.L. Anderson, N. Soga, J.F. Bell, Elastic constants and their measurement, 1975. doi:10.1115/1.3423687.

[67] O.L. Anderson, A simplified method for calculating the debye temperature from elastic constants, J. Phys. Chem. Solids. 24 (1963) 909–917, doi:10.1016/0022-3697(63)90067-2.

[68] X. Qin, X. Liu, W. Huang, M. Bettinelli, X. Liu, Lanthanide-activated phosphors based on 4f-5d optical transitions: theoretical and experimental aspects, Chem. Rev. 117 (2017) 4488–4527, doi:10.1021/acs.chemrev.6b00691.

[69] A.A. Sobol, V.E. Shukshin, A.I. Zaitsev, Raman spectroscopy of SrB_4O_7 single crystals in the temperature range 300–1273 K, Opt. Spectrosc. 121 (2016) 25–31, doi:10.1134/S0030400x16070201.

[70] J. Hanuza, J.Lorenc M.Mączka, A.A. Kaminskii, P. Becker, L. Bohatý, Recent Advances in linear and nonlinear Raman spectroscopy I, J. Raman Spectrosc. 38 (2007) 1538–1553, doi:10.1002/jrs.

[71] A.A. Sobol, V.E. Shukshin, L.V. Moiseeva, Study of Raman spectra in the processes of glass formation, crystallization, and melting of strontium diborate, Opt. Spectrosc. (English Transl. Opt. i Spektrosk. 121 (2016) 32–35, doi:10.1134/S0030400x16070213.

[72] A.L.D.J. Pereira, D. Santamariá-Pérez, R. Vilaplana, D. Errandonea, C. Popescu, E.L. Da Silva, J.A. Sans, J. Rodríguez-Carvajal, A. Munõz, P. Rodríguez-Hernández, A. Mujica, S.E. Radescu, A. Beltrán, A. Otero-De-La-Roza, M. Nalin, M. Mollar, F.J. Manjón, Experimental and theoretical study of $SbPO_4$ under compression, Inorg. Chem. 59 (2020) 287–307, doi:10.1021/acs.inorgchem.9b02268.

[73] D. Errandonea, O. Gomis, P. Rodriguez-Hernández, A. Munz, J. Ruiz-Fuertes, M. Gupta, S.N. Achary, A. Hirsch, F.J. Manjon, L. Peters, G. Roth, A.K. Tyagi, M. Bettinelli, High-pressure structural and vibrational properties of monazite-type $BiPO_4$, $LaPO_4$, $CePO_4$, and $PrPO_4$, J. Phys. Condens. Matter. 30 (2018) 065401, doi:10.1088/1361-648X/aaa20d.

[74] J.H. Denning, S.D. Ross, Speotra and Struotures, Spectrochim. Acta. 28A (1984) 1775–1785.

[75] S.D. Ross, The vibrational spectra of some minerals containing tetrahedrally co-ordinated boron, Spectrochim. Acta Part A Mol. Spectrosc. 28 (1972) 1555–1561, doi:10.1016/0584-8539(72)80126-0.

[76] S.D. Ross, Vibrational assignments in borates with the vaterite structure, J. Mol. Spectrosc. 29 (1969) 131–145, doi:10.1016/0022-2852(69)90093-9.

[77] F. Auzel, Upconversion and Anti-Stokes Processes with f and d Ions in Solids, Chem. Rev. 104 (2004) 139–173, doi:10.1021/cr020357g.

[78] J. Zhou, Q. Liu, W. Feng, Y. Sun, F. Li, Upconversion luminescent materials: advances and applications, Chem. Rev. 115 (2015) 395–465, doi:10.1021/cr400478f.

[79] F.M. Ryan, W. Lehmann, D.W. Feldman, J. Murphy, Fine structure in the optical spectra of divalent europium in the alkaline earth sulfates, J. Electrochem. Soc. 121 (1974) 1475, doi:10.1149/1.2401714.

[80] Y. Huang, J. Qin, Z. Fan, D. Wei, H.J. Seo, Photoenergy conversion behaviors of photoluminescence and photocatalysis in Silver-Coated $LiBaPO_4$:Eu^{2+}, Inorg. Chem. 58 (2019) 13161–13169, doi:10.1021/acs.inorgchem.9b02037.

[81] J. Xiang, J. Zheng, Z. Zhou, H. Suo, X. Zhao, X. Zhou, N. Zhang, M.S. Molokeev, C. Guo, Enhancement of red emission and site analysis in Eu^{2+} doped new-type structure $Ba_3CaK(PO_4)_3$ for plant growth white LEDs, Chem. Eng. J. 356 (2019) 236–244, doi:10.1016/j.cej.2018.09.036.

[82] C.E. Tyner, H.G. Drickamer, Studies of luminescence efficiency of Eu^{2+} activated phosphors as a function of temperature and high pressure, J. Chem. Phys. 67 (1977) 4116–4123, doi:10.1063/1.435388.

[83] N. Yamashita, Coexistence of the Eu^{2+} and Eu^{3+} centers in the CaO : Eu powder phosphor, J. Electrochem. Soc. 140 (1993) 840–843, doi:10.1149/1.2056169.

[84] R.P. Yavetskiy, E.F. Dolzhenkova, A.V. Tolmachev, S.V. Parkhomenko, V.N. Baumer, A.L. Prosvirnin, Radiation defects in SrB_4O_7:Eu^{2+} crystals, J. Alloys Compd. 441 (2007) 202–205, doi:10.1016/j.jallcom.2006.09.077.

[85] M.V. Hoffman, Eu^{2+} Emission in ternary alkaline earth aluminum fluorides, J. Electrochem. Soc. 119 (1972) 905, doi:10.1149/1.2404366.

[86] B. Latourrette, F. Guillen, C. Fouassier, Energy transfer from Eu^{2+} to trivalent rare earth ions in BaY_2F_8, Mater. Res. Bull. 14 (1979) 865–868.

[87] G. Blasse, On the Nature of the Eu2+ luminescence, Phys. Status Solidi Basic Res. 131 (1973) 5–8.

[88] W. Zhang, R. Hua, T. Liu, J. Zhao, L. Na, B. Chen, Preparation, photoluminescent properties and luminescent dynamics of $BaAlF_5$:Eu^{2+} nanophosphors, Mater. Res. Bull. 60 (2014) 247–251, doi:10.1016/j.materresbull.2014.08.039.

[89] H. Wang, M. Li, The ideal strength of gold under uniaxial stress: an ab initio study, J. Phys. Condens. Matter. 22 (2010) 1–6, doi:10.1088/0953-8984/22/29/295405.

[90] S. Mahlik, M. Grinberg, L. Shi, H.J. Seo, Pressure evolution of $LiBaF_3$:Eu^{2+} luminescence, J. Phys. Condens. Matter. 21 (2009) 8, doi:10.1088/0953-8984/21/23/235603.

[91] R. Hua, J. Yu, H. Jiang, C. Shi, Mild solvothermal synthesis and luminescent properties of the complex fluorides $KMgF_3$:Eu and $KZnF_3$:RE (RE = Eu, Ce), J. Alloys Compd. 432 (2007) 253–257, doi:10.1016/j.jallcom.2006.05.108.
[92] A. Meijerink, Make a comparison between the two isoelectronic, J. Lumin. 55 (1993).
[93] M.V. Hoffman, Alkaline earth aluminum fluoride compounds with Eu^{2+} activation, J. Electrochem. Soc. 118 (1971) 933, doi:10.1149/1.2408227.
[94] A. Ellens, A. Meijerink, G. Blasse, 6l emission and vibronic transitions of Eu^{2+} in $KMgF_3$, J. Lumin. 59 (1994) 293–301, doi:10.1016/0022-2313(94)90056-6.
[95] G. Boulon, J.C. Gacon, D. Trottier, A. Vedrine, Eu^{2+} Luminescence in KY_3F_{10}, Phys. Status Solidi. 93 (1979) 775–779, doi:10.1002/pssb.2220930236.
[96] J.M.P.J. Verstegen, J.L. Sommerdijk, Line emission of $SrBe_2Si_2O_7$:Eu^{2+} and $BaBe_2Si_2O_7$:Eu^{2+}, J. Lumin. 9 (1974) 297–301.
[97] D. Dutczak, T. Jüstel, C. Ronda, A. Meijerink, Eu^{2+} luminescence in strontium aluminates, Phys. Chem. Chem. Phys. 17 (2015) 15236–15249, doi:10.1039/c5cp01095k.
[98] G. Blasse, Thermal quenching of characteristic fluorescence, J. Chem. Phys. 51 (1969) 3529–3530, doi:10.1063/1.1672543.
[99] H. Kuroda, S. Shionoya, T. Kushida, Mechanism and Controlling Factors of Infrared-to-Visible Conversion Process in Er^{3+} and Yb^{3+}-Doped Phosphors, J. Phys. Soc. Japan. 33 (1972) 125–141, doi:10.1143/JPSJ.33.125.
[100] J. Sytsma, K.M. Murdoch, N.M. Edelstein, Spectroscopic studies and crystal–field analysis of Cm^{3+} and Gd^{3+} in $LuPO_4$, Phys. Rev. B. 52 (1995) 668–676.
[101] D.C. Wallace, H. Callen, Thermodynamics of crystals, Am. J. Phys. 40 (1972) 1718–1719, doi:10.1119/1.1987046.
[102] G. Grimvall, B. Magyari-Köpe, K.A.Persson OzoliņENM, Lattice instabilities in metallic elements, Rev. Mod. Phys. 84 (2012) 945–986, doi:10.1103/RevModPhys.84.945.
[103] M. Born, K. Huang, M. Lax, Dynamical Theory of Crystal Lattices, Am. J. Phys. 23 (1955) 474–474, doi:10.1119/1.1934059.
[104] D.C. Wallace, Thermoelasticity of stressed materials and comparison of various elastic constants, Phys. Rev. 162 (1967) 776–789, doi:10.1088/1751-8113/44/8/085201.
[105] Z. Zhou, B. Joós, Stability criteria for homogeneously stressed materials and the calculation of elastic constants, Phys. Rev. B - Condens. Matter Mater. Phys. 54 (1996) 3841–3850, doi:10.1103/PhysRevB.54.3841.
[106] J. Wang, J. Li, S. Yip, S. Phillpot, D. Wolf, Mechanical instabilities of homogeneous crystals, Phys. Rev. B. 52 (1995) 12627–12635, doi:10.1103/PhysRevB.52.12627.
[107] S.V. Rashchenko, A. Kurnosov, L. Dubrovinsky, K.D. Litasov, Revised calibration of the Sm:SrB_4O_7 pressure sensor using the Sm-doped yttrium-aluminum garnet primary pressure scale, J. Appl. Phys. 117 (2015) 2–7, doi:10.1063/1.4918304.
[108] F. Datchi, A. Dewaele, P. Loubeyre, R. Letoullec, Y.Le Godec, B. Canny, Optical pressure sensors for high-pressure-high-temperature studies in a diamond anvil cell, High Press. Res 27 (2007) 447–463, doi:10.1080/08957950701659593.
[109] T. Tröster, Optical studies of Non-Metallic compounds under pressure, Handb. Phys. Chem. Rare Earths. 33 (2003) 515–589, doi:10.1016/S0168-1273(02)33007-1.
[110] K.L. Bray, Transition metal and rare earth compounds: excited states, Transitions, Interactions I (2001).
[111] K.A.J. Gschneidner, L. Eyring, Handbook on the physics and chemistry of rare earth, 1986. doi:10.1016/s0925-8388(96)02845-9.
[112] Z. Barandiarán, L. Seijo, Quantum chemical analysis of the bond lengths in fn and f n-1 d1 states of Ce^{3+}, Pr^{3+}, Pa^{4+}, and U^{4+} defects in chloride hosts, J. Chem. Phys. 119 (2003) 3785–3790, doi:10.1063/1.1590952.
[113] R. Valiente, F. Rodríguez, J. González, H.U. Güdel, R. Martín-Rodríguez, L. Nataf, M.N. Sanz-Ortiz, K. Krämer, High pressure optical spectroscopy of Ce^{3+}-doped $Cs_2NaLuCl_6$, Chem. Phys. Lett. 481 (2009) 149–151, doi:10.1016/j.cplett.2009.09.059.
[114] J.L. Pascual, Z. Barandiarán, L. Seijo, Relation between high-pressure spectroscopy and $f^{n-1}d^1$ excited-state geometry: a comparison between theoretical and experimental results in SrF_2: Sm^{2+}, Phys. Rev. B - Condens. Matter Mater. Phys. 76 (2007) 1–6, doi:10.1103/PhysRevB.76.104109.

Supporting Information for

Pressure-driven Configurational Crossover between $4f^7$ and $4f^65d^1$ States – Giant Enhancement of Narrow Eu^{2+} UV-Emission Lines in SrB_4O_7 for Luminescence Manometry

Teng Zheng,[1] Marcin Runowski,[1,*] Plácida Rodríguez-Hernández,[2] Alfonso Muñoz,[2] Francisco J. Manjón,[3] Małgorzata Sójka,[4] Markus Suta,[5] Eugeniusz Zych,[4] Stefan Lis[1] and Víctor Lavín [6]

[1] *Adam Mickiewicz University, Faculty of Chemistry, Uniwersytetu Poznańskiego 8, 61-614 Poznań, Poland*

[2] *Departamento de Física, MALTA Consolider Team, Instituto de Materiales y Nanotecnología, Universidad de La Laguna, Apartado de Correos 456, E-38200 San Cristóbal de La Laguna, Santa Cruz de Tenerife, Spain*

[3] *Instituto de Diseño para la Fabricación y Producción Automatizada, MALTA Consolider Team, Universitat Politècnica de València, Cno. de Vera s/n, 46022 València, Spain*

[4] *Faculty of Chemistry, University of Wrocław, F. Joliot-Curie 14, 50-383 Wrocław*

[5] *Inorganic Photoactive Materials, Institute of Inorganic Chemistry, Heinrich Heine University Düsseldorf, Universitätsstr. 1, D-40225 Düsseldorf, Germany*

[6] *Departamento de Física, MALTA Consolider Team, and IUdEA, Universidad de La Laguna, Apartado de Correos 456, E-38200 San Cristóbal de La Laguna, Santa Cruz de Tenerife, Spain*

Table of Contents

I. Properties at ambient conditions

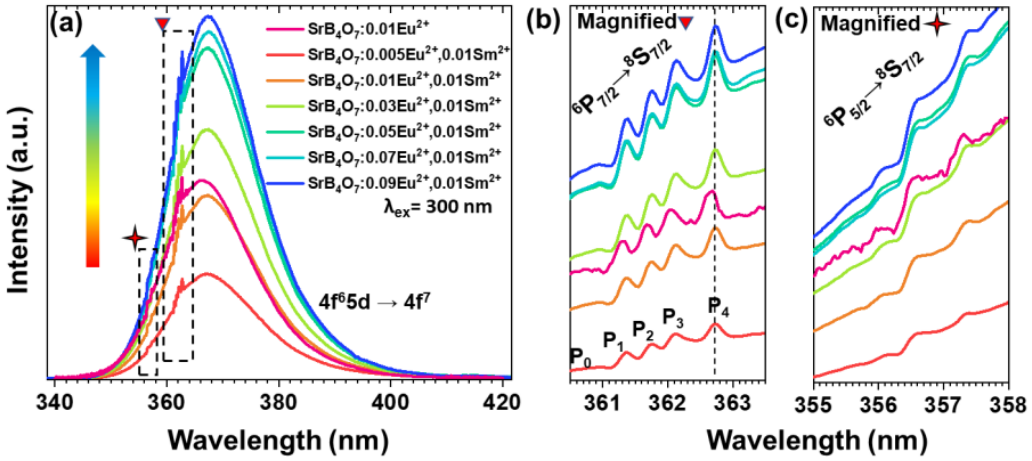

Figure S1. (a) Emission spectra in the UV range (340 - 420 nm), of the synthesized SrB_4O_7:0.01Eu^{2+} (without Sm^{2+}) and SrB_4O_7:0.01Sm^{2+}, *x* Eu^{2+} (*x* = 0.005 - 0.09) samples at room temperature and ambient pressure. (b) Magnified spectra in the "triangle" marked area, showing the $^6P_{7/2} \rightarrow {}^8S_{7/2}$ transitions. (c) Magnified spectra in the "star" marked area, showing the $^6P_{5/2} \rightarrow {}^8S_{7/2}$ transitions.

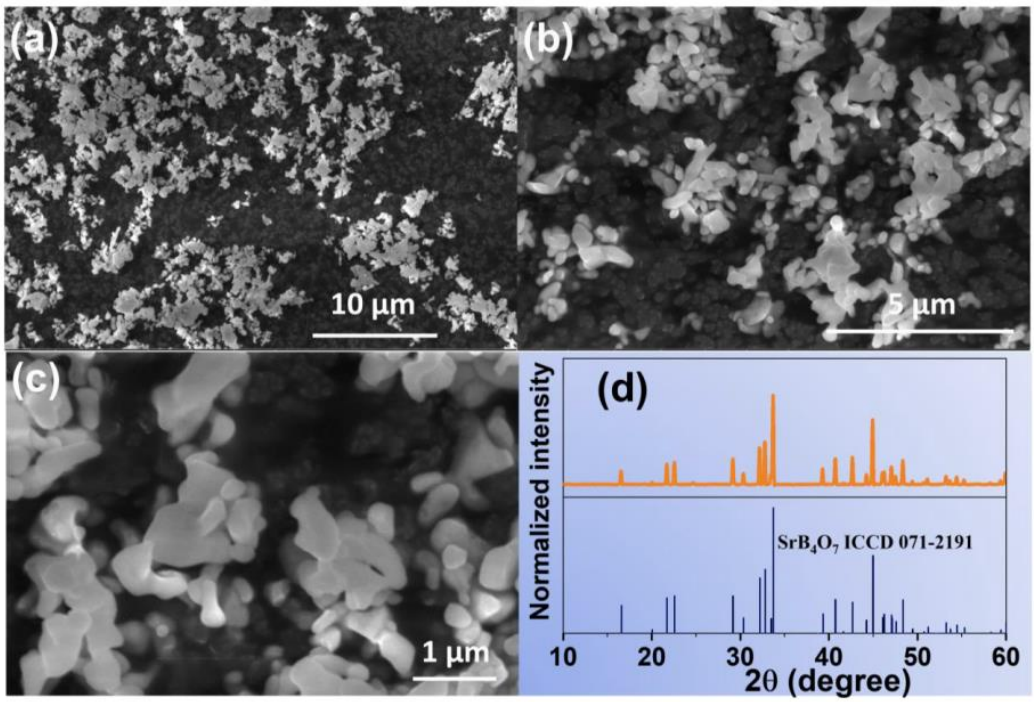

Figure S2. (a-c) SEM images of the optimal luminescent sample, i.e., SrB_4O_7:0.01Sm^{2+}, 0.03 Eu^{2+} phosphors at three different scales. (d) The indexed experimental XRD pattern of the selected sample. The line patterns correspond to the references from the ICDD standards database.

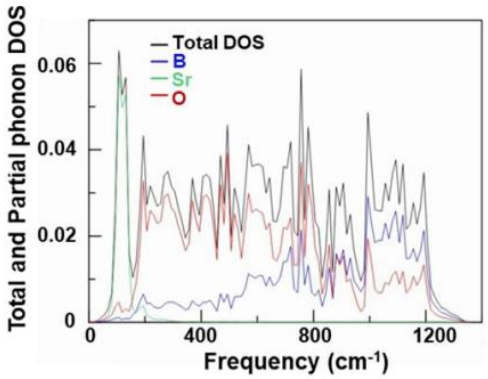

Figure S3. The theoretical total one-phonon density of states in black and the partial atomic contributions of Sr (green), O (red), and B (blue) to the one-phonon density of states in SrB_4O_7.

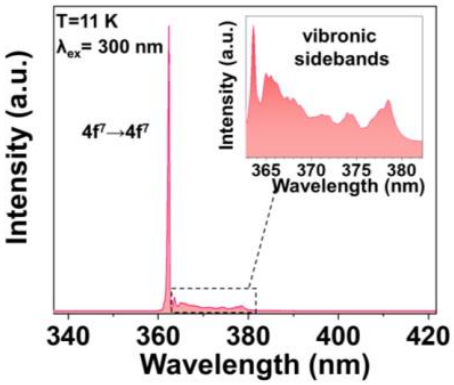

Figure S4. The magnified vibronic sidebands of the emission spectra of the SrB_4O_7:0.01Sm^{2+}, 0.03Eu^{2+} sample, measured at 11 K and ambient pressure.

II. Photoluminescence properties at low temperature

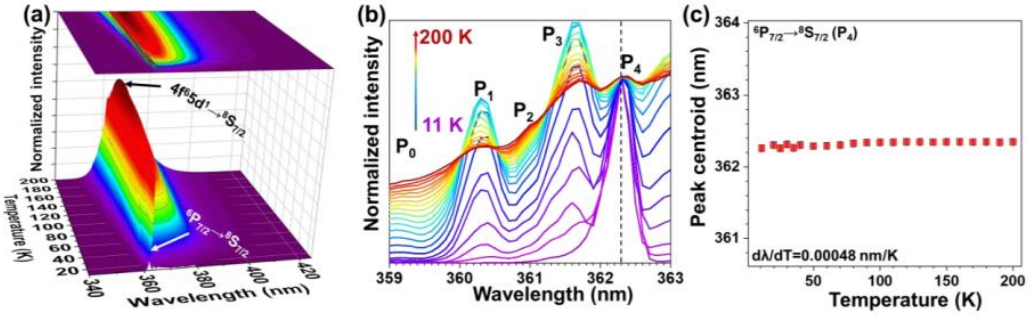

Figure S5. (a) Normalized emission spectra of SrB_4O_7:0.03Eu^{2+}, 0.01Sm^{2+} at selected measured temperatures and ambient pressure under 300 nm excitation. (b) The magnified normalized spectra, emphasizing on the $4f^7$ - $4f^7$ transitions of the Eu^{2+} emission in the sample. (c) Temperature dependence of the peak centroid of P_4 components of the $^6P_{7/2} \rightarrow {}^8S_{7/2}$ transition of Eu^{2+}.

III. Vibrational and Photoluminescence properties at high pressure

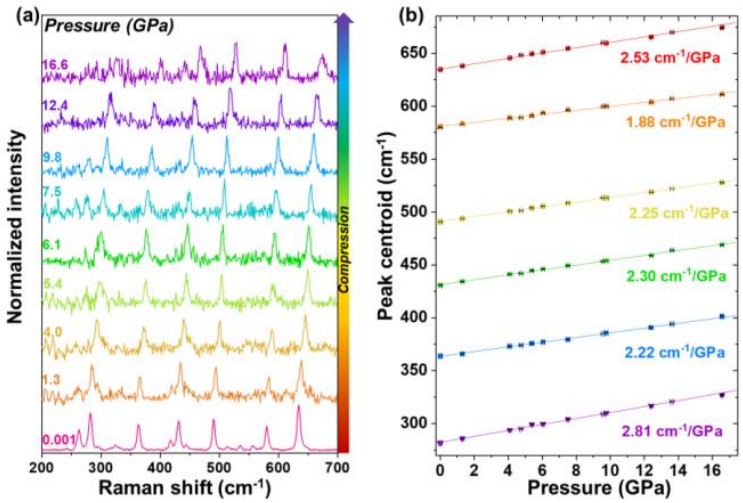

Figure S6. (a) Raman spectra of SrB_4O_7: $0.03Eu^{2+}$, $0.01Sm^{2+}$ at selected pressure values . (b) Pressure dependence of the experimental Raman-active mode frequencies in compression (filled symbols) and decompression (empty symbols); the continuous lines represent the applied linear fits.

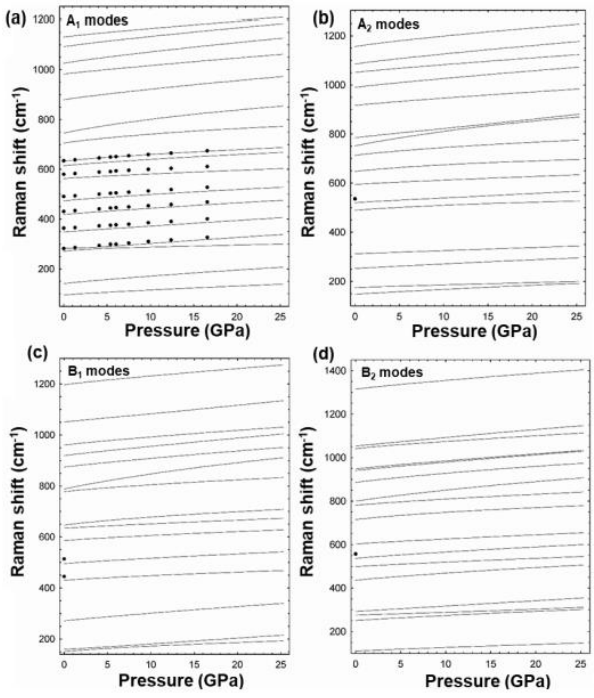

Figure S7. Theoretical (lines) and experimental (symbols) Raman-active mode frequencies of bulk SrB_4O_7 as a function of pressure.

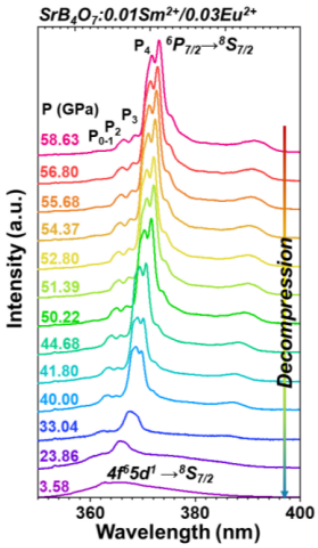

Figure S8. Non-normalized UV emission spectra of SrB_4O_7: 0.03 Eu^{2+}, 0.01Sm^{2+}, measured at the decompression cycle and room temperature under 280 nm excitation.

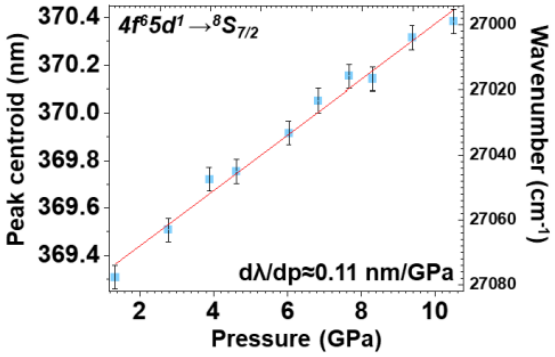

Figure S9. The spectral positions (peak centroid) of the $4f^65d^1 \rightarrow 4f^7(^8S_{7/2})$ transition of Eu^{2+} in the SrB_4O_7: 0.09 Eu^{2+}, 0.01Sm^{2+} sample, determined up to around 10.5 GPa, at which the Eu^{2+}-related $4f^65d^1 \rightarrow 4f^7$ emission is well-observed.

IV. Tables

Table S1. Cell parameters (*a*, *b*, *c*), atomic coordinates (*x*, *y*, *z*) at pressure = 0 GPa and 61 GPa based on theoretical calculation, bulk modulus (B_0) and its pressure derivative (B_0') of the SrB_4O_7 (space group $Pmn2_1$, no. 31).

SrB_4O_7 (0 GPa)	SrB_4O_7 (61 GPa)

a (Å)		10.7354			9.78803		
b (Å)		4.42930			4.11315		
c (Å)		4.23761			3.92452		
V(Å^3)		201.500			158.000		
Atomic species	Wyckoff positions	*x*	*y*	*z*	*x*	*y*	*z*
Sr(1)	2a	0	0.78832	0.49833	0	0.80675	0.45212
O(1)	2a	0	0.22619	-0.08078	0	0.18259	-0.08400
O(2)	4b	0.64085	0.35629	0.45492	0.62968	0.34336	0.42879
O(3)	4b	0.63502	0.72709	0.86377	0.63021	0.69282	0.88502
O(4)	4b	0.77752	0.13263	0.85989	0.76271	0.15059	0.88189
B(1)	4b	0.87849	0.32558	0.02622	0.87940	0.32986	0.02492
B(2)	4b	0.74904	0.82231	0.00294	0.78054	0.81736	0.01182
B_0(GPa) at 26 GPa		150.165					
B_0' at 26 GPa		4.12726					

Table S2. Theoretical elastic constants (in GPa) in SrB_4O_7 at ambient pressure. The experimental values taken from ref. [1] and the calculated values from ref. [2] have been also included for comparison.

	This work	**Ref.** [1]	**Ref.** [2]
C_{11}	282.2	304 (4)	318
C_{12}	77.9	70 (35)	132
C_{13}	60.8	49 (29)	90
C_{22}	328.7	268 (1)	370
C_{23}	49.4	55 (33)	114
C_{33}	359.5	378 (3)	355
C_{44}	110.8	139 (2)	106
C_{55}	127.8	120 (4)	87
C_{66}	120.8	133 (2)	124

Table S3. Elastic moduli B, G and E (in 0 GPa), Poisson's ratio (v)given in the Voigt, Reuss and Hill approximations, labeled with subscripts V, R and H in SrB_4O_7 at ambient conditions. A_U denotes the elastic anisotropy index.

	SrB_4O_7 at 0 GPa
B_V, B_R, B_H	149.62; 149.03; 149.33.
E_V, E_R, E_H	291.54; 288.29; 289.91.
G_V, G_R, G_H	124.03; 122.40; 123.22
v_V, v_R, v_H	0.175; 0.178; 0.176
B_V/G_V, B_R/G_R, B_H/G_H	1.206; 1.218; 1.212
A_U	0.071

Table S4. Theoretical and experimental Raman-active modes in SrB_4O_7 (in black) at ambient pressure. Values reported in ref. [3] (underlined) and ref. [4] (in brackets), which are compatible with our theoretical calculations, are also reported. The pressure dependence of the modes in bold font is shown in Figure 5e and S4. All values are in cm^{-1}.

Sym.	The.	Exp.	Sym.	The.	Exp.	Sym.	The.	Exp.
A_1^1	95.4	104, (102)	A_2^7	520.5	536, 535	A_2^{13}	916.7	926
B_2^1	110.1	117	B_2^8	536.8	557, 555, (535)	B_1^{12}	919.3	928, 930
B_2^2	130.1	142	**A_1^8**	**563.0**	**580, 580**	B_2^{14}	940.8	948, 938
A_1^2	141.4	151, (150)	B_1^6	585.9	609, (581)	B_2^{15}	948.2	962
A_2^1	147.3	156, (153)	A_2^8	594.6	616	B_1^{13}	960.4	969
B_1^1	150.6	160	B_2^9	602.9	634, (633)	A_1^{15}	982.7	995, 989, (988)
B_1^2	159.4		**A_1^9**	**614.3**	**635, 634, (633)**	A_2^{14}	989.9	997
A_2^2	174.3	(192)	A_1^{10}	632.9	641	B_1^{14}	1010.6	1012
B_2^3	250.9	242, (263)	B_1^7	634.2	650, (635)	A_1^{16}	1026.1	1046,1042
A_2^3	251.9	263, 263, (262)	B_1^8	646.4		B_2^{16}	1041.2	1055
B_1^3	271.2	282, (280)	A_2^9	647.4		B_1^{15}	1050.9	1068
A_1^3	**271.4**	**283, 282**	A_1^{11}	705.7	706, 705, (703)	A_2^{15}	1051.0	
B_2^4	275.3	(281)	A_2^{10}	713.2	720	B_2^{17}	1053.5	

A_1^4	282.3	294, (292)	B_2^{10}	715.1	730, (726)	A_2^{16}	1085.0	1138
B_2^5	292.4	301	A_1^{12}	745.2	741, (750)	A_1^{17}	1092.5	1100
A_2^4	311.8	325, 324, (325)	A_2^{11}	751.6	753	A_1^{18}	1131.2	1148
A_1^5	**348.4**	**364, 362, (361)**	B_1^9	777.5	781			1167
A_2^5	402.5	417	B_2^{11}	780.8		A_2^{17}	1156.0	1169,1167
A_1^6	**418.5**	**431, 431, (430)**	A_2^{12}	784.8	799			1176
B_1^4	430.4	445, 444, (442)	B_1^{10}	787.9		B_1^{16}	1196.9	
B_2^6	435.9	449, (439)	A_1^{13}	789.8	809, 807, (815)			1285
A_1^7	**473.8**	**491, 491, (490)**	B_2^{12}	799.6	814, (818)	B_2^{18}	1315.1	1345
A_2^6	489.6	500, (490)	B_1^{11}	874.1	890			1374
B_1^5	495.5	514, 513, (514)	A_1^{14}	879.7	888, 885, (886)			1501
B_2^7	498.8	517, (491)	B_2^{13}	886.1	893			1659

Table S5. Theoretical Raman-active zero-pressure mode frequencies and pressure coefficients of SrB_4O_7 according to a linear fit up to 5 GPa.

Sym.	(cm^{-1})	dω/dP (cm^{-1}/GPa)	Sym.	(cm^{-1})	dω/dP (cm^{-1}/GPa)	Sym.	(cm^{-1})	dω/dP (cm^{-1}/GPa)
A_1^1	95.4	2.2	A_2^7	520.5	2.0	A_2^{13}	916.7	3.1
B_2^1	110.1	1.8	B_2^8	536.8	3.2	B_1^{12}	919.3	3.8
B_2^2	130.1	3.4	A_1^8	563.0	2.0	B_2^{14}	940.8	4.1
A_1^2	141.4	3.2	B_1^6	585.9	2.2	B_2^{15}	948.2	4.0
A_2^1	147.3	2.1	A_2^8	594.6	1.9	B_1^{13}	960.4	3.4
B_1^1	150.6	2.5	B_2^9	602.9	2.5	A_1^{15}	982.7	3.6
B_1^2	159.4	2.0	A_1^9	614.3	2.8	A_2^{14}	989.9	3.8
A_2^2	174.3	1.2	A_1^{10}	632.9	3.0	B_1^{14}	1010.6	5.7
B_2^3	250.9	2.4	B_1^7	634.2	1.9	A_1^{16}	1026.1	4.9
A_2^3	251.9	2.0	B_1^8	646.4	3.6	B_2^{16}	1041.2	3.8
B_1^3	271.2	3.2	A_2^9	647.4	3.2	B_1^{15}	1050.9	3.3

A_1^3	271.4	2.3	A_1^{11}	705.7	4.0	A_2^{15}	1051.0	3.4
B_2^4	275.3	1.4	A_2^{10}	713.2	3.6	B_2^{17}	1053.5	3.9
A_1^4	282.3	1.6	B_2^{10}	715.1	3.9	A_2^{16}	1085.0	4.4
B_2^5	292.4	2.5	A_1^{12}	745.2	6.3	A_1^{17}	1092.5	4.4
A_2^4	311.8	1.4	A_2^{11}	751.6	6.5	A_1^{18}	1131.2	3.6
A_1^5	348.4	2.4	B_1^9	777.5	3.1	A_2^{17}	1156.0	4.7
A_2^5	402.5	1.7	B_2^{11}	780.8	3.2	B_1^{16}	1196.9	3.7
A_1^6	418.5	2.7	A_2^{12}	784.8	3.9	B_2^{18}	1315.1	4.3
B_1^4	430.4	2.0	B_1^{10}	787.9	6.5			
B_2^6	435.9	3.6	A_1^{13}	789.8	3.5			
A_1^7	473.8	2.7	B_2^{12}	799.6	5.5			
A_2^6	489.6	2.3	B_1^{11}	874.1	3.6			
B_1^5	495.5	2.3	A_1^{14}	879.7	4.5			
B_2^7	498.8	2.2	B_2^{13}	886.1	4.6			

Table. S6. Red-shift of the $4f^6 5d^1 \rightarrow 4f^7$ broad band in materials reported in literature.

Host matrix	Energy (cm^{-1})	Energy shift (cm^{-1}/GPa)	Pressure range (GPa)	Reference
$BaCN_2$		-384	0 - 5	[5]
$SrAl_2O_4$	18500	-375	0 - 4	[6]
$CaAl_2O_4$	22900	-290	0 - 10	[6]
$BaBr_2$	24700	-225	0 - 10	[7]
$BaBr_2$	21200	-200	10 - 27	[7]
EuF_2	30300	-175	0 - 8	[8]
SrF_2		-174	0 - 5	[9]
$CaBPO_5$	24800	-150	0 - 10	[6]
BaF_2		-139	2 - 7	[9]
Ba_2SiO_4	19600	-127	0 - 10	[6]
$Ca_2P_2O_7$	23300	-70	0 - 10	[6]

SrB_4O_7		-8.5	0 - 10	this work

Table S7. Performance of the reported optical pressure sensors based on the materials doped with $Ln^{2+/3+}$ or Cr^{3+}, operating with different manometric parameters - MP (line shift, FWHM, band ratio, lifetime). Some of the d(MP)/d*P* (cm^{-1}/GPa) values are estimated from spectra in the literature.

Active ion	**Host**	**Transition**	**MP**	**d(MP)/d*P* (nm/GPa)**	**d(MP)/d*P* (cm^{-1}/GPa)**	**FWHM (nm)**	**T-shift (nm/K)**	**λ (nm)**	**Ref.**
Eu^{2+}	SrB_4O_7	$^6P_{7/2}\rightarrow{}^8S_{7/2}$	line shift	0.17	-12.84	~0.22	4.8×10^{-4}	362.7	this work
Sm^{2+}	SrB_4O_7	$^5D_0\rightarrow{}^7F_0$	line shift	0.255	-5.41	0.2	-1×10^{-4}	685	[10]
Sm^{2+}	SrB_2O_4	$^5D_0\rightarrow{}^7F_0$	line shift	0.24	-5.11	0.15	-1×10^{-4}	685	[11]
Sm^{2+}	SrFCl	$^5D_0\rightarrow{}^7F_0$	line shift	1.1	~-22.8	0.15	-2.3×10^{-3}	690	[12]
Cr^{3+}	Al_2O_3	$^2E\rightarrow{}^4A_2$	line shift	0.365	~-7.6	0.75	6.8×10^{-3}	694	[13]
Cr^{3+}	$YAlO_3$	$^2E\rightarrow{}^4A_2$	line shift	0.70	~-13.4	~11.5	7.6×10^{-3}	723	[14]
Er^{3+}	YF_3	$^4F_{9/2}\rightarrow{}^4I_{15/2}$ (Stark)	line shift	0.186	-4.18	-	-3×10^{-4}	665	[15]
Er^{3+}	$NaBiF_4$	$^4I_{13/2}\rightarrow{}^4I_{15/2}$ (Stark)	line shift	-0.80	3.54	62	-	1503	[16]
Er^{3+}	SrF_2	$^4F_{9/2}\rightarrow{}^4I_{15/2}$	lifetime	7.7%	-	-	-	653	[17]
		$^4S_{3/2}\rightarrow{}^4I_{15/2}$	lifetime	6.4%	-	-	-	538	
		$^2H_{11/2}\rightarrow{}^4I_{15/2}$	lifetime	6.2%	-	-	-	516	
Nd^{3+}	$YAlO_3$	$^4F_{3/2}\rightarrow{}^4I_{9/2}$ (Stark)	line shift	-0.13	3.15	-	1×10^{-6}	875	[14]
Eu^{3+}	$Y_3Al_5O_{12}$	$^5D_0\rightarrow{}^7F_1$	line shift	0.197	-5.7	~0.5	-5.4×10^{-4}	591	[16]
Eu^{2+}	$BaLi_2Al_2Si_2N_6$	$4f^65d–4f^7$	line shift	1.58	~-53.32	~ 60.5	-	532	[18]
Sm^{3+}	$Y_3Al_5O_{12}$	$^4G_{5/2}\rightarrow{}^6H_{7/2}$ (Stark)	line shift	0.30	~-7.85	~3.81	2.3×10^{-4}	618	[19]
Tm^{3+}	$LaPO_4$	$^1G_4\rightarrow{}^3H_6$	line shift	0.1	~-4.43	14	-2×10^{-3}	475	[20]
		$^3H_4\rightarrow{}^3H_6$/ $^1G_4\rightarrow{}^3H_6$	band ratio	8%	-	-	-		
Ce^{3+}	$Y_6Ba_4(SiO_4)_6F_2$	$^2F_J\rightarrow{}^2D_J$ (excitation)	line width	2.5%	-	43	-	342	[21]

		$^2D_J \rightarrow {}^2F_J$ (emission)	line width	1.5%	-	124	-	466	
			line shift	0.63	-28.62	124	-	466	

References in Supporting information:

[1] I. Martynyuk-Lototska, T. Dudok, O. Mys, R. Vlokh, Elastic, piezooptic and acoustooptic properties of SrB_4O_7 and PbB_4O_7 crystals, Opt. Mater. (Amst). 31 (2009) 660–667. https://doi.org/10.1016/j.optmat.2008.06.020.

[2] V.I. Zinenko, M.S. Pavlovskii, A.I. Zaitzev, A.S. Krylov, A.S. Shinkorenko, Vibrational spectra and elastic piezoelectric and polarization properties of the α-SrB_4O_7 crystal, J. Exp. Theor. Phys. 115 (2012) 455–461. https://doi.org/10.1134/S1063776112080195.

[3] A.A. Sobol, V.E. Shukshin, A.I. Zaitsev, Raman spectroscopy of SrB_4O_7 single crystals in the temperature range 300–1273 K, Opt. Spectrosc. 121 (2016) 25–31. https://doi.org/10.1134/S0030400X16070201.

[4] J. Hanuza, M.Mączka, J. Lorenc, A.A. Kaminskii, P. Becker, L. Bohatý, Recent Advances in linear and nonlinear Raman spectroscopy I, J. Raman Spectrosc. 38 (2007) 1538–1553. https://doi.org/10.1002/jrs.

[5] Y. Masubuchi, S. Nishitani, S. Miyazaki, H. Hua, J. Ueda, M. Higuchi, S. Tanabe, Large red-shift of luminescence from $BaCN_2$:Eu^{2+} red phosphor under high pressure, Appl. Phys. Express. 13 (2020) 9–12. https://doi.org/10.35848/1882-0786/ab8055.

[6] C.E. Tyner, H.G. Drickamer, Studies of luminescence efficiency of Eu^{2+} activated phosphors as a function of temperature and high pressure, J. Chem. Phys. 67 (1977) 4116–4123. https://doi.org/10.1063/1.435388.

[7] T. Tröster, S. Schweizer, M. Secu, J.M. Spaeth, Luminescence of $BaBr_2$:Eu^{2+} under hydrostatic pressure, J. Lumin. 99 (2002) 343–347. https://doi.org/10.1016/S0022-2313(02)00371-X.

[8] P.J. Wang, H.G. Drickamer, High pressure optical studies of rare earth ions in CaF_2 and other fluorides, J. Chem. Phys. 4444 (1973) 4444–4446. https://doi.org/10.1063/1.1679005.

[9] D.B. Gatch, D.M. Boye, Y.R. Shen, M. Grinberg, Y.M. Yen, R.S. Meltzer, Pressure dependence of the impurity-trapped exciton emission in BaF_2: Eu and Bax $Sr_{1-x}F_2$: Eu, Phys. Rev. B - Condens. Matter Mater. Phys. 74 (2006) 3–8. https://doi.org/10.1103/PhysRevB.74.195117.

[10] F. Datchi, R. LeToullec, P. Loubeyre, Improved calibration of the SrB_4O_7:Sm^{2+} optical pressure gauge: Advantages at very high pressures and high temperatures, J. Appl. Phys. 81 (1997) 3333–3339. https://doi.org/10.1063/1.365025.

[11] M. Runowski, P. Woźny, V. Lavín, S. Lis, Optical pressure nano-sensor based on lanthanide doped SrB_2O_4:Sm^{2+} luminescence – Novel high-pressure nanomanometer,

Sensors Actuators, B Chem. 273 (2018) 585–591. https://doi.org/10.1016/j.snb.2018.06.089.

[12] P. Taylor, B. Lorenz, Y.R. Shen, W.B. Holzapfel, High Pressure Research : An International Characterization of the new luminescence pressure sensor SrFCl : Sm, (n.d.) 37–41.

[13] H.K. Mao, J. Xu, P.M. Bell, Calibration of the ruby pressure gauge to 800 kbar under quasi-hydrostatic conditions, J. Geophys. Res. 91 (1986) 4673. https://doi.org/10.1029/jb091ib05p04673.

[14] J.D. Barnett, S. Block, G.J. Piermarini, An optical fluorescence system for quantitative pressure measurement in the diamond-anvil cell, Rev. Sci. Instrum. 44 (1973) 1–9. https://doi.org/10.1063/1.1685943.

[15] S. Goderski, M. Runowski, P. Woźny, V. Lavín, S. Lis, Lanthanide Upconverted Luminescence for Simultaneous Contactless Optical Thermometry and Manometry-Sensing under Extreme Conditions of Pressure and Temperature, ACS Appl. Mater. Interfaces. 12 (2020) 40475–40485. https://doi.org/10.1021/acsami.0c09882.

[16] M.A. Antoniak, S.J. Zelewski, R. Oliva, A. Żak, R. Kudrawiec, M. Nyk, Combined Temperature and Pressure Sensing Using Luminescent $NaBiF_4$:Yb,Er Nanoparticles, ACS Appl. Nano Mater. 3 (2020) 4209–4217. https://doi.org/10.1021/acsanm.0c00403.

[17] M. Runowski, J. Marciniak, T. Grzyb, D. Przybylska, A. Shyichuk, B. Barszcz, A. Katrusiak, S. Lis, Lifetime nanomanometry-high-pressure luminescence of up-converting lanthanide nanocrystals-SrF_2:Yb^{3+},Er^{3+}, Nanoscale. 9 (2017) 16030–16037. https://doi.org/10.1039/c7nr04353h.

[18] Y. Wang, T. Seto, K. Ishigaki, Y. Uwatoko, G. Xiao, B. Zou, G. Li, Z. Tang, Z. Li, Y. Wang, Pressure-Driven Eu^{2+}-Doped $BaLi_2Al_2Si_2N_6$: A New Color Tunable Narrow-Band Emission Phosphor for Spectroscopy and Pressure Sensor Applications, Adv. Funct. Mater. 30 (2020) 1–10. https://doi.org/10.1002/adfm.202001384.

[19] N.J. Hess, G.J. Exarhos, Temperature and Pressure Dependence of Laser Induced Fluorescence in Sm: Yag “A New Pressure Calibrant, High Press. Res. 2 (1989) 57–64. https://doi.org/10.1080/08957958908201032.

[20] M. Runowski, A. Shyichuk, A. Tymiński, T. Grzyb, V. Lavín, S. Lis, Multifunctional Optical Sensors for Nanomanometry and Nanothermometry: High-Pressure and High-Temperature Upconversion Luminescence of Lanthanide-Doped Phosphates - $LaPO_4$/YPO_4:Yb^{3+}-Tm^{3+}, ACS Appl. Mater. Interfaces. 10 (2018) 17269–17279. https://doi.org/10.1021/acsami.8b02853.

[21] M. Runowski, P. Woźny, N. Stopikowska, Q. Guo, S. Lis, Optical Pressure Sensor Based on the Emission and Excitation Band Width (fwhm) and Luminescence Shift of Ce^{3+}-Doped Fluorapatite - High-Pressure Sensing, ACS Appl. Mater. Interfaces. 11 (2019) 4131–4138. https://doi.org/10.1021/acsami.8b19500.

5.4. Tm^{2+} activated SrB_4O_7 bifunctional sensor of temperature and pressure—highly sensitive, multi-parameter luminescence thermometry and manometry

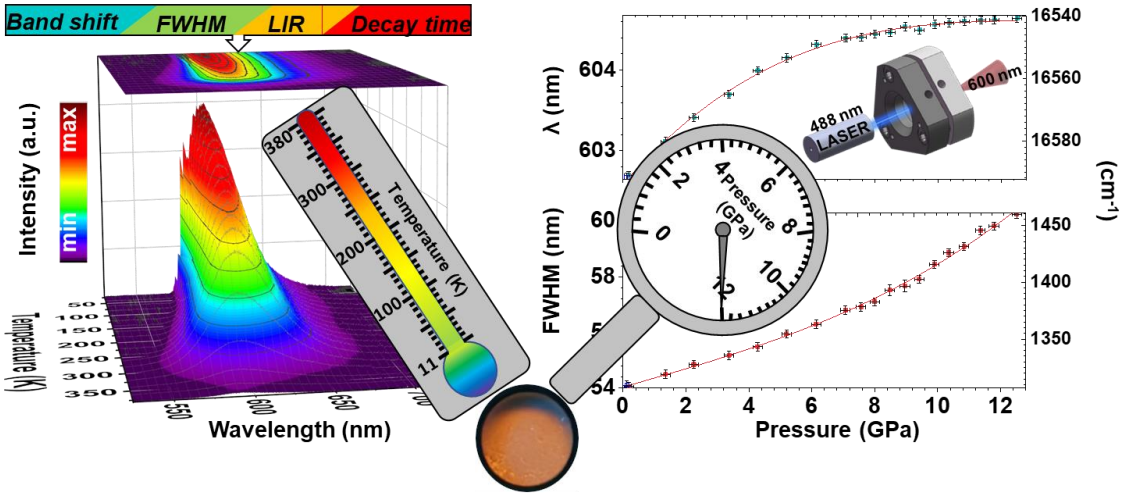

The result in this section were published in: Teng Zheng, Małgorzata Sójka, Marcin Runowski, Przemysław Woźny, Stefan Lis, and Eugeniusz Zych, Tm^{2+} Activated SrB_4O_7 Bifunctional Sensor of Temperature and Pressure — Highly Sensitive, Multi-Parameter Luminescence Thermometry and Manometry, Advanced Optical Materials, 2021, 2101507

Abstract of the section: Based on formal research, we have found that using the 5d-4f transition of Ln^{2+} for pressure sensing purposes can provide good and unexpected performances in manometry. Here, the Ph. D. candidate studied the Tm^{2+}-doped SrB_4O_7 phosphor material as a novel, contactless bifunctional and multimodal optical sensor for pressure and temperature measurement. The Ph. D. candidate synthesized a series of Tm^{2+} doped SrB_4O_7: samples using the high-temperature solid-state method in the air. The spectroscopic properties of SrB_4O_7:Tm^{2+} as a function of high pressure (up to ~13 GPa) and temperature (from 10 to 400 K) were investigated in detail. The 5d-4f emission band of Tm^{2+} exhibits a significant spectral shift in the spectrum and a broadening of the emission band with increment of both pressure and temperature. Such performance is due to a significant change of the vibronic components of the Tm^{2+} $4f^{12}5d \leftrightarrow 4f^{13}$ zero-phonon line. Excellent sensitivities to pressure (up to ~23.17 cm^{-1}/GPa) have been obtained using the emission bandwidth and its spectral position as pressure sensing parameters. Moreover, for the first time, optical temperature sensing can be realized *via* four different pathways in the synthesized material: bandwidth (3.85 cm^{-1}/K), band shift (1.44 cm^{-1}/K), band intensity ratio

(1.48 %/K) and luminescence lifetime (4.16 %/K), allowing good sensitivity to be maintained over a wide temperature range.

Contribution of Ph.D. student in this work: Conceptualization, material synthesis, structural and morphological characterization, conduction of the spectroscopic measurements, visualization, data analysis and curation, formal analysis, writing original draft and writing review & editing.

RESEARCH ARTICLE

ADVANCED OPTICAL MATERIALS
www.advopticalmat.de

Tm^{2+} Activated SrB_4O_7 Bifunctional Sensor of Temperature and Pressure—Highly Sensitive, Multi-Parameter Luminescence Thermometry and Manometry

Teng Zheng, Małgorzata Sójka, Marcin Runowski, Przemysław Woźny, Stefan Lis, and Eugeniusz Zych**

Noninvasive sensing of temperature and pressure offers new and exciting opportunities to investigate and monitor the variation of physicochemical and spectroscopic properties of materials under extreme conditions. In this work, Tm^{2+}-doped SrB_4O_7 phosphor material—a novel, contactless bifunctional, and multimodal optical sensor for pressure and temperature is reported. A series of SrB_4O_7: xTm^{2+} samples are synthesized via a high-temperature solid-state method in air. The impact of high pressure (up to ≈13 GPa) and temperature (from 10 to 400 K) on spectroscopic properties of SrB_4O_7:Tm^{2+} is investigated. The emission band of Tm^{2+} demonstrates a significant spectral shift and a band broadening as a function of both pressure and temperature. Such a result is a consequence of a significant change of vibronic components of the Tm^{2+} $4f^{12}5d \leftrightarrow 4f^{13}$ zero-phonon line. The emission bandwidth and its spectral position exhibit excellent sensitivities to pressure, that is, ≈23.17 and ≈–11.85 cm^{-1} GPa^{-1}, respectively. Furthermore, for the first time, it is shown that temperature sensing can be realized via four different pathways in a single material: i) bandwidth, ii) band shift, iii) band intensity ratio, and iv) luminescence lifetime, with maximal sensitivities of ≈3.85 cm^{-1} K^{-1}, 1.44 cm^{-1} K^{-1}, 1.48% K^{-1} and 4.16% K^{-1}, respectively.

1. Introduction

Pressure and temperature, as two fundamental physical quantities, affect all processes occurring in macroscopic environments, micron- and nano-sized areas, down to the interactions between atoms. Thus, different effects on the physicochemical characteristics of materials under extreme conditions of pressure and/or temperature, such as phase transitions, changes of spectroscopic and magnetic properties, as well as the formation of new materials, have been found.[1–8] Therefore, in the case of experiments carried out under extreme conditions, fast, precise, and non-invasive determination of temperature and/or pressure is crucial, alike in fundamental and technological research,[9–11] as well as for understanding the pressure- and/or temperature-induced changes taking place in materials and the corresponding pressure–temperature interdependences. Thus, in turn, it is important to precisely design materials of desired, predictable, and well-defined properties, which attract considerable attention of scientists and industrial manufacturers.

Compression of the materials may lead to a whole variety of effects, that is, the decrease of the unit cell volume, reduction of the crystal lattice constants, bonds shortening, as well as defects formation, phase transition, or amorphization causing alterations of the local environment symmetry, etc.[11,12] For a static high-pressure experiment in scientific research, the use of a diamond anvil cell (DAC) with an assemblage of a hydrostatic pressure transmitting media, an optical pressure sensor, and a very small amount of the sample (≈100–500 µm size), can meet the demand of uniform distribution of forces/pressure.[13–15] Such a technique allows observation of various photophysical changes taking place in the examined materials.[12] Currently, the most commonly used method for pressure determination in a DAC chamber is based on the fluorescence shift of Cr^{3+} R_1 line in ruby[16,17] or Sm^{2+} 0–0 ($^5D_0$–$^7F_0$) line in SrB_4O_7,[18–20] with the shift rates of ≈0.35 and ≈0.25 nm GPa^{-1}, respectively.

On the other hand, the use of thermosensitive phosphors as contactless temperature sensors offers fast, remote, high-sensitivity measurements with (sub)micron-sized resolution, surpassing conventional thermometers and thermocouples.[21–24] Furthermore, promising results have also been reported for cryogenic thermometry with the potential fields of applications in aerospace, superconducting magnets, macromolecular crystallography, and polar exploration.[25–30] However, the design of an effective contactless cryogenic thermometer with high thermal sensitivity is still an encountered challenge.

T. Zheng, M. Runowski, P. Woźny, S. Lis
Adam Mickiewicz University
Faculty of Chemistry
Uniwersytetu Poznańskiego 8, Poznań 61–614, Poland
E-mail: runowski@amu.edu.pl
M. Sójka, E. Zych
University of Wrocław
Faculty of Chemistry
14 F. Joliot-Curie, Wrocław 50–383, Poland
E-mail: eugeniusz.zych@chem.uni.wroc.pl
The ORCID identification number(s) for the author(s) of this article can be found under https://doi.org/10.1002/adom.202101507.

DOI: 10.1002/adom.202101507

In the case of temperature sensing, the most common approach in optical thermometry is the use of luminescence/fluorescence intensity ratio (LIR/FIR technique) of lanthanides 4f–4f transitions. This is due to the unique optical properties of lanthanide ions, such as long emission lifetimes, narrow absorption/emission lines, ladder-like electronic structure, possibility of excitation/emission in UV–vis–NIR spectral ranges, etc.[22,23,31] Despite the advantages of high repeatability, stability, and wide operating range, a limited number of reports have been published on Ln^{3+} doped thermometers exploiting the use of spectral position (peak centroid) or bandwidth (full width at half maximum, FWHM) of the emission band as thermometric parameters.[12,32,33] The possible reasons may be that the temperature-induced band shift or FWHM is usually small for 4f–4f transitions, compared to semiconducting quantum dots, carbon dots, gold clusters, etc.[32,34,35] A powerful strategy to overcome these limitations is to exploit the $4f^{n-1}5d^1$ excited configuration of the di- or tri-valent lanthanide ions (Ln^{2+}, Ln^{3+}), which is highly sensitive to the local coordination environment, and consequently to the contraction/expansion of the lattice volume caused by temperature or pressure changes.[10,11,36] Excellent stabilization of Ln^{2+} ions in strontium tetraborate (SrB_4O_7) host lattice has been reported,[37,38] demonstrating their high physicochemical stability at extreme conditions of pressure and temperature.[10]

In this work, we demonstrate Tm^{2+}-doped SrB_4O_7 material as a novel, highly sensitive, bifunctional, and multimodal (multiparameter) sensor for optical thermometry and manometry. We have stabilized thulium ion at its unusual +2 oxidation state in the synthesized materials, and used for the first time the luminescence properties of Tm^{2+} for either pressure sensing or temperature sensing. This material shows superior pressure sensitivity ($d(FWHM)/dP \approx 23.17\ cm^{-1}\ GPa^{-1}$, $d\lambda/dP \approx -11.85\ cm^{-1}\ GPa^{-1}$), comparing to the most used pressure sensor materials. Furthermore, to the best of our knowledge, SrB_4O_7:Tm^{2+} is the first example which can realize temperature sensing in four various pathways, that is, band shift, FWHM, decay time, and LIR, with very high sensitivity (maximal relative sensitivity = 4.16% K^{-1}) in a single material. The multi-parameter thermometry and manometry in Tm^{2+}-doped SrB_4O_7 material can compensate the shortcomings of sensors operating with only single parameter, providing high sensitivity in wide range of temperature or pressure. This multimodal sensor of temperature and pressure could be applied for monitoring either the temperature or pressure values of construction facilities such as bridges, buildings, and roads as a significant warning when the pressure or temperature exceeds a suitable range to prevent the occurrence of certain disasters.

2. Results and Discussion

2.1. Structural and Morphological Properties

In order to avoid phase segregation and minimize the concentration of defects caused by difference in the size of ionic radii (>11%) of Sr^{2+} and Tm^{2+},[39] which is induced by the ion substitution, a maximum doping concentration of 1 mol% Tm^{2+} was preserved, that is, $Sr_{1-x}B_4O_7$:xTm^{2+} (x = 0.001–0.01, Tm^{2+}). The description of the experimental part, including the synthesis and characterization of the phosphor is presented in Supporting Information file. Figure S1, Supporting Information, shows the measured powder X-ray diffraction (XRD) patterns of the SrB_4O_7:Tm^{2+} (0.1–1 mol%) materials. In the concentration range of x = 0.001–0.01, no noticeable impurity phases were detected, that is, the reflexes in the measured XRD patterns can be well indexed to the reference pattern of orthorhombic SrB_4O_7 phase (space group $Pmn2_1$), card no. 0712191, from the International Centre for Diffraction Data database.[40] **Figure 1**a shows a graphical representation of the orthorhombic SrB_4O_7 structure, depicting the coordination environment of ions embedded in the crystal lattice. In this crystal structure there is only one cationic site (point symmetry C_{2v}), where the Tm^{2+} ion substitutes the Sr^{2+} ion. Figure S2a–d, Supporting Information, presents SEM images of the obtained materials for different Tm^{2+} concentrations together with elemental mapping. All samples show similar morphology and size distribution of the micron-sized particles. The elemental mapping (Figure S2e–h, Supporting Information) and EDX spectra (Figure S2i, Supporting Information) confirm the presence of all the expected elements, Sr, B, O, and Tm, and their uniform distribution in the particles.

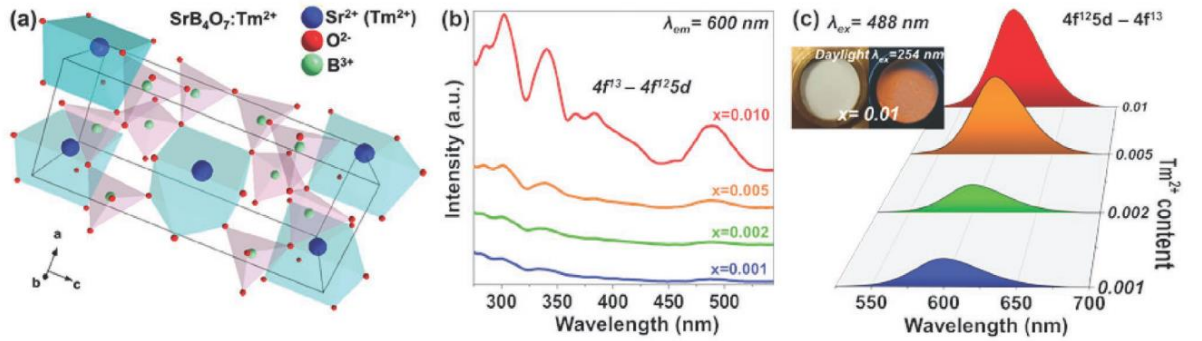

Figure 1. a) Graphical representation of the orthorhombic SrB_4O_7:Tm^{2+} crystal structure. b) Excitation spectra (λ_{em} = 600 nm) and c) emission spectra (λ_{ex} = 488 nm) of the $Sr_{1-x}B_4O_7$:xTm^{2+} samples (x = 0.001–0.01), and the corresponding luminescence photographs, taken in daylight and under 254 nm excitation.

2.2. Photoluminescence Properties at Ambient Conditions

The photoluminescence excitation (PLE) and emission spectra for the SrB_4O_7:Tm^{2+} (0.1–1 mol%) materials at ambient conditions are presented in Figure 1b,c. The PLE spectra (Figure 1b) show a broad structured band in the range of ≈250–550 nm, consisting of several peaks assigned to the Tm^{2+} $4f^{13} \rightarrow 4f^{12}5d$ transitions,[41] whose intensities increase with the Tm^{3+} concentration. These peaks are due to the effect of crystal-field splitting of the 5d levels.[42,43] Under excitation at 488 nm, all samples exhibit a single and broad emission band, centered ≈600 nm, whose intensity increases along with the dopant concentration (Figure 1c). This orange-red luminescence is attributed to the allowed interconfigurational $4f^{12}5d \rightarrow 4f^{13}$ transition of Tm^{2+}.[41] Detailed analysis of the Tm^{2+} luminescence will be discussed in the next paragraphs. The inset in Figure 1c presents a photograph of the sample taken in daylight under 254 nm excitation, clearly depicting its color of luminescence. Due to the most intense luminescence signal of the material containing the highest dopant concentration, that is, SrB_4O_7:$0.01Tm^{2+}$, it was selected for further experiments performed under high-pressure and temperature conditions.

In addition, the effect of the excitation wavelength (λ_{ex}) on the luminescence properties of the sample SrB_4O_7:$0.01Tm^{2+}$ was investigated.[30] The PL emission spectra, recorded at different λ_{ex} (see Figure S3, Supporting Information), reveal that the spectral position of the emission band is independent of the λ_{ex} used. The highest emission intensity was found upon 488 nm excitation, despite the fact more intense excitation bands are in the UV range. This is simply due to the greater intensity of the excitation light source (Xe-lamp) applied in the visible range.

2.3. Pressure Sensing Properties

The location (energy) of the lowest emitting level of the $4f^{12}5d^1$ excited configuration of Tm^{2+} is highly susceptible to alterations in the local coordination environment of the ion, which in turn can be affected by pressure and/or temperature changes.[10,44,45] The experimental setup applied for high-pressure luminescence measurements is schematically presented in **Figure 2**a. The experimental details of the DAC loading are given in the SI file. Normalized emission spectra of the sample SrB_4O_7:Tm^{2+} 1 mol% recorded in a DAC, under high pressure conditions up to 12.74 GPa, are shown in Figure 2b. As can be seen in the spectra presented in Figure 2b, a trace of ruby emission was found in the longer-wavelength band tail (≈670 nm) of the Tm^{2+} emission band. Another feature is located at ≈550 nm and appears when the pressure approaches 10 GPa. It corresponds to the zero-phonon lines (ZPLs), and possibly, to some extent to their vibronic components,[41] which will be discussed in detail in the next section.

Importantly, the $4f^{12}5d \rightarrow 4f^{13}$ emission band of Tm^{2+} undergoes a significant and monotonous, reversible redshift with the material compression. In other words, under high-pressure conditions, a decrease in the energy difference between the emitting level and the ground state is observed. This is due to the increased splitting of the 5d levels of Tm^{2+}, resulting from the strengthened crystal field when pressure increases.

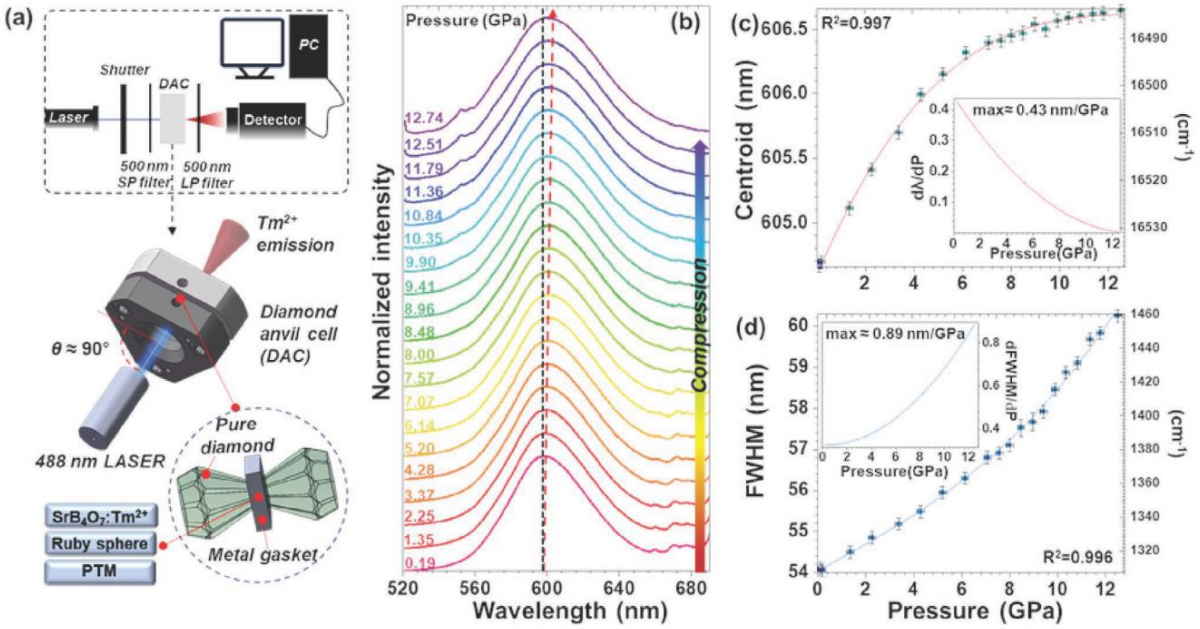

Figure 2. a) Scheme of the experimental setup used for high-pressure measurements. b) Normalized emission spectra for the SrB_4O_7:Tm^{2+} material, measured at different pressure values, under 488 nm laser excitation. c) The band centroid and d) FWHM of the Tm^{2+} emission band as a function of pressure. The filled symbols represent compression and the empty one decompression—they are practically indistinguishable due to the great reversibility. The inset of (c) and (d) is the corresponding determined sensitivity.

The redshift also results from the amplified nephelauxetic effect,[46,47] which is caused by the reduction of free-ion parameters with compression, associated with the increase of the covalent character of the Tm^{2+}—O^{2-} bonds.

On the other hand, the emission band also significantly and reversibly broadens with pressure, which can be clearly observed in Figure 2b. This effect is caused mainly by the I) pressure-induced enhancement of the crystal-field strength (improved band splitting); II) stronger electron–phonon coupling; III) increasing strains and distortions in the crystals.[48,49]

The calibration curves for the determined manometric (pressure sensitive) parameters, that is, band-shift and FWHM in compression–decompression cycles, are presented in Figure 2c. The band centroid of Tm^{2+} shifts from 604.69 to 606.61 nm (from 16 537.4 to 16 485.1 cm^{-1}) when the pressure increases from 0.19 to 12.74 GPa. The dependence of the band centroid as a function of pressure can be well-fitted (R^2 = 0.997) with a 3rd-order polynomial function. The pressure sensitivity expressed as $d\lambda/dP$ is presented in the inset of Figure 2c. The value of $d\lambda/dP$ decreases with increasing pressure, and reaches ≈–11.85 cm^{-1} GPa^{-1} at 0.19 GPa.

Furthermore, as mentioned above, a continuous broadening of the Tm^{2+} emission band was observed with increasing pressure. The calculated FWHM value of this band increases from ≈1307.0 cm^{-1} (54.06 nm) at the lowest pressure up to 1460.4 cm^{-1} (60.24 nm) at the highest pressure. The dependence of FWHM on pressure was also successfully fitted using a 3rd-order polynomial function (R^2 = 0.996). The determined pressure sensitivity, d(FWHM)/dP (see inset in Figure 2d) has the maximal value of ≈23.17 cm^{-1} GPa^{-1} at 12.74 GPa. Noteworthy, after decompression (see Figure 2c,d), when the pressure in DAC is released gradually to the ambient condition, the calculated band centroid (Figure 2c) and FWHM (Figure 2d) return to the values of the compression route, which indicates the great reversibility of both parameters under high pressure.

It is clear that the obtained shift-based sensitivity is higher, compared to the commonly used ruby[16,17] and SrB_4O_7:Sm^{2+} sensors[18–20] in the pressure range from ambient condition to 12 GPa, and similar to the value estimated for $Bi_2Al_4O_9$:Cr^{3+},[50] which classifies the developed luminescent manometer among the most sensitive pressure sensors. This indicates that the SrB_4O_7:Tm^{2+} material can be an excellent candidate for the highly sensitive pressure gauge. The determined fitting coefficients for both manometric parameters as a function of pressure, that is, band-shift and FWHM, are given in Table S1, Supporting Information.

2.4. Temperature Sensing Properties

The PLE spectra of the SrB_4O_7:0.01Tm^{2+} material were measured at 13, 100, 200, and 300 K and are presented in **Figure 3**a. The normalized excitation spectra show a similar band shape in the 13–300 K temperature range. Yet, at 13 K, numerous narrow lines are observed at the lower-energy side of the band, peaking at ≈480 nm. When the temperature increases to 100 K or above, the vibronic components are no longer exposed. As seen in Figure 3b, several narrow lines are clearly visible in the higher-energy part of the emission band. These results are very

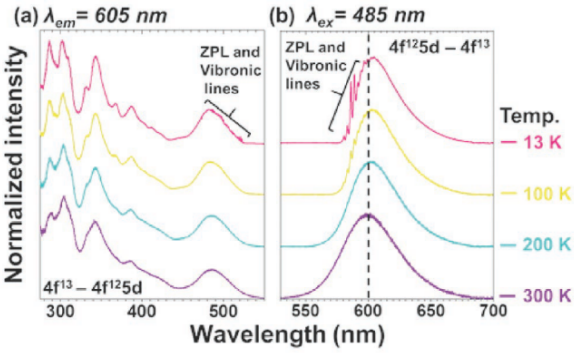

Figure 3. a) The normalized excitation and b) emission spectra of SrB_4O_7:Tm^{2+} material collected at 13, 100, 200, and 300 K.

similar to those reported by Schipper et al.,[41] where the authors attributed those narrow lines to the vibronic progression associated with a few ZPLs.[41] The vibronic component intensities decrease with temperature elevation, and a significant broadening and blue-shift of the Tm^{2+} $4f^{12}5d^1 \rightarrow 4f^{13}$ emission band is observed. Accordingly, such a significant band broadening in the higher energy (shorter wavelength) part of the emission band leads to a change in the bandwidth and its spectral position. Both effects may be used as thermometric parameters for temperature sensing purposes.

A simplified scheme of the experimental setup used for luminescence measurements under controlled temperature conditions is presented in **Figure 4**a. The technical details about temperature-dependent spectroscopic measurements are described in the SI file. Here, besides pressure sensing of the material, we investigated and used for the first time SrB_4O_7:Tm^{2+} as an optical thermometer, based on the temperature induced spectral shift, broadening of the emission band, LIR and decay time originating from the $4f^{12}5d^1 \rightarrow 4f^{13}$ transition of Tm^{2+}. For this purpose, the emission spectra of SrB_4O_7:Tm^{2+} were measured with high resolution, every 20 K, in the T-range of 13–380 K. Systematically, with increasing temperature, the emission band moves toward shorter wavelengths (especially the higher-energy part of the band), which can be clearly observed in the spectra in Figure 4b. As shown in the chromaticity diagram (CIE) in Figure 4c, when the temperature increases from 13 to 380 K, the luminescence color changes from red to orange-red.

To investigate the potential of the examined material as an optical thermometer, first, its thermometric performance was analyzed based on the bandwidth (FWHM) and spectral shift (band centroid) of the $4f^{12}5d \rightarrow 4f^{13}$ emission band of Tm^{2+}. It is worth noting that above 300 K, the FWHM as well as the band centroid change out of tendency with temperature due to thermal quenching of the emission intensity, indicating that the operating range of these sensing parameters of the thermometer is limited to 13–300 K (see Figure S4a,b, Supporting Information). Thus, we present in Figure 4d the dependence of the FWHM on temperature in the T-range of 13–300 K. The corresponding normalized spectra are shown in the inset. The FWHM increases significantly from 1004 to 1403 cm^{-1} (from 39.45 to 52.66 nm), when the temperature increases from 13 to 300 K. Thanks to unilateral expansion of the emission band,

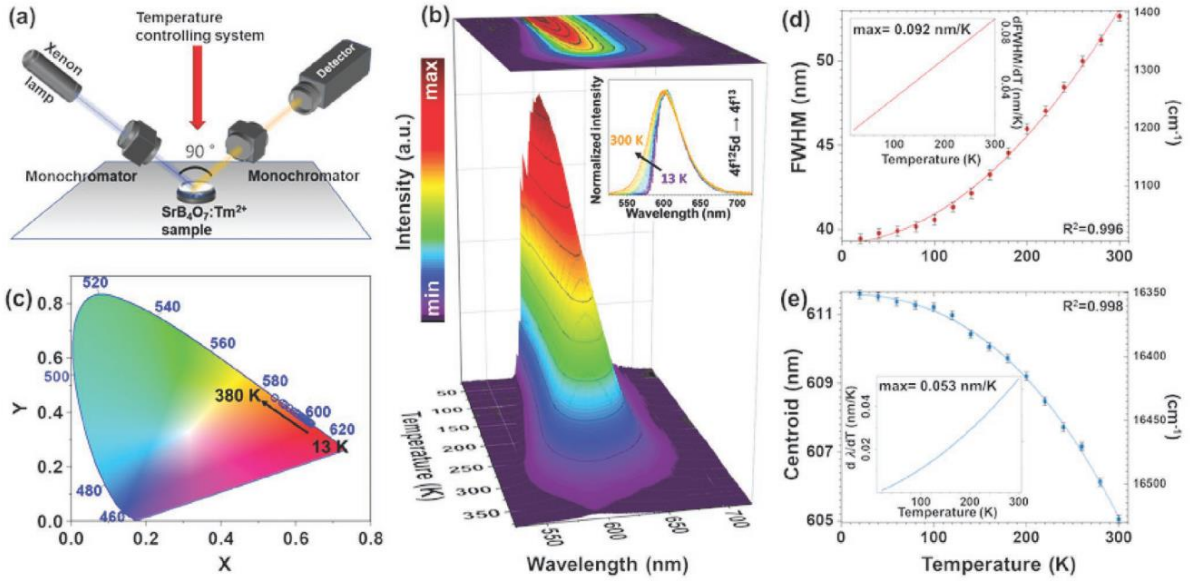

Figure 4. a) Scheme of the experimental setup used for temperature measurements. b) Emission spectra of SrB_4O_7:Tm^{2+} material measured in the *T*-range of 13–380 K; the inset shows the corresponding normalized emission spectra. c) CIE diagram for SrB_4O_7:Tm^{2+} as a function of temperature; λ_{ex} = 488 nm. d,e) The corresponding FWHM (d) and band centroid (e) of Tm^{2+} emission band as a function of temperature; the insets show the corresponding sensitivities as a function of temperature.

the band centroid shows a significant blue-shift from 16 351 to 16 529 cm^{-1} (from 611.6 to 605.0 nm), with increasing temperature from 13 to 300 K, respectively. Both parameters, that is, FWHM and band-shift were correlated with temperature, and successfully fitted to the 2nd- and 3rd-order polynomial functions, with R^2 = 0.993 and 0.998, respectively. The corresponding fitting parameters are listed in Table S1, Supporting Information. The determined temperature sensitivities for bandwidth (d(FWHM)/d*T*) as a function of temperature are presented in the inset of Figure 4d (red curve), revealing the maximal rate of the band broadening is ≈3.85 cm^{-1} K^{-1} at 300 K. The sensitivities for band-shift (dλ/d*T*) were also calculated (the blue curve in the inset of Figure 4e), showing the maximal shift rate is 1.44 cm^{-1} K^{-1} at 300 K.

The possibility of comparing the sensitivity of the SrB_4O_7:Tm^{2+} sensor with other luminescent thermometers using the emission band-shift or FWHM as thermometric parameter, is limited due to insufficient literature data. Several known examples are listed in **Table 1**. The performance of the developed SrB_4O_7:Tm^{2+} thermometer based on band-shift is comparable with the most sensitive $Na_4Mg_{0.940}Mn_{0.030}(WO_4)_3$ sensor material reported before, which is based on the d-block metal ion, that is, Mn^{4+}.[51] The performance of the other reported lanthanide-based band-shift thermometers is significantly inferior. Moreover, to the best of our knowledge, our sensor material presents the highest sensitivity among the reported lanthanide-based luminescent thermometers, when using the FWHM as a thermometric parameter (see Table 1).

In addition, we have also analyzed the ratiometric temperature sensing properties using the vibronic components and the broad band of Tm^{2+} d–f emission. It is clear in **Figure 5**a that the LIR of two vibronic components V_1 (located at ≈583.5 nm) and V_2 (at ≈586.1 nm), as well as the LIR of broad band emission (d–f; centered at ≈600 nm) to the most intense vibronic component V_2, significantly change with temperature. It is worth noting that, so far, there are no other reports about the use of vibronic components for temperature sensing purposes. As shown in Figure 5b,c, the LIR of V_1/V_2 and (d–f)/V_2 in the temperature range of 13–180 K (where V_1 and V_2 are observed) can be well fitted ($R^2 \geq 0.997$) to a 3rd- and 2nd-order polynomial functions (see Table S1, Supporting Information), respectively. The most reliable figure of merit for sensing based on band intensity ratio (as well as for the emission lifetimes) is relative sensitivity, S_r, which is usually expressed in %, and shows how the measured parameter changes per 1 K of absolute temperature.[51] The corresponding S_r values as a function of temperature were calculated according to Equation (1):

$$S_r = \frac{1}{LIR}\left|\frac{dLIR}{dT}\right| \times 100\% \quad (1)$$

As it can be seen in Figure 5d, for both (d–f)/V_2 and V_1/V_2, with increasing temperature, the S_r values increase first, and then decrease. The maximal S_r = 1.48% K^{-1} (at 82 K) and 0.86% K^{-1} (at 27 K) are achieved for the LIRs of (d–f)/V_2 and V_1/V_2, respectively. Please note that for determining the spectroscopic parameters as a function of temperature or pressure, the corresponding spectra were converted to the energy scale using the Jacobian transformation, minimizing quantitative error of the emission spectra analysis.[30,52]

Finally, we have measured the luminescence decay curves as a function of temperature for the $4f^{12}5d \rightarrow 4f^{13}$ transition of Tm^{2+}, in order to compare the results with the data reported by Solarz et al,[53] and to provide the missing theoretical model

Table 1. Temperature sensing performances, including maximal sensitivities for different luminescent thermometers based on the band-shift, FWHM, LIR, and emission lifetimes. Sensitivities marked with asterisks (*) are estimated from figures in the references.

Thermometers	Measured parameter	Maximal Sensitivity [x/K]	*T* [K]	*T*-range [K]	Ref.
$SrB_4O_7:Tm^{2+}$	band-shift	1.44 cm^{-1}	300	13–300	this work
LaF_3: Nd/LaF_3	band-shift	0.14 cm^{-1}	303–343	303–343	[32]
$LaPO_4:Tm^{3+}$, Yb^{3+}	band-shift	0.12 cm^{-1}	293–773	293–773	[48]
$Na_4Mg(WO_4)_3:Mn^{4+}$	band-shift	≈2.67 cm^{-1}*	300	100–400	[51]
$YAG:Ce^{3+}$	band-shift	−1.19 cm^{-1}	298–458	298–458	[60]
$YVO_4.Eu^{3+}$	band-shift	0.22 cm^{-1}*	700	250–700	[61]
$SrB_4O_7:Tm^{2+}$	FWHM	3.85 cm^{-1}	300	13–300	this work
$YAG:Ce^{3+}$	FWHM	−1.45 cm^{-1}	298–458	298–458	[60]
$YVO_4.Dy^{3+}$	FWHM	0.11 cm^{-1}	250–700	250–700	[61]
$YAlO_3$: Nd^{3+}	FWHM	≈0.21 cm^{-1}*	293–370	293–370	[62]
$SrB_4O_7:Tm^{2+}$	LIR	1.48%	82	13–180	this work
$LaPO_4:Tm^{3+}$, Yb^{3+}	LIR	3.0%	293	293–773	[48]
$NaYF_4$: Er^{3+}, Yb^{3+}	LIR	1.2%	300	16–300	[63]
SrF_2: Er^{3+}, Yb^{3+}	LIR	1.17%	300	298–383	[64]
Fluorotellurite glass: Er^{3+}	LIR	≈0.7%	550	83–863	[65]
α-$NaYF_4:Nd^{3+}$	LIR	0.96%	273	273–423	[66]
$Lu_2GeO_5:Pr^{3+}$	LIR	1.12%	515	150–550	[55]
$Lu_2SiO_5:Pr^{3+}$	LIR	3.54%	350	275–425	[55]
$Sr_2GeO_4:Pr^{3+}$	LIR	9.2%	65	25–275	[30]
α-$Ga_2O_3:Cr^{3+}$	LIR	1.05%	300	270–450	[67]
β-$Ga_2O_3:Cr^{3+}$	LIR	0.64%	300	210–450	[67]
$Bi_2Al_4O_9:Cr^{3+}$	LIR	1.24%	290	100–600	[68]
$ZnGa_2O_4:Cr^{3+}$	LIR	2.8%	310	77–450	[69]
$Bi_2Ga_4O_9:Cr^{3+}$	LIR	0.70%	300	80–450	[70]
$SrB_4O_7:Tm^{2+}$	lifetime	4.16%	337	13–400	this work
$KLu(WO_4)_2$: Ho^{3+}, Yb^{3+}	lifetime	0.39%	297	297–673	[71]
YVO_4: Ho^{3+}, Yb^{3+}	lifetime	1.35%	300	12–300	[72]
La_2O_3: Er^{3+}, Tm^{3+}, Yb^{3+}	lifetime	≈0.67%	298–333	298–333	[73]
$Gd_3Al_5O_{12}:Mn^{3+}$, Mn^{4+}	lifetime	2.08%	249	120–570	[74]
$Lu_2(Ge_{0.25}Si_{0.75})O_5$: Pr^{3+}	lifetime	1.45%	280	275–425	[74]
$Li(PO_3)_4$: Pr^{3+}	lifetime	0.62%	363	298–363	[75]
$Na(PO_3)_4$: Pr^{3+}	lifetime	0.59%	363	298–363	[75]
$K(PO_3)_4$: Pr^{3+}	lifetime	0.56%	363	298–363	[75]
PrP_5O_{14}	lifetime	0.46%	363	298–363	[75]
$Bi_2Ga_4O_9:Cr^{3+}$	lifetime	1.35%	500	10–500	[76]

for the experimental studies. Please note, that in the mentioned paper only the determined temperature-dependent lifetimes of Tm^{2+} were reported, and the obtained data were neither fitted to any function (which is crucial for temperature sensing), nor the theoretical model was provided. The recorded emission decay profiles show strong temperature dependence in the *T*-range of 13–400 K (**Figure 6**a). Therefore, it is tempting to use also this parameter for temperature detection. Figure 6b presents the temperature dependence of the determined lifetime values, derived from the single-exponential fits of the experimental decay curves. The resulting data points (emission lifetime values) can be well fitted using the double-barrier model and Equation (2):

$$\rho = \frac{1}{\tau} = \frac{1}{\tau_0} + \sum_{i=1}^{2} B_i \times \exp\left(-\frac{\Delta E_{ai}}{k_B T}\right) \quad (2)$$

where ρ and τ are the luminescence transition probability rate ($\rho_{NR} + \rho_R$) and decay time ($1/(\rho_{NR} + \rho_R)$), respectively; τ_0 represents radiative decay time ($1/\rho_R$) in the absence of luminescence quenching at low temperature; *B* is a parameter corresponding to the inverse of the nonradiative decay time at $T \rightarrow 0$ K; ΔE_a is

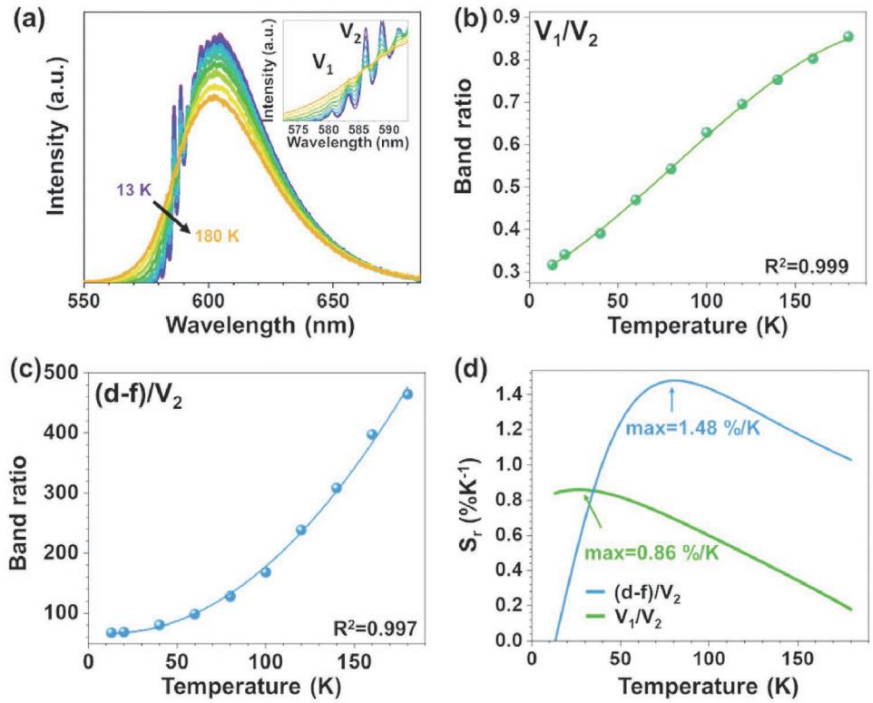

Figure 5. a) The emission spectra in temperature range of 13–180 K. The inset shows the magnified emission spectra focusing on the vibrational structure. Two vibronic components in the emission spectra located at 583.5 and 586.1 nm are marked as V_1 and V_2, respectively. b) The LIR between V_1 and V_2 components and c) the LIR between d–f broad band emission and V_2 component. d) The corresponding relative sensitivities (S_r) as a function of temperature.

the activation energy and k_B stands for Boltzmann constant (8.6177×10^{-5} eV K^{-1}). Table S2, Supporting Information, presents the derived fitting parameters.

The necessity of using two energy barriers results from the shape of the curve fitted to the experimental data points (Figure 6b). Yet, this is not a typical situation, as a single-barrier dependence is usually observed.[54–56] On the other hand, one may easily find examples in the literature where the single-barrier model is used, but the experimental points showed a clear deviation from it.[57] Such behavior indicates that two quenching processes operate to drain nonradiatively the electron, which happens to reach the 5d emitting level. The process controlled by lower activation energy is not efficient enough, however, to quench the $4f^{12}5d \rightarrow 4f^{13}$ emission completely and only when the E_{a2} energy barrier is rendered active at yet higher temperature the emission finally disappears. The dependence of photoconductivity on the energy of excitation photons can be of great help in dealing with this effect further, and could shed more light on its possible mechanism.[58,59]

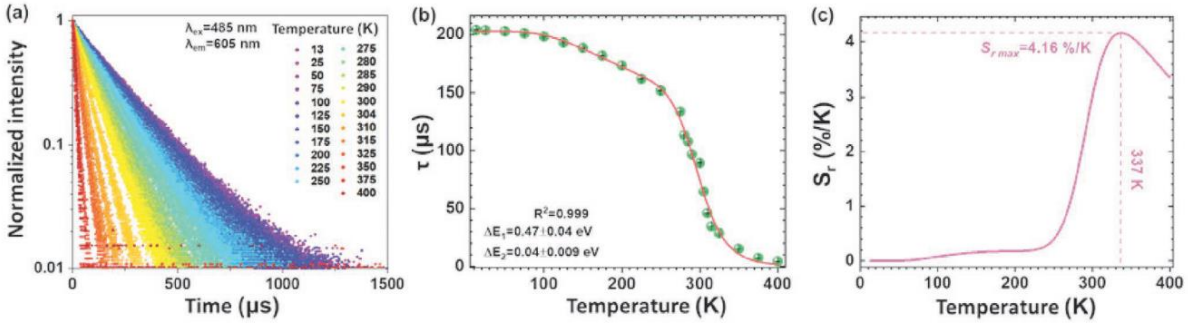

Figure 6. a) Luminescence decay curves for the SrB_4O_7:Tm^{2+} material (Tm^{2+}: 5d→4f transition), recorded in the *T*-range of 13–400 K, under 485 nm excitation. b) Temperature dependence of the determined luminescence lifetimes for Tm^{2+}. c) The corresponding relative sensitivity, S_r based on the Tm^{2+} emission lifetime.

Figure 6c presents the relative thermal sensitivity calculated according to the Equation (2) (where LIR is replaced with τ). The relative thermal sensitivity increases with temperature, until it reaches the maximal value of $S_{r\,max} = 4.16\%\ K^{-1}$ at 337 K. Afterward, S_r decreases to 3.36% K^{-1} at 400 K. As shown in Table 1, compared to other thermometers based on luminescence decay time, our material not only shows 4 parameters for temperature determination, but also, in each category, is one of the thermometers with the highest sensitivity within a relatively wide operating *T*-range. It is worth noting that the number of the reported optical thermometers in Table 1 are limited, due to the limited numbers reported for lanthanide or other transition metal ions based optical thermometer based on band-shift[32,48,51,60,61] and FWHM.[60–62] Please note that the developed sensor SrB_4O_7:Tm^{2+} is a very rare case among luminescence thermometers, where the relative sensitivity based on the decay time is higher than that obtained using the LIR. Thus, applying the developed optical thermometer, it is possible to measure temperature with very high sensitivity over the wide *T*-range.

The presented multi-parameter thermometry can overcome the disadvantages of a single temperature read-out approach, ensuring satisfactory relative thermal sensitivity in the whole temperature range studied. Summarizing performance of the thermometric parameters presented in Figures 4–6 and in Table 1, it seems that the concept of 4-paramter sensing allows temperature detection over the whole measured *T*-range, with good thermal sensitivity. In the cryogenic temperature range, that is, from ≈13 to 180 K the preferential (most sensitive) thermometric parameter is LIR, then from 100 to 300 K it is recommended to use band-shift or FWHM, and finally at the highest temperature range, that is, from 250 to 400 K (or higher) the best sensing pathway is based on the emission lifetimes. Last but not least, it should be mentioned that the SrB_4O_7:Tm^{2+} phosphor is not a perfect luminescence manometer or thermometer. Despite the very good performance, we are aware that the broadband luminescence of Tm^{2+} in SrB_4O_7:Tm^{2+} is a drawback, whose position, and consequently also shift, may be evaluated with a higher inaccuracy, compared to narrow ones. In addition, the high sensitivities are observed over narrow values of temperature or pressure only, while beyond these ranges they may fall to much lower values. This, however, is a quite common problem of reported luminescence sensors and may well be one of the important challenges to deal with in future.

3. Conclusions

We have developed a novel, very sensitive bifunctional and multi-parameter optical sensor of pressure and temperature, based on Tm^{2+} luminescence, operating in the visible spectral range (visual sensor). It was possible by the successful stabilization of thulium ion at its unusual +2 oxidation state (Tm^{2+}) in strontium tetraborate host matrices—SrB_4O_7, via a high-temperature solid-state preparation method. Their photoluminescence properties demonstrate a strong dependence on the state functions of pressure and temperature. An increase/decrease of pressure or temperature in the system results in the change of the spectral position (band centroid) of the $4f^{12}5d^1 \rightarrow 4f^{13}$ emission band, bandwidth (FWHM), its decay time (τ), and vibronic components. These phenomena are attributed to the change of vibronic components of the ZPLs of Tm^{2+} luminescence, enhanced strength of the crystal-field, improved electron–phonon coupling, and so forth.

The mentioned spectroscopic parameters were successfully correlated with pressure or temperature. The resulting sensing performances are remarkable, that is, $d(FWHM)/dP \approx 23.17\ cm^{-1}\ GPa^{-1}$, $d\lambda/dP \approx -11.85\ cm^{-1}\ GPa^{-1}$ (for manometry); $d\lambda/dT \approx 1.44\ cm^{-1}\ K^{-1}$ and $d(FWHM)/dT \approx 3.85\ cm^{-1}\ K^{-1}$ (for thermometry). In addition, the temperature dependence of the luminescence lifetime of Tm^{2+} $4f^{12}5d^1 \rightarrow 4f^{13}$ transition can also be effectively used for temperature readouts, showing an excellent thermal sensitivity of ≈4.2% K^{-1}. Hence, the use of the desired manometric or thermometric parameters allows very sensitive monitoring of either pressure or temperature in the system. This makes the SrB_4O_7:Tm^{2+} materials as truly multimodal and bifunctional luminescent sensors of these fundamental state functions. This work largely expands the scope of the applicability of Tm^{2+} activated phosphors, in both luminescence manometry and thermometry.

Supporting Information

Supporting Information is available from the Wiley Online Library or from the author.

Acknowledgements

This work was supported by the Polish National Science Centre, grant nos. 2016/23/D/ST4/00296, 2017/25/B/ST5/00824 and 2016/21/B/ST5/00110. T.Z. is also grateful to grant No. POWR.03.02.00–00-i020/17 financed by European Union through the European Social Fund under the Operational Program Knowledge Education Development. Publication partially financed by the program "Excellence Initiative–Research University".

Conflict of Interest

The authors declare no conflict of interest.

Data Availability Statement

Research data are not shared.

Keywords

luminescence thermometry, multifunctional sensors, multimodal luminescent thermometer, optical manometry, Tm^{2+} emission

Received: July 23, 2021
Revised: August 18, 2021
Published online:

[1] W. Kim, M. S. Jung, S. Lee, Y. J. Choi, J. K. Kim, S. U. Chai, W. Kim, D. G. Choi, H. Ahn, J. H. Cho, D. Choi, H. Shin, D. Kim, J. H. Park, *Adv. Energy Mater.* **2018**, *8*, 1702369.
[2] F. Bai, K. Bian, X. Huang, Z. Wang, H. Fan, *Chem. Rev.* **2019**, *119*, 7673.

[3] T. Yin, Y. Fang, W. K. Chong, K. T. Ming, S. Jiang, X. Li, J. L. Kuo, J. Fang, T. C. Sum, T. J. White, J. Yan, Z. X. Shen, *Adv. Mater.* **2018**, *30*, 1705017.
[4] L. Zhang, C. Liu, L. Wang, C. Liu, K. Wang, B. Zou, *Angew. Chem., Int. Ed.* **2018**, *57*, 11213.
[5] M. Somayazulu, P. Dera, A. F. Goncharov, S. A. Gramsch, P. Liermann, W. Yang, Z. Liu, H. K. Mao, R. J. Hemley, *Nat. Chem.* **2010**, *2*, 50.
[6] K. Randall McClain, C. A. Gould, K. Chakarawet, S. J. Teat, T. J. Groshens, J. R. Long, B. G. Harvey, *Chem. Sci.* **2018**, *9*, 8492.
[7] F. Q. Zu, *Metals* **2015**, *5*, 395.
[8] R. Tian, S. Zhang, M. Li, Y. Zhou, B. Lu, D. Yan, M. Wei, D. G. Evans, X. Duan, *Adv. Funct. Mater.* **2015**, *25*, 5006.
[9] S. Goderski, M. Runowski, P. Woźny, V. Lavín, S. Lis, *ACS Appl. Mater. Interfaces* **2020**, *12*, 40475.
[10] T. Zheng, M. Runowski, P. Woźny, S. Lis, V. Lavín, *J. Mater. Chem. C* **2020**, *8*, 4810.
[11] Y. Wang, T. Seto, K. Ishigaki, Y. Uwatoko, G. Xiao, B. Zou, G. Li, Z. Tang, Z. Li, Y. Wang, *Adv. Funct. Mater.* **2020**, *30*, 2001384.
[12] M. Runowski, in *Handbook of Nanomaterials in Analytical Chemistry*, (Ed. C. M. Hussain), Elsevier, New York **2019**, pp. 227–273.
[13] J. D. Barnett, S. Block, G. J. Piermarini, *Rev. Sci. Instrum.* **1973**, *44*, 1.
[14] W. A. Bassett, T. Takahashi, P. W. Stook, *Rev. Sci. Instrum.* **1967**, *38*, 37.
[15] G. J. Piermarini, C. E. Weir, *J. Res. Natl. Bur. Stand., Sect. A* **1962**, *66A*, 325.
[16] P. M. Bell, H. K. Mao, K. Goettel, *Science* **1984**, *226*, 542.
[17] H. K. Mao, J. Xu, P. M. Bell, *J. Geophys. Res.* **1986**, *91*, 4673.
[18] C. Zhao, H. Li, Y. Wang, J. Jiang, Y. He, *High Pressure Res.* **2017**, *37*, 18.
[19] Q. Jing, Q. Wu, L. Liu, J. A. Xu, Y. Bi, Y. Liu, H. Chen, S. Liu, Y. Zhang, L. Xiong, Y. Li, J. Liu, *J. Appl. Phys.* **2013**, *113*, 023507.
[20] F. Datchi, R. LeToullec, P. Loubeyre, *J. Appl. Phys.* **1997**, *81*, 3333.
[21] J. Rocha, C. D. S. Brites, L. D. Carlos, *Chem. - Eur. J.* **2016**, *22*, 14782.
[22] C. D. S. Brites, P. P. Lima, N. J. O. Silva, A. Millán, V. S. Amaral, F. Palacio, L. D. Carlos, *Nanoscale* **2012**, *4*, 4799.
[23] H. Peng, M. I. J. Stich, J. Yu, L. N. Sun, L. H. Fischer, O. S. Wolfbeis, *Adv. Mater.* **2010**, *22*, 716.
[24] Y. Gao, Y. Bando, *Nature* **2002**, *415*, 599.
[25] D. Ananias, F. A. A. Paz, D. S. Yufit, L. D. Carlos, J. Rocha, *J. Am. Chem. Soc.* **2015**, *137*, 3051.
[26] Z. Wang, D. Ananias, A. Carné-Sánchez, C. D. S. Brites, I. Imaz, D. Maspoch, J. Rocha, L. D. Carlos, *Adv. Funct. Mater.* **2015**, *25*, 2824.
[27] X. Liu, S. Akerboom, M. De Jong, I. Mutikainen, S. Tanase, A. Meijerink, E. Bouwman, *Inorg. Chem.* **2015**, *54*, 11323.
[28] Y. Cui, H. Xu, Y. Yue, Z. Guo, J. Yu, Z. Chen, J. Gao, Y. Yang, G. Qian, B. Chen, *J. Am. Chem. Soc.* **2012**, *134*, 3979.
[29] M. Back, J. Ueda, M. G. Brik, S. Tanabe, *ACS Appl. Mater. Interfaces* **2020**, *12*, 38325.
[30] M. Sójka, J. F. C. B. Ramalho, C. D. S. Brites, K. Fiaczyk, L. D. Carlos, E. Zych, *Adv. Opt. Mater.* **2019**, *7*, 1901102.
[31] C. D. S. Brites, P. P. Lima, N. J. O. Silva, A. Millán, V. S. Amaral, F. Palacio, L. D. Carlos, *Adv. Mater.* **2010**, *22*, 4499.
[32] U. Rocha, C. Jacinto Da Silva, W. Ferreira Silva, I. Guedes, A. Benayas, L. Martínez Maestro, M. Acosta Elias, E. Bovero, F. C. J. M. Van Veggel, J. A. García Solé, D. Jaque, *ACS Nano* **2013**, *7*, 1188.
[33] H. Kusama, O. J. Sovers, T. Yoshioka, *Jpn. J. Appl. Phys.* **1976**, *15*, 2349.
[34] Q. Dai, Y. Zhang, Y. Wang, M. Z. Hu, B. Zou, Y. Wang, W. W. Yu, *Langmuir* **2010**, *26*, 11435.
[35] L. M. Maestro, E. M. Rodríguez, F. S. Rodríguez, M. C. I. De La Cruz, A. Juarranz, R. Naccache, F. Vetrone, D. Jaque, J. A. Capobianco, J. G. Solé, *Nano Lett.* **2010**, *10*, 5109.
[36] M. Runowski, P. Woźny, V. Lavín, S. Lis, *Sens. Actuators, B* **2018**, *273*, 585.
[37] T. Zheng, M. Runowski, P. Woźny, S. Lis, *J. Alloys Compd.* **2020**, *822*, 153511.
[38] M. Suta, F. Lavoie-Cardinal, C. Wickleder, *Angew. Chem., Int. Ed.* **2020**, *59*, 10949.
[39] R. D. Shannon, *Acta Crystallogr., Sect. A: Found. Crystallogr.* **1976**, *32*, 751.
[40] A. Perloff, S. Block, *Acta Crystallogr.* **1966**, *20*, 274.
[41] W. J. Schipper, A. Meijerink, G. Blasse, *J. Lumin.* **1994**, *62*, 55.
[42] J. Grimm, O. S. Wenger, K. W. Krämer, H. U. Güdel, *J. Lumin.* **2007**, *126*, 590.
[43] O. M. Ten Kate, K. W. Krämer, E. Van Der Kolk, *Sol. Energy Mater. Sol. Cells* **2015**, *140*, 115.
[44] A. Baran, S. Mahlik, M. Grinberg, E. Zych, *J. Phys.: Condens. Matter* **2013**, *25*, 025603.
[45] K. Winskiewski, S. Mahlik, M. Grinberg, H. J. Seo, *J. Lumin.* **2011**, *131*, 306.
[46] S. Zhou, X. Wei, X. Li, Y. Chen, C. Duan, M. Yin, *Sens. Actuators, B* **2017**, *246*, 352.
[47] R. Reisfeld, C. K. Jørgensen, *Lasers and Excited States of Rare Earths*, Springer, New York **1977**.
[48] M. Runowski, A. Shyichuk, A. Tymiński, T. Grzyb, V. Lavín, S. Lis, *ACS Appl. Mater. Interfaces* **2018**, *10*, 17269.
[49] M. Runowski, P. Woźny, N. Stopikowska, Q. Guo, S. Lis, *ACS Appl. Mater. Interfaces* **2019**, *11*, 4131.
[50] M. Back, J. Ueda, H. Hua, S. Tanabe, *Chem. Mater.* **2021**, *33*, 3379.
[51] D. K. Amarasinghe, F. A. Rabuffetti, *Chem. Mater.* **2019**, *31*, 10197.
[52] J. Mooney, P. Kambhampati, *J. Phys. Chem. Lett.* **2013**, *4*, 3316.
[53] P. Solarz, J. Komar, M. Głowacki, M. Berkowski, W. Ryba-Romanowski, *RSC Adv.* **2017**, *7*, 21085.
[54] J. Pejchal, M. Nikl, E. Mihokova, A. Novoselov, A. Yoshikawa, R. T. Williams, *J. Lumin.* **2009**, *129*, 1857.
[55] M. Sójka, C. D. S. Brites, L. D. Carlos, E. Zych, *J. Mater. Chem. C* **2020**, *8*, 10086.
[56] K. Fiaczyk, S. Omagari, A. Meijerink, E. Zych, *J. Lumin.* **2018**, *198*, 163.
[57] J. Ueda, A. Meijerink, P. Dorenbos, A. J. J. Bos, S. Tanabe, *Phys. Rev. B* **2017**, *95*, 014303.
[58] E. Van Der Kolk, P. Dorenbos, C. W. E. Van Eijk, S. A. Basun, G. F. Imbusch, W. M. Yen, *Phys. Rev. B: Condens. Matter Mater. Phys.* **2005**, *71*, 165120.
[59] J. Ueda, S. Tanabe, T. Nakanishi, *J. Appl. Phys.* **2011**, *110*, 053102.
[60] W. Zhang, G. Wang, Z. Cai, G. W. Baxter, S. F. Collins, *Opt. Mater. Express* **2016**, *6*, 3482.
[61] A. Ćirić, S. Stojadinović, M. D. Dramićanin, *Sens. Actuators, A* **2019**, *295*, 450.
[62] M. A. Hernández-Rodríguez, A. D. Lozano-Gorrín, I. R. Martín, U. R. Rodríguez-Mendoza, V. Lavín, *Sens. Actuators, B* **2018**, *255*, 970.
[63] S. Zhou, K. Deng, X. Wei, G. Jiang, C. Duan, Y. Chen, M. Yin, *Opt. Commun.* **2013**, *291*, 138.
[64] S. Balabhadra, M. L. Debasu, C. D. S. Brites, R. A. S. Ferreira, L. D. Carlos, *J. Phys. Chem. C* **2017**, *121*, 13962.
[65] M. Haouari, A. Maaoui, N. Saad, A. Bulou, *Sens. Actuators, A* **2017**, *261*, 235.
[66] D. Wawrzynczyk, A. Bednarkiewicz, M. Nyk, W. Strek, M. Samoc, *Nanoscale* **2012**, *4*, 6959.
[67] M. Back, J. Ueda, H. Nambu, M. Fujita, A. Yamamoto, H. Yoshida, H. Tanaka, M. G. Brik, S. Tanabe, *Adv. Opt. Mater.* **2021**, *9*, 2100033.
[68] M. Back, J. Ueda, J. Xu, K. Asami, M. G. Brik, S. Tanabe, *Adv. Opt. Mater.* **2020**, *8*, 2000124.

[69] J. Ueda, M. Back, M. G. Brik, Y. Zhuang, M. Grinberg, S. Tanabe, *Opt. Mater.* **2018**, *85*, 510.
[70] M. Back, E. Trave, J. Ueda, S. Tanabe, *Chem. Mater.* **2016**, *28*, 8347.
[71] O. A. Savchuk, J. J. Carvajal, M. C. Pujol, E. W. Barrera, J. Massons, M. Aguilo, F. Diaz, *J. Phys. Chem. C* **2015**, *119*, 18546.
[72] M. K. Mahata, T. Koppe, K. Kumar, H. Hofsäss, U. Vetter, *Sci. Rep.* **2016**, *6*, 25590.
[73] A. Siaï, P. Haro-González, K. Horchani-Naifer, M. Férid, *Sens. Actuators, B* **2016**, *234*, 541.
[74] L. Marciniak, K. Trejgis, *J. Mater. Chem. C* **2018**, *6*, 7092.
[75] S. Gharouel, L. Labrador-Páez, P. Haro-González, K. Horchani-Naifer, M. Férid, *J. Lumin.* **2018**, *201*, 372.
[76] M. Back, J. Ueda, M. G. Brik, T. Lesniewski, M. Grinberg, S. Tanabe, *ACS Appl. Mater. Interfaces* **2018**, *10*, 41512.

WILEY-VCH

Supporting Information

Tm^{2+} activated SrB_4O_7 Bifunctional Sensor of Temperature and Pressure - Highly-sensitive, Multi-parameter Luminescence Thermometry and Manometry

Teng Zheng, Małgorzata Sójka, Marcin Runowski,* Przemysław Woźny, Stefan Lis, Eugeniusz Zych*

Experimental part

Materials and synthesis. $SrCO_3$ (99.9%, Sigma-Aldrich), H_3BO_3 (pure p.a., Chempur Poland), and Tm_2O_3 (99.99%, Stanford Materials) were used as starting materials. A high-temperature solid-state method in the air was exploited to synthesize the $Sr_{1-x}B_4O_7$: $x$$Tm^{2+}$ (x=0.001, 0.002, 0.005 and 0.01) materials. Stoichiometric amounts of $SrCO_3$, H_3BO_3, and Tm_2O_3 were ground for 20 min in an agate mortar. Then the mixture was transferred to a porcelain crucible and covered with a lid. Subsequently, a preliminary heat-treatment was performed at 700 ^{o}C for 5 h. Then, the sample was ground and heated twice at 850 ^{o}C for 5 h. Such materials were ground before measurements were executed.

Characterization at ambient condition. Structural characterization was performed by powder X-ray diffraction (XRD) measurements with a Brucker AXS D8 Advance diffractometer, using Cu $K_{\alpha1}$ radiation (λ=1.5406 Å). The measurements were executed in the 10-60 degree range and the step of 0.05 degree. The morphological characterization and elemental mapping based on the energy-dispersive X-ray (EDX) analysis, were made using an FEI Quanta 250 FEG scanning electron microscope with an EDAX detector. The emission and excitation spectra at ambient condition were

measured using a Hitachi F-7000 spectrofluorometer at ambient conditions, and the powder samples were mounted in a quartz holder. The spectra were corrected for the apparatus response of the system.

DAC loading procedure. A Merrill-Bassett diamond anvil cell (DAC) was applied for the high-pressure measurements. The pressure inside DAC chamber was tuned using three metal screws. The metal gasket used for DAC was made of stainless-steel sheet, with thickness of 250 μm and a hole size of ≈150 μm. The gaskets were pre-indented to 80 μm (sample thickness). The sample and a single micron-sized ruby ball (< 10 μm in diameter) were loaded in the DAC chamber. Subsequently, the pressure transmitting medium (solvent system of methanol/ethanol/water=16:3:1(vol.)) was then filled in the DAC chamber, to maintain hydrostatic conditions during the compression process.

Photoluminescence measurements at high-pressure conditions. The high-pressure studies of photoluminescence properties were performed using Andor Shamrock 500i Spectrograph equipped with a detector of iDus (silicon) CCD camera. A focusable, 488 nm continuous wave laser was applied as an excitation light source. The sample in the DAC was placed in an optimal configuration with 180° detection geometry (back-illuminated configuration). The 488 nm laser light was focused on the sample and the emission light was collected from the opposite side of the DAC. All spectra were corrected for the apparatus response of the system.

Pressure Calibration. The shift of the ruby R_1 fluorescence line was monitored to determine the pressure value in the system. The pressure values in DAC were determined based on the standard ruby calibration curve, provided in http://kantor.50webs.com/ruby.htm.

Photoluminescence measurements at controlled temperature conditions.

The temperature-dependent measurements were performed using an FLS1000 Fluorescence spectrometer (Edinburgh Instruments Ltd.) equipped with a 450W Xenon arc lamp as a continuous

excitation source. The spectra were recorded in the 13 – 480 K temperature range with the 20 K step, using a Hamamatsu R928P high-gain photomultiplier cooled to -22 °C with a Peltier plate. Emission spectra were corrected for the wavelength dependence of the spectral response of the recording system and excitation spectra were corrected for the incident light intensity. The luminescence decay curves were measured using a 60 W Xenon flash lamp. A closed-cycle helium cryostat operating under the control of a Model 336 temperature controller from Lake Shore Cryotronics, Inc. was used to control the temperature. The sample was mounted on a Cu-holder using Silver Adhesive 503 from Electron Microscopy Sciences.

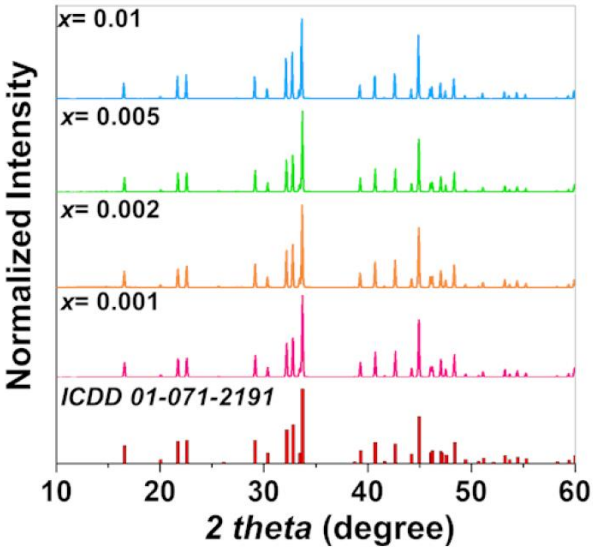

Figure S1. Powder XRD patterns of SrB_4O_7:$x$$Tm^{2+}$ samples (x=0.001, 0.002, 0.005 and 0.01) with reference pattern (ICDD no. 01-071-2191).

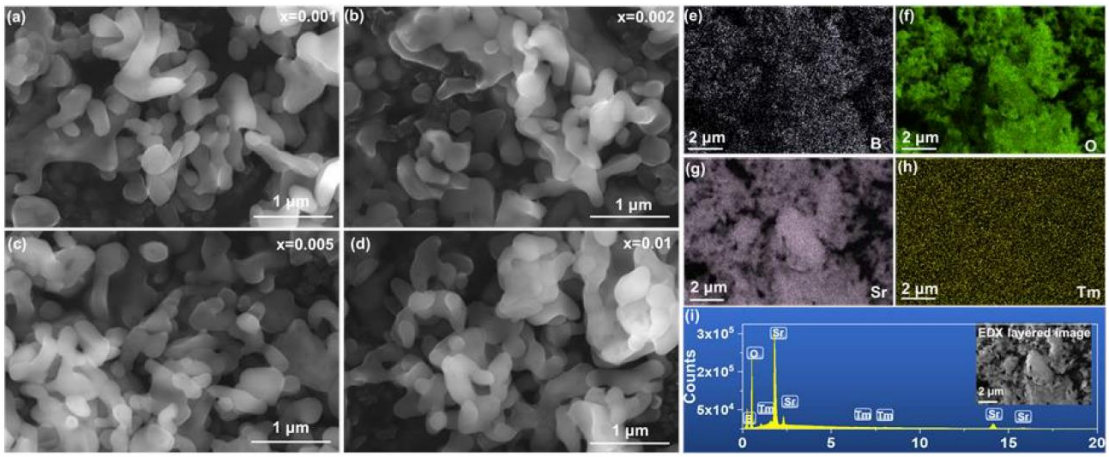

Figure S2. (a-d) SEM images of the SrB_4O_7:$x$$Tm^{2+}$ samples (x=0.001-0.01). (e-h) Elemental mapping and (i) EDX spectrum of the SrB_4O_7:0.01Tm^{2+} sample.

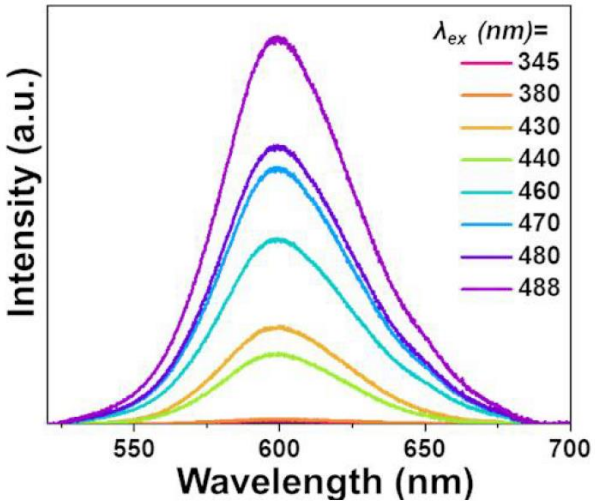

Figure S3. Emission spectra of the SrB_4O_7:0.01Tm^{2+} sample at different excitation wavelengths.

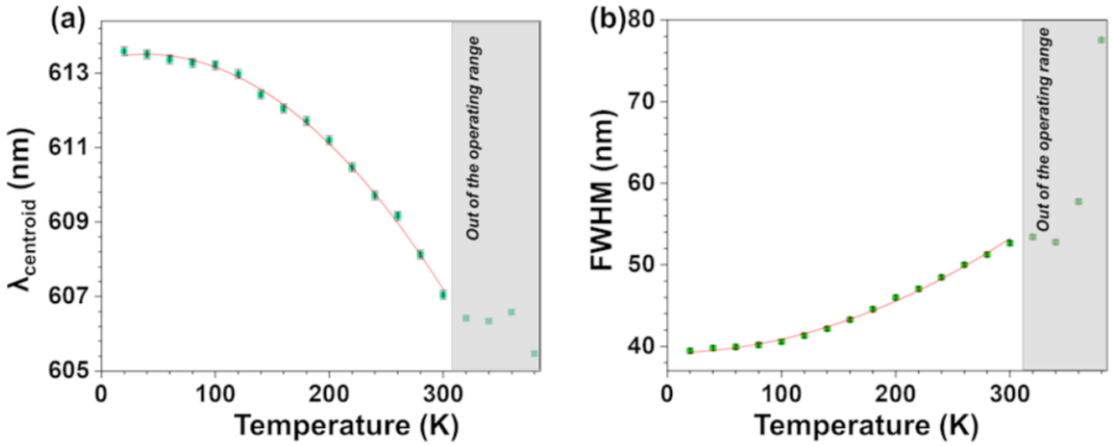

Figure S4. (a) The band centroid and (b) FWHM of Tm^{2+} emission band in whole measured temperature range. The shaded area marks the region in where the thermometric parameters become relatively random due to the thermally-induced signal quenching (close to noise level), indicating that optical thermometer being out of its operating range.

Table S1. Determined fitting parameters by using 2nd ($y=B_0+B_1x+B_2x^2$) or 3rd-order ($y=B_0+B_1x+B_2x^2+B_3x^3$) polynomial functions, for pressure and temperature measurements. MP represents the measured spectroscopic parameter.

State function	MP	B_0	B_1	B_2	B_3	R^2
Pressure	$\lambda_{Centroid}$	604.59	0.44	-0.03	7.94×10^{-4}	0.997

	FWHM	54.04	0.33	-7.44×10^{-4}	1.24×10^{-3}	0.996
Temperature	$\lambda_{Centroid}$	611.57	8.37×10^{-4}	-4.46×10^{-5}	-1.00×10^{-7}	0.998
	FWHM	39.18	3.02×10^{-3}	1.45×10^{-4}	-	0.996
	LIR (V_1/V_2)	0.28	2.19×10^{-3}	1.94×10^{-5}	-7.91×10^{-8}	0.998
	LIR (d-f/V_2)	69.75	-0.39	1.47×10^{-2}	-	0.997

Table S2. Fitting parameters obtained by means of double-barrier model function based on decays of 5d→4f luminescence.

$$\rho = \frac{1}{\tau} = \frac{1}{\tau_0} + \sum_{i=1}^{2} \mathrm{B}_i \times \exp\left(-\frac{\Delta E_{ai}}{k_B T}\right)$$

τ_0 (s^{-1})	B_1	E_{a1} (eV)	B_2	E_{a2} (eV)	R^2
4765.88	4.49E11	0.47	8337.32	0.04	0.999

6. physicochemical characterization and novel sensing strategies of non-linear optical thermometry based Ln^{3+} doped $BaTiO_3$ materials

6.1. Nonlinear optical thermometry—a novel temperature sensing strategy via second harmonic generation (SHG) and upconversion luminescence in $BaTiO_3$: Ho^{3+}, Yb^{3+} perovskite

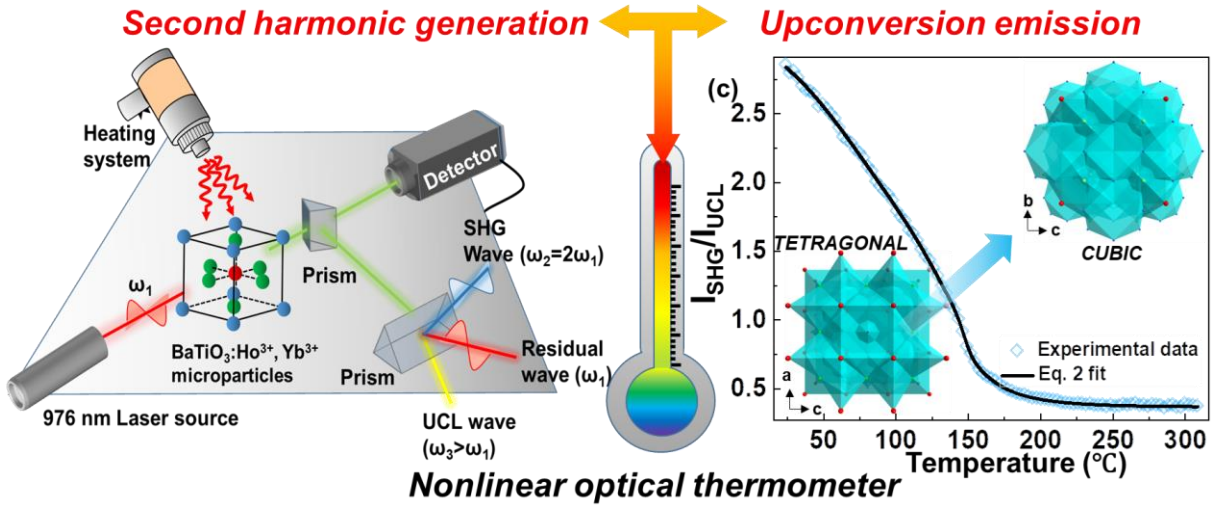

The result in this section were published in: Teng Zheng, Marcin Runowski, Inocencio R. Martín, Stefan Lis, Mauricio Vega, and Jaime Llanos, Nonlinear Optical Thermometry — A Novel Temperature Sensing Strategy via Second Harmonic Generation (SHG) and Upconversion Luminescence in $BaTiO_3$: Ho^{3+}, Yb^{3+} Perovskite, Advanced Optical Materials, 2021, 9, 2100386.

Abstract of the section: The Ph. D. candidate had the opportunity to participate in preliminary research on SHG related non-linear optical spectroscopy in the $BaTiO_3$ host lattice. The study of non-linear optical spectroscopy in the $BaTiO_3$ host lattice is motivated by the simultaneous observation of SHG and UCL, as well as interesting phases adopted at the wide temperature of $BaTiO_3$. SHG is a powerful tool for sensing of various intrinsic properties related to the symmetry change of materials. The Ph. D. candidate studied the feasibility of the optical temperature sensing method via the simultaneous use of SHG and UCL processes in $BaTiO_3$:Ho^{3+}, Yb^{3+}. Under NIR laser excitation, the evolution of SHG and UCL band intensity ratio was correlated with temperature and calibrated within the temperature range of 25 - 305 ℃. The band intensity ratio between SHG and UCL allows the detection of phase transitions from non-centrosymmetric to

centrosymmetric systems, and vice versa. From the point of view of luminescent temperature sensing, the study reported provides a novel and effective approach to optical temperature sensing - non-linear optical thermometry, with high sensitivity of up to 2.78 % $℃^{-1}$.

Contribution of Ph.D. student in this work: Conceptualization, structural and morphological characterization, conduction of the spectroscopic measurements, visualization, data analysis and curation, formal analysis, writing original draft and writing review & editing.

ADVANCED OPTICAL MATERIALS
www.advopticalmat.de

Nonlinear Optical Thermometry—A Novel Temperature Sensing Strategy via Second Harmonic Generation (SHG) and Upconversion Luminescence in $BaTiO_3:Ho^{3+},Yb^{3+}$ Perovskite

Teng Zheng, Marcin Runowski, Inocencio R. Martín, Stefan Lis, Mauricio Vega, and Jaime Llanos*

Nonlinear optical spectroscopy may be a powerful tool for sensing of various intrinsic properties of materials and different state functions of the system. This is due to the strong dependence of nonlinear phenomena on numerous physicochemical factors. The feasibility of simultaneously employing the second harmonic generation (SHG) and upconversion luminescence (UCL) processes in $BaTiO_3:Ho^{3+},Yb^{3+}$ for optical temperature sensing is demonstrated for the first time. Under 976 nm laser excitation, the evolution of the SHG and UCL band intensity ratio is correlated with temperature and calibrated within the temperature range of 25–305 °C. The band intensity ratio between SHG and UCL exhibits a sigmoidal dependence on temperature, and, hence, it can allow the detection of phase transitions from non-centrosymmetric to centrosymmetric systems, and vice versa. Most importantly, from the perspective of optical temperature sensing, this work provides a novel and effective strategy for nonlinear optical thermometry, with high sensitivity of up to 2.78% $°C^{-1}$.

T. Zheng, Dr. M. Runowski, Prof. S. Lis
Adam Mickiewicz University
Faculty of Chemistry
Uniwersytetu Poznańskiego 8, Poznań 61–614, Poland
E-mail: runowski@amu.edu.pl

Dr. M. Runowski, Prof. I. R. Martín
Universidad de La Laguna
Instituto de Materiales y Nanotecnología IMN
Departamento de Física
Apdo. Correos 456, Santa Cruz de Tenerife, San Cristóbal de La Laguna, Tenerife E-38200, Spain

Dr. M. Vega
Departament de Química Inorgànica and Institut de Recerca de Química Teòrica i Computacional
Universitat de Barcelona
Diagonal 645, Barcelona 08028, Spain

Dr. M. Vega
Departamento de Química
Universidad Católica del Norte
Avda. Angamos, Antofagasta 0610, Chile

Dr. J. Llanos
Departamento de Química
Universidad Católica del Norte
P.O. Box 1280, Antofagasta, Chile

The ORCID identification number(s) for the author(s) of this article can be found under https://doi.org/10.1002/adom.202100386.

DOI: 10.1002/adom.202100386

1. Introduction

In the realm of nonlinear optics, second harmonic generation (SHG) and upconversion luminescence (UCL) phenomena emerge as very important and fundamental second-order nonlinear optical processes. SHG is a polarization-sensitive, instantaneous nonlinear optical (NLO) process, in which the transformation of two photons of the frequency ω into a single photon with double the initial frequency (2ω) can be realized.[1–4] It is associated with induced polarization, which does not originate from the real absorption, so it can greatly reduce the probability of photobleaching or other photodamage phenomena. It can be used as a probe for determining the spontaneous polarization caused by the alignment of electric dipole moments in the case of ferroelectric crystals.[5,6] In addition, the symmetry variations in materials, e.g., the few-layer MoS_2 and h-BN, can be probed via optical SHG process.[7,8]On the other hand, the UCL phenomenon is based on the multiphoton absorption processes, resulting in conversion of low-energy photons into higher-energy ones, as well.[9–13] The UCL phenomena occur usually in the inorganic materials containing lanthanide ions (Ln^{3+}), thanks to unique, ladder-like electronic structure of Ln^{3+}. Under the NIR laser light excitation, the Ln^{3+}-doped materials can exhibit UCL originating from their 4f–4f transitions (which are partially forbidden by Laporte selection rules, and provide unique luminescence features), enabling high variety of applications, including temperature and pressure sensing, optical heating, photocatalytic technique, bioimaging, drug-delivery, and so forth.[14–21]

Perovskite materials have unique features that make them promising candidates in various fields, such as solar cells, ferroelectric materials, solid-state lasers, etc.[22–28] Titanate perovskites have received extensive attention, especially thanks to their splendid piezoelectric and emissive properties.[29,30] Barium titanate perovskite has a relatively low phonon energy (≈700 cm^{-1}), favoring high UCL efficiency.[31] Noteworthy, as the high-temperature phase of ABO_3-type perovskite $BaTiO_3$ (cubic;

$Pm\bar{3}m$, No.221) is cooled down from the high to room temperature, a non-centrosymmetric structure is obtained, due to the fact that the center ion Ti^{4+} and the oxygen octahedron (O_3 local symmetry) displace nonuniformly in respect to the corner ion Ba^{2+}.[32,33] With increasing temperature, different regions of the material change their crystallographic orientations, altering the crystal structure symmetry, and the phase transition (tetragonal to cubic) occurs, leading to enormous variability in the electric and spectroscopic features of the material.[34,35] Therefore, it is of crucial importance to determine the crystal symmetry transformation and the corresponding temperature in a noninvasive, rapid and simple way.[35–38]

The research and strategy of simultaneous employment of SHG and UCL for sensing purposes were motivated by disparate spectroscopic behaviors of SHG and UCL processes under controlled temperature conditions (25–305 °C), i.e., SHG is sensitive to the inversion symmetry breaking, while UCL is thermally quenched in a monotonous way. To the best of our knowledge, ratiometric thermometry utilizing both the SHG and UCL bands has not been proposed before. In this work, we successfully employed thermally induced spectroscopic changes (band intensity ratio) of two different NLO processes in $BaTiO_3$:Ho^{3+}, Yb^{3+} material for temperature sensing purposes. Our findings also suggest that the NLO thermometry may be a good tool to monitor phase transitions between non-centrosymmetric and centrosymmetric systems.

2. Results and Discussion

2.1. Optical Properties at Ambient Condition

Well-crystallized micrometer-sized tetragonal phase (space group P4mm) $BaTiO_3$:1% Ho^{3+},1% Yb^{3+}, $BaTiO_3$:1% Ho^{3+},5% Yb^{3+}, and $BaTiO_3$:1% Ho^{3+},10% Yb^{3+} perovskites were synthesized by a facile solid-state reaction method. The detailed crystal structure characterization of the synthesized samples, including X-ray diffraction, scanning electronic microscopy, energy dispersive X-ray analysis, as well as Raman and luminescence spectroscopy (including SHG) studies at ambient conditions, can be found in our previous paper.[38] Here, we focused on the interdependences between the observed nonlinear phenomena, i.e., UCL and SHG, and the corresponding studies as a function of temperature. The emission spectra of $BaTiO_3$ samples doped with 1% Ho^{3+} and x Yb^{3+} (x is the molar concentration of Yb^{3+}, i.e., 1%, 5%, and 10%) presented in **Figure 1**a, emphasize the impact of Yb^{3+} content on the UCL and SHG phenomena in $BaTiO_3$:Ho^{3+}, Yb^{3+} phosphors at room temperature. Under the 976 nm pulsed laser excitation, the emission spectra consist of a sharp band associated with the SHG process, centered at 488 nm (half of the excitation light wavelength), and two broader UCL bands centered at ≈550 and ≈650 nm, associated with the $^5S_2$, $^5F_4 \rightarrow {}^5I_8$ and $^5F_5 \rightarrow {}^5I_8$ transitions of Ho^{3+} ions, respectively. The sample with 1% Yb^{3+} exhibits the most intense SHG band, whereas the one with 10% Yb^{3+} shows the most intense UCL, which is due to the improved energy transfer from Yb^{3+} to Ho^{3+} ions, resulting from the higher concentration of Yb^{3+}. The reduction in SHG intensity is plausibly caused by the efficient interception of the excitation photons by Yb^{3+} ions, as well as by deterioration of SHG activity in the highly-doped perovskite structure. The emission intensity of the most intense band located at 550 nm (I_{UCL}) and the band located at 488 nm (I_{SHG}) were calculated via integrated peak area with abscissa of wavelength (in nm) used to obtain the corresponding band intensity ratio (I_{SHG}/I_{UCL}). The possible luminescence processes along with the energy level diagrams of SHG and UCL are shown in Figure 1b. In the SHG process (left of Figure 1b), two photons of optical frequency ω from the 976 nm laser beam are converted into one photon of 2ω frequency, resulting in the emission band located at 488 nm.[39,40] In the case of the UCL (right of Figure 1b) process, thanks to the large absorption cross-section of Yb^{3+} and the resonance between the energy levels of Ho^{3+} and Yb^{3+}, the energy transfer (ET) process from Yb^{3+} to Ho^{3+} takes place. Yb^{3+} ions in the ground state absorb photons at 976 nm: $^2F_{7/2} + h\nu$ (976 nm) $\rightarrow {}^2F_{5/2}$. The energy is then transferred from Yb^{3+} to the neighboring Ho^{3+} ions via ET processes, such as Yb^{3+} ($^2F_{5/2}$) + Ho^{3+} ($^5I_8$) → Ho^{3+} ($^5I_5$) + Yb^{3+} ($^2F_{7/2}$). Subsequently, the electrons populating the $^5I_5$ level are promoted to the $^5F_{2,3}$ and $^3K_8$ excited states of Ho^{3+} via another ET from a neighboring Yb^{3+} ion. The three levels later decay down to $^5S_2$, $^5F_4$, and $^5F_5$ levels, where the green and red UCL originate, respectively. ET can also promote Ho^{3+} electrons from $^5I_6$ to $^5S_2$, $^5F_4$

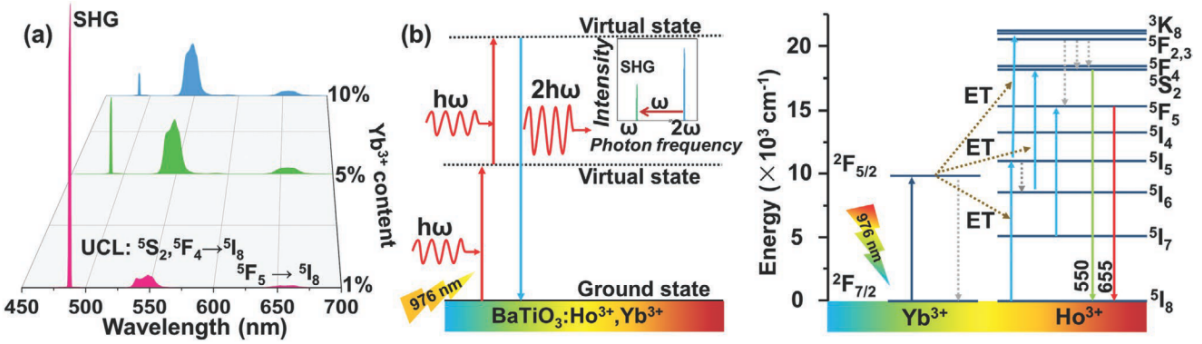

Figure 1. a) Emission spectra of the $BaTiO_3$:1% Ho^{3+},xYb^{3+} (x = 1%, 5%, and 10%) samples under excitation of 976 nm NIR (pulsed) laser. b) Simplified energy level diagrams showing the origin of SHG (left) and UCL processes (right) in the Ho^{3+}, Yb^{3+} codoped $BaTiO_3$ perovskite microparticles.

levels, as well as $^5I_7$ electrons to $^5F_5$. The direct absorption of the excitation photons by Ho^{3+} in its ground state is possible in principle, but the probability of such transitions is much lower than the Yb^{3+} absorption, due to the forbidden nature of the 4f–4f transitions in Ho^{3+}.

The emission spectra recorded at different excitation wavelengths (see Figure S1 in the Supporting Information) were measured, in order to confirm that the band located at 488 nm is correctly assigned to the SHG process. When changing the laser light source excitation wavelengths (λ_{ex}), the significant spectral shifts in the SHG peak position were observed. With a different λ_{ex}, the SHG bands are centered at $\lambda_{ex}/2$, confirming the fact that the sharp peak is due to the SHG process. It is worth noting that when λ_{ex} = 976 nm, the UCL bands show the most intense emission, which coincided well with the absorption maximum of Yb^{3+}.[41]

2.2. Optical Properties at High-Temperature Conditions

2.2.1. Temperature Dependent Nonlinear Phenomena – SHG and UCL

The setup for the luminescence experiments at variable-temperature (25–305 °C), used for the observation of the heat-driven phase transition of the $BaTiO_3$ structure is schematically presented in **Figure 2**a. According to the literature data, the phase transition from tetragonal crystal structure (P4mm, No.99) to cubic prototype phase ($Pm\bar{3}m$, No.221) occurs around 150 °C,[42] depending on the crystal polarization and other quality factors.[35,36,42–44] With the increasing temperature, the SHG intensity (I_{SHG}) is significantly influenced by the inversion symmetry change of the system.[45,46] Simultaneously, the behavior of the UCL process is affected by the thermal quenching effects and energy-back transfer from Ho^{3+} to Yb^{3+} ions.[47–49] It is worth noting, however, that a high concentration of Yb^{3+} ions in the structure can lead to the formation of irregularly distributed crystallographic defects in the perovskite crystals. These defects may influence the symmetry of the structure (and thus the probability of SHG). In order to better understand the effects of temperature and symmetry changes on the NLO processes, we selected the sample with the lowest concentration of Yb^{3+}, namely $BaTiO_3$: 1% Ho^{3+}, 1% Yb^{3+}. The variable-temperature emission spectra of the selected sample were measured in the 25–305 °C range. As shown in Figure 2b, under the NIR laser excitation, similarly, the SHG and UCL bands in the emission spectra show a strong dependence on temperature. In the temperature range studied, I_{SHG} exhibits a huge decrease up to ≈150 °C, and the rate of this decrease is much higher compared to that of the UCL thermal quenching (Figure 2b). When the temperature further increases, the relative intensity of SHG exhibits a slower rate of decrease (a plateau). Hence, this evident difference in the quenching rates of those NLO processes will result in the high thermal sensitivity of the proposed NLO ratiometric thermometer.

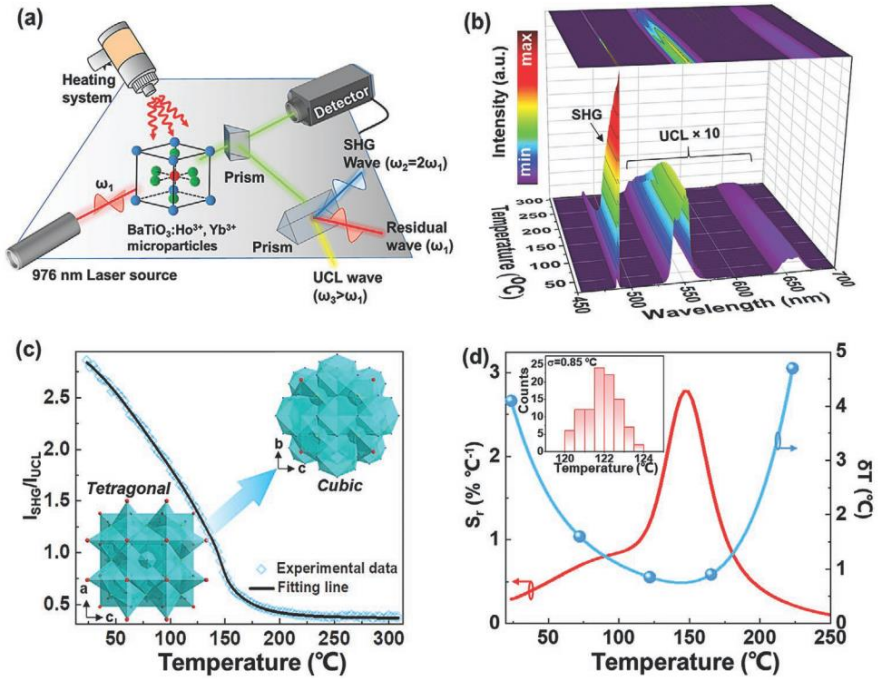

Figure 2. a) Schematic representation of the experimental setup used for the temperature-dependent SHG and UCL measurements. b) Temperature dependence of the emission spectra of the $BaTiO_3$:1% Ho^{3+},1% Yb^{3+} sample. c) I_{SHG}/I_{UCL} band intensity ratio as a function of temperature, and the corresponding fitting line (Equation (1)); d) Relative thermal sensitivity, S_r, and experimental temperature resolution, δT as a function of temperature (the inset shows an exemplary histogram for the determined experimental temperature resolution, i.e., the standard deviation of determined temperature via the band intensity ratios I_{SHG}/I_{UCL}, obtained from the 100 repeatability measurements at 122 °C, for the material studied).

From the perspective of the new ratiometric NLO thermometer development, the crucial step is the analysis of the variable-temperature spectra, i.e., the intensity ratio between the SHG band and the $^5S_2$, $^5F_4 \rightarrow {}^5I_8$ UCL band (I_{SHG}/I_{UCL}) as a function of temperature. As shown in Figure 2c, I_{SHG}/I_{UCL} exhibits a sigmoidal dependence on the temperature in the 25–305 °C range. As expected, above ≈150 °C, I_{SHG}/I_{UCL} undergoes the inflection point, i.e., the I_{SHG}/I_{UCL} changes the trend of rapid decline and begins to gradually display the invariable trend as the temperature further increases. Such a significant change in the band intensity ratio I_{SHG}/I_{UCL} is due to the intrinsic phase transition of the randomly-oriented (nonpolarized) perovskite crystals,[42] from the broken inversion symmetry to inversion symmetry, which is well confirmed for $BaTiO_3$ in different reports.[34,36,42,43,50–52] The relative change in the I_{SHG}/I_{UCL} ratio is associated with the SHG process, which is forbidden in the cubic phase of $BaTiO_3$ (centrosymmetric structure). However, the SHG signal does not completely disappear (see Figure 2b), even at the highest temperature measured. This is because, in reality, there are always some crystallographic defects that are inevitably induced by dopant ion substitution during high temperature synthesis (e.g., different ionic radii and oxidation states of Ti^{4+} versus Ho^{3+} / Yb^{3+}). Most plausibly, such defects cause a distortion of the structure from an ideal centrosymmetric cubic phase. Thus, these two NLO processes, i.e., the evolution of I_{SHG}/I_{UCL}, can be used to qualitatively detect the transformation from the non-centrosymmetric to centrosymmetric structure, which, in some respects, is crucial in the study of surfaces and domain walls in ferroelectrics, metal surface melting, catalytic processes, liquid crystal, and biological surface studies.[6,53]

2.2.2. NLO Temperature Sensing Performance

In order to give an analytical expression to the observed dependence of the I_{SHG}/I_{UCL} ratio on temperature, the following function was fitted to the experimental data

$$\frac{I_{SHG}}{I_{UCL}} = y_0 + \sum_i \frac{A_i}{e^{(T-T_{xi})\times p_i} + 1} \quad (1)$$

where T is the temperature, A_i is the amplitude, T_x is the "middle point" temperature, y_0 is the vertical offset, p is the fitting parameter (which has the units of reciprocal temperature), and i is the number of required components. The experimental data fit well ($R^2 \geq 0.999$) to Equation (1) and the parameters of y_0, A_1, T_{x1}, p_1, A_2, T_{x2}, p_2, A_3, T_{x3}, p_3 are 0.3674, 1.9589, 72.4, 0.0291, 0.7144, 135.9, 0.0706, 0.1825, 147.0, 0.3784, respectively. Equation (1) provides a good analytical expression, useful, *e.g.*, for luminescence thermometry calibration.

In order to quantitatively present the feasibility of temperature sensing of the developed NLO thermometer, the relative temperature sensitivities, S_r (% °C^{-1}) were calculated. In this case, the value of S_r is defined as

$$S_r = 100\% \times \frac{1}{(I_{SHG}/I_{UCL})} \times \frac{d(I_{SHG}/I_{UCL})}{dT} \quad (2)$$

As demonstrated in Figure 2d, the S_r values change dramatically with increasing temperature, and the maximum relative temperature sensitivity ($S_{r\,max}$) was found to be about 2.78% °C^{-1} at 146 °C, *i.e.*, within the temperature range of the interest.

In order to better determine the validity of the developed NLO thermometer, the repetitive measurements of 100 spectra at a constant temperature were conducted, and this procedure was repeated five times at the selected temperature values (24, 72, 122, 165, and 223 °C). Afterwards, based on the calculated I_{SHG}/I_{UCL} ratios and the calibration curve (Equation (1)), we determined and plotted the corresponding temperature values (see the exemplary histogram in the inset of Figure 2d). The determined temperature values were fitted to the Gauss function, and the experimental temperature resolutions, δT were determined (δT is equal to full width at half maximum of the Gauss peak),[17,54] i.e., δT = 4.1, 1.6, 0.85, 0.9, 4.7 °C at temperature values 24, 72, 122, 165, 223 °C, respectively. These results further indicate that developed NLO thermometer shows excellent temperature sensing performance, and it can monitor temperature precisely and accurately over a relatively wide temperature range.

Nowadays, the most commonly applied, convenient and sensitive technique of optical temperature sensing is based on the use of fluorescence/luminescence intensity ratio (FIR/LIR), which can provide high sensing accuracy and precision.[55,56] In order to compare our NLO thermometer based on the I_{SHG}/I_{UCL} ratio to inorganic Ln^{3+}-based optical thermometers utilizing the FIR/LIR technique, we have summarized the performance of optical thermometers operating in a similar temperature range (up to about 300 °C) in **Table 1**. It is evident that the developed NLO thermometer provides higher thermal sensitivity than the commonly used FIR/LIR based thermometers working in a similar temperature range. This highly-sensitive NLO sensor exploits a new and effective pathway for contactless temperature sensing—the NLO thermometry, which is a promising alternative method to conventional FIR/LIR thermometry.

3. Conclusions

In summary, the temperature dependences of the SHG and UCL phenomena in the optically active $BaTiO_3$:Ho^{3+}, Yb^{3+} perovskite material were investigated in the temperature range of 25–305 °C. The band intensity ratio I_{SHG}/I_{UCL} for $BaTiO_3$:Ho^{3+}, Yb^{3+} undergoes a significant inflection point during the gradual tetragonal-to-cubic phase transition, which confirms that it is a powerful new tool for detecting the symmetry change of the crystals. Most advantageously, the intensity ratio of these NLO processes, i.e., SHG to UCL, can also be used as a new thermometric parameter, which provides an excellent relative sensitivity of 2.78% °C^{-1}. This highly sensitive, novel NLO temperature sensor opens new horizons in optical thermometry, showing the possibility of applying various NLO effects for sensing purposes. Moreover, the appropriately designed materials, exhibiting the combination of SHG and UCL processes, could be potentially used in the photodynamic therapy (PDT) applications.

Table 1. Maximal relative temperature sensitivity ($S_{r\,max}$ at a given T value), temperature range (T-range) of the most used LIR/FIR based Ln^{3+} doped inorganic luminescent thermometers (operating in a similar T-range), along with our NLO thermometer.

Compound	Dopant ion	Transition	$S_{r\,max}$ [% °C^{-1}]	T [°C]	T-range [°C]	Ref.
Y_2O_3	Ho^{3+}, Yb^{3+}	$^5F_4/^5S_2 \rightarrow {}^5I_8$	0.71	290	27–327	[57]
$CaMoO_4$	Ho^{3+}, Yb^{3+}	$^3K_8/^5F_3 \rightarrow {}^5I_8$	0.66	80	30–270	[58]
$Ca_3La_6Si_6O_{24}$	Ho^{3+}, Yb^{3+}	$^5F_5/^5F_4$, $^5S_2 \rightarrow {}^5I_8$	0.15	20	30–230	[59]
$BiPO_4$	Ho^{3+}, Yb^{3+}	$^5F_{5(1)}/^5F_{5(2)} \rightarrow {}^5I_8$	1.05	150	40–300	[60]
ZrO_2	Ho^{3+}, Yb^{3+}	$^5F_5/^5F_4$, $^5S_2 \rightarrow {}^5I_8$	0.40	67	2–277	[61]
$SrWO_4$	Er^{3+}, Yb^{3+}	$^2H_{11/2}/^4S_{3/2} \rightarrow {}^4I_{15/2}$	1.50	245	27–245	[62]
Y_2SiO_5	Er^{3+}, Yb^{3+}	$^2H_{11/2}/^4S_{3/2} \rightarrow {}^4I_{15/2}$	0.70	327	27–327	[63]
$Na_2La_2Ti_3O_{10}$	Pr^{3+}	$^1D_2/^3P_0 \rightarrow {}^3H_4$	1.96	270	30–270	[64]
YAG	Pr^{3+}	$^1D_2/^3P_0 \rightarrow {}^3H_4$	0.25	320	20–320	[65]
$YAlO_3$	Nd^{3+}	$^2H_{9/2}$, $^4F_{5/2}$/ $^4F_{3/2} \rightarrow {}^4I_{9/2}$	1.83	20	20–338	[66]
$NaEuF_4$	Eu^{3+}	$^5D_1/^5D_0 \rightarrow {}^7F_1$	0.43	–	25–250	[67]
β-$NaY_{0.8}Gd_{0.2}F_4$	Eu^{3+}-Dy^{3+}	$^4F_{9/2} \rightarrow {}^6H_{13/2}/^5D_0 \rightarrow {}^7F_2$	0.23	30	30–290	[68]
	Eu^{3+}-Tb^{3+}	$^5D_4 \rightarrow {}^7F_5/^5D_0 \rightarrow {}^7F_1$	0.76	30	30–290	[68]
	Tb^{3+}-Dy^{3+}	$^5D_4 \rightarrow {}^7F_5/^4F_{9/2} \rightarrow {}^6H_{13/2}$	0.50	30	30–290	[68]
Y_2O_3	Eu^{3+}-Nd^{3+}	$^4F_{5/2} \rightarrow {}^4I_{9/2}/^5D_0 \rightarrow {}^7F_4$	2.58	107	27–237	[69]
YF_3@Ga_2O_3 (glass ceramics)	Yb^{3+}-Er^{3+}-Cr^{3+}	$^2H_{11/2}$ /$^4S_{3/2} \rightarrow {}^4I_{15/2}$	0.25	243	30–290	[70]
Y_2O_3	Er^{3+}, Yb^{3+}, Eu^{3+}	$^2H_{11/2}/^4S_{3/2} \rightarrow {}^4I_{15/2}$	1.03	320	30–320	[71]
$NaLuF_4$	Tm^{3+}, Yb^{3+}, Gd^{3+}	$^6P_{9/2}/^6I_{7/2} \rightarrow {}^8S_{7/2}$	0.29	25	25–250	[72]
$BaTiO_3$ (NLO sensor)	Ho^{3+}, Yb^{3+}	$I_{SHG}/(I_{UCL}$:$^5F_4$, $^5S_2 \rightarrow {}^5I_8)$	2.78	146	25–305	this work

Supporting Information

Supporting Information is available from the Wiley Online Library or from the author.

Acknowledgements

This work was financially supported by the Polish National Science Centre (Grant No. UMO-2016/21/B/ST5/00110), by Ministerio de Ciencia e Innovación of Spain (MICIIN) under the National Program of Sciences and Technological Materials (PID2019-106383GB-C44 and PID2019-107335RA-I00) and Gobierno de Canarias (ProID2020010067) and EU-FEDER funds. T.Z. is grateful to Grant No. POWR.03.02.00–00-i020/17 financed by European Union through the European Social Fund under the Operational Program Knowledge Education Development. J.L. thanks Fondecyt (Grant No. 1181302–74190051). M.V. appreciates the financial support of ANID/Scholarship Program/POSTDOCTORADO BECAS CHILE/2018-7419005. M.R. is a recipient of the Bekker Programme scholarship (PPN/BEK/2018/1/00206/U/00001) supported by the Polish National Agency for Academic Exchange.

Conflict of Interest

The authors declare no conflict of interest.

Data Availability Statement

Research data are not shared.

Keywords

multifunctional optical sensor, nonlinear luminescent thermometer, second harmonic generation (SHG), temperature detection, upconversion emission

Received: February 23, 2021
Revised: March 17, 2021
Published online:

[1] H. Yu, N. Z. Koocher, J. M. Rondinelli, P. S. Halasyamani, *Angew. Chem., Int. Ed.* **2018**, *57*, 6100.
[2] A. Molinos-Gómez, M. Maymó, X. Vidal, D. Velasco, J. Martorell, F. López-Calahorra, *Adv. Mater.* **2007**, *19*, 3814.
[3] M. Flörsheimer, M. Küpfer, C. Bosshard, H. Looser, P. Günter, *Adv. Mater.* **1992**, *4*, 795.
[4] H. J. Simon, N. Bloembergen, *Phys. Rev.* **1968**, *171*, 1104.
[5] N. Kato, *Biophys. Rev.* **2019**, *11*, 399.
[6] S. A. Denev, T. T. A. Lummen, E. Barnes, A. Kumar, V. Gopalan, *J. Am. Ceram. Soc.* **2011**, *94*, 2699.
[7] Y. Li, Y. Rao, K. F. Mak, Y. You, S. Wang, C. R. Dean, T. F. Heinz, *Nano Lett.* **2013**, *13*, 3329.
[8] W. Feng, C. Han, F. Li, *Adv. Mater.* **2013**, *25*, 5287.
[9] A. Nadort, J. Zhao, E. M. Goldys, *Nanoscale* **2016**, *8*, 13099.
[10] M. K. Tsang, G. Bai, J. Hao, *Chem. Soc. Rev.* **2015**, *44*, 1585.
[11] M. Runowski, P. Woźny, S. Lis, V. Lavín, I. R. Martín, *Adv. Mater. Technol.* **2020**, *5*, 1901091.
[12] C. Ramana, V. Atuchin, V. Kesler, V. Kochubey, L. Pokrovsky, V. Shutthanandan, U. Becker, R. Ewing, *Appl. Surf. Sci.* **2007**, *253*, 5368.

[13] C. S. Lim, A. Aleksandrovsky, V. Atuchin, M. Molokeev, A. Oreshonkov, *Crystals* **2020**, *10*, 912.
[14] T. Zheng, M. Runowski, P. Woźny, S. Lis, V. Lavín, *J. Mater. Chem. C* **2020**, *8*, 4810.
[15] C. D. S. Brites, P. P. Lima, N. J. O. Silva, A. Millán, V. S. Amaral, F. Palacio, L. D. Carlos, *Adv. Mater.* **2010**, *22*, 4499.
[16] M. Runowski, P. Woźny, N. Stopikowska, Q. Guo, S. Lis, *ACS Appl. Mater. Interfaces* **2019**, *11*, 4131.
[17] M. Runowski, P. Wozny, N. Stopikowska, I. R. Martín, V. Lavín, S. Lis, *ACS Appl. Mater. Interfaces* **2020**, *12*, 43933.
[18] Y. Gao, F. Huang, H. Lin, J. Zhou, J. Xu, Y. Wang, *Adv. Funct. Mater.* **2016**, *26*, 3139.
[19] J. Zhang, Y. Huang, L. Jin, F. Rosei, F. Vetrone, J. P. Claverie, *ACS Appl. Mater. Interfaces* **2017**, *9*, 8142.
[20] G. R. Tan, M. Wang, C. Y. Hsu, N. Chen, Y. Zhang, *Adv. Opt. Mater.* **2016**, *4*, 984.
[21] W. Zhao, Y. Zhao, Q. Wang, T. Liu, J. Sun, R. Zhang, *Small* **2019**, *15*, 1.
[22] L. Gil-Escrig, M. Roß, J. Sutter, A. Al-Ashouri, C. Becker, S. Albrecht, *Sol. RRL* **2021**, *5*, 2000553.
[23] P. S. C. Schulze, A. J. Bett, M. Bivour, P. Caprioglio, F. M. Gerspacher, Ö. Kabaklı, A. Richter, M. Stolterfoht, Q. Zhang, D. Neher, M. Hermle, H. Hillebrecht, S. W. Glunz, J. C. Goldschmidt, *Sol. RRL* **2020**, *4*, 1.
[24] F. Di Mei, L. Falsi, M. Flammini, D. Pierangeli, P. Di Porto, A. J. Agranat, E. DelRe, *Nat. Photonics* **2018**, *12*, 734.
[25] M. Li, Y. Xu, S. Han, J. Xu, Z. Xie, Y. Liu, Z. Xu, M. Hong, J. Luo, Z. Sun, *Adv. Mater.* **2020**, *32*, 1.
[26] G. Pacchioni, *Nat. Rev. Mater.* **2021**, *4*, 41578.
[27] C. Martin, *Nat. Mater.* **2012**, *11*, 1002.
[28] T. H. Han, S. Tan, J. Xue, L. Meng, J. W. Lee, Y. Yang, *Adv. Mater.* **2019**, *31*, 1.
[29] D. Liu, C. Jin, F. Shan, J. He, F. Wang, *ACS Appl. Mater. Interfaces* **2020**, *12*, 17443.
[30] D. Maurya, A. Pramanick, K. An, S. Priya, *Appl. Phys. Lett.* **2012**, *100*, 172906.
[31] A. Patra, C. S. Friend, R. Kapoor, P. N. Prasad, *Chem. Mater.* **2003**, *15*, 3650.
[32] M. Acosta, N. Novak, V. Rojas, S. Patel, R. Vaish, J. Koruza, G. A. Rossetti, J. Rödel, *Appl. Phys. Rev.* **2017**, *4*, 041305.
[33] Q. Zhang, T. Cagin, W. A. Goddard, *Proc. Natl. Acad. Sci. USA* **2006**, *103*, 14695.
[34] H. Bae, K. T. Lee, *RSC Adv.* **2019**, *9*, 2451.
[35] E. Aksel, J. L. Jones, *Sensors* **2010**, *10*, 1935.
[36] G. Philippot, C. Elissalde, M. Maglione, C. Aymonier, *Adv. Powder Technol.* **2014**, *25*, 1415.
[37] Y. I. Yuzyuk, *Phys. Solid State* **2012**, *54*, 1026.
[38] M. Vega, I. R. Martin, J. Llanos, *J. Alloys Compd.* **2019**, *806*, 1146.
[39] W. Xu, H. Zhao, Y. Li, L. Zheng, Z. Zhang, W. Cao, *Sensors Actuators, B* **2013**, *188*, 1096.
[40] X. Wang, X. Li, S. Xu, L. Cheng, J. Sun, J. Zhang, B. Chen, *J. Alloys Compd.* **2018**, *754*, 222.
[41] M. Runowski, N. Stopikowska, S. Lis, *Dalton Trans.* **2020**, *49*, 2129.
[42] J. Wang, K. Jin, H. Yao, J. Gu, X. Xu, C. Ge, C. Wang, M. He, G. Yang, *Appl. Phys. Lett.* **2018**, *112*, 102904.
[43] S. Nayak, B. Sahoo, T. K. Chaki, D. Khastgir, *RSC Adv.* **2014**, *4*, 1212.
[44] M. Acosta, N. Novak, V. Rojas, S. Patel, R. Vaish, J. Koruza, G. A. Rossetti, J. Rödel, *Appl. Phys. Rev.* **2017**, *4*, 041305.
[45] P. Guyot-Sionnest, H. Hsiung, Y. R. Shen, *Phys. Rev. Lett.* **1986**, *57*, 2963.
[46] T. F. Heinz, M. M. T. Loy, W. A. Thompson, *Phys. Rev. Lett.* **1985**, *54*, 63.
[47] Q. Zhang, G. Chen, G. Zhang, J. Qiu, D. Chen, *J. Appl. Phys.* **2009**, *106*, 113102.
[48] Y. Yu, Y. Zheng, F. Qin, L. Liu, C. Zheng, G. Chen, Z. Zhang, W. Cao, *Opt. Commun.* **2011**, *284*, 1053.
[49] X. X. Zhang, P. Hong, M. Bass, B. H. T. Chai, *Appl. Phys. Lett.* **1993**, *63*, 2606.
[50] M. Selvaraj, V. Venkatachalapathy, J. Mayandi, S. Karazhanov, J. M. Pearce, *AIP Adv.* **2015**, *5*, 117119.
[51] F. H. Schader, N. Khakpash, G. A. Rossetti, K. G. Webber, *J. Appl. Phys.* **2017**, *121*, 064109.
[52] G. C. Manika, K. S. Andrikopoulos, G. C. Psarras, *Molecules* **2020**, *25*, 2686.
[53] R. C. Miller, *Appl. Phys. Lett.* **1964**, *5*, 17.
[54] O. A. Savchuk, J. J. Carvajal, C. Cascales, M. Aguiló, F. Díaz, *ACS Appl. Mater. Interfaces* **2016**, *8*, 7266.
[55] C. D. S. Brites, P. P. Lima, N. J. O. Silva, A. Millán, V. S. Amaral, F. Palacio, L. D. Carlos, *Nanoscale* **2012**, *4*, 4799.
[56] M. Runowski, N. Stopikowska, D. Szeremeta, S. Goderski, M. Skwierczyńska, S. Lis, *ACS Appl. Mater. Interfaces* **2019**, *11*, 13389.
[57] J. Zhou, Y. Chen, R. Lei, H. Wang, Q. Zhu, X. Wang, Y. Wu, Q. Yang, S. Xu, *Ceram. Int.* **2019**, *45*, 7696.
[58] R. Dey, A. Kumari, A. K. Soni, V. K. Rai, *Sens. Actuators, B* **2015**, *210*, 581.
[59] J. Zhang, Z. Hua, *J. Lumin.* **2018**, *201*, 217.
[60] N. Wang, Z. Fu, Y. Wei, T. Sheng, *J. Alloys Compd.* **2019**, *772*, 371.
[61] M. Li, T. Xie, X. Tu, J. Xu, R. Lei, S. Zhao, S. Xu, *Opt. Mater.* **2019**, *97*, 109478.
[62] A. Pandey, V. K. Rai, V. Kumar, V. Kumar, H. C. Swart, *Sens. Actuators, B* **2015**, *209*, 352.
[63] N. Rakov, G. S. MacIel, *Sens. Actuators, B* **2012**, *164*, 96.
[64] Y. Gao, F. Huang, H. Lin, J. Xu, Y. Wang, *Sens. Actuators, B* **2017**, *243*, 137.
[65] S. Hu, C. Lu, X. Liu, Z. Xu, *Opt. Mater.* **2016**, *60*, 394.
[66] M. A. Hernández-Rodríguez, A. D. Lozano-Gorrín, I. R. Martín, U. R. Rodríguez-Mendoza, V. Lavín, *Sens. Actuators, B* **2018**, *255*, 970.
[67] Y. Tian, B. Tian, C. Cui, P. Huang, L. Wang, B. Chen, *Opt. Lett.* **2014**, *39*, 4164.
[68] M. Ding, J. Hou, Z. Cui, H. Gao, C. Lu, J. Xi, Z. Ji, D. Chen, *Ceram. Int.* **2018**, *44*, 7930.
[69] S. Zhou, X. Wei, X. Li, Y. Chen, C. Duan, M. Yin, *Sens. Actuators, B* **2017**, *246*, 352.
[70] D. Chen, Z. Wan, Y. Zhou, X. Zhou, Y. Yu, J. Zhong, M. Ding, Z. Ji, *ACS Appl. Mater. Interfaces* **2015**, *7*, 19484.
[71] V. K. Rai, A. Pandey, R. Dey, *J. Appl. Phys.* **2013**, *113*, 083104.
[72] K. Zheng, Z. Liu, C. Lv, W. Qin, *J. Mater. Chem. C* **2013**, *1*, 5502.

ADVANCED OPTICAL MATERIALS

Supporting Information

for *Adv. Optical Mater.,* DOI: 10.1002/adom.202100386

Nonlinear Optical Thermometry—A Novel Temperature Sensing Strategy via Second Harmonic Generation (SHG) and Upconversion Luminescence in $BaTiO_3$:Ho^{3+},Yb^{3+} Perovskite

Teng Zheng, Marcin Runowski, Inocencio R. Martín, Stefan Lis, Mauricio Vega, and Jaime Llanos*

Supporting Information

Non-linear Optical Thermometry – A Novel Temperature Sensing Strategy via Second Harmonic Generation (SHG) and Upconversion Luminescence in $BaTiO_3:Ho^{3+}$, Yb^{3+} Perovskite

Teng Zheng, Marcin Runowski, Inocencio R. Martín, Stefan Lis, Mauricio Vega and Jaime Llanos*

Experimental part

The synthesis part of our material can be found in our previous work [S1]. A tunable EKSPLA/NT342/3/ UVE 10 ns pulsed laser with optical parametric oscillator (OPO) operating at 10 Hz repetition rate was used as the excitation source to record the emission spectra. A CCD spectrometer (Andor Shamrock 303i) was used to receive the emitted light signal, which was focused on the entrance slit. The variable-temperature spectroscopic measurements at 25 - 305 °C, were carried out in a tubular electric furnace (Gero RES-E 230/3). A type K thermocouple in contact with the sample was used to control and monitor the temperature.

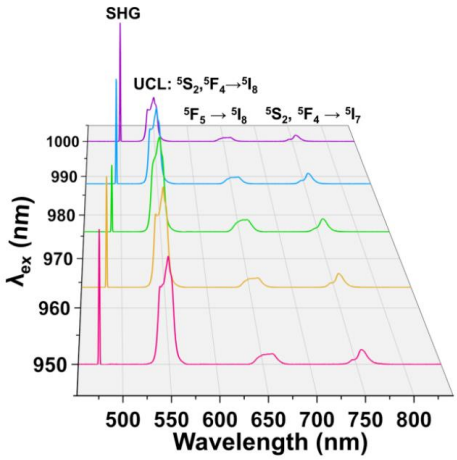

Figure S1. Emission spectra of $BaTiO_3$:1%Ho^{3+}, 5%Yb^{3+} phosphor as a function of excitation wavelength.

References

[S1] M. Vega, I. R. Martin, J. Llanos, J. Alloys Compd. 2019, 806, 1146.

6.2. Boltzmann vs. non-Boltzmann (non-linear) thermometry - Yb^{3+}-Er^{3+} activated dual-mode thermometer and phase transition sensor via second harmonic generation

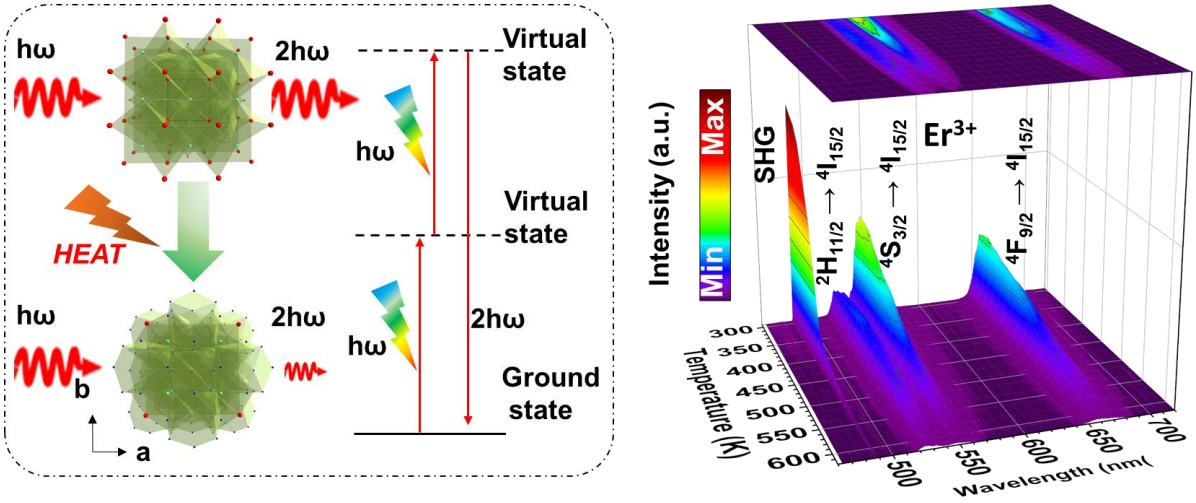

The result in this section were published in: Teng Zheng, Marcin Runowski, Przemysław Woźny, Bolesław Barszcz, Stefan Lis, Mauricio Vega, Jaime Llanos, Kevin Soler-Carracedo and Inocencio R. Martín, Boltzmann vs. non-Boltzmann (non-linear) thermometry - Yb^{3+}-Er^{3+} activated dual-mode thermometer and phase transition sensor via second harmonic generation, Journal of Alloys and Compounds, Journal of Alloys and Compounds, 2022, 906, 164329

Abstract of the section: Based on formal studies, with the concept of a non-linear optical process, a detailed comparison of thermometric performance between conventional Boltzmann-type thermometry and nonlinear optical thermometry should be presented. Therefore, in the process of chemical engineering, a series of optically active $BaTiO_3$ doped with Er^{3+}, Yb^{3+} perovskite materials was obtained to characterize temperature-dependent of NLO responses as well as thermometric performances. Upon 976 nm laser excitation, as expected, the samples show simultaneously intense UCL and SHG effects. The thermometric features were compared, i.e., Boltzmann luminescence thermometry (typical thermally-coupled levels of Er^{3+}), and NLO thermometry (SHG/UCL intensity ratio). The work demonstrates that the NLO thermometry approach shows better thermal sensitivity (≈ 4 %/K, at ~400 K) and smaller temperature resolution (δT = 0.07 K). Moreover, NLO spectroscopy based on SHG and UCL allows rapid, more precise and clearer detection of phase transitions. Our work presents that some non-Boltzmann, non-linear

thermometers can provide much more effective temperature sensing (compared to the commonly studied Boltzmann thermometers), while also working as accurate, rapid and non-invasive phase transition sensors.

Contribution of Ph.D. student in this work: Conceptualization, structural and morphological characterization, conduction of the spectroscopic measurements, visualization, data analysis and curation, formal analysis, writing original draft and writing review & editing.

Journal of Alloys and Compounds 906 (2022) 164329

Contents lists available at ScienceDirect

Journal of Alloys and Compounds

journal homepage: www.elsevier.com/locate/jalcom

Research Article

Boltzmann *vs.* non-Boltzmann (non-linear) thermometry - Yb^{3+}-Er^{3+} activated dual-mode thermometer and phase transition sensor via second harmonic generation

Teng Zheng[a], Marcin Runowski[a,d,*], Przemysław Woźny[a], Bolesław Barszcz[b], Stefan Lis[a], Mauricio Vega[c], Jaime Llanos[c], Kevin Soler-Carracedo[d], Inocencio R. Martín[d]

[a] Adam Mickiewicz University, Faculty of Chemistry, Uniwersytetu Poznańskiego 8, 61-614 Poznań, Poland
[b] Institute of Molecular Physics, Polish Academy of Sciences, Mariana, Smoluchowskiego 17, 60-179 Poznań, Poland
[c] Departamento de Química, Universidad Católica del Norte, Avda. Angamos 0610, Antofagasta, Chile
[d] Universidad de La Laguna, Departamento de Física, Apdo. Correos 456 E-38200, San Cristóbal de La Laguna, Santa Cruz de Tenerife, Spain

ARTICLE INFO

Article history:
Received 17 November 2021
Received in revised form 8 February 2022
Accepted 21 February 2022
Available online 24 February 2022

Keywords:
Non-linear optical thermometry, Second harmonic generation (SHG)
Upconverting materials
Luminescent sensor
Thermal sensing, phase transition detection

ABSTRACT

Second harmonic generation (SHG) and upconversion luminescence (UCL), as second-order nonlinear optical (NLO) effects, are crucial in modern optics and optoelectronics. Here, through the chemical engineering process we obtained a series of optically active $BaTiO_3$: Er^{3+}, Yb^{3+} perovskite materials, exhibiting temperature-dependent NLO responses. Upon 976 nm laser light irradiation, the micron-sized, polycrystalline samples show simultaneously intense UCL and SHG effects. Comparison of the thermometric features based on luminescence thermometry, *i.e.*, band intensity ratio based on thermally-coupled levels of Er^{3+}, and NLO thermometry, *i.e.*, SHG/UCL intensity ratio, shows that the superior thermal sensitivity (≈ 4%/K, at ~400 K) and excellent temperature resolution ($\delta T = 0.07$ K) is achieved for the NLO thermometry approach. Furthermore, the combination of NLO spectroscopy with UCL allows rapid, more precise and clear phase transition detection (from tetragonal to cubic phase at around 386 K), compared to conventional structural methods, such as X-ray diffraction and Raman spectroscopy. Our work suggests that some non-Boltzmann, non-linear thermometers can provide much more effective temperature readouts (compared to the commonly studied Boltzmann thermometers), simultaneously working as accurate, rapid and non-invasive phase transition sensors.

1. Introduction

Second harmonic generation (SHG), third harmonic generation (THG), sum frequency generation (SFG) and four-wave mixing (FWM) are considered as typical nonlinear optical (NLO) phenomena [1,2]. SHG, also called frequency doubling, is a process of conversion of two identical "input" photons at the fundamental frequency into a single "output" photon at the double-harmonic frequency [3–5]. It is highly sensitive to symmetry change (forbidden in materials with inversion symmetry) in crystal structure or interfaces of the materials [3,6–9], which does not actually involve any real absorptions. The intensity of SHG in materials can be influenced by several quality factors: I) second-order nonlinear coefficient, which differs depending on the particular material; II) the orientation of the crystal axes in respect to the excitation beam direction (phase match), which is indirectly related to the efficiency of the SHG; and III) polarization [10]. In contrast to single crystals, the polycrystalline materials consist of plenty of grains (small crystallites) showing random orientation, allowing observation of the averaged SHG signal without a phase-match in each crystal, in respect to the excitation beam optical path (geometry) [5]. SHG active materials are widely used as sensitive probes of material surfaces and interfaces, ferroelectric domains, biological surfaces, *etc.*, mainly due to their unprecedentedly high sensitivity to symmetry changes in various systems [11–14].

Lanthanide (Ln^{3+}) activated upconverting luminescent (UCL) materials have been widely applied in various fields, such as luminescence thermometry, bio-imaging, optical devices, photodynamic therapy (PDT), *etc* [15–19]. It is mainly due to their superior spectroscopic properties, *e.g.*, sharp emission bands,

* Corresponding author at: Adam Mickiewicz University, Faculty of Chemistry, Uniwersytetu Poznańskiego 8, 61-614 Poznań, Poland.
E-mail address: runowski@amu.edu.pl (M. Runowski).

https://doi.org/10.1016/j.jallcom.2022.164329
0925-8388/

absence of strong auto-fluorescence, high penetration depth in biological system, *etc* [18,20–29]. UCL is a non-linear process, which is based on absorption of two or more lower-energy photons (usually from the NIR region), followed by the anti-Stokes emission of one higher energy photon [30–32]. For generation of intense UCL, the combination of Er^{3+} activator and Yb^{3+} sensitizer ions, embedded in inorganic host matrix is commonly chosen. This is mainly due to the large absorption cross-section in the near-infrared region of Yb^{3+}, as well as the energy overlap between Er^{3+} and Yb^{3+} ions, leading to highly efficient energy transfer (ET) up-conversion processes [33–35].

Barium titanate ($BaTiO_3$), one of the family of the perovskite materials [36–43], has drawn wide attention due to its unique ferroelectric, photocatalytic and electro-optic properties [44,45]. Besides, when introducing suitable Ln^{3+} dopant ions in the host matrix, it is possible to endow the material with luminescence properties. Moreover, thanks to a relatively low cutoff photon energy (~700 cm^{-1}) of the titanate crystal lattice [46], it is possible to achieve good up-conversion luminescence efficiency and satisfying thermometric performance [5,47]. $BaTiO_3$ adopts various phases over a wide temperature range, *i.e.*, rhombohedral, orthorhombic, tetragonal and cubic [48,49]. Importantly, according to literature data, the tetragonal crystals transform to cubic phase above the Curie temperature (T_C, ~393 K) in $BaTiO_3$, leading to a sharp change in their dielectric and ferroelectric properties, induced by intrinsic structure change [48–50]. In case of cubic $BaTiO_3$, the Ti^{4+} ions are supposed to be located in the center of an 6-neighboring-oxygen-formed octahedron with O_h symmetry, while, for tetragonal phase, the Ti^{4+} ions possess the symmetry of C_{4v}, where one oxygen anion (O^{2-}) is slightly displaced in the direction of the *c* axis.

Temperature is a fundamental and important parameter not only in thermodynamics and statistical mechanics, but also in various industrial and scientific fields. Ln^{3+}-activated luminescent thermometers show advantages of non-invasive, fast, contactless and sensitive determination of temperature with high spatial resolution, where conventional thermometers are ineffective [15,16,51–54]. The dominant and most sensitive pathway in luminescence thermometry is to apply the luminescence/fluorescence intensity ratio (LIR/FIR) technique based on thermally-coupled levels (TCLs) of Ln^{3+}. Recently, a new and effective thermometric strategy was developed, *i.e.*, the non-linear optical (NLO) thermometry using SHG and UCL, exhibiting superior sensitivity and thermal resolutions. For instance, da Silva et al. reported that based on Tm^{3+} doped $NaNbO_3$ nanocrystals, and using the intensity ratio between SHG and UCL, the relative thermal sensitivity of ~12%/K can be achieved. In our previous paper, we reported that based on the NLO thermometry in the Ho^{3+}/Yb^{3+} doped system, it is possible to obtain excellent thermal resolution of 0.85 K and satisfactory relative sensitivity of 2.78%/K. [5,55] However, there is very limited data reported about NLO thermometry and a detailed performance comparison (experimental studies) between the classical luminescence thermometry and NLO thermometry in optically active materials is still missing.

Here, we present the NLO spectroscopy as a powerful tool for both temperature and phase transition sensing, exemplified on $BaTiO_3$: Er^{3+}, Yb^{3+} perovskite. For the first time, two optical thermometric pathways are realized simultaneously in a single material, *i.e.*, luminescence thermometry utilizing TCLs of Er^{3+} and NLO thermometry based on SHG/UCL band intensity ratios. The advantage of the NLO thermometry, *i.e.*, higher relative thermal sensitivity (S_r) of ≈ 4%/K *vs.* ≈ 1.2%/K for the luminescence thermometry was demonstrated. Furthermore, we introduced the SHG/UCL band intensity ratio as a parameter for phase transition detection, from tetragonal to cubic phase in the synthesized materials.

2. Experimental

2.1. Synthesis of $BaTiO_3$ perovskite microparticles

Stoichiometric amounts of $Ti(OC_4H_9)_4$ (97%), $Er(NO_3)_3$ (99.9%), $Yb(NO_3)_3$ (99.9%), and $CH_3COO)_2Ba$ (> 99.9%) were used to synthesize the $BaTi_{0.95-x}O_3$: *x* Er^{3+}, 0.05 Yb^{3+} (*x* is the molar concentration of Er^{3+}, *i.e.*, 1%, 5% and 9%) as starting materials. Proper amount of Ba $(CH_3COO)_2$ was dissolved in 20 mL acetic acid (denoted as a solution A). Subsequently, 2 mL of $Ti(OC_4H_9)_4$ was diluted with 8 mL of acetylacetone (denoted as a solution B). Then, the solution A was added dropwise to the solution B. This mixture was heated to 23 K on a hot plate for 2 h under continuous magnetic stirring, to form the solution containing titanium and barium cations (denoted as a solution C). Afterwards, 5 mL of the aqueous solution of $Er(NO_3)_3$ and $Yb(NO_3)_3$ was added to the solution C and heated to 373 K on a hot plate for 24 h, to evaporate water and obtain powder. Finally, the product obtained was ground in an agate mortar, placed in an alumina crucible and annealed for 2 h at 1273 K in a muffle furnace, in air atmosphere, to obtain the final product.

2.2. Characterization

To identify the phase purity of the synthesized sample, the powder X-ray diffraction (XRD) patterns were recorded by using a Bruker D8 Advance diffractometer equipped with a graphite monochromator operated at 40 kV and 30 mA, using CuKα radiation (λ = 1.54057 Å), in the 2θ range of 10–60°. A Renishaw research Ramanscope 1000 spectrometer equipped with a Peltier-cooled CCD detector and with Leica microscopes (excitation line: 785 nm) was used to measure Raman spectra at room temperature. The temperature-dependent Raman spectra were recorded by using the Horiba Jobin Yvon LabRam HR800 spectrometer with liquid nitrogen cooled CCD detector (He-Ne 632.82 nm laser, power of 1.77 mW). The laser beam was focused using a x20 long working distance objective, and the signal was recorded in backscattering geometry. For calibration of the Raman Shift the Si line at 520.7 cm^{-1} was used. The temperature for Raman spectra measurements was modulated by utilizing a Linkam THMS 600 temperature controlled system. Scanning electron microscopy (SEM) and energy-dispersive X-ray (EDX) spectra and mapping were recorded using a FEI Quanta 250 FEG scanning electron microscope with an EDAX detector. A tuneable, 10 ns pulsed optical parametric oscillator OPO (EKSPLA/NT342/3/UVE) laser was used as excitation light for recording the SHG and UCL emission spectra. The SHG and UCL signals were focused onto an optical fibre, coupled to a 0.303 m grating single Andor Shamrock SR-303i-A spectrometer and detected with a cooled, silicon CCD camera (Newton). The emission spectra were obtained using an excitation energy of the pulse laser of about 0.13 mJ, by focusing the laser beam onto a spherical spot of ≈ 50 μm in diameter, thus the energy density is ≈ 6600 mJ/cm^2. Considering that the repetition rate of the OPO laser is 10 Hz, the power used for acquisition of the emission spectra was ≈ 66 W/cm^2. This relatively low intensity of the excitation source prevents the laser-induced heating of the sample. The spectra were corrected for the equipment response. The temperature dependent spectroscopy measurements from room temperature to 575 K were carried out in a tubular electric furnace (Gero RES-E 230/3), using a type K thermocouple in contact with the sample to control the temperature.

3. Results and discussion

3.1. Properties at ambient condition

As shown in Fig. 1a, the experimental powder XRD patterns of the $BaTiO_3$: *x*Er^{3+}, 0.05 Yb^{3+} (*x* = 0.01, 0.05 and 0.09) fit well with the

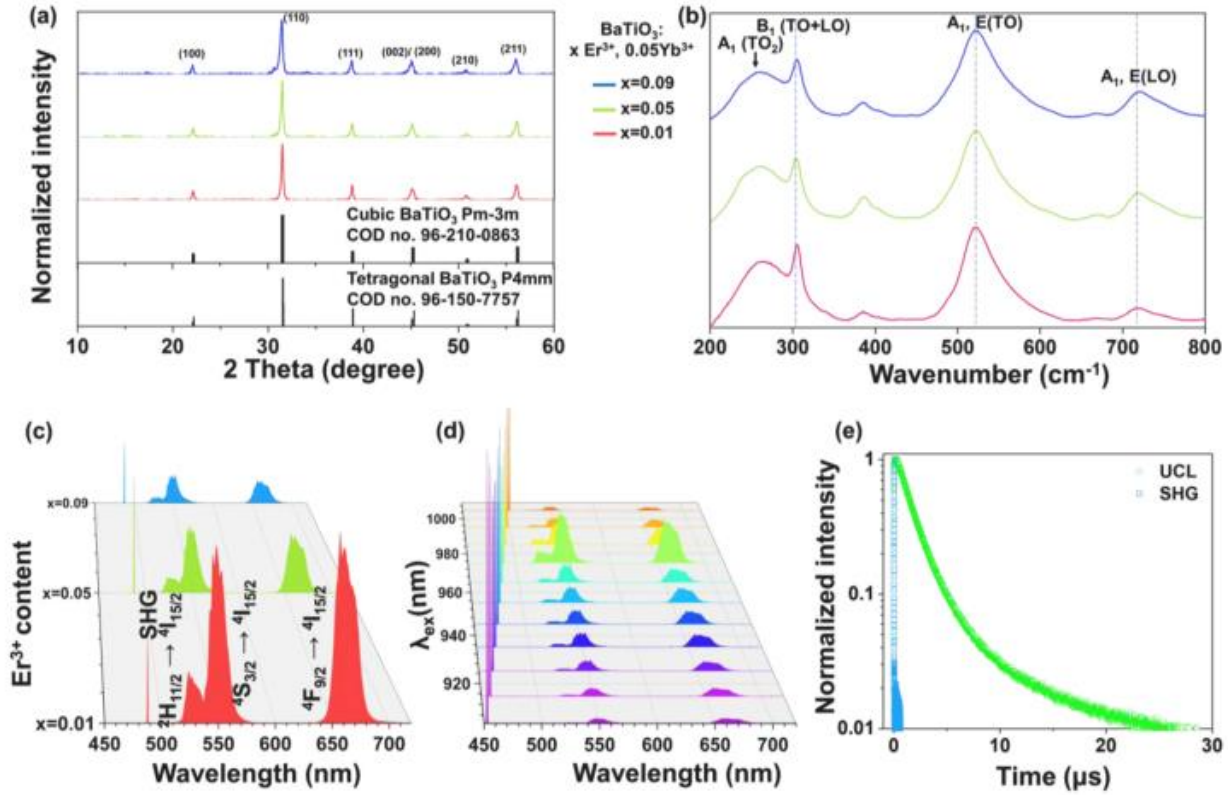

Fig. 1. (a) Powder XRD patterns and (b) Raman spectra of the $BaTiO_3$: xEr^{3+}, $0.05Yb^{3+}$ (x = 0.01, 0.05 and 0.09) materials. The marked (h, k, l) indices correspond to the lattice planes of tetragonal $BaTiO_3$ phase. (c) Emission spectra of the Ln^{3+}-doped $BaTiO_3$ samples as a function of Er^{3+} content, recorded at λ_{ex} = 976 nm; (d) emission spectra as a function of λ_{ex}; (e) signal decay curves for UCL of Er^{3+} ($^4S_{3/2} \rightarrow {}^4I_{15/2}$ transition) and SHG process.

reference pattern of tetragonal phase $BaTiO_3$ (a=b=3.999(9) Å, c= 4.017(0) Å, V= 64.269 Å^3, space group P4mm; card no. 96-150-7757), from Crystallography Open Database (COD). However, it is clearly seen that the reference pattern of the cubic phase (a=b=c=4.007(3) Å, V= 64.351 Å^3, space group Pm-3 m; card no. 96-210-0863) is very similar to the tetragonal one [56,57]. Hence, in order to try to distinguish the crystal structure of the synthesized materials, the Raman spectra were measured and shown in Fig. 1b. All samples show typical indicative peaks of tetragonal $BaTiO_3$ structure: ~304 cm^{-1} [B_1; E(TO+LO)], ~515 cm^{-1} [A_1; E(TO)], ~720 cm^{-1} [A_1; E(LO)], confirming the desired structure of the synthesized materials at room temperature [56]. With increasing doping concentration, the intensity of the band at ~719 cm^{-1} is slightly enhanced, which is attributed to the presence of more defects in the structure caused by the incorporation of the higher content of the Er^{3+} into the host matrix [58]. However, it is worth noting here that in this case, the Raman analysis may also not allow unambiguous distinction between the tetragonal and cubic phases (see the detailed discussion in the further part of the article, concerning temperature-dependent Raman spectra). This is because the Raman modes of the tetragonal and cubic phases are very similar are hard to distinguish, which can lead to undetected presence of the second phase in the sample [47].

The morphology of the selected sample, *i.e.*, $BaTiO_3$: 0.05 Er^{3+}, 0.05 Yb^{3+} was characterized by SEM technique, and the acquired microscopy images are shown in Fig. S1a-c. As shown, the materials obtained are composed of irregular micron-sized particles (~10–30 μm). Moreover, the EDX spectra and elemental mapping of the corresponding sample (shown in Fig. S1d-j) demonstrate that all elements (Ba, Ti, O, Er and Yb) are distributed evenly in the grains of the product, indicating the successful synthesis of the lanthanide-doped materials.

As presented in Fig. 1c, the UC emission spectra of the $BaTiO_3$: xEr^{3+}, $0.05Yb^{3+}$ (x = 0.01, 0.05 and 0.09) samples show the influence of Er^{3+} content on the UCL and SHG phenomena in the synthesized materials, at room temperature. Under NIR excitation with 976 nm laser, the emission spectra consist of several bands located in a visible spectral range, *i.e.*, a sharp line originated from SHG processes, centered at a half of the excitation wavelength, *i.e.*, 488 nm; green UCL emission bands located at ~525 and ~550 nm, originated from $^2H_{11/2} \rightarrow {}^4I_{15/2}$, $^4S_{3/2} \rightarrow {}^4I_{15/2}$ transitions of Er^{3+}, respectively, and red UCL band located at ~660 nm, originated from $^4F_{9/2} \rightarrow {}^4I_{15/2}$ transition of Er^{3+}. With increasing Er^{3+} content, the most intense SHG band was found for the sample containing 5 mol.% of Er^{3+}. The intensity of UCL decreases with increasing Er^{3+} content, which is due to concentration quenching effects (Er^{3+}-Er^{3+} cross-relaxation processes) [59–61], as shown Fig. 1c. In order to confirm the band located at 488 nm is correctly assigned to the SHG process, the emission spectra recorded at different excitation wavelengths (λ_{ex}) are shown in Fig. 1d. Tuning the excitation wavelength from 905 to 1025 nm, leads to the red-shift of the SHG peak, accordingly with $\lambda_{ex}/2$ dependence, further confirming the sharp band is associated with SHG process. As shown in Fig. 1e, the estimated effective lifetime from the luminescence decay curve recorded at λ_{em} = 550 nm ($^4S_{3/2} \rightarrow {}^4I_{15/2}$ transition of Er^{3+}) is about ~2 μs. Whereas, at λ_{em} = 488 nm the very fast decay (~5 ns) is related to the temporal limit, *i.e.*, delay of the detection system (instrumental response), because the SHG is an immediate process and occurs with the speed of light, further indicating the correct interpretation of the discussed phenomenon. Importantly, the dependence of the excitation power of

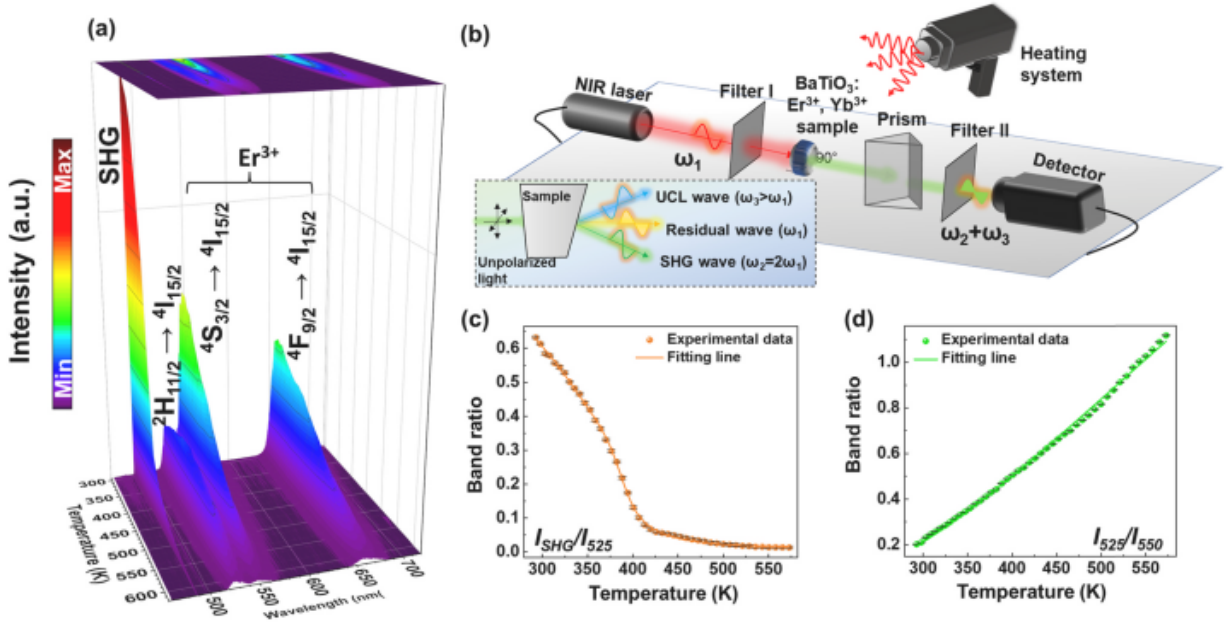

Fig. 2. (a) Variable-temperature emission spectra of the $BaTiO_3$:5% Er^{3+}, 5% Yb^{3+} sample. (b) Schematic representation of the experimental setup used for the measurements of NLO thermometry. (c) I_{SHG}/I_{525} and (d) I_{525}/I_{550} band intensity ratios as a function of temperature, and the corresponding fitting lines (Eq. 1 for I_{SHG}/I_{525} and Eq. 2 for I_{525}/I_{550}).

the UCL (at 550 nm) and SHG (at 488 nm, half of the excitation wavelength) are plotted in Fig. S2 in the SI data. As shown, the determined slope for both SHG and UCL are about 1.8, clearly indicating the same quadratic dependence of the SHG and UCL intensities *vs.* the excitation power (2nd order non-linear optical processes) [5,55].

3.2. Optical properties at high-temperature conditions

3.2.1. Luminescence thermometry and NLO thermometry

The temperature dependence of the emission spectra showing both SHG and UCL in $BaTiO_3$:Er^{3+}, Yb^{3+} material are shown in Fig. 2a, and the corresponding experimental setup for monitoring the behavior of SHG and UCL, at variable-temperature (330–575 K) conditions and the scheme of the SHG process in the synthesized sample are presented in Fig. 2b. The sample with most intense SHG signal, *i.e.*, $BaTiO_3$: 5% Er^{3+}, 5% Yb^{3+}, was selected for the measurements to investigate the effects of temperature on the NLO processes, as well as to explore and compare the performance of luminescence thermometry and NLO temperature sensing approach. The selection of the sample with most intense SHG signal is due to the expected giant deterioration of the SHG signal with increasing temperature (especially above phase transition temperature), as the intensity of UCL usually shows slower decreasing tendency with increasing temperature [5,55]. As shown in Fig. 2a, under NIR laser excitation, both intensities of SHG and UCL show a decreasing tendency with increasing temperature values. In comparison with UCL, the SHG shows a higher rate of signal decrease below ~400 K, and then exhibits a slower rate of change (a plateau). This is because the symmetry of $BaTiO_3$ crystals changes above that temperature, namely, the reversible phase transition from tetragonal crystal structure (P4mm) to cubic prototype phase (Pm3m) occurs [62–64], and the SHG process is forbidden in a centrosymmetric structure. Noteworthy, the SHG signal is not totally quenched even above the phase transition point [49,50,65]. This is plausibly due to (I) the crystal defects formed during the high-temperature synthesis, which are randomly distributed in the materials; (II) some crystals are still in the tetragonal phase, while most of the crystals have undergone a phase transition. On the other hand, the signal from UCL of Er^{3+} decreases monotonously with a significantly slower rate, compared to SHG process, due to the thermal quenching processes, *i.e.*, mainly enhanced multi-phonon relaxation and energy back transfer [66–68]. In order to explore the possibility of simultaneous employment of ratiometric luminescence and NLO thermometry (bimodal sensing), the emission intensities of the UCL bands located at 525 (I_{525}) and 550 nm (I_{550}), and the SHG band (I_{SHG}) were calculated *via* integration of their peak areas. The determined intensity ratio between the SHG peak and UCL band at 525 nm (I_{SHG}/I_{525}), and the intensity ratio between the thermally-coupled UCL emission bands at 525 and 550 nm (I_{525}/I_{550}) are shown in Fig. 2c and d, respectively. The I_{SHG}/I_{525} exhibits a sigmoidal dependence as a function of temperature, while the I_{525}/I_{550} shows a monotonic increasing tendency, typical of thermalized levels. A following analytical function can be well fitted (R^2 =0.999) to the corresponding experimental data:

$$\frac{I_{SHG}}{I_{525}} = y_0 + \sum_i \frac{A_i}{e^{(T-T_{xi})\times p_i} + 1} \quad (1)$$

Where T is the temperature, y_0 is the vertical offset, A_i is the amplitude, T_x is the "middle point" temperature and p is the fitting parameter. The fitting parameters of y_0, A_1, T_{x1}, p_1, A_2, T_{x2}, p_2, A_3, T_{x3} and p_3 are 0.5736, 0.1850, 387.6, 0.1151, −0.5579, 336.0, −0.0269, 0.0500, 147.0 and 0.3800, respectively. On the other hand, the values of luminescence intensity ratios attributed to the TCLs of Er^{3+}, *i.e.*, $^2H_{11/2}$ and $^4S_{3/2}$, were correlated with temperature and fitted (R^2=0.998) to the following equation, based on the Boltzmann distribution theory:

$$\frac{I_{525}}{I_{550}} = Bexp(\frac{-\Delta E}{kT}) \quad (2)$$

where B is a constant related to branching ratio of the transitions associated to the ground state, the rates of total spontaneous emission, states degeneracies and transitions angular frequencies [69]. ΔE is the energy difference between the TCLs of Er^{3+} and k is the Boltzmann constant. Based on Eq.2, the fitting parameters B

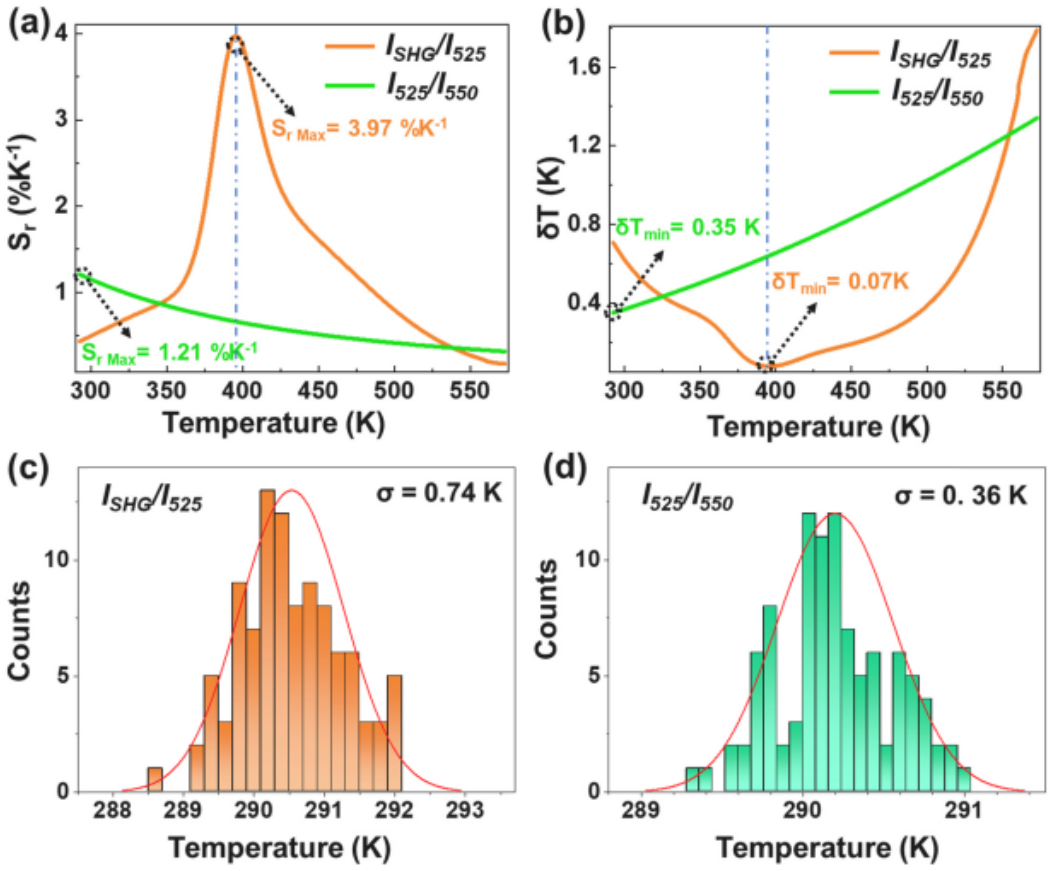

Fig. 3. (a) Relative thermal sensitivity S_r, and (b) the determined temperature resolution for I_{SHG}/I_{525} and I_{525}/I_{550}. The histogram for the determined experimental temperature resolution, *i.e.*, the standard deviation of determined temperature *via* (c) I_{SHG}/I_{525} and (d) I_{525}/I_{550}, obtained from the 100 repeatability measurements at 293 K.

= 6.5943, and the estimated energy difference $\Delta E = 494\ cm^{-1}$ were determined.

In order to get a deeper insight into the optical thermometric performances of the prepared materials and compare the NLO thermometry with conventional luminescence thermometry, the absolute sensitivity (S_a) and relative temperature sensitivities (S_r) were evaluated by using the following equation:

$$S_a = \left|\frac{dM_p}{dT}\right| \tag{3}$$

$$S_r = \frac{1}{M_p}\left|\frac{dM_p}{dT}\right| \times 100\% \tag{4}$$

where M_p is the sensing parameter, *i.e.*, I_{SHG}/I_{525} or I_{525}/I_{550}. Based on Eqs. (3) and (4) and the fitting results, the S_a and S_r values as a function of temperature for the NLO and luminescence thermometry were calculated and presented in Fig. S3 in SI and Fig. 3a, respectively. As shown, both the S_a and S_r values are strongly dependent on temperature. The maximal S_a using I_{SHG}/I_{525} or I_{525}/I_{550} are 0.008 K^{-1} at 386 K and 0.003 K^{-1} at 514 K, respectively, indicating the NLO thermometry exhibits higher thermal sensitivity. The S_r based on I_{SHG}/I_{525} parameter improves when temperature increases from 293 to 396 K, achieving its maxima of about 3.97%/K at 396 K. Then it shows a reflection point, decreasing with further temperature elevation. This sharp change in S_r is related to the phase transition from tetragonal to cubic $BaTiO_3$, which will be further discussed in the next paragraph. On the other hand, the S_r based on I_{525}/I_{550} shows a monotonic decreasing tendency with temperature, and the highest value was 1.21%/K at 293 K. In comparison, the S_r values based on NLO thermometry are much higher (~3.3 times) than the ones based on the conventional UCL thermometry, further indicating the NLO thermometry is more sensitive approach for optical temperature detection. However, it is worth noting here that this NLO sensing approach works most effectively in the case of the systems with reversible phase transitions, allowing sensing repeatability and monitoring alike increasing and decreasing temperature values.

Furthermore, the theoretical temperature resolutions (δT), *i.e.*, the uncertainties of temperature determination of the synthesized material, were calculated based on the following equation:

$$\delta T = \frac{1}{S_r}\ \frac{\delta \mathrm{MP}}{\mathrm{MP}} \tag{4}$$

where δMP is the uncertainty of determination of the band intensity ratio values, related to signal-to-noise ratio. As shown in Fig. 3b, the minimum values of the δT obtained based on I_{SHG}/I_{525} (~0.07 K at 396 K) are about 5 times lower than the ones based on I_{525}/I_{550} (~0.35 K at 293 K), indicating the NLO thermometry has higher precision than conventional luminescence thermometry. In order to confirm validity of the theoretical δT, the repetitive measurements of 100 spectra at room temperature were conducted. On the basis of the corresponding band intensity ratios and the fitting curves for temperature calibration, the determined temperature values from the repetitive measurements for I_{SHG}/I_{525} or I_{525}/I_{550} were presented respectively in the Fig. 3c and d. The experimental values of δT for I_{SHG}/I_{525} and I_{525}/I_{550} (equal to the full width at half maximum of the

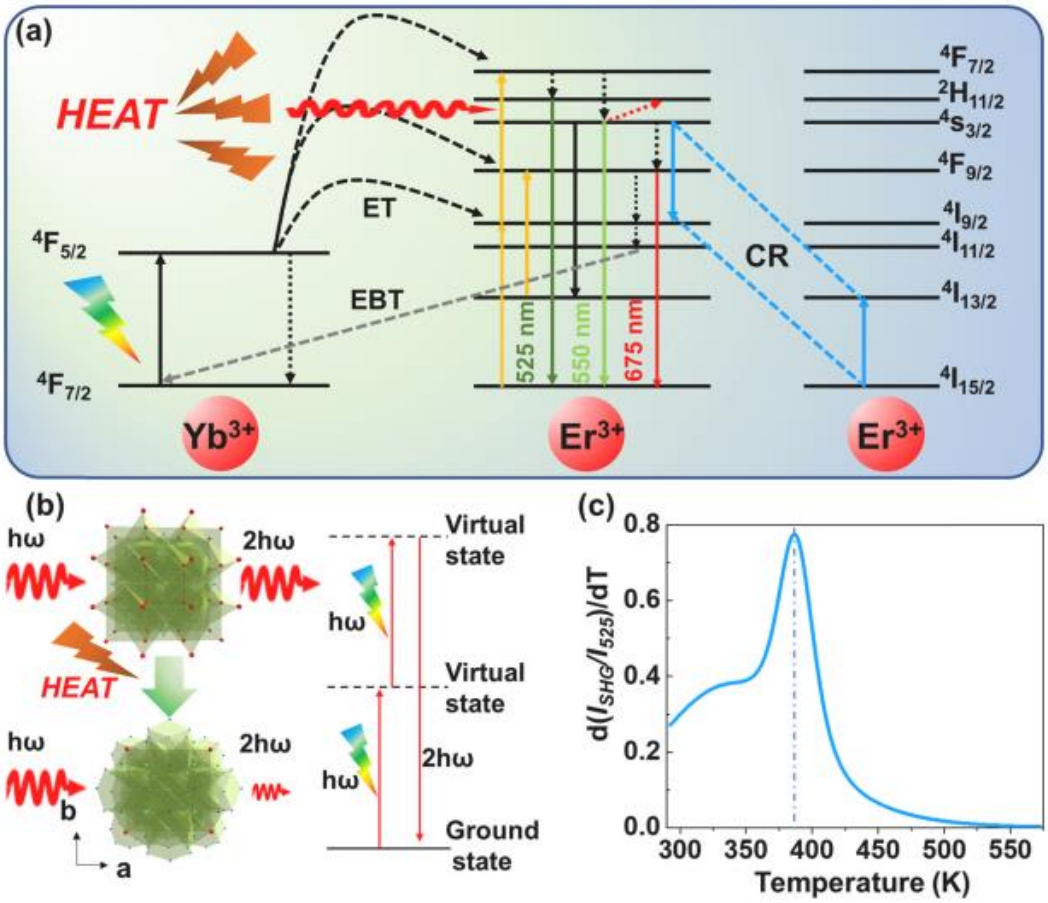

Fig. 4. (a) Scheme of the proposed energy mechanisms for UCL. (b) Scheme of phase transitions at T_C (left) and the simplified energy level diagram for SHG (right). (c) The derivative values by temperature for the I_{SHG}/I_{UCL} for phase transition determination.

Gauss peak) obtained from the repetitive measurements are 0.74 and 0.36 K, which agree well with the theoretical δT, *i.e.*, 0.71 and 0.35 K for I_{SHG}/I_{525} or I_{525}/I_{550}, further confirming reliability of the determined thermal resolutions.

3.2.2. Mechanism and phase transition detection

In order to clarify the influence of temperature on the UCL and SHG mechanisms in the $BaTiO_3$: $0.05Er^{3+}$, $0.05Yb^{3+}$ micron-sized particles, the corresponding energy levels scheme for UCL and SHG phenomena, including the major energy transfer (ET) process, radiative and non-radiative processes, *etc.*, are shown in Fig. 4a and b, respectively. As shown in Fig. 4a, under 976 nm laser excitation, the electrons initially populated at $^2F_{7/2}$ ground state are pumped into $^2F_{5/2}$ excited state in Yb^{3+}. Then the incident energy is absorbed and transferred towards a neighboring Er^{3+} ions, *i.e.*, $^2F_{5/2} + {}^4I_{15/2} \rightarrow {}^2F_{7/2} + {}^4I_{11/2}$ (ET) process. Afterwards, the second ET process takes place, *i.e.*, $^2F_{5/2} + {}^4I_{11/2} \rightarrow {}^2F_{7/2} + {}^4F_{7/2}$. Thus, the electrons populating the $^4I_{11/2}$ state are pumped to the $^4F_{7/2}$ state of Er^{3+} ions. Afterwards, the non-radiative (NR) decay occurs (marked with black dashed lines), leading to the population of Er^{3+} TCLs, namely $^2H_{11/2}$ and $^4S_{3/2}$ excited states. With increasing temperature, the population of Er^{3+} TCLs (band intensity ratio 525/550 nm) follows the Boltzmann distribution, as discussed in the previous paragraph. Moreover, the energy back transfer (EBT) and multi-phonon relaxation processes are responsible for the overall decrease of UCL intensity as a function of temperature [70–72]. On the other hand, *via* a SHG process (see Fig. 4b,), the materials synthesized absorb two low-energy photons (hω) and produce one photon with higher energy (2hω). However, the signal of SHG can be highly weakened, when the phase transforms from the non-centrosymmetric towards centrosymmetric system.

Many works have reported the temperature value (Curie point, T_C) of the phase transition (from tetragonal to cubic) in $BaTiO_3$ as ~393 K [49,50,65,73–75]. One effective pathway for determining T_C is based on electric properties in $BaTiO_3$ ferroelectrics, *i.e.*, by significant difference in ferroelectric hysteresis loop (ferroelectric to paraelectric phase) or the sharp change of dielectric constant as a function of temperature [49,50,65]. However, such measurements of ferroelectric properties and dielectric constant are difficult and time-consuming for polycrystalline materials, because in such a case they can be performed only for the ceramics or film materials. Moreover, there are some other experimental factors hampering the mentioned measurements, such as the difficulties in implementation of electric polarization process and the necessity of using sophisticated experimental setup. That is why, in order to monitor the phase transition, the temperature dependent Raman spectra of the $BaTiO_3$: $0.05Er^{3+}$, $0.05Yb^{3+}$ sample were measured and shown in Fig. S4 in the Supporting Information (SI) file. Unfortunately, it turned out that using this approach one cannot unambiguously determine the phase transition between tetragonal phase and cubic phase (similarly to

other reports about temperature-dependent Raman spectroscopy for $BaTiO_3$) [56,76–79]. This is because, the Raman modes for both phases are apparently quite similar, and neither the existing peaks disappear, nor the new ones appear above the T_C value, hampering the clear distinction of cubic and tetragonal phase structures [56,76–79]. Here, we demonstrate that using the developed NLO method, combining the SHG and UCL phenomena, *i.e.*, I_{SHG}/I_{525}, it is possible to identify the phase transition temperature point (T_C) precisely, rapidly and in a non-invasive way (which was hardly accessible by other optical methods, for such class of materials so far). The analysis of derivative of the measured spectroscopic parameter, *i.e.*, $d(I_{SHG}/I_{525})/dT$ as a function of temperature (shown in Fig. 4c), allows observation of the sharp change in its thermal evolution, clearly indicating the phase transition temperature in the material studied. Noteworthy, the $d(I_{SHG}/I_{525})/dT$ shows a clear reflection point at the phase transition temperature ~386 K, which is very close to the reported T_C values (~393 K) [49,50,65,73–75]. Such a strategy is a new and very effective approach for phase transition detection (and T_C determination), from broken inversion symmetric structure to centrosymmetric structure and *vice versa*.

It is worth noting, that in principle the SHG process is usually much less efficient than UCL one. That is why, in order to achieve comparable intensities of the UCL and SHG, either the UC emission efficiency should be relatively low, or the SHG process should be very efficient. Hence, despite of the good temperature sensing performance, the necessity of using high-energy (and high-cost) pulsed lasers for SHG, combined with relatively low UCL efficiency of different samples, may be a drawback for development of such NLO thermometers for some real applications. Importantly, the use of SHG for optical thermometry applications require the use of nanosecond (or shorter) pulse laser sources, which might create some technical difficulties in their utilization for temperature sensing of different systems in various conditions/environments.

4. Conclusions

Here we have shown that the NLO spectroscopy, *i.e.*, combination of SHG and UCL effects in a suitable, optically active material may be a new and powerful tool for optical thermometry and detection of phase transitions from broken inversion symmetric to centrosymmetric structure and *vice versa*. The developed optical probe based on the synthesized, polycrystalline (micron-sized) $BaTiO_3$: Er^{3+}, Yb^{3+} material exhibits dual-mode temperature readouts, *i.e.*, using traditional luminescence thermometry based on TCLs of Er^{3+} and NLO thermometry based on SHG and UCL intensity ratios. In comparison to conventional luminescence thermometry, the advantages of superior thermal sensitivity (maximal $S_r \approx 4\%/K$ at around 400 K) and excellent temperature resolution ($\delta T = 0.07$ K at ≈400 K) are confirmed for the NLO thermometry approach. Furthermore, the NLO spectroscopy allows precise, rapid and unambiguous phase transition detection from tetragonal to cubic phase at ≈ 386 K, compared to conventional pathways based on structural methods (such as Raman spectroscopy and XRD). In summary, our work shows that the NLO spectroscopy can not only be an accurate and highly sensitive, remote temperature sensing approach, but also a novel and effective detection tool in the structural studies of phase transitions and symmetry alterations in various systems.

CRediT authorship contribution statement

Teng Zheng: Conceptualization, Methodology, Software, Validation, Formal analysis, Investigation, Data curation, Writing – original draft, Visualization. **Marcin Runowski**: Conceptualization, Data curation, Writing – review & editing, Supervision, Funding acquisition. **Przemysław Woźny** Methodology, Formal analysis, Validation. **Bolesław Barszcz:** Methodology, Investigation, Validation. **Stefan Lis:** Supervision, Resources, Project administration, Funding acquisition. **Mauricio Vega:** Methodology, Visualization, Data curation. **Jaime Llanos:** Methodology, Investigation, Validation. **Kevin Soler-Carracedo:** Methodology, Investigation, Software, Formal analysis. **Inocencio R. Martín**: Conceptualization, Resources, Project administration, Validation, Supervision, Writing – review & editing.

Declaration of Competing Interest

The authors declare that they have no known competing financial interests or personal relationships that could have appeared to influence the work reported in this paper.

Acknowledgements

This work is financially supported by the Polish National Science Centre (grant No. UMO-2016/21/B/ST5/00110), by Ministerio de Ciencia e Innovación de Spain (MICIIN) under the National Program of Sciences and Technological Materials (PID2019-106383GB-C44 and PID2019-107335RA-I00) and Gobierno de Canarias (ProID2020010067) and EU-FEDER funds. Poland. TZ is also grateful to grant No. POWR.03.02.00–00-i020/17 financed by European Union through the European Social Fund under the Operational Program Knowledge Education Development. J. Llanos thanks Fondecyt (Grant 1181302). M. Vega appreciates the financial support of ANID/Scholarship Program/POSTDOCTORADO BECAS CHILE/2018-7419005.

Appendix A. Supporting information

Supplementary data associated with this article can be found in the online version at doi:10.1016/j.jallcom.2022.164329.

References

[1] S. Suresh, A. Ramanand, D. Jayaraman, P. Mani, Review on theoretical aspect of nonlinear optics, Rev. Adv. Mater. Sci. 30 (2012) 175–183.
[2] K.M. Ok, E.O. Chi, P.S. Halasyamani, Bulk characterization methods for non-centrosymmetric materials: second-harmonic generation, piezoelectricity, pyroelectricity, and ferroelectricity, Chem. Soc. Rev. 35 (2006) 710–717, https://doi.org/10.1039/b511119f
[3] J.F. McGilp, A review of optical second-harmonic and sum-frequency generation at surfaces and interfaces, J. Phys. D Appl. Phys. 29 (1996) 1812–1821, https://doi.org/10.1088/0022-3727/29/7/016
[4] G. Bachelier, J. Butet, I. Russier-Antoine, C. Jonin, E. Benichou, P.F. Brevet, Origin of optical second-harmonic generation in spherical gold nanoparticles: local surface and nonlocal bulk contributions, Phys. Rev. B Condens. Matter Mater. Phys. 82 (2010) 1–5, https://doi.org/10.1103/PhysRevB.82.235403
[5] T. Zheng, M. Runowski, I.R. Martín, S. Lis, M. Vega, J. Llanos, Nonlinear optical thermometry—a novel temperature sensing strategy via Second Harmonic Generation (SHG) and upconversion luminescence in $BaTiO_3$:Ho^{3+},Yb^{3+} perovskite, Adv. Opt. Mater. 3 (2021) 2100386, https://doi.org/10.1002/adom.202100386
[6] S.A. Denev, T.T.A. Lummen, E. Barnes, A. Kumar, V. Gopalan, Probing ferroelectrics using optical second harmonic generation, J. Am. Ceram. Soc. 94 (2011) 2699–2727, https://doi.org/10.1111/j.1551-2916.2011.04740.x
[7] E.D. Mishina, T.V. Misuryaev, N.E. Sherstyuk, V.V. Lemanov, A.I. Morozov, A.S. Sigov, T. Rasing, Observation of a near-surface structural phase transition in $SrTiO_3$, Phys. Rev. Lett. 85 (2000) 3664–3667.
[8] G.T. Boyd, T. Rasing, J.R.R. Leite, Y.R. Shen, Local-field enhancement on rough surfaces of metals, semimetals, and semiconductors with the use of optical second-harmonic generation, Phys. Rev. B 30 (1984) 519–526, https://doi.org/10.1103/PhysRevB.30.519
[9] J. Butet, P.F. Brevet, O.J.F. Martin, Optical second harmonic generation in plasmonic nanostructures: from fundamental principles to advanced applications, ACS Nano 9 (2015) 10545–10562, https://doi.org/10.1021/acsnano.5b04373
[10] M. Mutailipu, Z. Yang, S. Pan, Toward the enhancement of critical performance for deep-ultraviolet frequency-doubling crystals utilizing covalent tetrahedra, accounts, Mater. Res. 2 (2021) 282–291, https://doi.org/10.1021/accountsmr.1c00028
[11] R.J. Zeches, M.D. Rossell, J.X. Zhang, A.J. Hatt, Q. He, C.H. Yang, A. Kumar, C.H. Wang, A. Melville, C. Adamo, G. Sheng, Y.H. Chu, J.F. Ihlefeld, R. Erni, C. Ederer, V. Gopalan, L.Q. Chen, D.G. Schldin, N.A. Spaldin, L.W. Martin, R. Ramesh, A strain-driven morphotropic phase boundary in bife03, Science 326 (2009) 977–980, https://doi.org/10.1126/science.1177046 (80-.).

[12] K.J. Choi, M. Biegalski, Y.L. Li, A. Sharan, J. Schubert, R. Uecker, P. Reiche, Y.B. Chen, X.Q. Pan, V. Gopalan, L.Q. Che, D.C. Schlom, C.B. Eom, Enhancement of ferroelectricity in strained $BaTiO_3$ thin films, Science 306 (2004) 1005–1009, https://doi.org/10.1126/science.1103218 (80-.).

[13] A. Vasudevarao, A. Kumar, L. Tian, J.H. Haeni, Y.L. Li, C.J. Eklund, Q.X. Jia, R. Uecker, P. Reiche, K.M. Rabe, L.Q. Chen, D.G. Schlom, V. Gopalan, Multiferroic domain dynamics in strained strontium titanate, Phys. Rev. Lett. 97 (2006) 2–5, https://doi.org/10.1103/PhysRevLett.97.257602

[14] C.C. Neacsu, B.B. Van Aken, M. Fiebig, M.B. Raschke, Second-harmonic near-field imaging of ferroelectric domain structure of $YMnO_3$, Phys. Rev. B Condens. Matter Mater. Phys. 79 (2009) 1–4, https://doi.org/10.1103/PhysRevB.79.100107

[15] C.D.S. Brites, A. Millán, L.D. Carlos, Lanthanides in luminescent thermometry, Handb. Phys. Chem. Rare Earths, Elsevier B.V., 2016, pp. 339–427, https://doi.org/10.1016/bs.hpcre.2016.03.005

[16] D. Jaque, F. Vetrone, Luminescence nanothermometry, Nanoscale 4 (2012) 4301–4326, https://doi.org/10.1039/c2nr30764b

[17] S. Zhuo, M. Shao, S.T. Lee, Upconversion and downconversion fluorescent graphene quantum dots: ultrasonic preparation and photocatalysis, ACS Nano 6 (2012) 1059–1064, https://doi.org/10.1021/nn2040395

[18] H. Dong, L.D. Sun, C.H. Yan, Energy transfer in lanthanide upconversion studies for extended optical applications, Chem. Soc. Rev. 44 (2015) 1608–1634, https://doi.org/10.1039/c4cs00188e

[19] M. Runowski, A. Shyichuk, A. Tymiński, T. Grzyb, V. Lavín, S. Lis, Multifunctional optical sensors for nanomanometry and nanothermometry: high-pressure and high-temperature upconversion luminescence of lanthanide-doped phosphates - $LaPO_4/YPO_4$:Yb^{3+}-Tm^{3+}, ACS Appl. Mater. Interfaces 10 (2018) 17269–17279, https://doi.org/10.1021/acsami.8b02853

[20] K. Soler-Carracedo, I.R. Martin, M. Runowski, L.L. Martín, F. Lahoz, A.D. Lozano-Gorrín, F. Paz-Buclatin, Luminescent Nd^{3+}-based microresonators working as optical vacuum sensors, Adv. Opt. Mater. 8 (2020) 1–9, https://doi.org/10.1002/adom.202000678

[21] Y.C. Lin, M. Bettinelli, M. Karlsson, Unraveling the mechanisms of thermal quenching of luminescence in Ce^{3+}-doped garnet phosphors †, Chem. Mater. 31 (2019) 3851–3862, https://doi.org/10.1021/acs.chemmater.8b05300

[22] L.D. Carlos, R.A.S. Ferreira, V. De Zea Bermudez, B. Julián-López, P. Escribano, Progress on lanthanide-based organic–inorganic hybrid phosphors, Chem. Soc. Rev. 40 (2011) 536–549, https://doi.org/10.1039/c0cs00069h

[23] W. Zheng, P. Huang, D. Tu, E. Ma, H. Zhu, X. Chen, Lanthanide-doped upconversion nano-bioprobes: electronic structures, optical properties, and biodetection, Chem. Soc. Rev. 44 (2015) 1379–1415, https://doi.org/10.1039/c4cs00178h

[24] A. Gnach, A. Bednarkiewicz, Lanthanide-doped up-converting nanoparticles: merits and challenges, Nano Today 7 (2012) 532–563, https://doi.org/10.1016/j.nantod.2012.10.006

[25] K. Maciejewska, L. Marciniak, Multimodal Stokes and Anti-Stokes luminescent thermometers based on GdP_5O_{14} co-doped with Cr^{3+} and Nd^{3+} ions, Chem. Eng. J. 402 (2020) 126197, https://doi.org/10.1016/j.cej.2020.126197

[26] A. Benayas, Near infrared-emitting nanoparticles for biomedical applications, Med. Microbiol. Immunol. 209 (2020) 489–498, https://doi.org/10.1007/978-3-030-32036-2

[27] R. Marin, D. Jaque, A. Benayas, Switching to the brighter lane: pathways to boost the absorption of lanthanide-doped nanoparticles, Nanoscale Horiz. 6 (2021) 209–230, https://doi.org/10.1039/d0nh00627k

[28] C.D.S. Brites, K. Fiaczyk, J.F.C.B. Ramalho, M. Sójka, L.D. Carlos, E. Zych, Widening the temperature range of luminescent thermometers through the intra- and interconfigurational transitions of Pr^{3+}, Adv. Opt. Mater. 6 (2018) 1–5, https://doi.org/10.1002/adom.201701318

[29] W. Piotrowski, K. Trejgis, K. Maciejewska, K. Ledwa, B. Fond, L. Marciniak, Thermochromic luminescent nanomaterials based on Mn^{4+}/Tb^{3+} codoping for temperature imaging with digital cameras, ACS Appl. Mater. Interfaces 12 (2020) 44039–44048, https://doi.org/10.1021/acsami.0c11730

[30] Y. Pan, X. Xie, Q. Huang, C. Gao, Y. Wang, L. Wang, B. Yang, H. Su, L. Huang, W. Huang, Inherently Eu^{2+}/Eu^{3+} codoped Sc_2O_3 nanoparticles as high-performance nanothermometers, Adv. Mater. 30 (2018) 3–8, https://doi.org/10.1002/adma.201705256

[31] S. Goderski, M. Runowski, P. Woźny, V. Lavín, S. Lis, Lanthanide upconverted luminescence for simultaneous contactless optical thermometry and manometry-sensing under extreme conditions of pressure and temperature, ACS Appl. Mater. Interfaces 12 (2020) 40475–40485, https://doi.org/10.1021/acsami.0c09882

[32] T. Zheng, X. Qiu, L. Zhou, M. Runowski, S. Lis, P. Du, L. Luo, Multiple ratiometric nanothermometry operating with Stark thermally and non-thermally-coupled levels in upconverting $Y_{2-x}MoO_6$:xEr^{3+} nanoparticles, J. Alloy. Compd. 864 (2021), https://doi.org/10.1016/j.jallcom.2021.158891

[33] M. Runowski, P. Woźny, S. Lis, V. Lavín, I.R. Martín, Optical vacuum sensor based on lanthanide upconversion−luminescence thermometry as a tool for ultralow pressure sensing, Adv. Mater. Technol. 5 (2020) 1901091, https://doi.org/10.1002/admt.201901091

[34] Z. Xu, M. Quintanilla, F. Vetrone, A.O. Govorov, M. Chaker, D. Ma, Harvesting lost photons: plasmon and upconversion enhanced broadband photocatalytic activity in core@shell microspheres based on lanthanide-doped $NaYF_4$, TiO_2, and Au, Adv. Funct. Mater. 25 (2015) 2950–2960, https://doi.org/10.1002/adfm.201500810

[35] J. Zhang, Y. Huang, L. Jin, F. Rosei, F. Vetrone, J.P. Claverie, Efficient upconverting multiferroic core@shell photocatalysts: visible-to-near-infrared photon harvesting, ACS Appl. Mater. Interfaces 9 (2017) 8142–8150, https://doi.org/10.1021/acsami.7b00158

[36] Y. Rong, Y. Hu, A. Mei, H. Tan, M.I. Saidaminov, S. Il Seok, M.D. McGehee, E.H. Sargent, H. Han, Challenges for commercializing perovskite solar cells, Science 361 (2018), https://doi.org/10.1126/science.aat8235 (80-.).

[37] Y.M. You, W.Q. Liao, D. Zhao, H.Y. Ye, Y. Zhang, Q. Zhou, X. Niu, J. Wang, P.F. Li, D.W. Fu, Z. Wang, S. Gao, K. Yang, J.M. Liu, J. Li, Y. Yan, R.G. Xiong, An organic-inorganic perovskite ferroelectric with large piezoelectric response, Science 357 (2017) 306–309, https://doi.org/10.1126/science.aai8535 (80-.).

[38] N. Nuraje, K. Su, Perovskite ferroelectric nanomaterials, Nanoscale 5 (2013) 8752–8780, https://doi.org/10.1039/c3nr02543h

[39] B. Zhuang, Y. Liu, S. Yuan, H. Huang, J. Chen, D. Chen, Glass stabilized ultra-stable dual-emitting Mn-doped cesium lead halide perovskite quantum dots for cryogenic temperature sensing, Nanoscale 11 (2019) 15010–15016, https://doi.org/10.1039/c9nr05831a

[40] D. Kumar Singh, K. Mondal, J. Manam, Improved photoluminescence, thermal stability and temperature sensing performances of K+ incorporated perovskite BaTiO3:Eu3+ red emitting phosphors, Ceram. Int. 43 (2017) 13602–13611, https://doi.org/10.1016/j.ceramint.2017.07.069

[41] C. Martin, Perovskite photovoltaics, Nat. Mater. 11 (2012), https://doi.org/10.1038/nmat3515 (1002–1002).

[42] G. Pacchioni, Highly efficient perovskite LEDs, Nat. Rev. Mater. 6 (2021) 108, https://doi.org/10.1038/s41578-021-00280-5

[43] T.H. Han, S. Tan, J. Xue, L. Meng, J.W. Lee, Y. Yang, Interface and defect engineering for metal halide perovskite optoelectronic devices, Adv. Mater. 31 (2019) 1–35, https://doi.org/10.1002/adma.201803515

[44] G. Jyothi, L.S. Kumari, K.G. Gopchandran, White emitting Dy^{3+} activated perovskite titanates and energy transfer by Eu^{3+} codoping, Ceram. Int. 43 (2017) 12044–12056, https://doi.org/10.1016/j.ceramint.2017.06.058

[45] Z. Dai, J. Xie, W. Liu, X. Wang, L. Zhang, Z. Zhou, J. Li, X. Ren, Effective strategy to achieve excellent energy storage properties in lead-free $BaTiO_3$-based bulk ceramics, ACS Appl. Mater. Interfaces 12 (2020) 30289–30296, https://doi.org/10.1021/acsami.0c02832

[46] D.P. Dutta, A. Ballal, J. Nuwad, A.K. Tyagi, Optical properties of sonochemically synthesized rare earth ions doped $BaTiO_3$ nanophosphors: probable candidate for white light emission, J. Lumin 148 (2014) 230–237, https://doi.org/10.1016/j.jlumin.2013.11.071

[47] M. Vega, I.R. Martin, J. Llanos, Near-infrared to visible upconversion and second harmonic generation in $BaTiO_3$:Ho^{3+} and $BaTiO_3$:Ho^{3+}/Yb^{3+} phosphors, J. Alloy. Compd. 806 (2019) 1146–1152, https://doi.org/10.1016/j.jallcom.2019.07.311

[48] E. Aksel, J.L. Jones, Advances in lead-free piezoelectric materials for sensors and actuators, Sensors 10 (2010) 1935–1954, https://doi.org/10.3390/s100301935

[49] M. Acosta, N. Novak, V. Rojas, S. Patel, R. Vaish, J. Koruza, G.A. Rossetti, J. Rödel, BaTiO3-based piezoelectrics: Fundamentals, current status, and perspectives, Appl. Phys. Rev. 4 (2017), https://doi.org/10.1063/1.4990046

[50] P.R. Potnis, N.T. Tsou, J.E. Huber, A review of domain modelling and domain imaging techniques in ferroelectric crystals, Materials 4 (2010) 417–447, https://doi.org/10.3390/ma4020417

[51] L. Labrador-Páez, M. Pedroni, A. Speghini, J. García-Solé, P. Haro-González, D. Jaque, Reliability of rare-earth-doped infrared luminescent nanothermometers, Nanoscale 10 (2018) 22319–22328, https://doi.org/10.1039/c8nr07566b

[52] C.D.S. Brites, P.P. Lima, N.J.O. Silva, A. Millán, V.S. Amaral, F. Palacio, L.D. Carlos, A luminescent molecular thermometer for long-term absolute temperature measurements at the nanoscale, Adv. Mater. 22 (2010) 4499–4504, https://doi.org/10.1002/adma.201001780

[53] C.D.S. Brites, P.P. Lima, N.J.O. Silva, A. Millán, V.S. Amaral, F. Palacio, L.D. Carlos, Thermometry at the nanoscale, Nanoscale 4 (2012) 4799–4829, https://doi.org/10.1039/c2nr30663h

[54] M.D. Dramićanin, Trends in luminescence thermometry, J. Appl. Phys. 128 (2020), https://doi.org/10.1063/5.0014825

[55] J.F. da Silva, C. Jacinto, A.L. Moura, Giant sensitivity of an optical nanothermometer based on parametric and non-parametric emissions from Tm^{3+} doped $NaNbO_3$ nanocrystals, J. Lumin 226 (2020), https://doi.org/10.1016/j.jlumin.2020.117475

[56] H. Hayashi, T. Nakamura, T. Ebina, In-situ Raman spectroscopy of $BaTiO_3$ particles for tetragonal-cubic transformation, J. Phys. Chem. Solids 74 (2013) 957–962, https://doi.org/10.1016/j.jpcs.2013.02.010

[57] S. Kappadan, T.W. Gebreab, S. Thomas, N. Kalarikkal, Tetragonal $BaTiO_3$ nanoparticles: an efficient photocatalyst for the degradation of organic pollutants, Mater. Sci. Semicond. Process 51 (2016) 42–47, https://doi.org/10.1016/j.mssp.2016.04.019

[58] T. Badapanda, V. Senthil, S. Panigrahi, S. Anwar, Diffuse phase transition behavior of dysprosium doped barium titanate ceramic, J. Electroceram. 31 (2013) 55–60, https://doi.org/10.1007/s10832-013-9808-x

[59] D. Ramachari, L. Rama Moorthy, C.K. Jayasankar, Gain properties and concentration quenching of Er^{3+}-doped niobium oxyfluorosilicate glasses for photonic applications, Opt. Mater. 36 (2014) 823–828, https://doi.org/10.1016/j.optmat.2013.12.013

[60] Y. Ding, X. Zhang, H. Gao, S. Xu, C. Wei, Y. Zhao, Enhancement on concentration quenching threshold and upconversion luminescence of β-$NaYF_4$:Er^{3+}/Yb^{3+} co-doping with Li^+ ions, J. Alloy. Compd. 599 (2014) 60–64, https://doi.org/10.1016/j.jallcom.2014.02.050

[61] P. Du, Y. Liu, Y.J. Kim, J.S. Yu, One-pot synthesis of homogeneous EuF_3 nanoplates: a near-ultraviolet light-induced red-emitting bifunctional platform for in vitro cell imaging and solid-state lighting, ChemistrySelect 4 (2019) 2275–2280, https://doi.org/10.1002/slct.201803982

[62] C. Chen, X. Zhao, Y. Wang, H. Zhang, H. Deng, X. Li, X. Jiang, X. Jiang, H. Luo, Giant strain and electric-field-induced phase transition in lead-free $(Na_{0.5}Bi_{0.5})TiO_3$-

$BaTiO_3$-$(K_{0.5}Na_{0.5})NbO_3$ single crystal, Appl. Phys. Lett. 108 (2016) 0–4, https://doi.org/10.1063/1.4939851
[63] M. Hinterstein, M. Knapp, M. Hölzel, W. Jo, A. Cervellino, H. Ehrenberg, H. Fuess, Field-induced phase transition in $Bi_{1/2}Na_{1/2}TiO_3$-based lead-free piezoelectric ceramics, J. Appl. Crystallogr. 43 (2010) 1314–1321, https://doi.org/10.1107/S0021889810038264
[64] C. Tian, F. Wang, X. Ye, Y. Xie, T. Wang, Y. Tang, D. Sun, W. Shi, Bipolar fatigue-resistant behavior in ternary $Bi_{0.5}Na_{0.5}TiO_3$-$BaTiO_3$-$SrTiO_3$ solid solutions, Scr. Mater. 83 (2014) 25–28, https://doi.org/10.1016/j.scriptamat.2014.03.027
[65] D. Fu, M. Itoh, Role of Ca off-centering in tuning the ferroelectric phase transitions in $Ba(Zr,Ti)O_3$ system, Ferroelectric Materials - synthesis and characterization, http://dx.doi.org/10.5772/61017.
[66] X.X. Zhang, P. Hong, M. Bass, B.H.T. Chai, Ho^{3+} to Yb^{3+} back transfer and thermal quenching of upconversion green emission in fluoride crystals, Appl. Phys. Lett. 63 (1993) 2606–2608, https://doi.org/10.1063/1.110445
[67] A. Dobrowolska, B. Dierre, C.M. Fang, H.T. Hintzen, P. Dorenbos, Thermal quenching of Eu^{2+} emission in Ca- and Sr-Ga_2S_4 in relation with VRBE schemes, J. Lumin. 184 (2017) 256–261, https://doi.org/10.1016/j.jlumin.2016.12.022
[68] T. Zheng, L. Luo, P. Du, A. Deng, W. Li, Ferroelectric, upconversion emission and optical thermometric properties of color-controllable Er^{3+}-doped $Pb(Mg_{1/3}Nb_{2/3})O_3$-$PbTiO_3$-$Pb(Yb_{1/2}Nb_{1/2})O_3$ ferroelectrics, J. Eur. Ceram. Soc. 38 (2018) 575–583, https://doi.org/10.1016/j.jeurceramsoc.2017.09.035
[69] S.A. Wade, S.F. Collins, G.W. Baxter, Fluorescence intensity ratio technique for optical fiber point temperature sensing, J. Appl. Phys. 94 (2003) 4743–4756, https://doi.org/10.1063/1.1606526
[70] C.B. Layne, W.H. Lowdermilk, M.J. Weber, Multiphonon relaxation of rare-earth ions in oxide glasses, Phys. Rev. B 16 (1977) 10–20, https://doi.org/10.1103/PhysRevB.16.10
[71] J. Liu, H. Deng, Z. Huang, Y. Zhang, D. Chen, Y. Shao, Phonon-assisted energy back transfer-induced multicolor upconversion emission of Gd_2O_3:Yb^{3+}/Er^{3+} nanoparticles under near-infrared excitation, Phys. Chem. Chem. Phys. 17 (2015) 15412–15418, https://doi.org/10.1039/c5cp01632k
[72] J.I. Eldridge, Luminescence decay-based Y_2O_3:Er phosphor thermometry: Temperature sensitivity governed by multiphonon emission with an effective phonon energy transition, J. Lumin. 214 (2019) 116535, https://doi.org/10.1016/j.jlumin.2019.116535
[73] P.V. Balachandran, D. Xue, T. Lookman, Structure-Curie temperature relationships in $BaTiO_3$ -based ferroelectric perovskites: anomalous behavior of $(Ba,Cd)TiO_3$ from DFT, statistical inference, and experiments, Phys. Rev. B 93 (2016) 1–12, https://doi.org/10.1103/PhysRevB.93.144111
[74] A. Karvounis, F. Timpu, V.V. Vogler-Neuling, R. Savo, R. Grange, Barium titanate nanostructures and thin films for photonics, Adv. Opt. Mater. 8 (2020) 1–23, https://doi.org/10.1002/adom.202001249
[75] Y.J. Kim, J.W. Hyun, Effects of Nb^{5+} addition on microstructure and dielectric properties of $BaTiO_3$, Appl. Sci. Converg. Technol. 26 (2017) 143–147, https://doi.org/10.5757/asct.2017.26.5.143
[76] K. Madhan, R. Thiyagarajan, C. Jagadeeshwaran, A. Paul Blessington Selvadurai, V. Pazhanivelu, K. Aravinth, W. Yang, R. Murugaraj, Investigations on the phase transition of Mn-doped $BaTiO_3$ multifunctional ferroelectric ceramics through Raman, dielectric, and magnetic studies, J. Sol. Gel Sci. Technol. 88 (2018) 584–592, https://doi.org/10.1007/s10971-018-4835-3
[77] Y.I. Yuzyuk, Raman scattering spectra of ceramics, films, and superlattices of ferroelectric perovskites: a review, Phys. Solid State 54 (2012) 1026–1059, https://doi.org/10.1134/S1063783412050502
[78] J. Pokorný, U.M. Pasha, L. Ben, O.P. Thakur, D.C. Sinclair, I.M. Reaney, Use of Raman spectroscopy to determine the site occupancy of dopants in $BaTiO_3$, J. Appl. Phys. 109 (2011), https://doi.org/10.1063/1.3592192
[79] L.F. Zhu, B.P. Zhang, L. Zhao, J.F. Li, High piezoelectricity of $BaTiO_3$-$CaTiO_3$-$BaSnO_3$ lead-free ceramics, J. Mater. Chem. C 2 (2014) 4764–4771, https://doi.org/10.1039/c4tc00155a

Supporting Information for

Boltzmann vs. non-Boltzmann (non-linear) thermometry - Yb^{3+}-Er^{3+} Activated Dual-mode thermometer and Phase Transition sensor via Second Harmonic Generation

Teng Zheng[1], Marcin Runowski[1,4,*], Przemysław Woźny,[1] Bolesław Barszcz[2], Stefan Lis[1], Mauricio Vega[3], Jaime Llanos[3], Kevin Soler-Carracedo[4] and Inocencio R. Martín[4]

[1]*Adam Mickiewicz University, Faculty of Chemistry, Uniwersytetu Poznańskiego 8, 61-614 Poznań, Poland*

[2]*Institute of Molecular Physics, Polish Academy of Sciences, Mariana, Smoluchowskiego 17, 60-179 Poznań, Poland*

[3]*Departamento de Química, Universidad Católica del Norte, Avda. Angamos 0610, Antofagasta, Chile*

[4]*Universidad de La Laguna, Departamento de Física, Apdo. Correos 456 E-38200, San Cristóbal de La Laguna, Santa Cruz de Tenerife, Spain*

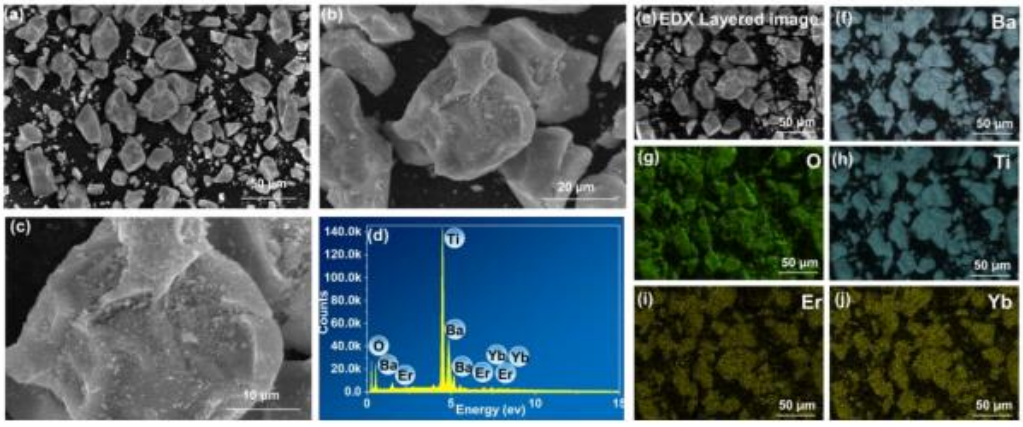

Fig. S1. (a-c) SEM images. (d) EDX spectrum and (e-j) EDX mapping of the $BaTiO_3$: 5% Er^{3+}, 5%Yb^{3+} micron-sized particles.

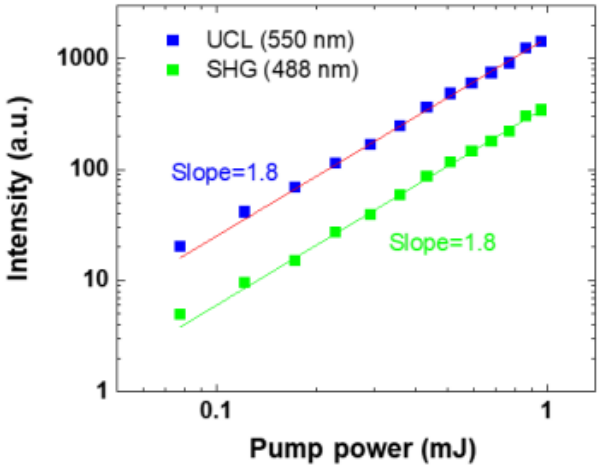

Fig. S2. Dependences of the integrated up-conversion luminescence (UCL) at 550 nm and second-harmonic generation (SHG) intensities vs. excitation power (log-log plot), under excitation at 976 nm. The indicated slope values determined by linear fits correspond to the number of photons participating in the given process.

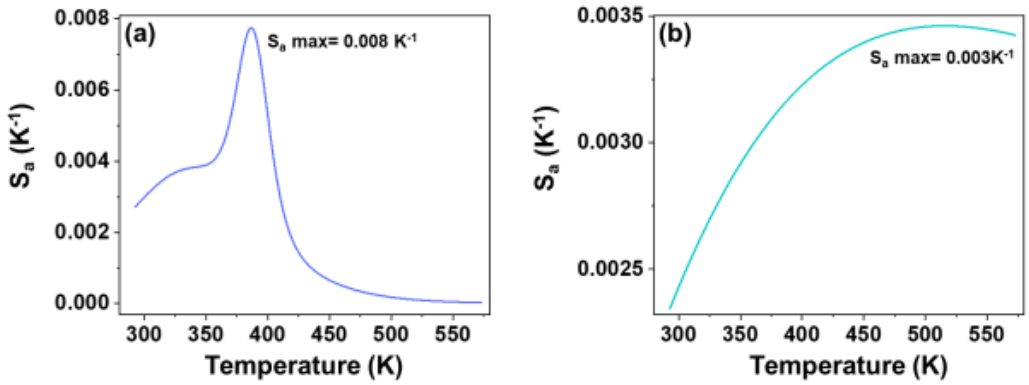

Fig. S3. The determined absolute sensitivities for (a) I_{SHG}/I_{525} and (b) I_{525}/I_{550}.

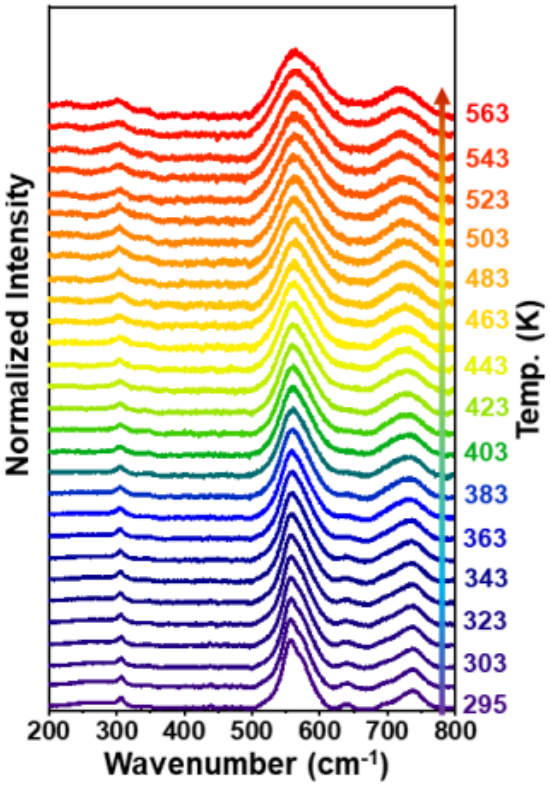

Fig. S4. The temperature-dependent Raman spectra for the $BaTiO_3$: 5% Er^{3+}, 5%Yb^{3+} micron-sized particles.

7. Abstract

The doctoral dissertation is devoted to the investigation of the structural, morphological and PL performances of selected inorganic oxide host matrices, i.e., SrB_4O_7 and $BaTiO_3$, doped with Ln^{2+} or Ln^{3+}. The main goal of the work was to develop and characterize thoroughly new strategies for the optical manometer and thermometer.

For the implementation of the tasks, several series of luminescent materials based on SrB_4O_7:Eu^{2+}, SrB_2O_4:$Eu^{2+/3+}$, $Sr_3(BO_3)_2$: $Eu^{2+/3+}$, SrB_4O_7:Eu^{2+}, Sm^{2+}, SrB_4O_7: Tm^{2+}, $BaTiO_3$:Er^{3+}-Yb^{3+} and $BaTiO_3$:Ho^{3+}-Yb^{3+} phosphors were synthesized. For pressure sensing, we applied the inter-configurational 5d-4f transitions, which are very sensitive to the external crystalline environment, in the case of novel pressure sensors with high sensitivity, excellent pressure sensing luminescence signal (thus wider pressure sensing range), etc.

First, several candidates of borate matrices, i.e., SrB_4O_7, SrB_2O_4 and $Sr_3(BO_3)_2$, were selected and characterized for stabilization of Ln^{2+} (using Eu^{2+} as an example). The influence of the matrix on the structural, morphological and PL properties has been systematically investigated and analysed. Subsequently, several strategies of optical pressure sensing were proposed: I) the strategy of luminescent signal enhancement (~ 60 times) of Sm^{2+}: $^5D_0 \rightarrow {}^7F_0$ peak through the $Eu^{2+} \rightarrow Sm^{2+}$ ET process in the co-doped SrB_4O_7 pressure sensor; The developed sensor also exhibits good pressure shift, excellent temperature independence and a wide pressure sensing range. II) The strategy to use the pressure-enhanced (enhancement by 3 orders magnitude) 4f-4f emission of Eu^{2+} in SrB_4O_7 for the optical pressure detection towards the higher-pressure range (~60 GPa). A systematic experimental and computational analysis was performed to reveal the reason of the enhancement, i.e., the electrons transfer from 5d→4f levels and the pressure-driven Configurational Crossover between $4f^7$ and $4f^65d^1$ States. III) For the first time, the 5d-4f emission of Tm^{2+} in the same matrix has been applied as a bifunctional platform, which can provide satisfactory sensing performance for luminescent pressure and temperature sensing over a wide pressure/temperature range.

On the other hand, SHG and UCL were observed simultaneously in the well-established $BaTiO_3$ matrix doped with Ln^{3+}. SHG is a polarization-sensitive, instantaneous nonlinear optical process, which is sensitive to changes in the symmetry of materials (between centrosymmetric and non-centrosymmetric structure). Thus, novel temperature sensing strategy was developed – non-

linear optical thermometry based on symmetry-sensitive SHG and thermal-sensitive UCL processes in the well-established $BaTiO_3$ matrix doped with Ho^{3+}-Yb^{3+}. Moreover, the PL and thermometric analysis in the Er^{3+}-Yb^{3+} co-doped $BaTiO_3$ system allows for a detailed comparison of conventional Boltzmann thermometry (based on TCLs of Er^{3+}) and non-linear optical thermometry, which indicates superior thermometric performances of the later. The research presented in the doctoral dissertation is an innovative and very successful contribution to the development of materials science, especially in the field of optical pressure and temperature sensing.

Prof. dr hab. Stefan Lis
(names and surnames of the co-author)

Załącznik Nr 10
do zasad

Adam Mickiewicz University in Poznań
(full name of the unit represented by the author)

STATEMENT

I declare that in the doctoral dissertation entitled:

Lanthanide (III or II) activated SrB_4O_7 and $BaTiO_3$ materials for Luminescent Manometry and Non-linear Optical Thermometry

my contribution consisted of:

I am co-authors of the papers:

Teng Zheng, Marcin Runowski, Inocencio R. Martín, Stefan Lis, Mauricio Vega, and Jaime Llanos, Nonlinear Optical Thermometry — A Novel Temperature Sensing Strategy via Second Harmonic Generation (SHG) and Upconversion Luminescence in $BaTiO_3$: Ho^{3+}, Yb^{3+} Perovskite, Advanced Optical materials (IF 2020= 9.926), 2021, 9, 2100386

Teng Zheng, Małgorzata Sójka, Marcin Runowski, Przemysław Woźny, Stefan Lis, and Eugeniusz Zych, Tm^{2+} Activated SrB_4O_7 Bifunctional Sensor of Temperature and Pressure — Highly Sensitive, Multi-Parameter Luminescence Thermometry and Manometry, Advanced Optical materials (IF 2020= 9.926), 2021, 2101507.

Teng Zheng, Marcin Runowski, Przemysław Woźny, Stefan Lis, Victor Lavin, Huge enhancement of Sm^{2+} emission via Eu^{2+} energy transfer in a SrB_4O_7 pressure sensor, Journal of Materials Chemistry C (IF 2020=7.393), 2020, 8, 4810-4817(8).

Teng Zheng, Marcin Runowski, Przemysław Woźny, Stefan Lis, Influence of matrix on the luminescence properties of Eu^{2+}/Eu^{3+} doped strontium borates: SrB_4O_7, SrB_2O_4 and $Sr_3(BO_3)_2$, exhibiting multicolor tunable emission, Journal of Alloys and Compounds (IF2020= 5.316), 2020, 822, 153511-153519 (9).

Teng Zheng, Marcin Runowski, Przemysław Woźny, Bolesław Barszcz, Stefan Lis, Mauricio Vega, Jaime Llanos, Kevin Soler-Carracedo and Inocencio R. Martín, Boltzmann vs. non-Boltzmann (non-linear) Thermometry - Yb^{3+}-Er^{3+} Activated Dual-mode Thermometer and Phase Transition Sensor via Second Harmonic Generation, Journal of Alloys and Compounds, Journal of Alloys and Compounds (IF2020= 5.316), 2022, 906, 164329.

Teng Zheng, Marcin Runowski, Plácida Rodríguez-Hernández, Alfonso Muñoz, Francisco J. Manjón, Małgorzata Sójka, Markus Suta, Eugeniusz Zych, Stefan Lis and Víctor Lavín, Pressure-driven Configurational Crossover between $4f^7$ and $4f^65d^1$ States – Giant Enhancement of Narrow Eu^{2+} UV-Emission Lines in SrB_4O_7 for Luminescence Manometry, Acta Materialia, 10.1016/j.actamat.2022.117886.

I contributed to these papers in many ways, e.g., conceptualization, writing - review & editing, supervision, resources, project administration, funding acquisition, conceptualization, writing - review & editing, visualization, data curation, etc.

Poznań, 22-03-29
(rr-mm-dd)

(legible signature)

Dr hab. Marcin Runowski
(names and surnames of the co-author)

Załącznik Nr 10
do zasad

Universidad de La Laguna
(full name of the unit represented by the author)

STATEMENT

I declare that in the doctoral dissertation entitled:

Lanthanide (III or II) activated SrB_4O_7 and $BaTiO_3$ materials for Luminescent Manometry and Non-linear Optical Thermometry

my contribution consisted of:

I am co-author of the papers:

Teng Zheng, Marcin Runowski, Inocencio R. Martín, Stefan Lis, Mauricio Vega, and Jaime Llanos, Nonlinear Optical Thermometry — A Novel Temperature Sensing Strategy via Second Harmonic Generation (SHG) and Upconversion Luminescence in $BaTiO_3$: Ho^{3+}, Yb^{3+} Perovskite, Advanced Optical materials, 2021, 9, 2100386

Teng Zheng, Małgorzata Sójka, Marcin Runowski, Przemysław Woźny, Stefan Lis, and Eugeniusz Zych, Tm^{2+} Activated SrB_4O_7 Bifunctional Sensor of Temperature and Pressure — Highly Sensitive, Multi-Parameter Luminescence Thermometry and Manometry, Advanced Optical materials, 2021, 2101507.

Teng Zheng, Marcin Runowski, Przemysław Woźny, Stefan Lis, Victor Lavin, Huge enhancement of Sm^{2+} emission via Eu^{2+} energy transfer in a SrB_4O_7 pressure sensor, Journal of Materials Chemistry C, 2020, 8, 4810-4817(8).

Teng Zheng, Marcin Runowski, Przemysław Woźny, Stefan Lis, Influence of matrix on the luminescence properties of Eu^{2+}/Eu^{3+} doped strontium borates: SrB_4O_7, SrB_2O_4 and $Sr_3(BO_3)_2$, exhibiting multicolor tunable emission, Journal of Alloys and Compounds, 2020, 822, 153511-153519 (9).

Teng Zheng, Marcin Runowski, Przemysław Woźny, Bolesław Barszcz, Stefan Lis, Mauricio Vega, Jaime Llanos, Kevin Soler-Carracedo and Inocencio R. Martín, Boltzmann vs. non-Boltzmann (non-linear) Thermometry - Yb^{3+}-Er^{3+} Activated Dual-mode Thermometer and Phase Transition Sensor via Second Harmonic Generation, Journal of Alloys and Compounds, Journal of Alloys and Compounds, 2022, 906, 164329.

Teng Zheng, Marcin Runowski, Plácida Rodríguez-Hernández, Alfonso Muñoz, Francisco J. Manjón, Małgorzata Sójka, Markus Suta, Eugeniusz Zych, Stefan Lis and Víctor Lavín, Pressure-driven Configurational Crossover between $4f^7$ and $4f^65d^1$ States – Giant Enhancement of Narrow Eu^{2+} UV-Emission Lines in SrB_4O_7 for Luminescence Manometry, Acta Materialia, 10.1016/j.actamat.2022.117886.

I contributed to these papers in many ways, e.g., conceptualization, writing - review & editing of the manuscript, supervision, resources, project administration, funding acquisition, visualization, data curation, etc.

La Laguna, Spain. 2022.03.31
(rr-mm-dd)

(legible signature)

Universidad Católica del Norte

Quimica UCN

Prof. Dr. Jaime Llanos
(names and surnames of the co-author)

Załącznik Nr 10

do zasad

Universidad Católica del Norte
(full name of the unit represented by the author)

STATEMENT

I declare that in the doctoral dissertation entitled:

Lanthanide (III or II) activated SrB_4O_7 and $BaTiO_3$ materials for Luminescent Manometry and Non-linear Optical Thermometry my contribution consisted of:

I am co-author of the papers:

Teng Zheng, Marcin Runowski, Inocencio R. Martín, Stefan Lis, Mauricio Vega, and Jaime Llanos, Nonlinear Optical Thermometry — A Novel Temperature Sensing Strategy via Second Harmonic Generation (SHG) and Upconversion Luminescence in $BaTiO_3$: Ho^{3+}, Yb^{3+} Perovskite, Advanced Optical materials, 2021, 9, 2100386

Teng Zheng, Marcin Runowski, Przemysław Woźny, Bolesław Barszcz, Stefan Lis, Mauricio Vega, Jaime Llanos, Kevin Soler-Carracedo and Inocencio R. Martín, Boltzmann vs. non-Boltzmann (non-linear) Thermometry - Yb^{3+}-Er^{3+} Activated Dual-mode Thermometer and Phase Transition Sensor via Second Harmonic Generation, Journal of Alloys and Compounds, Journal of Alloys and Compounds, 2022, 906, 164329.

I contributed to these papers in many ways, e.g., synthesis of the $BaTiO_3$ materials, visualization, data curation, funding acquisition, etc.

Antofagasta, Chile, 2022-03-31

Dr. Jaime Llanos

Antofagasta
Avda. Angamos 0610
Fono: (55) 2355 624
www.ucn.cl

MSc Kevin Soler-Carracedo
(names and surnames of the co-author)

Universidad de La Laguna
(full name of the unit represented by the author)

Załącznik Nr 10
do zasad

STATEMENT

I declare that in the doctoral dissertation entitled:

Lanthanide (III or II) activated SrB_4O_7 and $BaTiO_3$ materials for Luminescent Manometry and Non-linear Optical Thermometry

my contribution consisted of:

I am co-authors of the paper:

Teng Zheng, Marcin Runowski, Przemysław Woźny, Bolesław Barszcz, Stefan Lis, Mauricio Vega, Jaime Llanos, Kevin Soler-Carracedo and Inocencio R. Martín, Boltzmann vs. non-Boltzmann (non-linear) Thermometry - Yb^{3+}-Er^{3+} Activated Dual-mode Thermometer and Phase Transition Sensor via Second Harmonic Generation, Journal of Alloys and Compounds, Journal of Alloys and Compounds, 2022, 906, 164329.

I contributed to the paper in spectroscopic measurements, visualization, data curation, etc.

La Laguna, Spain. ....31-03-2022.....
(rr-mm-dd)

.....
(legible signature)

Prof. Dr. Plácida Rodríguez-Hernández
(names and surnames of the co-author)

Universidad de La Laguna
(full name of the unit represented by the author)

Załącznik Nr 10
do zasad

STATEMENT

I declare that in the doctoral dissertation entitled:

Lanthanide (III or II) activated SrB_4O_7 and $BaTiO_3$ materials for Luminescent Manometry and Non-linear Optical Thermometry

my contribution consisted of:

I am co-author of the paper:

Teng Zheng, Marcin Runowski, Plácida Rodríguez-Hernández, Alfonso Muñoz, Francisco J. Manjón, Małgorzata Sójka, Markus Suta, Eugeniusz Zych, Stefan Lis and Víctor Lavín, Pressure-driven Configurational Crossover between $4f^7$ and $4f^65d^1$ States – Giant Enhancement of Narrow Eu^{2+} UV-Emission Lines in SrB_4O_7 for Luminescence Manometry, Acta Materialia, 10.1016/j.actamat.2022.117886.

I contributed to the paper in theoretical calculation, data curation, etc.

La Laguna, Spain. 31 march 2022
(rr-mm-dd)
31/03/2022

Plácida Rodríguez
(legible signature)

Załącznik Nr 10
do zasad

Prof. Dr. Víctor Lavín.
Head of The Department of Physics.
Faculty of Sciences.
Universidad de La Laguna.
Apartado de Correos 456.
E-38200 San Cristóbal de La Laguna.
Santa Cruz de Tenerife.
Spain (España).
Phone: +34 922 318 321
E-mail: vlavin@ull.edu.es

STATEMENT

I declare that in the doctoral dissertation entitled:

Lanthanide (III or II) activated SrB_4O_7 and $BaTiO_3$ materials for Luminescent Manometry and Non-linear Optical Thermometry

I am co-author of the papers:

1.- Teng Zheng, Marcin Runowski, Przemysław Woźny, Stefan Lis, **Víctor Lavín**.
Huge enhancement of Sm^{2+} emission via Eu^{2+} energy transfer in a SrB_4O_7 pressure sensor,
Journal of Materials Chemistry C (IF 2020=7.393), 2020, 8, 4810-4817(8).

2.- Teng Zheng, Marcin Runowski, Plácida Rodríguez-Hernández, Alfonso Muñoz, Francisco J. Manjón, Małgorzata Sójka, Markus Suta, Eugeniusz Zych, Stefan Lis and **Víctor Lavín.**
Pressure-driven Configurational Crossover between $4f^7$ and $4f^65d^1$ States – Giant Enhancement of Narrow Eu^{2+} UV-Emission Lines in SrB_4O_7 for Luminescence Manometry,
Acta Materialia, 10.1016/j.actamat.2022.117886.

and I contributed to the papers in many ways, e.g., writing - review & editing, visualization, data curation, correction of the manuscript, supervision, resources, etc.

In San Cristóbal de La Laguna, Spain, March 31st, 2022

VÍCTOR LAVÍN

UNIVERSIDAD DE LA LAGUNA
DEPARTAMENTO DE FÍSICA

Dr. Bolesław Barszcz
(names and surnames of the co-author)

Załącznik Nr 10
do zasad

Institute of Molecular Physics, Polish Academy of Sciences
(full name of the unit represented by the author)

STATEMENT

I declare that in the doctoral dissertation entitled:

Lanthanide (III or II) activated SrB_4O_7 and $BaTiO_3$ materials for Luminescent Manometry and Non-linear Optical Thermometry

my contribution consisted of:

I am co-author of the paper:

Teng Zheng, Marcin Runowski, Przemysław Woźny, Bolesław Barszcz, Stefan Lis, Mauricio Vega, Jaime Llanos, Kevin Soler-Carracedo and Inocencio R. Martín, Boltzmann vs. non-Boltzmann (non-linear) Thermometry - Yb^{3+}-Er^{3+} Activated Dual-mode Thermometer and Phase Transition Sensor via Second Harmonic Generation, Journal of Alloys and Compounds, Journal of Alloys and Compounds, 2022, 906, 164329.

I contributed to the paper in the measurements of the temperature-dependent Raman spectra, data curation etc.

Poznań, Poland. 2022-03-31
(rr-mm-dd)

Bolesław Barszcz
(legible signature)

Prof. Dr hab. Eugeniusz Zych
(names and surnames of the co-author)

Załącznik Nr 10
do zasad

University of Wrocław, Faculty of Chemistry
(full name of the unit represented by the author)

STATEMENT

I declare that in the doctoral dissertation entitled:

Lanthanide (III or II) activated SrB_4O_7 and $BaTiO_3$ materials for Luminescent Manometry and Non-linear Optical Thermometry

my contribution consisted of:

I am co-author of the paper:

Teng Zheng, Marcin Runowski, Plácida Rodríguez-Hernández, Alfonso Muñoz, Francisco J. Manjón, Małgorzata Sójka, Markus Suta, Eugeniusz Zych, Stefan Lis and Víctor Lavín, Pressure-driven Configurational Crossover between $4f^7$ and $4f^65d^1$ States – Giant Enhancement of Narrow Eu^{2+} UV-Emission Lines in SrB_4O_7 for Luminescence Manometry, Acta Materialia, 10.1016/j.actamat.2022.117886.

I contributed to the papers in writing - review & editing, supervision, resources, etc.

Wrocław, Poland. 2022-04-01
(rr-mm-dd)

……
(legible signature)

Prof. Dr hab. Francisco J. Manjón
(names and surnames of the co-author)

Załącznik Nr 10
do zasad

Universitat Politècnica de València
(full name of the unit represented by the author)

STATEMENT

I declare that in the doctoral dissertation entitled:

Lanthanide (III or II) activated SrB_4O_7 and $BaTiO_3$ materials for Luminescent Manometry and Non-linear Optical Thermometry

my contribution consisted of:

I am co-author of the paper:

Teng Zheng, Marcin Runowski, Plácida Rodríguez-Hernández, Alfonso Muñoz, Francisco J. Manjón, Małgorzata Sójka, Markus Suta, Eugeniusz Zych, Stefan Lis and Víctor Lavín, Pressure-driven Configurational Crossover between $4f^7$ and $4f^65d^1$ States – Giant Enhancement of Narrow Eu^{2+} UV-Emission Lines in SrB_4O_7 for Luminescence Manometry, Acta Materialia, 10.1016/j.actamat.2022.117886.

I contributed to the paper in performing experimental Raman scattering measurements and discussing the assignment of Raman-active modes to their corresponding theoretical symmetries.

Firmado por Francisco Javier Manjón Herrera el día 31 de marzo de 2022 con un certificado emitido por ACCVCA-120

València, Spain. 2022-03-31
(rr-mm-dd)

Francisco J. Manjón
(legible signature)

Jun.-Prof. Dr. Markus Suta
(names and surnames of the co-author)

Załącznik Nr 10
do zasad

Heinrich Heine University Düsseldorf
(full name of the unit represented by the author)

STATEMENT

I declare that in the doctoral dissertation entitled:

Lanthanide (III or II) activated SrB_4O_7 and $BaTiO_3$ materials for Luminescent Manometry and Non-linear Optical Thermometry

My contribution consisted of:

I am co-author of the paper:

Teng Zheng, Marcin Runowski, Plácida Rodríguez-Hernández, Alfonso Muñoz, Francisco J. Manjón, Małgorzata Sójka, Markus Suta, Eugeniusz Zych, Stefan Lis and Víctor Lavín, Pressure-driven Configurational Crossover between $4f^7$ and $4f^65d^1$ States – Giant Enhancement of Narrow Eu^{2+} UV-Emission Lines in SrB_4O_7 for Luminescence Manometry, Acta Materialia, 10.1016/j.actamat.2022.117886.

I contributed to the paper in writing - review & editing, data curation, correction of the manuscript, scientific comments concerning data interpretation, etc.

Institut für Anorganische Chemie
Photoaktive Materialien
Heinrich-Heine-Universität Düsseldorf
Universitätsstr. 1
40225 Düsseldorf

Düsseldorf, Germany, 31-03-2022
(rr-mm-dd)

(legible signature & stamp)

Dr. Mauricio Vega
(names and surnames of the co-author)

Universidad Católica del Norte
(full name of the unit represented by the author)

Załącznik Nr 10
do zasad

STATEMENT

I declare that in the doctoral dissertation entitled:

Lanthanide (III or II) activated SrB_4O_7 and $BaTiO_3$ materials for Luminescent Manometry and Non-linear Optical Thermometry

my contribution consisted of:

I am co-author of the paper:

Teng Zheng, Marcin Runowski, Inocencio R. Martín, Stefan Lis, Mauricio Vega, and Jaime Llanos, Nonlinear Optical Thermometry — A Novel Temperature Sensing Strategy via Second Harmonic Generation (SHG) and Upconversion Luminescence in $BaTiO_3$: Ho^{3+}, Yb^{3+} Perovskite, Advanced Optical materials, 2021, 9, 2100386

Teng Zheng, Marcin Runowski, Przemysław Woźny, Bolesław Barszcz, Stefan Lis, Mauricio Vega, Jaime Llanos, Kevin Soler-Carracedo and Inocencio R. Martín, Boltzmann vs. non-Boltzmann (non-linear) Thermometry - Yb^{3+}-Er^{3+} Activated Dual-mode Thermometer and Phase Transition Sensor via Second Harmonic Generation, Journal of Alloys and Compounds, Journal of Alloys and Compounds, 2022, 906, 164329.

I contributed to the paper in synthesis of the $BaTiO_3$ materials, visualization, data curation, etc.

Antofagasta, Chile. 01-04-2022
(rr-mm-dd)

Mauricio Vega P.
(legible signature)

Dr. Przemysław Woźny
(names and surnames of the co-author)

Załącznik Nr 10
do zasad

Adam Mickiewicz University in Poznań
(full name of the unit represented by the author)

STATEMENT

I declare that in the doctoral dissertation entitled:

Lanthanide (III or II) activated SrB_4O_7 and $BaTiO_3$ materials for Luminescent Manometry and Non-linear Optical Thermometry

my contribution consisted of:

I am co-author of the papers:

Teng Zheng, Małgorzata Sójka, Marcin Runowski, Przemysław Woźny, Stefan Lis, and Eugeniusz Zych, Tm^{2+} Activated SrB_4O_7 Bifunctional Sensor of Temperature and Pressure — Highly Sensitive, Multi-Parameter Luminescence Thermometry and Manometry, Advanced Optical materials (IF 2020= 9.926), 2021, 2101507.

Teng Zheng, Marcin Runowski, Przemysław Woźny, Stefan Lis, Victor Lavin, Huge enhancement of Sm^{2+} emission via Eu^{2+} energy transfer in a SrB_4O_7 pressure sensor, Journal of Materials Chemistry C (IF 2020=7.393), 2020, 8, 4810-4817(8).

Teng Zheng, Marcin Runowski, Przemysław Woźny, Stefan Lis, Influence of matrix on the luminescence properties of Eu^{2+}/Eu^{3+} doped strontium borates: SrB_4O_7, SrB_2O_4 and $Sr_3(BO_3)_2$, exhibiting multicolor tunable emission, Journal of Alloys and Compounds (IF2020= 5.316), 2020, 822, 153511-153519 (9).

Teng Zheng, Marcin Runowski, Przemysław Woźny, Bolesław Barszcz, Stefan Lis, Mauricio Vega, Jaime Llanos, Kevin Soler-Carracedo and Inocencio R. Martín, Boltzmann vs. non-Boltzmann (non-linear) Thermometry - Yb^{3+}-Er^{3+} Activated Dual-mode Thermometer and Phase Transition Sensor via Second Harmonic Generation, Journal of Alloys and Compounds, Journal of Alloys and Compounds (IF2020= 5.316), 2022, 906, 164329.

I contributed to the paper in many ways, e.g., spectroscopic measurements, writing - review & editing, visualization, data curation, etc.

Poznań, Poland. 2022-03-30
(rr-mm-dd)

P. Woźny
(legible signature)

Dr. Małgorzata Sójka
(names and surnames of the co-author)

Załącznik Nr 10
do zasad

University of Wrocław, Faculty of Chemistry
(full name of the unit represented by the author)

STATEMENT

I declare that in the doctoral dissertation entitled:

Lanthanide (III or II) activated SrB_4O_7 and $BaTiO_3$ materials for Luminescent Manometry and Non-linear Optical Thermometry

my contribution consisted of:

I am co-author of the paper:

Teng Zheng, Marcin Runowski, Plácida Rodríguez-Hernández, Alfonso Muñoz, Francisco J. Manjón, Małgorzata Sójka, Markus Suta, Eugeniusz Zych, Stefan Lis and Víctor Lavín, Pressure-driven Configurational Crossover between $4f^7$ and $4f^65d^1$ States – Giant Enhancement of Narrow Eu^{2+} UV-Emission Lines in SrB_4O_7 for Luminescence Manometry, Acta Materialia, 10.1016/j.actamat.2022.117886.

I contributed to the paper in low-temperature spectroscopic measurements, data curation, correction of the manuscript, comments, etc.

Wrocław, Poland 2022-03-31
(rr-mm-dd)

M. Sójka
(legible signature)

Prof. Dr. Alfonso Muñoz
(names and surnames of the co-author)

Universidad de La Laguna,
(full name of the unit represented by the author)

Załącznik Nr 10
do zasad

STATEMENT

I declare that in the doctoral dissertation entitled:

Lanthanide (III or II) activated SrB_4O_7 and $BaTiO_3$ materials for Luminescent Manometry and Non-linear Optical Thermometry

my contribution consisted of:

I am co-author of the paper:

Teng Zheng, Marcin Runowski, Plácida Rodríguez-Hernández, Alfonso Muñoz, Francisco J. Manjón, Małgorzata Sójka, Markus Suta, Eugeniusz Zych, Stefan Lis and Víctor Lavín, Pressure-driven Configurational Crossover between $4f^7$ and $4f^65d^1$ States – Giant Enhancement of Narrow Eu^{2+} UV-Emission Lines in SrB_4O_7 for Luminescence Manometry, Acta Materialia, 10.1016/j.actamat.2022.117886.

I contributed to the papers in writing - review & editing, visualization, data curation, theoretical calculation, etc.

La Laguna, Spain. March-31-2022

Prof.Dr. Alfonso Muñoz

Departamento de Física
Universidad de La Laguna

Universidad
de La Laguna

Prof. Dr. Inocencio R. Martín
(names and surnames of the co-author)

Załącznik Nr 10
do zasad

Universidad de La Laguna
(full name of the unit represented by the author)

STATEMENT

I declare that in the doctoral dissertation entitled:
Lanthanide (III or II) activated SrB_4O_7 and $BaTiO_3$ materials for Luminescent Manometry and Non-linear Optical Thermometry
My contribution consisted of:
I am co-author of the papers:
Teng Zheng, Marcin Runowski, Inocencio R. Martín, Stefan Lis, Mauricio Vega, and Jaime Llanos, Nonlinear Optical Thermometry — A Novel Temperature Sensing Strategy via Second Harmonic Generation (SHG) and Upconversion Luminescence in $BaTiO_3$: Ho^{3+}, Yb^{3+} Perovskite, Advanced Optical materials, 2021, 9, 2100386
Teng Zheng, Marcin Runowski, Przemysław Woźny, Bolesław Barszcz, Stefan Lis, Mauricio Vega, Jaime Llanos, Kevin Soler-Carracedo and Inocencio R. Martín, Boltzmann vs. non-Boltzmann (non-linear) Thermometry - Yb^{3+}-Er^{3+} Activated Dual-mode Thermometer and Phase Transition Sensor via Second Harmonic Generation, Journal of Alloys and Compounds, Journal of Alloys and Compounds, 2022, 906, 164329.

I contributed to these papers in many ways, e.g., conceptualization, supervision, resources, project administration, funding acquisition, writing - review & editing, visualization, data curation, etc.

La Laguna, Spain 2022-03-31 signature